Freie Universität Berlin

HZB Helmholtz Zentrum Berlin

Investigations of Photoinduced Ultrafast Dynamics in Metal Coordination Complexes Using Time-Resolved Photoemission and Absorption Spectroscopy

Im Fachbereich Physik der Freie Universität Berlin
eingereichte Dissertation

zur Erlangung des akademischen Grades eines Doktors der Naturwissenschaften (Dr. rer. nat.)

vorgelegt von

Azhr Abdulzahraa Raheem

Berlin
2019

1st Reviewer:	Dr. Iain Wilkinson
2nd Reviewer:	Prof. Dr. Martin Weinelt

Disputation am: 08. Oktober 2019

Contents

List of Tables

List of Figures

DEDICATION

For

My Wife

and my children

Murtadha

Zaid

Mohammed

and **Maryam**

Abstract

Photoinduced charge flow in transition-metal (TM) complexes is a driving fundamental process in light-harvesting catalytic materials. Thus, interrogating the timescales and mechanisms of these processes- that occur on ultrafast timescales- helps to facilitate the development of efficient molecular devices, such as switches. Here, the electronic structure and excited state dynamics of two prototypical TM complexes, ferricyanide $[Fe(CN)_6]^{3-}$ and nitroprusside $[Fe(CN)_5NO]^{2-}$, were investigated as promising candidates as molecular switches. The associated time-dependent spectra of the ground and valence excited states and ultrafast kinetics are reported. These studies represent a necessary step towards establishing the ultrashort pulse extreme ultraviolet (XUV) time-resolved photoelectron spectroscopy (TRPES) technique as a means to investigate dynamic electronic structure in aqueous solution.

Femtosecond TRPES was applied to investigate isomerization of aqueous nitroprusside. Using ultrashort pump pulses at two different energies, different metal-to-ligand charge transfer (MLCT) excited states were populated, leading to different isomerization processes and final states. Photoisomerization triggered at 2.48 eV generated a metastable state, MS2, via rotation of the NO ligand by 90°. Similarly, 3.1 eV excitation induced a NO ligand rotation of 180°, and formation of another metastable state, MS1. In both cases, the photoelectron yield was sensitive to this rotational isomerization. By probing the system with ultrashort XUV pulses (21^{st} harmonic of 800 nm, 32.6 eV) the population dynamics of the MS1 and MS2 states were observed. The TRPES spectra highlighted a short-lived intermediate state on the way to MS2 population. The complete rotation (90° rotation angle) was found to occur in less than 240 fs after photoexcitation. Further TRPES results highlight generation of the MS1 state (180° rotation angle) on a considerably longer timescale, $\sim$7.8 ps after optical excitation.

In the ferricyanide studies, both femtosecond TRPES and UV/Vis transient absorption spectroscopy (TA) experiments were performed to investigate the ultrafast electronic dynamics. 32.6 eV and white light supercontinuum probes were used in the TRPES and TA experiments, respectively. A detailed investigation of the relaxation pathways following optical ligand-to-metal charge transfer (LMCT) excitation was, therefore, performed to obtain spectral and kinetic information on the energy- and charge-flow processes occurring in aqueous ferricyanide. Additionally, in the TRPES experiments, different polarization alignments of the pump and probe beams were used to investigate and identify the electronic dynamics. Both methods yielded information about the initial and subsequently populated electronic states. Strong evidence for spin crossover followed by geometrical distortions due to vibronic interactions in the excited electronic states was observed. Electronic relaxation was found to occur on $<$200 fs timescales for the LMCT state and $<$1 ps for the subsequently populated ligand field, LF, state(s). In contrast, the repopulation of the ground state, via an additional unidentified excited state, ES, is considerably slower. The PES results corroborate previous findings, indicating an ES lifetime of 10-20 ps, while the TA results indicate lifetimes of $\sim$ 150 ps.

Deutsche Kurzfassung

Die photoinduzierte Ladungstransferdynamik in Übergangsmetall (transition metal, TM) Koordinationskomplexen ist einer der wichtigsten grundlegenden Schritte in Lichtsammelprozessen in katalytischen Materialien. Die Beschreibung der Eigenschaften des angeregten Zustands kann dazu beitragen, die auf ultraschnellen Zeitskalen stattfindenden physikalischen und chemischen Prozesse besser zu verstehen, und damit die Entwicklung funktioneller molekularer Schalter zu erleichtern. In dieser Arbeit wird die elektronische Struktur zweier prototypischer TM-Komplexe, Ferricyanid $[Fe(CN)_6]^{3-}$ und Natriumnitrosylprussiat $[Fe(CN)_5NO]^{2-}$ untersucht. Solche Moleküle sind vielversprechende Kandidaten für die Verwendung als molekulare Schalter aufgrund der in ihnen gefundenen lichtinduzierten Änderungen der Konformationsisomerie. Mittels zeitaufgelöster Experimente konnten sowohl die zeitabhängigen Spektren des Grundzustands und der angeregten Zustände, als auch deren assoziierte ultraschnelle Kinetiken gemessen werden. Im ersten Teil dieser Arbeit wird.

Femtosekunden-Photoelektronenspektroskopie (TRPES) zur Untersuchung der Isomerisierungsprozesse von Natriumnitrosylprussiat in wässriger Lösung eingesetzt. Die Isomerisierung ist gekennzeichnet durch Drehungen des NO-Liganden um 90° bzw. 180°, welche durch. Photoanregung bei 2.48 eV bzw. 3.1 eV ausgelöst werden. In beiden Fällen, die als metastabile Zustände MS2 bzw. MS1 bezeichnet werden, ist die Elektronenemissionsausbeute empfindlich auf diese Rotationsisomerisierung. Durch Abfragen des Systems mit ultrakurzen extremultravioletten (XUV) Pulsen (32.55 eV, 21^{te} Harmonische der Fundamentalwellenlänge von 800 nm) werden Informationen über die Population beider metastabiler Zustände gesammelt. Die PES-Spektren liefern Hinweise auf einen kurzlebigen Zwischenzustand während des Aufbaus der Konfiguration MS2. Wir konnten zeigen, dass der komplette Rotationsprozess um 90° nach Photoanregung in weniger als 240 fs auftritt, während die Erzeugung des Zustandes MS1 mit ca. 7.8 ps erheblich länger dauert.

Zur Untersuchung der Dynamik in Ferricyanid wird neben TRPES auch Femtosekunden transiente Absorptionsspektroskopie (TA) eingesetzt, wobei ein optisches Superkontinuum in den TA-Experimenten als Sonde zum Einsatz kommt. Die Kombination dieser beiden Techniken ermöglicht eine gründliche Untersuchung der Relaxationswege nach optischer Ligand-zu-Metall-Ladungstransfer-Anregung (LMCT), und somit der Energie- und Ladungstransferprozesse von Ferricyanid in wässriger Lösung. Es finden sich starke Anzeichen für einen sogenannten Spin Crossover, welcher zu geometrischen Verzerrungen durch vibronische Wechselwirkungen in den angeregten elektronischen Zuständen führt. Die Relaxation des LMCT Zustandes erfolgt auf Zeitskalen von < 200 fs, während der nachfolgende Ligandenfeld (LF) Zustand mit < 1 ps zerfällt. Im Gegensatz dazu ist die Rückkehr in den Grundzustand über einen zusätzlichen angeregten Zustand, ES, deutlich langsamer. Die vorliegenden PES-Ergebnisse bestätigen die Ergebnisse in der Literatur und weisen auf eine Lebensdauer von 10-20 ps für den ES Zustand hin, während die TA-Ergebnisse Lebensdauern von 150 ps zeigen.

Chapter 1

General Overview and Motivations

Understanding the structure of atomic and molecular systems, which are the basic building units of materials in nature, and revealing the dynamics of their interactions with light is of fundamental relevance throughout different fields of science [1]. In particular, knowledge of the fundamental properties of light-harvesting materials facilitates the control of their physical and chemical behavior and the efficient development of functional devices. Furthermore, insights into the photoinduced processes occurring in materials, such as photosynthesis or photoswitching, provides new information that can be used to optimize solutions for efficient light-energy harvesting devices.

One of the grand challenges in the exploration of the structure and function of molecular and material systems is the investigation of the complex dynamics of correlated nuclear geometry and electron configuration rearrangement following photo-excitation processes. Such investigations require the development and application of different methods and techniques to gain a full description of the microscopic behavior of atomic, molecular and material systems. In addition, the dynamic photo-physical and photo-chemical processes that occur in molecular and material systems such as motion of nuclei, coupled rearrangement of electronic configurations, and associated breaking/ forming of chemical bonds, take place on femto to nanosecond timescales. Accordingly, the time-domain interrogation of such fast dynamics requires ultrashort time-resolution and precision timing equipment. Different spectroscopic methods have been established to acquire such information [2–6]. With the development of ultrashort pulse laser sources, the evolution of time-resolved spectroscopic investigations has provided comprehensive insights into the dynamic behavior and, hence, mechanisms of operation of functional materials. The combination of ultrashort pulsed lasers and high-performance detection devices has provided powerful tools to directly investigate transient species in molecular and material systems.

Static electronic structure can be interrogated by applying a single light beam and measuring the absorption of, florescence from, or electron emission from molecular or material systems. Implementation of a pair of precisely-timed ultrashort laser pulses in a pump-probe configuration allows investigation of the electronic dynamics during a time interval following an

initial photo-excitation process [7, 8]. Such time-resolved spectroscopy techniques have proven extremely useful in interrogating the population dynamics of electronically excited states of molecular systems [9–13]. Various approaches of pump-probe techniques are employed as spectroscopic probes, including Raman spectroscopy, florescence spectroscopy, photoemission spectroscopy, and transient absorption spectroscopy [2, 14–16]. Employing these techniques across different spectral ranges, a comprehensive suite of probes of molecular behavior are available, with tunable light sources covering a wide range of photon energies with high temporal resolution and selective probes of different molecular/material properties. Such methodologies can provide us with complete photophysical information of molecular systems in the gas, solid, and liquid states [13, 17]. One route to extract such information in the time domain is to perform pump-probe spectroscopy experiments. Here, a photophysicochemical processes is initiated in a sample by applying a first (pump) pulse with a desired photon energy. The temporal evolution of the system is monitored by creating a detectable signal by applying a delayed probe pulse at a well-defined delay time. The arrival time of the two laser pulses is adjusted by precisely controlling the time delay between them, either electronically or via differential path lengths. The signal which is produced by the second (probe) pulse, ideally gives us information about the electron (and potentially nuclear geometry) dynamics of the system under investigation. By using this method, the evolution of different electronically excited states can be followed within the range of applied time delay between the two pulses on timescales greater than the duration of the pulses employed. One should also mention that the photophysicochemical characteristics of the photo-active molecules can be comprehensively understood by combining results obtained from various spectroscopic methods. Using the information obtained from multiple different methods represents an incisive approach to ascertain knowledge of various excited state processes such as isomerization, spin crossover, intramolecular charge transfer, etc. [18–21].

Nowadays, the development of photo-active materials is of great interest in many fields of physics, chemistry, biology, and material science. In novel materials, excited molecular states with particularly desirable properties-such as light-emission, energy conversion via artificial photosynthesis, and fast photosensitizers- are formed, making these materials useful in different application spaces [22–24]. The associated photoactive molecules can be used as components in much larger molecular devices, which are called photoactive functional materials. Such devices are considered for the development of future energy sources based on photovoltaics and photocatalysis and are capable of converting light energy into chemical energy via electronic transitions in molecules [25–28].

A particularly interesting class of photo-active systems is the transition-metal (TM) coordination complexes. These complexes efficiently absorb electromagnetic radiation over a broad range of photon energies extending across the UV and visible spectral regions. The photophysicochemical properties of TM systems, as well as the variety of their excited states are particularly interesting aspects, making these compounds attractive for a range of innovative

technologies [29]. TM complexes can be applied in many scientific and medical fields such as photodynamic therapy [30–32], dye-sensitized solar cells [33–35], artificial photosynthesis [25, 36], photocatalysis [37], biological imaging [32, 38], sensors [32], and photoswitching molecular systems [39].

Among TM coordination complexes, compounds containing iron as the central metal are of special interest. The high natural abundance of iron and the cheapness of its complexes make it one of the promising candidates for various scientific applications such as, photocatalysis, magnetic switches, data storage, data display, and optical devices [40–45]. Furthermore, because of the importance of understanding fundamental processes in nature, the study of the electron dynamics of such compounds is an important issue for the scientific community and society more generally .

In the present study, the photoemission spectroscopy (PES) and transient absorption spectroscopy (TAS) techniques have been employed to investigate the photoinduced electron dynamics of two different molecular systems in aqueous solution. In both studies, the photon energy of the pump pulse was tuned to efficiently promote the molecular system from the electronic ground state to electronically excited states which exhibit an intramolecular charge transfer between the metal center and ligands in the molecule of interest.

With the PES technique, an extreme ultraviolet (XUV) probe pulse of sufficiently high photon energy was applied in order to overcome the binding energy of the valence electrons and, thus, to promote them to the ionization continuum. The recorded PES spectra contain significant contributions from the populated excited states, allowing us to extract qualitative and quantitative information about the transient electronic structure of the molecule. The advantage of photoemission spectroscopy is that it allows determination of the absolute binding energies of the electronic configurations of static and transient states of the molecules under investigation. However, in the photoemission experiment, high vacuum conditions are required for the detection of the nascent photoelectron kinetic energy distributions, a challenging thing to achieve in the vicinity of a volatile liquid sample. In order to facilitate such experiments in the liquid phase, the liquid micro-jet technique was used to inject the sample into the laser-sample interaction region as an aqueous solution.

UV/Visible transient absorption spectroscopy (TAS) is also used in the present work. In this technique, the electronic dynamics are monitored by determining the changes in the absorption of a broadband probe spectrum following the application of pump excitation pulses. White light continuum generation is used as a probe source in these experiments.

The spectroscopic work in this thesis focuses on the evolution of the excited state electronic structure of two different molecular systems, namely nitroprusside $[Fe^{II}(CN)_5NO]^{2-}$ and ferricyanide $[Fe^{III}(CN)_6]^{3-}$ have been studied as photo-active molecular systems. Observation of the formation of linkage isomers in nitroprusside in an aqueous solution is investigated. Femtosecond time-resolved spectroscopy of nitroprusside allowed us to probe the early-time dynamics of transient species formation and isomerization following excitation to two different

electronic states. The lifetimes of the transient states were accordingly extracted. The ferricyanide model system underwent intramolecular charge transfer upon excitation with visible laser light. For the ferricyanide system, the photoinduced dynamics were studied by applying pump-probe polarization-dependent transient PES and TAS spectroscopy. These studies allowed points of contention regarding the nature of the initially photoexcited states in ferricyanide to be clarified.

This thesis consists of the following chapters: Chapter 2 gives an introduction to transition metal complexes, including a general description of the photoinduced processes that occur in the samples which are studied in the present work. It also gives an overview of the preexisting literature on the mechanism of isomerization in nitroprusside and excited state relaxation dynamics in ferricyanide molecules. Chapter 3 presents the methodological background relevant to the transient photoemission and absorption spectroscopy experiments. In Chapter 4, a description of the two spectroscopic setups, including the laser system and the generation of the pump and probe pulses, is presented. In Chapter 5, the experimental data and the interpretation of the ultrafast kinetics of linkage isomerism in nitroprusside aqueous solution is presented. Chapter 6 reports and discusses the experimental results of the ferricyanide aqueous solution, where the excited state electron dynamics were studied using different polarizations of the pump beam. Finally, Chapter 7 gives a conclusion of the findings obtained in this work for both molecular systems.

Chapter 2

Introduction

2.1 Transition Metal Complexes

Transition metal (TM) complexes are species of ligand coordination compounds which play important roles in biology, chemistry, physics, and material science. Accordingly, an understanding of their molecular structure and behavior, drives their application in the chemical industry and gives vital insights into the function of biological systems [46, 47]. Small TM molecular systems are studied as models in many fields where complex interactions involving multiple electronic states are prevalent. These include material synthesis, catalysis, solar energy conversion, photophysics, and photochemistry research [48–52]. Light-induced population of excited states of the TM complexes in the UV-visible range of the electromagnetic spectrum is an important facet of these compounds, resulting in reactions such as photochemical substitution, isomerization, and dissociation/radical formation [53–55]. Such photoactive materials provide an efficient way of energy harvesting in the UV/Visible spectral ranges [39, 56]. In general, the TM molecules consist of a central d-block metal atom or ion (such as Cr, Mn, Fe, Co, Ni, Ru) surrounded and bonded to a group of ionic or molecular functional groups which are referred to as ligands (like CN, CO, pyridine). In TM complexes, the central metal ion forms bonds with a number of ligands, according to the coordination number which is specific to the metal atom and potentially its oxidation state.

2.1.1 Electronic Configurations of Transition Metal Complexes

The characterization of photo-active molecules in transient excited states and the description of the photophysicochemical behavior of molecular systems can be understood through analysis of the molecular orbitals. TM complexes, having an open d-shell, can possess coordination numbers between 2 and 9, which are decisive in determining the mechanisms of the light-driven processes occurring in transition metal complexes [57–60]. Coordination numbers from four to six are rather common and such TM complexes have been studied extensively. For

complexes which have coordination numbers of four and five, the molecular symmetry group can be described as tetrahedral or square-planar with associated group symmetries of (T_d) or (D_{4h}), respectively, whereas hexa-coordinated complexes can be described as having octahedral (O_h) symmetry. In particular, in the present work, the samples of interest display a coordination number of six and octahedral symmetry.

The characteristics of metal-ligand configurations in the TM complexes are often adequately explained by ligand-field theory [61]. This theory explains the magnetic and electric properties, stabilities, color, reactivity, and the electronic and geometrical structures of TM complexes by describing the composition of the molecular orbitals and revealing the bonding nature between the metal core and the ligands [61, 62]. Likewise, this theory successfully describes the hybridization between the metal and ligand orbitals according to the orbital symmetry [61, 62]. The theory assumes that the molecular orbitals are formed via linear combinations of the metal atomic orbitals (d, s and p) and the ligand molecular orbitals (σ, π) [62].

In octahedral complexes, the frontier molecular orbitals of the central metal are normally the partially filled d orbitals. The atomic d orbital electron probability distributions have five different shapes (d_{z^2}, $d_{x^2-y^2}$, d_{xy}, d_{yz}, and d_{zx}) that can be aligned relative to the x, y, and z molecular axes. The interaction between the ligand orbitals and the orbital of the metal center gives rise to the formation of both bonding and antibonding orbitals in TM complexes [62]. As a result of this interaction and the associated electric field in an octahedral system, the five orbitals of the center atom are split into the threefold degenerate e_g set and twofold degenerate t_{2g} set. The electrons in the d_{z^2} and $d_{x^2-y^2}$ orbitals, which belong to the e_g set, have higher energy compared to the electrons of d_{xy}, d_{xz} and d_{yz} orbitals of symmetry type t_{2g} (see figure 2.1 for illustration). The separation in energy between the t_{2g} and e_g orbitals is named the ligand field splitting parameter and is symbolized (Δ_o). The value of the ligand field splitting parameter depends on many factors, including the nature of the ligands positioned around the central metal ion, and the number of electrons in the d-shell of the central metal ion [63]. For coordination compounds such as TM complexes, the energy difference between the split d-orbitals often defines the color of the coordination complex, as the associated optical absorption bands occur in the visible range. In general, the photoinduced electronic changes that occur following absorption represent interesting and fundamental effects which influence the useful properties of TM complexes.

Different excited states can be populated by irradiation with light, via electric-dipole-allowed electronic transitions that satisfy the Franck-Condon principle [64]. One of the interesting properties of TM complexes is the variety of excited states that occur, which depend on the electronic configuration, the molecular geometric, and the type of the bond between the central metal atom and ligands. Namely, the rich amount and tailorability of excited states in TM complexes leads to their outstanding photophysical and photochemical properties and high photo-reactivity.

Under photo-excitation of TM complexes, electrons can be transferred from or to the asso-

ciated ligands, i.e., ligand-to-metal charge transfer (LMCT) or metal-to-ligand charge transfer (MLCT) can occur. Transferring electron density between the metal-centered states (MC), the ligand field states (LF), and between ligands (ligand-to-ligand charge transfer states, LLCT), additional transitions can take place [65–68]. Following the aforementioned charge transfer transitions, ultrafast processes such as internal conversion and intersystem crossing (ISC) and the population of long-lived excited states may also take place in TM complexes [22, 69]. Thermodynamically, excited states are unstable, decaying via either photon emission or non-radiatively, or potentially leading to the dissociation of one or more metal-ligand bonds [69–71]. The mechanism of electronic relaxation from the excited state(s) to the ground state can involve the formation of metastable (MS) states. Such transitions from the initial excited state to other excited states can occur depending on the state spin multiplicities, proximities of the states in nuclear coordinate space, the state coupling matrix elements and the excited state coupled electronic-nuclear dynamics [14, 72–74]. Relaxation to other electronic states can also produce changes of bond length [75] and breakage or formation of bonds [76].

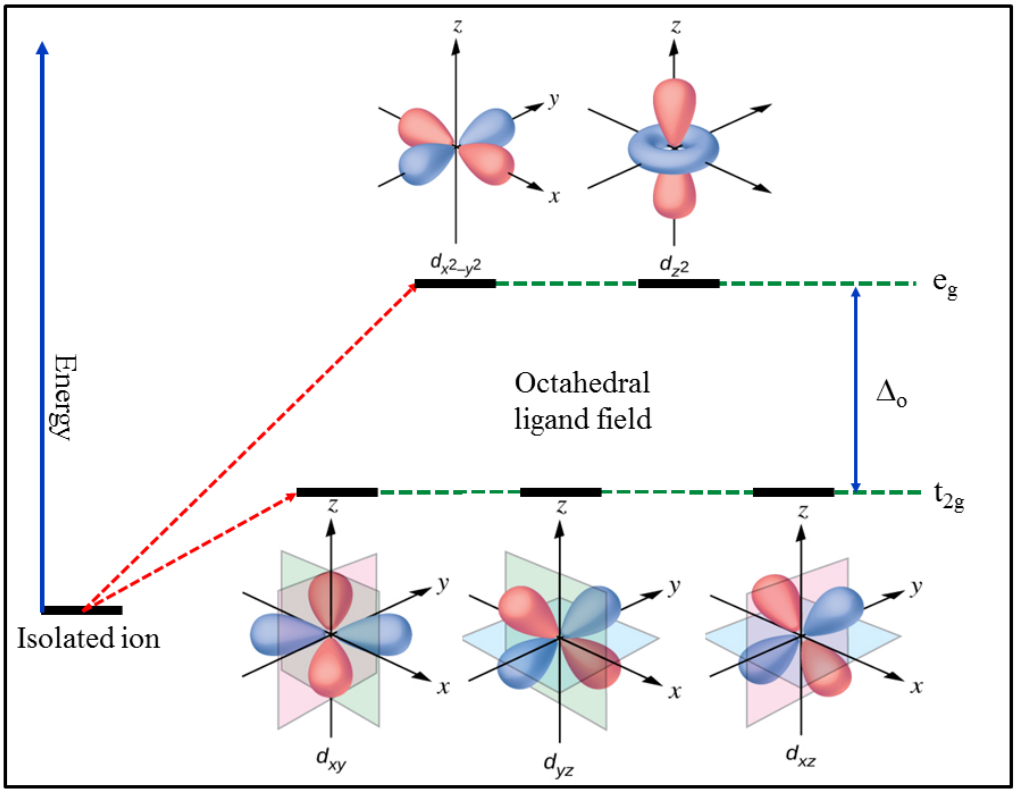

Figure 2.1: Splitting characteristics of the five d orbitals (d_{z^2}, $d_{x^2-y^2}$, d_{xy}, d_{yz}, and d_{zx}) in an octahedral geometry system and ligand field.

The photo-induced and non-radiative transitions are occurring in TM complexes responsible for the different species, kinetics, and reactions of the molecular system. The transient species, formed during the relaxation process, are associated with different electronic and/or geometric configurations of the molecule, leading to different properties compared to the ground state.

Some of these electronic states show a high sensitivity to the environment, for example by exhibiting luminescence or color changes, and thus, they are relevant for sensing, imaging, and photo-labeling applications [77, 78]. The timescale for different relaxation pathways strongly depends on the electronic configuration of the molecular system, the type of transition and its environment.

Photo-excitation generally populates a number of vibrationally excited states in the electronically excited state due to a range of non-zero Franck-Condon factors. Thus, one should also consider that a part of the relaxation behavior of the electronically excited states is associated with intra-and intermolecular vibrational energy transfer, which can potentially be monitored via vibrational and some vibronically sensitive time-resolved spectroscopies.

2.2 Isomerization

A photoisomerization process involves a light-induced transformation of a molecule from a specific geometric arrangement of the atoms into a molecule with the same molecular formula but with the atoms arranged differently in the molecule [79]. In this particular case, isomers of TM complexes are formed when one or more ligands can be connected to the metal atom(s) in different ways. The isomerization process frequently leads to changes in the chemical, physical, structural and optical properties of the molecular system [80, 81]. Thus, understanding this process is important in the application of TM complexes, particularly photo-switching and photo-chromic devices. There are two main patterns of isomerism, structural isomerism, and stereoisomerism. Structural isomerism occurs when the molecular systems have the same molecular formula but exhibit different bonding patterns and different arrangements of atoms. Whereas stereoisomerism represents compounds having the same molecular formula but differing in the relative orientation and positions of the atoms in three-dimensional space. Linkage isomerism, which is of interest in this work, is a kind of isomerism where the molecular systems have the same structure but different connectivity of ligands with the TM center. Therefore, they belong to the second type, stereoisomerism. Such metallic complexes, which can undergo photo-switching, are very important in many fields such as medicine, chemistry or physics [82–85] and spectroscopic observations of such molecules provide useful insights into the electronic relaxation processes which may occur following photo-excitation and during the isomerization and subsequent relaxation events.

2.2.1 Light-Induced Linkage-Isomers of the Nitroprusside Complex

A large family of complexes showing linkage isomerism are the nitrosyl compounds with the general composition $[ML_x(NO)]^n$, where M represents a transition metal (e.g., Fe, Ni, Ru, and Os), x represents the number of ligands, n is the total charge of the molecule, and L denotes a ligand such as F^-, Cl^-, CN^-, NH_3, and NO [39, 86, 87]. Among these complexes,

$Na_2[Fe^{II}(CN)_5NO]$ (sodium nitroprusside) is a prototypical system for studying the generation of the photoinduced nitrosyl linkage isomerism complexes [88]. Sodium nitroprusside is a TM complex with an octahedral symmetry, which consists of an iron atom center, cyanide groups, and a nitro moiety ligand. This molecule has two accessible metastable linkage isomer states $[Fe^{II}(CN)_5(\eta_1\text{-ON})]^{2-}$ and $[Fe^{II}(CN)_5(\eta_2\text{-NO})]^{2-}$ named the MS1 and MS2 states, respectively [89]. In both cases, transferring electrons from the iron atom to the NO ligand induces a rotation of the NO ligand. Thus, the formation of the metastable states MS1 and MS2 can be triggered by MLCT excitation from the iron center to the NO orbital configuration.

The molecular orbital configuration of nitroprusside was obtained through spectroscopic investigations of the energy level structure of this molecule [90, 91]. Such information is the key to understanding the charge transitions that lead to metastable states in the system. In addition, the relevant molecular orbital level diagram facilitates interpretation of the absorption spectrum. A part of the energy level diagram for $[Fe^{II}(CN)_5(ON)]^{2-}$, which was computed by Manoharan and Gray, is shown in figure 2.2 [91]. This diagram includes orbitals originating from hybridization of the π and σ-orbitals for both the CN and NO ligands and the 3d-, 4s-, and 4p-orbitals of iron. The ground state of the nitroprusside molecule has a valence shell of 42 electrons located in the hybridized orbitals shown in figure 2.2. The highest occupied molecular orbital (HOMO) in the ground state can be labeled as the $2b_2(xy)$ orbital, within the C_{4v} symmetry point group. The lowest unoccupied molecular orbital (LUMO) is labeled as the $7e(\pi^*NO)$ molecular orbital. The HOMO orbital, $2b_2(xy)$, is filled with 2 electrons, which are mainly localized at the metal atom [90,91]. The 6e orbital (HOMO-1), which lies closely to the HOMO orbital, is filled with 4 electrons and also contributes to the photo-excitation process in the UV range. The 7e orbital mainly arises from hybridization of the iron d-orbital and π(NO) orbitals, whereas the CN orbitals have a rather small contributions.

By absorption of a photon of 2.48 eV energy (500 nm), nitroprusside can be readily electronically excited via a transition from the $2b_2(xy)$ (HOMO) into the antibonding $7e(\pi^*NO)$ (LUMO) orbital. This photon energy corresponds to the 20,200 cm^{-1} separation between the $2b_2(xy)$ and 7e energy levels reported in Ref. [91]. Another transition occurs at approximately 26,600 cm^{-1} (3.1 eV or 400nm) corresponding to photo-excitation from the occupied 6e(xz,yz) (HOMO-1) molecular orbital to the antibonding $7e(\pi^*NO)$ (LUMO) [91]. These two electronic transitions initiate the population of the metastable states, MS1 and MS2, respectively. In addition, many other electronic ligand-ligand transitions can occur in nitroprusside following excitation in the UV range. However, these transitions are beyond the focus of the present work.

Relative information about the orbital energy levels can be experimentally obtained by measuring the UV/Vis absorption spectra of the sample. The spectral shape of the absorption bands depends on the differences in energy between the orbital energy levels at the probed nuclear geometry and their occupancy. The absorption spectrum of the sample solution,with concentration of 100 mM and using a cuvette with 0.1 mm thickness, in the wavelength range of 350-750 eV was obtained in the present work using a UV/Vis spectrophotometer (Implen, Nano). This

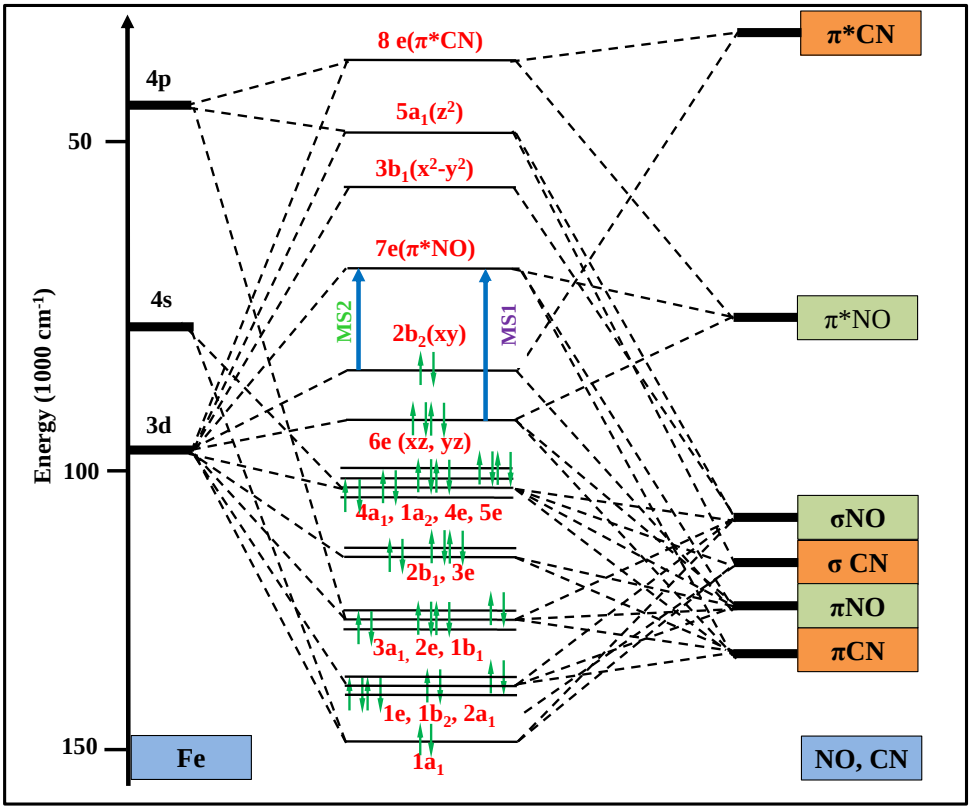

Figure 2.2: Molecular orbital diagram of the nitroprusside, $[Fe^{II}(CN)_5NO]^{2-}$, molecule [90,91]

absorption spectrum was used to characterize the initial electronic transitions in the nitroprusside sample. All measurements were performed at ambient temperature. The absorption spectrum of nitroprusside solution is shown in figure 2.3. As can be seen in the figure, the absorption spectrum exhibits two pronounced peaks. A superposition of two Gaussian profiles was used to fit the spectrum. From the fit routine, the widths and the positions of the peaks can be identified in the spectrum. One of the peaks is located at a 400 nm wavelength, corresponding to a 3.1 eV photon energy and exhibits a higher intensity than the other peak which is positioned at wavelength of a 500 nm (∼2.5 eV photon energy). These two peaks are associated with the electronic transitions between the 6e (HOMO-1) and $2b_2$ (MOMO) molecular orbitals to the antibonding7e molecular orbital (LUMO), respectively. Since the energy difference between the $2b_2$ and 6e levels was reported to be 6400 cm^{-1}, the measured aqueous absorption spectrum is in a good agreement with the calculated energy level diagram of the nitroprusside sample [91]. Both the 500 nm (2.5 eV) and 400 nm (3.1 eV) excitations correspond to a singlet-singlet MLCT transitions, which can be utilized to indirectly populate the MS2 and MS1 states in the nitroprusside molecule.

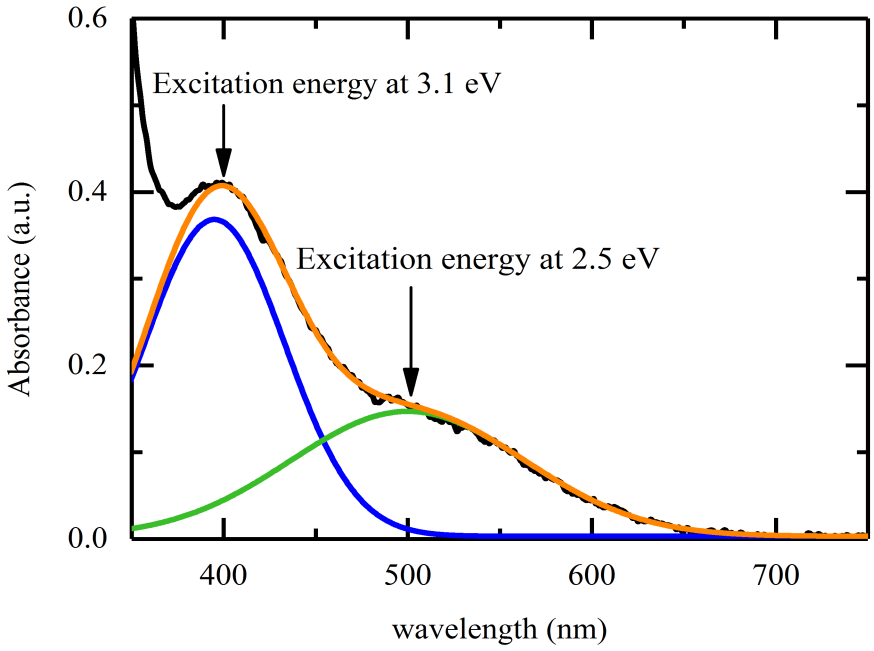

Figure 2.3: The absorbance spectrum of nitroprusside molecules in aqueous solution. The solid lines represent the decomposition of the measured spectrum into contributions of two different MLCT excitation bands characterized by Gaussian profiles. The excitation photon energies used in the PES experiment are indicated by the arrows.

2.2.2 Nature and Molecular Structure of the Metastable States MS1 and MS2 in Nitroprusside

Photoinduced rearrangements in the nitroprusside molecule are attributed to the NO ligand, which can be oriented in different ways with respect to the central metal atom, leading to the isomerization phenomenon. Besides its application as a blood-pressure-regulative agent [92], the nitroprusside compound has received much attention in the last few decades due to its applications as a prototypical system for the investigation of charge-transfer processes and isomerization reactions [93–97]. Further potential applications include a light-induced N-O release for photodynamic therapy [98], optical switching and dynamic holography [99, 100], and photoinduced chemical reactions [87]. Being initially discovered by Mössbauer spectroscopy in 1977 [94], the photophysics of isomerism have been extensively studied in crystals [101–105], and more recently also in solutions, where the $[Fe^{II}(CN)_5NO]^{2-}$ ion is spatially separated from its counter-ion [93, 106–108]. Structural and spectroscopic properties were described by many theoretical calculations, which have been performed to interpret the photophysics of this molecule [109, 110]. Different techniques have been used to investigate isomerism in nitroprusside molecules, such as transmission Mössbauer spectroscopy (TMS) [111–113], soft X-ray absorption spectroscopy [114], holography [115–117], infrared spectroscopy [106, 118], Raman spectroscopy [102], differential scanning calorimetry [96, 119], neutron diffraction [104],

and UV/Visible absorption spectroscopy [93]. These studies revealed that the final product of the isomerization reaction depends on the applied photon energy. This can be understood by considering cuts of the electronic potential energy surfaces along the coordinate of linkage isomerization (corresponding to geometry-optimized configurations of the electronic ground state for the given Fe–N–O valence angle). Figure 2.4 shows the cuts of the potential energy surface for the ground state (black curve), as well as for the lowest excited singlet (red) and triplet (green) electronic states along the ground state minimum energy path [120]. Under irradiation with blue-green light (450–560 nm), the nitroprusside molecule is promoted from its singlet ground state (GS) with a central metal and ligand NO angle of <Fe–N–O = 180° to the MLCT excited state, corresponding to the transition from the HOMO (predominately $2b_2(xy)$), to the LUMO (predominately π^*NO) [90]. This transition triggers the geometrical reorganization of the Fe–NO bond towards an almost orthogonal (<Fe–N–O$\approx$ 77°) side-on metastable configuration of NO, labeled the MS2 state [101, 104, 105].

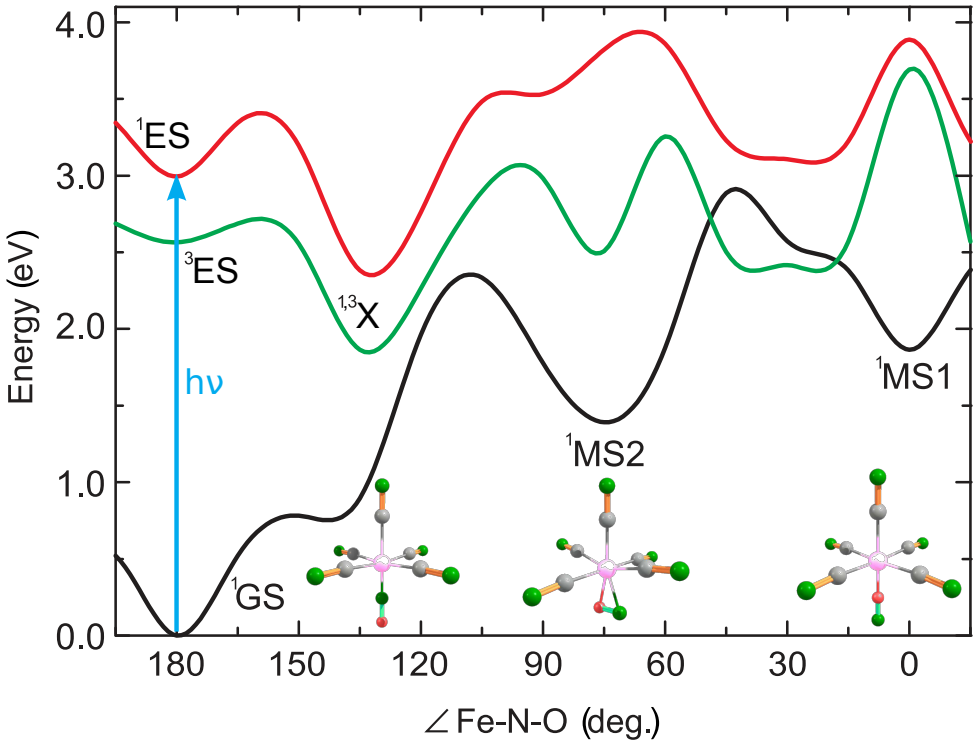

Figure 2.4: Calculated minimum energy path on the ground state potential energy surface along the coordinate of linkage isomerization of nitroprusside (relaxed potential for the fixed Fe–N–O valence angle), shown as the black curve. Also shown are cuts of the potential energy surfaces of the lowest excited singlet (red) and triplet (green) electronic states along this ground state minimum energy path. The geometric configurations of the GS, MS1, and MS2 minimum are shown as insets [120]. A possible intermediate state in a potential well on the route to MS2 is highlighted on the singlet and triplet ES states as ^{1,3}X.

Using light of shorter wavelength (<450 nm) results in the population of a higher-lying excited state via the HOMO (6e(xz,yz)) to LUMO (π^*NO) transition, not shown in figure 2.4

[90].This transition to MLCT excited state leads to the formation of the isonitrosyl (Fe–O–N) metastable configuration, MS1 [101, 104, 105], corresponding to a higher-lying local minimum of the ground state potential energy surface at <Fe–O–N = 0° (see figure2.4).

Extended irradiation can also lead to re-excitation from MS1 or MS2 into higher-lying excited states, from where relaxation to other regions of nuclear geometric coordinate space of the electronic ground state or to the metastable MS1, MS2 states is possible [119,121]. In particular, continuous exposure to radiation in the range of 900–1200 nm leads to transfer of about 30–35% of the anions from MS1 into MS2 with the rest repopulating the ground state [97, 121, 122]. In addition, the spontaneous relaxation from the MS states towards the GS equilibrium configuration proceeds radioactively and is thermally activated. Furthermore, both the MS1 and the MS2 states, can be depopulated and transferred back to the ground state when irradiated with light in the red to infrared wavelength range between 600–900 nm for MS1 and in the spectral range of 600–1200 nm for MS2, or thermally by increasing the temperature of the sample to overcome the potential barriers of these configuration minima [97, 121, 122].

2.2.3 Relaxation Dynamics of Linkage Isomerism in Nitroprusside

The photosensitive metallic nitroprusside system has drawn particular attention as a photoswitchable molecule which has unique properties that can be directly controlled by light. To understand the important components of the mechanism of the photoreaction, it is a necessity to identify the lifetimes of the metastable states.

Several research groups have studied electron dynamics in nitroprusside molecules under different conditions. Such investigations indicate that, at temperatures below 200 K, both metastable states (MS1, MS2) have lifetimes greater than 10^9 s [123, 124]. Due to this long lifetime, the nitroprusside molecule attracted the interest of many research groups as a promising functional material for use in light-energy-storage elements. Utilizing nanosecond transient absorption (TA) spectroscopy at ambient temperature, Schaniel *et al* have determined the corresponding lifetime of MS2 to be 180 ns in single crystals and 110 ns in aqueous solution [93]. They found that the population density of MS2 also depends on the intensity and pulse duration of the applied irradiation, as well as on the temperature. Another research group found that the lifetime of MS1 at room temperature is approximately 110 ns when sodium nitroprusside is dissolved in methanol [108]. More recent femtosecond transient absorption (TA) studies addressed the initial excited state relaxation processes to the metastable states directly. They revealed that the relaxation from the initial excited state ES to MS2 is monoexponential with a time constant of about 300 fs in single crystals, the concurrent direct back transfer from ES to GS was found to proceed in the same time range, and the over-all population-transfer efficiency from GS to MS2 was about 10% [100, 125]. Complementary picosecond IR transient absorption experiments in methanol solutions by Lynch *et al* have confirmed the previously reported values for the lifetimes of the MS1 and MS2 states (i.e., the relaxations from the MS1 and MS2 states

towards the GS state) [108]. The IR transient absorption technique provided evidence for an ultrafast transition (in ≤ 25 fs) from the initially populated ES to an intermediate state X, from which MS2 state was assumed to be populated with a time constant of 300 fs [108]. However, the limited time resolution of the IR transient absorption experiments did not allow the early-time dynamics of photoexcited nitroprusside molecules to be decisively studied. Additionally, for the population of the MS1 state has yet to be studied using the spectroscopic techniques. Thus, the mechanism of formation of this state is still unclear.

In general, despite previous extensive investigations, the description of the isomerism process in nitroprusside, including the determination of the lifetimes of the initially excited state, the identification of the pathways to the metastable states (MS1 and MS2), the competing relaxation channels, and the measurement of absolute electron binding energies of the involved states, is not complete and requires further investigations.

Here, we apply femtosecond transient photoelectron spectroscopy (PES), to investigate the excitation to the two lowest-lying singlet MLCT states and the subsequent early-time dynamics of the NO ligand of nitroprusside in aqueous solution. After excitation with the desired pump pulse photo energy, the electron photoemission yield produced with extreme ultraviolet (XUV) photons provides information about the lifetime of the MLCT states, as well as the population dynamics of the MS1and MS2 states. It further enables the determination of the electronic binding energies of the ground and intermediate states. The high time resolution achieved in the present experiment allows us to track the electron dynamics on a time scale shorter than those reported previously.

2.3 Excited-State Dynamics in Transition Metal Complexes

During the past decades, many studies focused on the photophysics of TM complexes, which was motivated by their potential applications in fields such as electrochemistry, catalysis, energy conversion, and switchable optical devices [49, 126–129]. Beyond these applications, these complexes have fascinating photophysical properties and serve as model systems to understand the fundamental concepts of photo-excited materials [130, 131]. For a comprehensive understanding of photo-active TM complexes, it is crucial to reveal the lifetime and pathways of their photoinduced electron dynamics [132]. With the innovation and development of ultrafast spectroscopic techniques, a new research field of studying intramolecular charge transfer processes in transition metal complexes has been established in the time domain. These studies revealed mechanism of intramolecular relaxation processes such as intersystem crossing, internal conversion, intramolecular vibrational energy redistribution, and vibrational cooling. Depending on the structure of the molecular system, such intramolecular relaxation processes can be extremely fast. Moreover, in soft-matter systems, the influence of the environment may also be a crucial factor affecting the mechanism of electron transfer and relaxation dynamics [133, 134].

2.3.1 Ferricyanide as a Model System

Transition metal complexes have been extensively studied to understand charge transfer reactions in solutions, where the solvent has important effects on the molecular dynamics. Among various transition metal complexes, hexacyanoferrate has received much attention as a suitable model system to study the effects of electron dynamics [132]. Depending on the oxidation state of the iron, this TM complex can carry a different overall negative charge in solution. In particular, ferrocyanide $[Fe^{II}(CN)_6]^{4-}$ or ferricyanide $[Fe^{III}(CN)_6]^{3-}$ molecules can be formed. Hexacyanoferrate consists of an iron metal ($Fe^{3+/2+}$) center bound to six cyanide ligands (see the right panel of figure 2.6). There were many studies on the photophysicochemical dynamics of hexacyanoferrate that aimed to reveal the ligand exchange mechanism and the photooxidation processes of this compound under different conditions. The absorption spectra of $[Fe^{III}(CN)_6]^{3-}$ and $[Fe^{II}(CN)_6]^{4-}$ were measured as early as the 1940s [135–138]. Later, ligand field transitions, giving rise to absorption bands of the complex were observed, opening the door to studies of π back-bonding [136]. The soft X-ray photoelectron (PE) spectroscopy technique was used to measure the spectra of iron aqueous solutions for both the ferrocyanide and ferricyanide complexes [139]. This study focused on the valence electronic structure of ferrous (Fe^{2+}) and ferric (Fe^{3+}) irons in hexacyano complexes dissolved in water [139]. Another research group characterized the charge transfer excitations in ferricyanide using resonant inelastic x-ray scattering [140]. The optical absorption spectroscopy technique was used to investigate the splitting of 3d energy levels in aqueous $Fe^{2+/3+}$ complexes [141]. Other researchers have focused on studying the charge-transfer-to-solvent (CTTS) effects and the binding energy (BE) of the solvated electron arising from UV photodetachment of ferrocyanide in water [142].

2.3.2 Electronic Structure of the Ferricyanide Ion

In particular, the ferricyanide anion has served as a popular molecular system for studying the intramolecular charge-transfer between central metal atoms and ligands in TM complexes. Figure 2.5 shows the absorption spectrum of ferricyanide in the UV-Visible light range at room temperature using a spectrophotometer (Implen, Nano). The sample concentration was 10 mM and a cuvette of 0.1 mm thickness was used. The absorption spectrum of ferricyanide exhibits many bands in the shown wavelength range of 230-550 nm. One should note that there are no peaks occurring at >450 nm in the ferricyanide ion spectrum, which means there are no dipole-allowed photoinduced electronic transitions in this range. Therefore, the rest of the spectrum at longer wavelengths is not shown. In the shorter wavelength absorption spectrum one can see the appearance of two overlapping peaks at 421 nm and 398 nm. Two other separated bands appear at 303 and 260 nm. According to the literature, these bands in the spectrum can be attributed to the intramolecular charge transfer transitions of LMCT character [136, 137, 143]. There are two other transitions lying on the shoulders of the peak at 303 nm, having maximum at $\sim$ 285 and 325 nm. These peaks are assigned to LF transitions [137, 143]. At lower wavelengths (higher

photon energies), not shown in the present spectrum, the absorption bands of ferricyanide are defined by MLCT transitions [21, 136, 143]. One should mention that ferricyanide ions can be prepared from salts with different cations such as Li^+, Na^+, K^+. For different cations, the relative intensities and positions of all bands of ferricyanide which appear in the absorption spectrum remain the same [144].

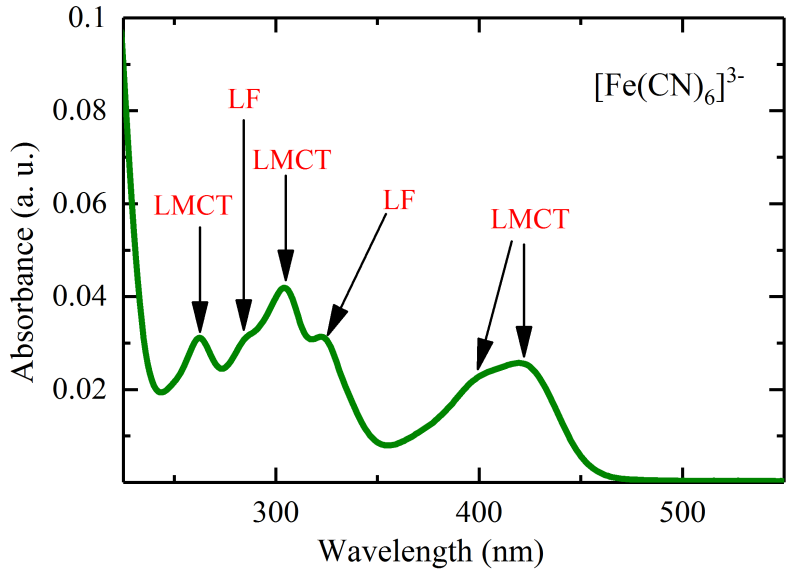

Figure 2.5: The absorption spectrum of ferricyanide in aqueous solution. The labeled peaks represent the contributions of different LMCT excitations and ligand field transitions, LF, which is taken from references [21, 136, 145]. The excitation photon energy used in the present study (TRPES) is 400 nm.

Many researches have focused on the interpretation of the absorption spectra of ferricyanide and ferrocyanide [136, 145–148]. This interpretation is based on the calculated electronic structure of ferricyanide and ferrocyanide molecules. Such ferricyanide calculations provide information about the energy level and molecular orbital scheme of this system, enabling the interpretation of the various bands of the absorption spectra. Figure 2.6 shows the molecular orbital diagram of the ground state of ferricyanide calculated using an extended Hückel molecular orbital calculation [143]. The ground state of ferricyanide has a low spin configuration [136, 145]. The d^5 shell of iron results in an octahedral symmetry of the ferricyanide complex that is split into a degenerate ^2E and a lower nondegenerate ^2A state by spin-orbit coupling effects [149]. The ground state of ferricyanide with a partially full electronic d^5 sub-shell, has the molecular configuration $((a_{1g})^2\ (t_{1u})^6\ (e_g)^4\ (t_{2g})^5\ (e_g{}^*)^0\ (t_{2g}{}^*)^0)$, where the unoccupied molecular orbitals are $e_g{}^*$ and $t_{2g}{}^*$ [150]. Figure 2.6 shows how the molecular orbitals (bonding and antibonding) are composed by combining the CN ligand orbitals and the electronic orbitals of the iron atom (s, p, d). In more details, the a_{1g} is generated from the CN orbital (σ) and 4s orbital of the iron atom [151]. The molecular orbitals t_{1u} (HOMO–2) and e_g (HOMO–1) are composed as

π_{CN}–donor (86%) + Fe(d_{xy}, d_{yz}, d_{xz}) (10%) and σ_{CN}–bonding (78%)+ Fe(d_{x^2}–d_{y^2},d_{z^2}) (21%) orbitals, respectively [152]. The HOMO, which is referred to as the t_{2g} molecular orbital in the D_{3d} symmetry point group, is generated by the combination of Fe(d_{xy}, d_{yz}, d_{xz}) (77%) + π_{CN}–acceptor (12%) + π_{CN}–donor (12%) orbitals [152]. The LUMO molecular orbital (e^*_g) is composed of Fe(d_{x^2}-$_{y^2}$, d_{z^2}) (54%) + σ_{CN}–donor (42%) + σ_{CN}–acceptor (2%) [152]. The higher energy molecular orbitals are mainly localized on the σ and π orbitals of the CN ligands [152].

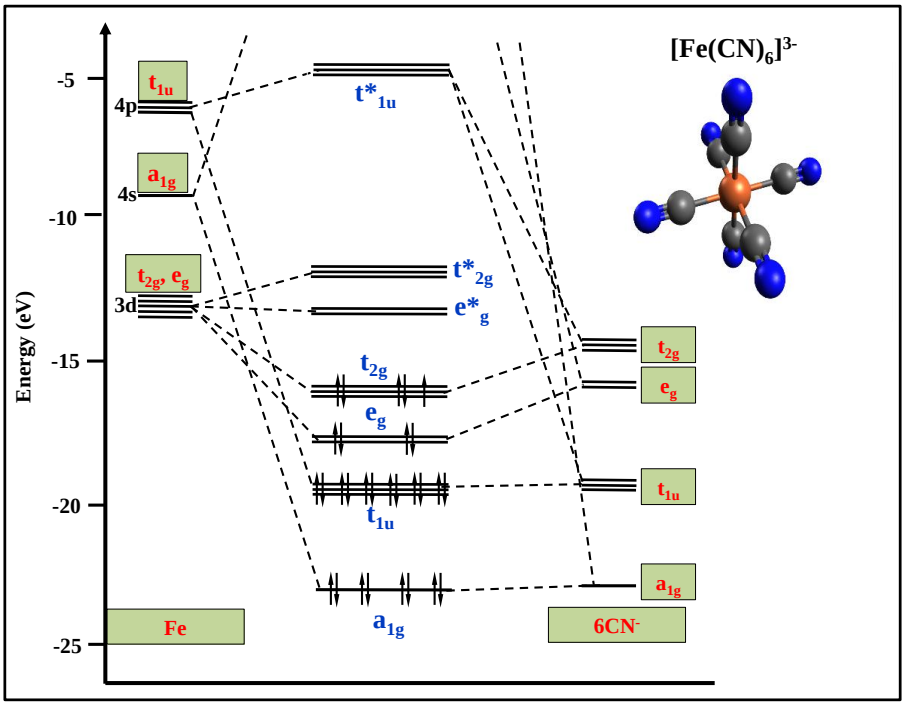

Figure 2.6: The structure and molecular orbital diagram of the ferricyanide, $[Fe(CN)_6]^{3-}$, molecule [143]

The observed positions of the bands at 420 nm (2.95 eV) and 398 nm (3.11 eV) in the absorption spectrum can be assigned as having LMCT character from the t_{1u} ligand orbital to t_{2g} and e_g metal orbital, respectively [147]. The calculated energy level scheme predicts four other charge transfer bands at 303 nm, 260 nm, 285 nm, and 325 nm to be $t_{2g} \longrightarrow t_{2u}$, $t_{2g} \longrightarrow t_{1u}$, $t_{2g} \longrightarrow e_g$, $t_{2g} \longrightarrow t_{1g}$ transitions, respectively [136, 137, 145, 153]. In the present study, the electronic transitions at a 400 nm excitation wavelength is utilized to initiate electron dynamics in the ferricyanide anion.

2.3.3 Light-Induced Relaxation Dynamics in Ferricyanide

The ultrafast photodynamics of ferricyanide have been intensively studied as a model system of a photoswitchable coordination complex [154–156]. Prampolini *et al* have investigated the structural and dynamic properties of ferro- and ferricyanide in aqueous solution by employing the IR spectroscopy technique [157]. They provided a detailed description of the structure and

dynamics of ferricyanide and ferrocyanide dissolved in water and heavy water, D_2O. Recently, Zhang *et al* have used a polarization-resolved pump (UV)-probe (mid-IR) spectroscopy to investigate the dynamics of electron-hole localization in ferricyanide after excitation of an LMCT state at a wavelength of 400 nm [154]. In this study, evidence was obtained about electron localization occurring following a structural reorganization of the system on a picosecond time scale. This charge localization depends on the solvent, preserving the octahedral symmetry of the electronic ground state in the LMCT excited state by delocalizing the ligand hole on the six ligands [134]. Later, using the experimental setup described in chapter 4, Engel *et al* have studied ferricyanide aqueous solutions using ultrafast XUV photoemission spectroscopy to monitor the electron relaxation dynamics following optical excitation at 400 nm [132]. They found evidence for ultrafast spin crossover followed by geometrical distortions in the excited electronic states. The latter result provides a rather different interpretation of the electron relaxation pathway in comparison to the localization/delocalization model [132]. Engel *et al* suggested a sequential relaxation process, giving rise to the double exponential decay of the LMCT state with time constants of 176^{+50}_{-32} fs and 749^{+129}_{-96} fs, respectively. More recently, another research group has studied the charge-transfer and impulsive electronic-vibrational energy conversion in ferricyanide aqueous solutions using ultrafast photoelectron and transient infrared techniques [154]. They considered, however, that there is a mono-exponential decay of the LMCT state to the ground state within an approximately 0.5 ps time scale. Furthermore, they found that the ferricyanide molecular system stays in the electronic ground state with significant vibrational excitation which completely decays on a 10 ps time scale.

The recent research focused on interrogating the initial population dynamics and interpreting the observed ultrafast electron dynamics in terms of a well-established energy-domain picture of the ferricyanide system [132, 154]. However, a complete description of the relaxation dynamics of this system following photo-excitation remains an open issue. In particular, the question remains about the primary and subsequently populated electronic states involved in the relaxation processes. In the present work, we aim to provide a robust description of these relaxation processes and to provide a consistent treatment of our own experiments and the somewhat contradictory literature. For this purpose, the electron population distributions associated with various states have been followed using two polarization-resolved techniques, photoelectron spectroscopy (PES) and UV/Visible transient absorption spectroscopy (TAS).

Chapter 3

Experimental Methods

3.1 Femtosecond Pump-Probe Time-Resolved Spectroscopy

The study of electronic structural dynamics of solutions and solid materials following photoexcitation is a key to understanding photo-catalytic material behaviors and their functions. Ultrafast time-resolved spectroscopy, based on sample interaction with pairs of ultrashort laser pulses, represents a powerful tool for investigating and characterizing the electronic and structural properties of transient states. In particular, femtosecond time-resolved methods facilitate the study of excited-state molecular dynamics or molecular processes such as charge and energy transfer, molecular rearrangements as well as the detection of intermediate excited states in chemical reactions [13, 158, 159]. The principle of pump-probe time-resolved spectroscopy involves at least two laser pulses where the first pulse, with appropriate photon energy, causes the photo-induced population of excited states in a sample molecular or material system at a defined time. This pulse is referred to as a pump. The subsequent relaxation processes occurring in the molecular or material system or the chemical reaction that follows after the photo-induced excitation, are interrogated by interaction with a second pulse, known as the probe. The arrival time of the probe pulse is defined and can be accurately varied on the femtosecond timescale with respect to the pump. Thus, by monitoring the probe signal as a function of the time delay between the pump and probe pulses, the time-dependent evolution of the excited state, induced by the pump pulse, can be investigated with femtosecond resolution. Here we use femtosecond time-resolved photoelectron and UV-Visible absorption spectroscopy to study electronic transitions, ionization and absorption dynamics of the studied samples. The dynamical information of electronic processes, traced by the temporal progression of the excited state signals, typically ranges from the microsecond to sub-picosecond regime. To investigate such dynamics, the transient PES and TAS techniques can be utilized in various optical configurations spanning a wide range of time-resolutions from the millisecond through to the attosecond regime. A primary concern in femtosecond (or attosecond) time-resolved experiments is minimization of the pump and probe pulse durations and the characterization of the temporal width of the combined

effect of the laser pulses, which determines the time resolution in the experiments.

3.2 Ultrashort Laser Pulses

3.2.1 Mathematical Description of Ultrashort Laser Pulses

The electric field of a laser pulse can be described as follows [160]:

$$E(z,t) = E_o(z,t)e^{-i(kz-\omega_o t+\phi_o)}, \tag{3.1}$$

where $E_o(z,t)$ is the amplitude of the electric field, k is the wave vector at central frequency ω_o, and ϕ_o represents the temporal phase of the pulses frequency components at t = 0. The wave vector and frequency of the laser pulse are connected by $k = n(\omega)\omega/c$ with $n(\omega)$ being the wavelength-dependent refractive index and c being the speed of light.

The laser pulse can be expressed, at a certain position in space where kz is set to zero, by multiplying the plane wave representation equation with a time dependent envelope, A(t), as follows [160]:

$$E(z,t) = E_o A(t)e^{i(\omega_o t-\phi(t))}, \tag{3.2}$$

where $\phi(t)$ is a time-dependent phase, that defines the relative phase between the envelope and the carrier frequency and how the frequency components of the ultrashort pulse evolve in time. The temporal shape of laser pulses are frequently described by a Gaussian envelope with the following formula:

$$A(t) = e^{-\frac{t^2}{2\sigma^2}}, \tag{3.3}$$

where σ is the width of the Gaussian envelope and is related to the Full-Width-Half-Maximum (FWHM) of the pulse by:

$$FWHM = \sqrt{2ln2}\sigma. \tag{3.4}$$

The associated temporal evolution of the electric field of such laser pulse is shown in figure 3.1a.

The laser field can also be described in the frequency domain, where the link between time and frequency is given by the Fourier transform relations [160, 161]:

$$\begin{aligned} E(\omega) &= \int_{-\infty}^{\infty} \varepsilon(t)e^{i\omega t}dt \\ \varepsilon(t) &= \frac{1}{2\pi}\int_{-\infty}^{\infty} E(\omega)e^{-i\omega t}d\omega \end{aligned} \tag{3.5}$$

The Fourier transform of a Gaussian pulse in the time-domain produces a Gaussian envelope

in the energy-domain, resulting in a complex valued spectrum with the following form [160]:

$$E_o(\omega) = \frac{E_o}{\tau\sqrt{2\pi}} e^{\frac{-(\omega-\omega_o)^2}{2\tau^2}} e^{-i\varphi(\omega)}, \tag{3.6}$$

where $\tau = 1/\sigma$ and $\varphi(\omega)$ is the spectral phase.

There is a relation between temporal and spectral characteristics of the laser field through the uncertainty principle and Fourier transform theory, which defines a lower limit for the product of the temporal width in seconds, Δt, and bandwidth, $\Delta\nu$, in Hertz. Accordingly, in order to generate laser pulses with a short duration, it is necessary to employ a sufficiently broad spectral bandwidth.

The relationship between the spectral width $\Delta\omega$ and the duration Δt of a pulse can be expressed as:

$$\Delta\omega\Delta t \geq K \tag{3.7}$$

where equality to K is the minimum value associated with the shortest pulse possible from a specified bandwidth. This corresponds to unique value of the spectral/temporal phase. The pulse shape determines the minimum value, for example this constant is 0.441 for a Gaussian function. This relationship leads to the time–energy uncertainty principle, which has several important consequences in ultrashort pulse optics and light-matter interactions.

When short optical pulses propagate through a dispersive medium the frequency-dependent refractive index of the medium modifies the temporal and spectral phase of the propagating pulse. In transparent media, different frequency (or wavelength) components of ultrashort pulses exhibit different refractive indices and since the velocity of light in the material is proportional to its refractive index, this leads to them propagating at different velocities. This effect is called optical dispersion, which is a linear optical phenomenon. Dispersion is often characterized in two ways, depending on the type of transparent material. If the shorter wavelength components propagate through the material more slowly than the longer ones, the pulse can be described as positively or up-chirped. Otherwise, when the shorter wavelength components travel faster than the longer wavelength components, the pulse can be described as negatively or down-chirped. As a result of both dispersion cases, when a short optical pulse propagates through a transparent medium it experiences a group delay, a duration variation and a frequency chirp. An example of a linear positive/up chirp is shown in figure 3.1 b.

If a short pulse described by equation 3.6 has propagated a distance, x, through a transparent medium (e.g. a piece of glass or a prism), the optical pulse in the spectral domain can be written as [161]:

$$E(\omega, x) = E_o(\omega) e^{[-ik(\omega)x]}, \tag{3.8}$$

where k(ω) is a frequency-dependent propagation factor and can be expressed as $k(\omega) = n(\omega)/c$ and $n(\omega)$ is the frequency-dependent refractive index of the material.

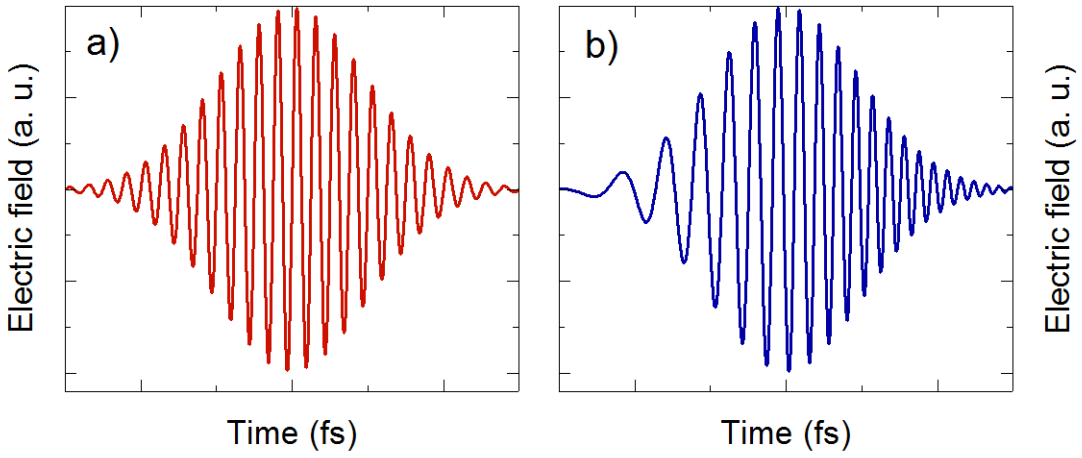

Figure 3.1: Time evolution of the electric field associated with an ultrashort pulse, a) a transform limited and b) a positively linearly chirped pulse

In order to analytically calculate the propagation effects, the propagation factor can be rewritten by applying a Taylor expansion as a function of the angular frequency [161]:

$$k(\omega) = k(\omega_o) + k^{'}(\omega - \omega_o) + \frac{1}{2}k^{''}(\omega - \omega_2)^2 + ..., \tag{3.9}$$

where

$$k^{'} = (\frac{dk(\omega)}{d\omega})_{\omega_o} = (\frac{1}{v_g(\omega)})_{\omega_o}$$

$$k^{''} = (\frac{dk(\omega)^2}{d\omega^2})_{\omega_o} = \frac{d}{d\omega}(\frac{1}{v_g(\omega)})_{\omega_o} = \frac{\lambda^3}{2\pi c^2}\frac{d^2n}{d\lambda^2}$$

The third term in Equation 3.9 is known as group velocity dispersion (GVD) where $v_g(\omega)$ is the group velocity and the derivative of its inverse with respect to angular frequency is proportional to group velocity dispersion (GVD). The sign of $k^{''}$ depends on the curvature of the dispersion of the index, $d^2n/d\lambda^2$. For the $k^{''}(\omega_o) > 0$ case, which is the most usual situation, the refractive index decreases as the wavelength increases, leading to the longer wavelengths propagating faster and thus positive chirp or up-chirp occurring. For negative $k^{''}(\omega_o) < 0$, the GVD is negative and thus negative chirp or down-chirp is produced where the spectral components with the shorter wavelengths propagate faster.

The temporal broadening of an ultrashort pulse due to linear dispersion is usually an undesirable effect in time-resolved spectroscopy experiments due to the resulting reduction of experimental time resolution. To minimize such effects, optical components in femtosecond beam lines (such as lenses, polarizers) are made as thin as possible. Furthermore, where time resolution must be maximized, prism, grating, or chirped mirror compressors must be used to minimize GVD (or higher order dispersion terms) to produce as close as possible to transform limited pulses at the experiment.

3.2.2 Synthesis of Ultrashort Pulses

Ultrashort pulsed lasers have been extensively applied in order to investigate physical and chemical processes which take place on extremely short time scales, such as molecular vibrations, charge transfer processes and molecular conformational changes [13,159,162]. These processes may take place on a femto to picosecond time scales, thus, laser pulses with similar or shorter pulse durations are required to resolve these processes in the time-domain. In order to generate such ultrashort laser pulses, an active optical medium with broad spectral bandwidth emission characteristics is required. Ultrashort laser pulses are generated based on mode-locking processes. This process takes place in an optical resonator (or cavity). In the simplest case, the cavity consists of at least two mirrors, which are positioned in a linear arrangement, and a gain medium. One of these mirrors is highly reflective and the other is semi-transparent. Titanium:sapphire (Ti:Sa) crystals have been established as dominant ultrashort pulse gain media since the 1980s due to their broad emission band in the spectral range of 670–1070 nm [163–166]. When laser waves are reflected back and forth in the cavity making many passes through the gain medium, the electromagnetic waves add up constructively inside the resonator, generating a discrete set of standing waves. Only wavelengths that constructively interfere with themselves survive in the cavity, i.e. those that satisfy the condition:

$$n = \frac{\lambda}{L_c}, n = 1, 2, 3 \tag{3.10}$$

where L_c is the cavity length.

The large range of frequencies in the gain profile of the active medium leads to the generation of different longitudinal modes in the laser cavity. These modes start independently from each another and their phases are generally random, resulting in a continuous wave (CW) mode of lasing. However, all lasing modes satisfy the condition in equation 3.10 and those with identical (or very similar) phases generate a train of pulses where the distances between adjacent pulses are equal to twice the cavity length.

To generate ultrashort laser pulses from the maximum number of frequency modes, the oscillating optical waves must propagate with equal phases on each pass through the cavity. This can be achieved by supporting the laser cavity with a component that enhances cavity losses when the laser operates in a random longitudinal phase, i.e. a CW, regime. Otherwise, this component should enhance lasing when the phases of different modes are (near) equal and short pulses with high intensities are produced. This principle is the basis of a method called Kerr lens mode-locking. The idea of mode-locking in the cavity relies on decreasing losses by fixing the phase relation of the oscillating pulses in the laser cavity [161, 164].

The Kerr lens mode-locking technique, which relies on the optical Kerr effect, has become a common way to produce phase-locked, femtosecond duration laser pulses. This technique produces an ultrashort pulse by superposition of many electromagnetic waves of different frequencies, to produce an optical wave packet with a defined phase relation between the frequency

components. At the unique point where all frequency components have the same phase delay, the pulse is at its shortest and can be referred to as Fourier transform limited.

An ultrashort pulse oscillator makes use of near transform limited pulses and the Kerr effect in the active medium to selectively focus short pulses. This is achieved by setting up the oscillator cavity around this Kerr lens. High pulse intensities and the associated focusing of the intra-cavity laser beam result in short pulses being efficiently amplified. Thus, an intensity dependent loss mechanism is introduced to favor mode-locking and ultrashort pulses production.

The Kerr lens mode-locking depends on the intensity-dependent refractive index of a transmissive medium. In such a medium, the refractive index can be described by:

$$n = n_o + n_2 I, \tag{3.11}$$

Where n_o is the linear refractive index, n_2 is a nonlinear refractive index, and I is the intensity of the laser pulse.

The intensity of the laser beam, which propagates in the medium, often has a near Gaussian spatial distribution in the transverse plane perpendicular to the propagation direction. Propagation of such a beam in the nonlinear medium leads to changes of the refractive index of this medium, where the high intensities that occur at the center of the beam produce a large change of refractive index and a lower change of the refractive index occurs at the beam edges. In normally dispersive media, this leads to the pulse edge traveling faster than the high intensity component at the center of the beam. Thus, the medium acts as a lens and the beam is focused. The higher the intensity of the beam, the harder the focusing (up to the limits of free-carrier generation, and potentially optical damage).

Ultrashort pulse oscillator gain media are usually continuously pumped. The non-linear intracavity Kerr-lensing occurs due to noise fluctuations (that are often piezo-driven), that result in transient intensity increases that favor pulsing and selective-amplification of pulses over a CW background.

The mode-locking mechanism is enhanced by inserting an aperture in the cavity in order to allow only the focused, high-intensity beams to pass. Generally, a physical aperture is not used as the Ti:Sa crystal can be used to both focus and aperture the beam, when the Kerr lens is approximately set. As a result, only the focused light will be able to travel in the cavity and be amplified. The produced short pulses are outcoupled through a partially reflective cavity mirror (the output coupler), generating a train of pulses.

In addition, in a Ti:Sa laser cavity, when a short pulse travels through the Ti:Sa crystal, any other transmissive optics, and any air or gas in the cavity, a linear dispersion occurs. Therefore, as a short pulse propagates in the cavity, the pulse is continuously broadened time, preventing ultrashort pulse operation. The associated linear dispersion can be compensated by putting a pair of prisms or a set of chirped mirrors in the cavity, which introduce net negative group delay dispersion, and hence the positive chirp accumulated by the pulses propagating through material

in the cavity can be compensated and ultrashort pulses are generated by the oscillator [167,168].

3.3 Fundamental Aspects of Linear and Non-linear Optics

3.3.1 Nonlinear Polarization, Phase-matching, and Pump Pulse Generation

Efficient excitation of sample systems occurs at sample resonances. Therefore, to linearly and efficiently excite arbitrary samples, we require pump pulses with specific pump photon energies. In the present work, second harmonic generation or a specific wavelength produced by an optical parametric amplifier (OPA) have been applied as pump sources. In general, the process of producing different wavelengths is based on the application of intense laser fields in nonlinear optical media.

When an electric field (E) interacts with atoms, molecules, or materials, the electron density is polarized and displaced from the nucleus. In this case, a macroscopic electric dipole moment is created in a material. The induced electric dipole per volume of the material is called polarization (P). In principle, by investigating the induced polarization of the molecular system, a given material may be characterized depending on its response to the incident electromagnetic field. The response of any optical medium depends on the strength of the incident laser field. At a low intensity of the incident laser field, the induced polarization predominantly exhibits a linear response, proportional to the field strength of the applied electromagnetic wave. In this limit, the polarization under the influence of the applied laser field E(t) is time-dependent. The relationship between the induced polarization and the applied optical field can be described as [169, 170]:

$$\overrightarrow{P}(t) = \varepsilon_o \chi \overrightarrow{E}(t), \tag{3.12}$$

where ε_o is the electric permittivity of the vacuum and (χ) is the first-order optical susceptibility of the material.

In the linear regime, the polarization of the medium only carries those frequencies which are presented in the originally applied wave. Thus, the incident light wavelength remains unchanged.

When the intensity of the applied laser field is high, the polarization of the medium can no longer be described as linear. In this regime, a nonlinear interaction between the electrons in the material and the field give rise to many effects, such as the generation of new frequencies or modulation of the properties of the incident fields. The relation between the polarization and the incident laser field can be expressed as a power series. Including the linear term in equation

3.12, the total polarization becomes [169, 170]:

$$\begin{aligned} P(t) &= \varepsilon_o(\chi^{(1)}E(t) + \chi^{(2)}E(t)^2 + \chi^{(3)}E(t)^3 + ...) \\ &= P^{(1)}(t) + P^{(2)}(t) + P^{(3)}(t) + ..., \end{aligned} \tag{3.13}$$

where $\chi^{(2)}$and $\chi^{(3)}$ correspond to the second and third order nonlinear susceptibilities, and $P^{(1)}, P^{(2)}$ and $P^{(3)}$ are the first-order, second-order and third-order polarization, respectively.

Different nonlinear physical processes arise from the various orders of the nonlinear polarization. These processes facilitate the generation of waves with new frequencies.

We now consider a wave which propagates along the z direction with frequency ω. This field can be described as:

$$E(t) = E_o cos(\omega t), \tag{3.14}$$

where E_o is the amplitude of the incident field. From equations 3.13 and 3.14 and by using relevant trigonometric relations, the total polarization of the medium can be expressed [170]:

$$\begin{aligned} P(t) = \varepsilon_0(&\frac{1}{2}\chi^{(2)}E^2 + (\chi^{(1)}E + \frac{3}{4}\chi^{(3)}E^3)cos(\omega t) \\ &+ \frac{1}{2}\chi^{(2)}E^2 cos(2\omega t) + \frac{1}{4}\chi^{(3)}E^3 cos(3\omega t)), \end{aligned} \tag{3.15}$$

The first term of equation 3.15 is independent of the frequency and is referred to as optical rectification. According to this term, the input field can induce a DC electric field in the optical material which is generally very weak. The second term contains the nonlinear contribution to the refractive index at the same frequency of the applied field. This process gives rise to the intensity dependence of the medium refractive index. The third term includes oscillation at twice the frequency of the input light, 2ω. This process is called second-harmonic generation (SHG). The last term of the equation describes a third-order nonlinear process, which is referred to as third harmonic generation (THG) that produces a 3ω output. The efficiency of the higher order nonlinear process is typically lower because the higher order susceptibilities, $\chi^{(>2)}$, have lower values. Thus, second order, $\chi^{(2)}$, processes are generally the most efficient routes for generating light at new frequencies. In equation 3.13, the set of nonlinear terms acts as a source of different frequencies. Moreover, each component can be responsible for energy transfer between different components of the field at different applied frequencies. Hence, several interesting nonlinear phenomena generally occur simultaneously. Further frequencies can be generated if we consider the application of several electromagnetic waves of different frequencies propagating through the medium. In the quadratic term of equation 3.13, not only SHG processes occur but the sum or difference frequencies of the imposed fields can be generated. For a detailed description of the generation of the new frequencies, let us consider two superimposed fields oscillating with frequencies of ω_1 and ω_2 and propagating along the z-direction. The electric

field for this superposition can be described as:

$$E(t) = E_1 cos(\omega_1 t) + E_2 cos(\omega_2 t). \tag{3.16}$$

Here E_1 and E_2 are the amplitudes of the incident fields.

Below we consider the second order polarization term along the z-direction. Thus we have:

$$E(t)^2 = E_1^2 cos(\omega_1 t)^2 + E_2^2 cos(\omega_2 t)^2 + 2E_1 E_2 cos(\omega_1 t) cos(\omega_2 t), \tag{3.17}$$

By using the following trigonometric relations:

$$cos^2(\theta) = 1/2 + 1/2 cos(2\theta),$$

$$cos(\theta)cos(\phi) = 1/2 cos(\theta + \phi) + 1/2 cos(\theta - \phi),$$

The second-order polarization can be written as:

$$\begin{aligned} E(t)^2 = \varepsilon_o \chi^{(2)} [\frac{1}{2}(E_1^2 + E_2^2) + \frac{1}{2}E_1^2 cos(2\omega_1 t) + \frac{1}{2}E_2^2 cos(2\omega_2 t) \\ + E_1 E_2 cos((\omega_1 + \omega_2)t) + E_1 E_2 cos((\omega_1 - \omega_2)t)], \end{aligned} \tag{3.18}$$

The above equation represents a new electric field which contains several interesting terms, such as the two field time-independent rectification term, terms oscillating at twice the input frequencies, ($2\omega_1$ and $2\omega_2$), associated with SHG, as well as terms oscillating at the sum of the input frequencies, ($\omega_1 + \omega_2$), and at the difference of the input frequencies ($\omega_1 - \omega_2$). These last two terms are responsible for two different nonlinear processes. The first of them is called sum-frequency generation (SFG) which creates a new frequency depending on the sum of the input frequencies. The second process is called difference-frequency generation (DFG), which results in a frequency equal to the difference between the two input frequencies. Optical parametric amplifiers (OPAs) are specific examples of devices making use of this effect. These phenomena as well as the second harmonic generation process are illustrated in figure 3.2. Summarizing, different nonlinear terms of the induced polarization, lead to processes of different orders of nonlinearity. In particular, the second-order polarization $P^{(2)}$ can result in second-harmonic generation (SHG), sum-frequency generation (SFG), difference-frequency generation (DFG) and optical rectification (OR). The third order polarization $P^{(3)}$ also induce useful and potentially undesirable processes such as third harmonic generation (THG), phase conjugation, self-focusing and self-phase modulation [169, 170]. The associated new frequencies are microscopically generated simultaneously. However, the efficient creation of a usable output wave via one of these processes, requires well-defined phase-matching conditions. Phase-matching considerations are especially important to favor a particular desired process in the nonlinear medium.

The nonlinear crystals, which are used as a medium to produce new frequencies from the

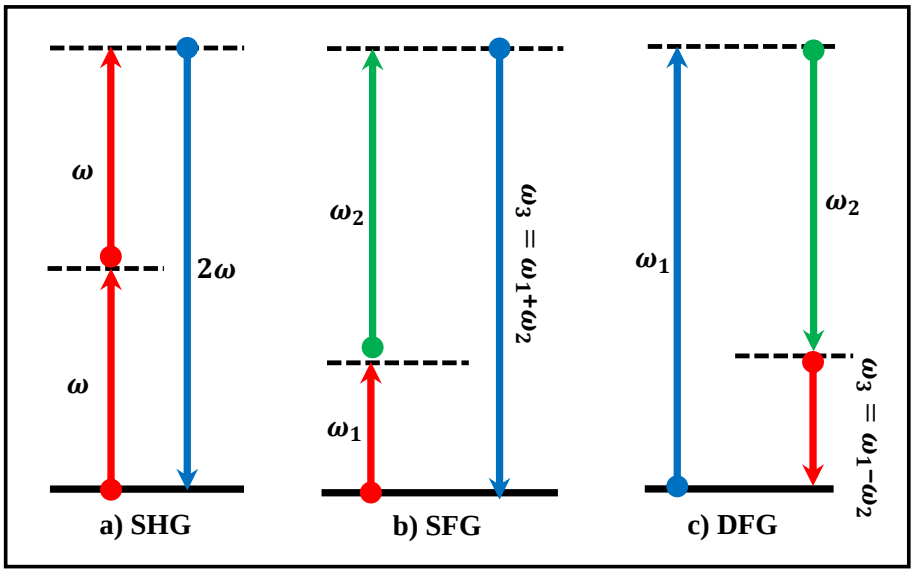

Figure 3.2: Energy-level diagram describing a) second-harmonic generation, b) sum-frequency generation, and c) difference-frequency generation.

applied optical field are generally anisotropic, i.e. the relevant refractive index and polarizability is dependent on the polarization of the applied optical field. Accordingly, such anisotropic optical media exhibit double refraction phenomena (birefringence). Birefringent crystals are categorized in two types, uniaxial and biaxial birefringent crystals, which depends on whether the crystal has one or two optical axes, respectively. Generally, when an optical field travels through a uniaxial crystal, this field will split into two components. The first component will propagate in accordance with an angle-independent (but frequency-dependent) refractive index, referred to as the ordinary beam (o) and the other will propagate in accordance with a refractive index which is dependent on the angle that the incident beam makes with the optical axis, with this component referred to as the extraordinary beam (e). The value of the birefringence in a uniaxial optical crystal is the difference between the refractive index of the ordinary beam (n_o) and the refractive index of the extraordinary beam (n_e). For $n_o > n_e$, the crystal is termed a negative uniaxial crystal, otherwise, when $n_o < n_e$, it is a positive uniaxial crystal. In a nonlinear optical crystal, both the incident wave and any newly generated wave must travel in the crystal at the same phase velocity to efficiently generate the new frequencies. Otherwise, a phase slip will occur that will eventually lead to destructive interference between the waves generated at different points in the medium.

To understand how the phase-matching condition can be achieved for a specific fundamental wavelength, figure 3.3 shows a two-dimensional projection of the refractive index for a nonlinear crystal in the xz-plane. The refractive indices of the ordinary, n_o, and extraordinary beam, n_e, are shown as solid and dashed lines, respectively. The refractive index of an anisotropic crystal is the same in all directions, so the refractive index is depicted as spherical. Whilst the refractive index of an anisotropic crystal is represented as an ellipsoid. When the fundamen-

tal optical field passes through the crystal at an angle θ with respect to the optical axis, the refractive index is given by:

$$\frac{1}{n_e(\theta)^2} = \frac{sin^2\theta}{n_e^2} + \frac{cos^2\theta}{n_o^2}, \tag{3.19}$$

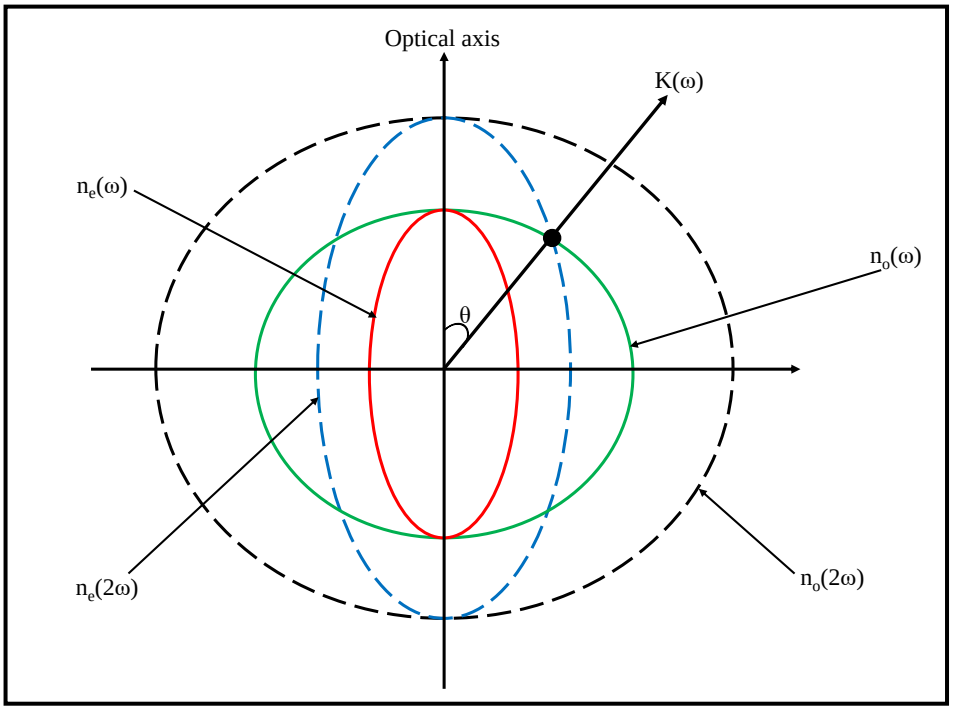

Figure 3.3: Refractive index variation for fundamental and second harmonic beams in a uniaxial crystal.

In particular, SHG is a good example which can be used as an instructive tool to define proper phase matching conditions in a birefringent crystal, in this case for a SHG process. A beta barium borate crystal, (BBO), a negative uniaxial crystal, is the most common type used in such a case. The condition for the proper phase matching angle is n(2ω) = 2n(ω). In figure 3.3 , the angle (θ) is between the propagating optical beam and the optical axis of the crystal. The ellipses represent all refractive indices of the extraordinary waves and the circles are for the ordinary beams. As can be seen, the refractive indices of the ordinary wave (fundamental) and the extraordinary wave (second harmonic) can be matched at the intersection point, which is shown with a black dot in the figure. Using birefringent, transmissive crystals, phase matching can be achieved by appropriately orienting the crystal. Here, the angles of the polarization of the fundamental field are adjusted with respect to the optical axis in order to set the same phase velocity of the two fields as they propagate inside the nonlinear medium shapes of facilitat-

ing efficient SHG. Such a scheme can be readily generalized SFG and DFG (including OPA) processes [170].

It should be mentioned that not all crystals exhibit second-order nonlinearities, which are related to the crystal symmetry. The even-order susceptibilities are zero in materials that have inversion symmetry. Accordingly, the induced polarization is also zero [170].

3.3.2 Self-Phase Modulation and the Generation of White Light Supercontinua

The mechanism behind the generation of a white light continuum (WLC) is the, $\chi^{(3)}$, self-phase modulation process. Self-phase modulation (SPM) occurs when an intense laser field interacts with a nonlinear medium, modifying the spectral phase and amplitude of the incident laser pulse differently for the various frequencies existing in the pulse. The modification of the pulse spectrum manifests as a frequency broadening of the laser pulse.

The electric field of a laser pulse propagating in a medium, can be described as follows:

$$E(z,t) = E_o(z,t)e^{i(knz-\omega_o z)} = E_o(z,t)e^{i\phi}, \tag{3.20}$$

where $k = \frac{2\pi}{\lambda}$ is the wave number, E_o (z,t) is the pulse envelope of the laser field, ω_o is the central frequency of pulsed laser, n is the time-dependent refractive index of the material, and ϕ is the temporal phase of the laser field.

When a laser beam of high intensity propagates inside a polarizable medium, the refractive index is modulated due to the nonlinear response (see equation 3.11). Therefore, the electric field of the applied laser in the medium over a length L can be rewritten as:

$$E(L,t) = E_o(L,t)e^{i(kn_oL+kn_2I(t)L-\omega_o t)} = E_o e^{i(\phi_{NL}(L,t)+\phi_o)}, \tag{3.21}$$

where $\phi_{NL}(L,t)$ is the nonlinear time-dependent phase which results from the time-varying intensity I(t) of the wave. Solving equation 3.21 with respect to the time-dependent phase, yields [161]:

$$\phi_{NL}(t) = \frac{n_2 I(t) L\omega_o}{c}, \tag{3.22}$$

where c is the speed of light.

The nonlinear temporal phase changes during the propagation of the pulse in a medium are related to the changes in the frequency of the laser pulse, which leads to the frequency modulation. The induced frequency change $\Delta\omega$(t) is equal to the difference between the frequency ω(t) and the central frequency ω_o, thus $\omega(t)$ can be expressed as [161]:

$$\Delta\omega(t) = \frac{\partial}{\partial t}\phi_{NL}(t) - \omega_o = -n_2\frac{dI(t)}{dt}\frac{\omega_o}{c} \tag{3.23}$$

According to equation 3.23, when a high-intensity pulse propagates in a medium, its frequency will be shifted by an amount which is dependent on the intensity of this pulse. Figure 3.4 shows the temporal variation of the frequency of a pulse which is caused by associated non-linear temporal variation of the phase.

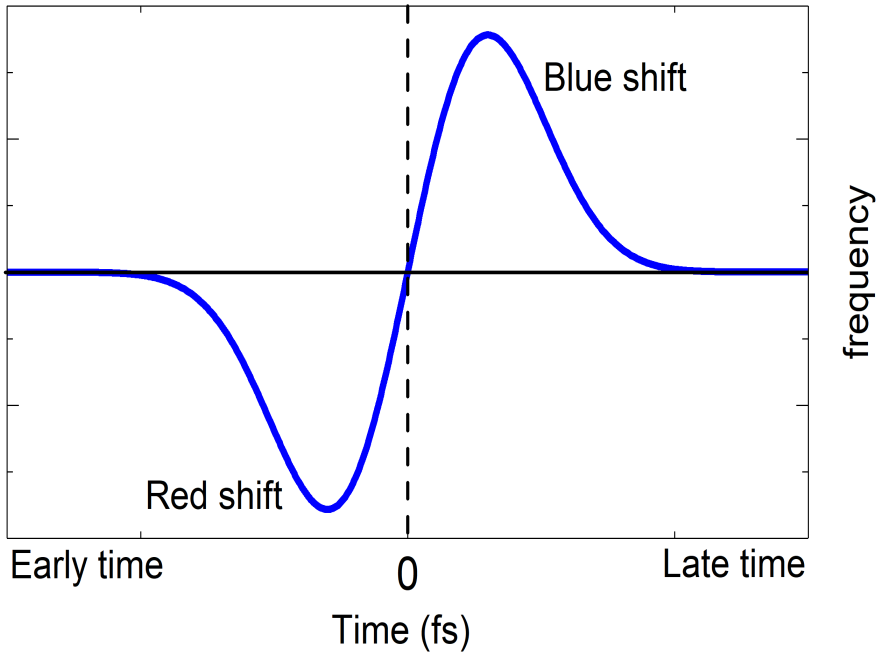

Figure 3.4: Frequency shifts in a nonlinear medium.

This phase variation leads to a red shift of the frequencies at the leading edge of the pulse, whilst phase variation leads to a blue shift at the trailing edge of the pulse. This produces a lower instantaneous frequency at the leading edge (when the frequency is decreased) and a higher instantaneous frequency at the trailing edge (when the frequency is increased), causing the whole spectrum to broaden in time.

3.3.3 Cross-Phase Modulation

Cross-phase modulation (XPM) is the phase modulation of a laser pulse which takes place due to a time-dependent alteration of the refractive index of a material in the presence of a second, intense, laser beam. This process may occur in time-resolved experiments when two pulses are overlapped temporally and spatially, manifesting as shifts of the probe spectrum as a function of delay time between the two pulses. At the beginning of the overlap between the pump-probe pulses, when the leading edge of the pump pulse overlaps with trailing edge of the probe pulse, the XPM effect leads to shifting of the probe spectrum to longer wavelengths (red). Whilst, at the end of the overlap between the two pulses, when the trailing edge of the pump pulse overlaps, a shift will occur to shorter wavelengths (blue) due to the XPM effect. In the

TAS experiment, the time-dependent nonlinear refractive-index change is induced by the pump pulse and observed via the probe pulse spectrum.

The XPM signal is produced without any energy transfer to or from the sample, i.e. it does not arise due to the system under investigation. This means the effect also arises to varying degrees in essentially transparent materials such as the solvent or the silica cuvette.

As a result of this effect, a strong signal occurs at around time zero. This effect, which is a TAS equivalent to the (multiphoton or laser-assisted stimulated emission) cross-correlation in PES, can thus be used to estimate the time zero position when the pump and probe pulses are overlapped in the sample. The XPM effect can be formulated mathematically by the differential optical signal $D(\omega,t_d)$ induced by pumping as [171]:

$$D(\omega,t_d) = -12\frac{\omega|a_1|^2\sigma_e}{\sqrt{|\eta|}} \times Im(exp[-\frac{[t_d+t_0(\omega)]^2}{\eta\tau_1^2} + i\frac{t_0(\omega)}{\beta\tau_2^2}\frac{t_d+t_0(\omega)}{\eta\tau_1^2} + (\frac{t_0(\omega)}{2\beta\tau_2^2})\frac{1}{\eta\tau_1^2} - \frac{i\varphi}{2}]) \tag{3.24}$$

where $\varphi = arctan(\frac{Im\eta}{Re\eta})$, t_d is the pump-probe delay, $\tau_{1,2}$ are the Gaussian pulse durations of the pump and probe pulses, β denotes the chirp rate, ω is the probe frequency, the σ_e is the instantaneous electronic response to amplitude, a_1, of the non-chirped pump pulse, $\eta = 1 + \frac{2\xi^2}{\alpha}, \alpha = 1 - i2\beta\tau_2^2, \xi = \tau_2/\tau_1$

The TA spectra exhibit another effect, which is called temporal chirp. The word chirp is used to describe the temporal offset of wavelengths within a spectrally broadband pulse. This chirp arises from the variation of the refractive index with frequency in the media, inducing optical elements air and the sample itself. Due to the transmissive broad bandwidth of ultrashort laser pulses and the dispersion properties of all materials, an increase or decrease of the total pulse duration occurs as the pulse propagates. For higher photon energies (lower wavelengths), the refractive index is larger. Thus, this effect can be explained by the dispersive conditions of the transparent medium, the photons of longer wavelengths travel faster in a medium than the ones with shorter wavelengths. The probe pulse chirp results in a wavelength-dependent shift, $t_o(\omega)$, of the initially populated resonant state signal, as well as for the cross-phase modulation signal in the TA spectroscopy technique.

3.4 Transient XUV Photoelectron Spectroscopy

In this thesis, the investigation of intermolecular charge and energy transfer in TM complexes in aqueous solution is surveyed extensively using the time-resolved photoelectron spectroscopy (TRPES) technique. Since the coupled electronic and nuclear dynamics of molecules takes place on the femto to picosecond timescale, ultrashort laser pulses can be used to interrogate such problems in the time-domain. The combination of the TRPES technique with ultrashort laser pulses represents a powerful tool to explore the molecular system evolution as it is sensitive to nuclear dynamics, electronic configuration, and the excitation and relaxation channels via the

photoelectrons produced through photoionization.

3.4.1 Principles of Time-Resolved Photoelectron Spectroscopy

The TRPES technique has been established as one of the most important methods to study dynamic processes of molecular systems, which occur on the ultrafast time scales [14, 162]. These processes, such as direct dissociation, ultrafast internal conversion, isomerization, and vibrational energy redistribution, often lead to both structural and charge density rearrangements of molecules [161, 172–175]. This methodology was used as a possible tool for the study of the bulk and surface electronic states of solids in the 1980s using picosecond time-resolved PES [176]. Application of ultrafast laser pulse in TRPES technique has led to breakthroughs in our understanding of fundamental chemical processes [162, 177, 178]. Such research revealed the mechanism of chemical reactions ranging in complexity from bond-breaking in diatomic molecules to excited multi-state dynamics in larger organic and biological molecules [162, 179].

The principle of the pump-probe TRPES technique is based on applying two ultrashort light pulses, with the first pump pulse being used to bring the atom or molecule into an excited, time-evolving state by absorbing a photon. This may lead to the promotion of electrons from the equilibrium ground state to an unstable excited state. The probe pulse is used to promote the electrons in the excited state(s) and potentially the ground state above the vacuum level, causing ionization. The principle of extreme ultraviolet (XUV) photoemission experiments is based on measuring the kinetic energy of the emitted photoelectrons from the sample at different time delays between the pump and XUV probe pulses. With this technique, it is possible to determine the transient population density of the electronic states, with different binding energies. The binding energies of the excited state as well as the ground state are determined based on the known energy of the absorbed incident photons ($h\upsilon$) and the measured kinetic energies. With (E_{kin}) representing the observed kinetic energy, the binding energy (E_{Bind}) of electrons can be defined as [180]:

$$E_{Bind} = h\upsilon - E_{Kin} \tag{3.25}$$

A schematic representation of the TRPES principle using extreme ultraviolet (XUV) probe pulses is shown in figure 3.5. An ultrashort laser pump (typically a specifically chosen visible or UV wavelength generated using a femtosecond pulse optical parameter amplifier (OPA) system or by generating a harmonic of the femtosecond pulse laser source) is used, for example, to excite the electrons from the highest occupied molecular orbital (HOMO) into the lowest unoccupied molecular orbital (LUMO) (see figure 3.5), producing a non-equilibrium excited state. In order to avoid multi-photon photoemission processes, the pulse energy/intensity of the pump should not significantly exceed the multi-photon ionization threshold of the sample. When the energy gap between the ground state and an excited state is equal to the incident photon energy of the pump beam, sample molecules maybe resonantly promoted to the excited state. Optimization of the laser wavelength and the intensity of the pump beam plays an important

role to increase the population of electrons in the excited state while minimizing multi-photon excitation.

The XUV probe pulse, with a sufficiently high photon energy, is used to photo-ionize the molecules, producing photoelectrons with defined kinetic engines. With the use of the XUV-light, the initially occupied states, as well as the electronic states populated by the photo-excitation process, are probed simultaneously via excitation above the vacuum level. The information obtained from this experiments can be considered to be dependent on the population and nature of the occupied and unoccupied molecular orbitals. By measuring the kinetic energy (and potentially angular and spin distribution) of the photoemitted electrons, the initial (ground), intermediate (excited), and final (photo-oxidized) states of the sample molecules can be investigated. Thus, the electron dynamics, including the energetics and lifetime of the excited states and their relaxation pathways can be monitored using the TRPES technique.

At the moment when the pump and probe pulses arrive at the sample at the same time, their arrival defines the time-zero (t_0) of the experiment. A molecule in the ground state absorbs a photon from the pump pulse, with the excitation process triggering the investigated dynamics. At a short time delay between the two pulses (the two pulses still overlap temporally), the electrons in the initially populated excited state and the unexcited ground state can be promoted to the vacuum level by absorbing photons from the pump and/or probe beam. The photoemitted electrons gain a high kinetic energy by absorption of the XUV photon, with this process potentially occurring via short-lived neutral and/or photo-oxidized states. At a very short time delay (near to time zero), the excited state has a maximum population. When the experiment is performed under favorable pump intensity conditions and temporal overlap of the two pulses is diminished, the non-linear resonant laser-assisted photo effect disappears [181].

The electronic population of the pump-excited state also decreases due to the molecule- and environmental-driven relaxation of electrons to the lower-lying excited states, including the equilibrium ground state. These mechanisms lead to a decrease in the electronic population of the excited state and a reduced signal of the associated ionized electrons, as shown in the upper left panel of figure 3.5. The decay of such excited state populations can be described by exponential decay behavior, $e^{-\Delta t/\tau}$, where τ represents the lifetime of an excited state .

Recording the photoemission spectrum at subsequent time intervals gives the characteristics of the studied material at a particular time delay, Δt. The electronic dynamics of the molecules can be monitored by displaying the photoelectron spectrum for various time delays of the pump with respect to the probe pulse. A high temporal resolution for spectra recorded using the TRPES experiment is achieved when the duration of both pump and probe pulses are short. The temporal resolution of the experiment is defined by a cross-correlation (CC), where the convolution of the pump and probe pulses determines the electron yield signal as the time delay between them is swept over.

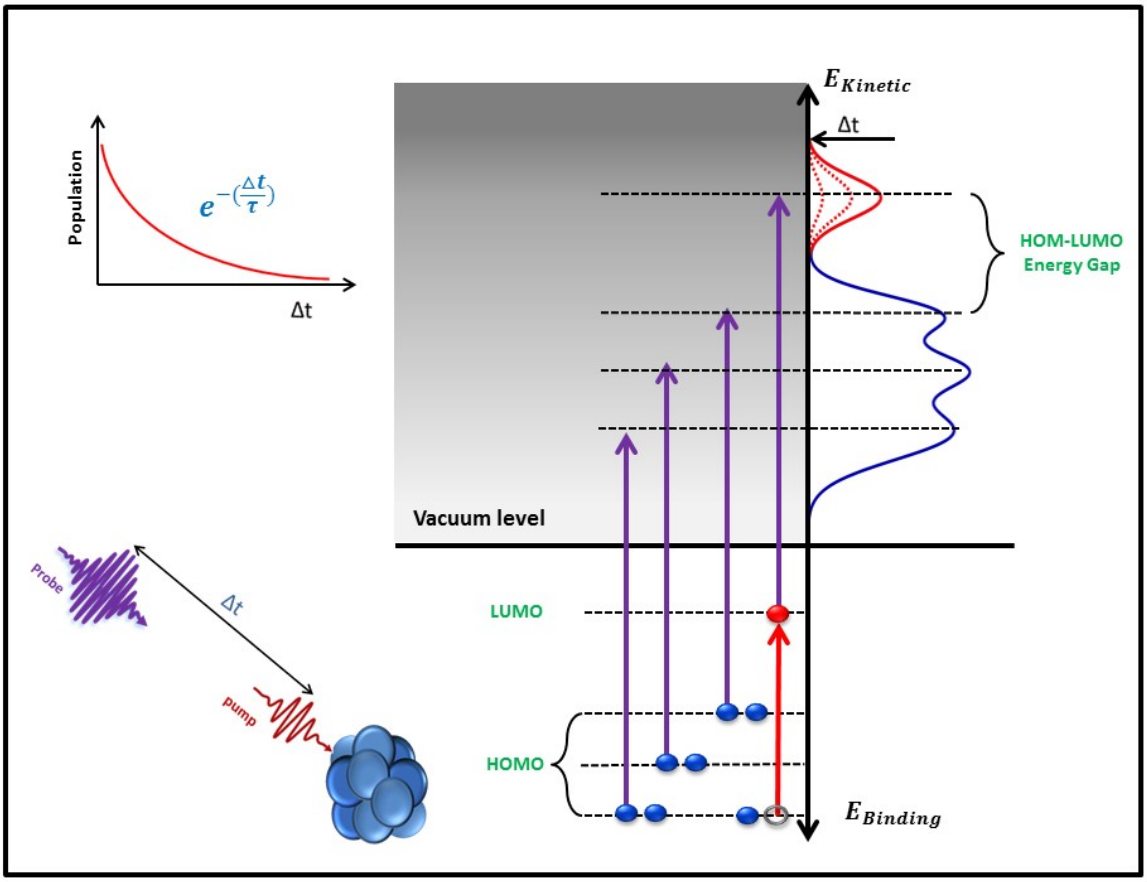

Figure 3.5: Schematic representation of the pump-probe TRPES experiment. A molecule in the initial ground state absorbs a photon from the pump beam and it is promoted to the excited state, in this case via HOMO⟶LUMO transition. Upon absorption of highly energetic XUV photons, a single photon is sufficient to emit electrons from the ground state as well as from the excited state to the vacuum level. The kinetic energy spectrum of the emitted electrons is measured, which represents the characteristics of the molecules at a certain time delay Δt (blue and red curves). At zero-time delay, a maximum electronic population of the excited states is probed (the red curve). When the pump and probe pulses no longer temporally overlap, the electronic population in the excited state decreases as the excited electronic distribution relaxes with the population of lower-lying states, including the ground state (the red dashed curves). Applying different time delays between the pump and the XUV probe pulse yields a perspective on the electronic under dynamics and the chemical changes occurring in the molecules over the probed time delay.

Finally, one can summarize femtosecond pump-probe PES experiments with the following four steps: (i) the preparation of excited statesat a well-defined time; the nature of which depend on the excitation energy, laser intensity, pulse duration/temporal shape of the pump laser field and the transition probability between the ground state and the excited state of the sample pump-prepared. (ii) the dynamical evolution of the photoexcited material. (iii) the probing of the

nonstationary superposition state at a well-defined time and (iv) repetition of steps (i)-(iii) at different pump-probe delay times to build up the TRPES spectrum [162].

3.4.2 Generation of ultrashort XUV pulses

As previously discussed, a pulsed XUV light source can be used in TRPES experiments as a probe pulse. In this experiment, the XUV light is the 21st harmonic of an ultrashort pulse titanium: sapphire laser system. This pulse is created using high-order nonlinear optical processes.

High harmonic generation (HHG) occurs when an intense short laser pulse interacts with an atomic, molecular, material system [182–185]. This process occurs when an intense laser field interacts with the medium non-perturbatively to produce electrons, that are driven in the laser field, resulting in emission of coherent radiation at multiples of the incident laser frequency [186]. In the gas-phase, HHG light can be produced by focusing an ultra-short laser pulse (usually with near-infrared wavelengths) to an intensity of the order of 10^{13}–10^{14} W/cm^2 in a noble gas medium [187, 188]. Since the first observation of low-order harmonic generation (second and third harmonics) in crystals [189–191], rapid progress in high order frequency up-conversion process has occurred. In 1978, Reintjes *et al* succeeded to generate the fifth- and seventh-harmonics of an Nd:YAG laser [192]. Bokor *et al* produced the 7th harmonic of the 248-nm output of an Excimer laser in helium gas, where the nonlinear interaction took place by focusing the laser beam onto a supersonic helium gas jet [193]. Using ultrashort pulse lasers, the development of XUV light sources has continued, allowing high order harmonics to be produced with a relatively high photon flux and short pulse durations. In 1987, applying a pulsed laser of 350 fs pulse duration, McPherson *et al* successfully generated the 17th harmonic order from the interaction of intense ultraviolet krypton fluoride Excimer laser pulses (248 nm, $\sim$20 mJ pulse energy) with neon gas [194]. From then onwards, many other studies on harmonic generation have been performed to achieve higher harmonic orders and higher conversion efficiencies. For example, Li *et al* observed the 21st harmonic in Xenon, 29th harmonic in Krypton, and 33rd harmonic in Argon at the fundamental wavelength of 1064 nm of a mode-locked Nd-YAG laser with 30 fs pulse duration and an intensity of 3×10^{13} W/cm^2 [195]. A systematic study of HHG in different noble gases has been made with subpicosecond pulsed laser fundamental sources. The observation of harmonic emission has been found up to the 15th in He, 13th in Ne, and 9th in Ar, Kr, and Xe gas [196]. In 1993, L'Huillier *et al* observed the 29th harmonic in Xe, the 57th harmonic in Ar, and the 135th harmonic in Ne gas by using an Nd: glass laser with a pulse duration of 1 ps and a 1053 nm central wavelength [197]. Nowadays, modern laser technology is culminating in the generation of intense few-cycle laser pulses that facilitate the generation of subfemtosecond, toward attosecond, extreme ultraviolet/x-ray pulses with a high up-conversion efficiency [198–200].

With such developments, using HHG light as a probe source has become a viable approach to monitor the electronic structure and ultrafast photodynamics of gaseous and condensed phase

materials [120, 132, 201, 202]. The generated HHG light has a number of useful characteristics. The high photon energies, bandwidths of the pulses, short pulse durations/high temporal coherence, relatively small divergence /high spatial coherence, and relatively high photon flux make this light source useful in the investigation of ultrafast dynamics, particularly in the condensed phase. Moreover, due to the half-cycle nature of the HHG process, pulse durations in the range of femtoseconds to attoseconds may be produced [203, 204]. This has lead to HHG light being adopted in a wide range of practical applications such as surface dynamics [205], high-resolution imaging [206, 207], and molecular dynamics studies [208–210].

HHG light provides coherent radiation in the high-frequency range which can extend to the soft x-ray regime [211, 212]. Only odd harmonic orders are produced in the HHG spectrum by the interaction of a single ultrashort laser pulses with a gaseous medium. This is due to the inversion symmetry of the nonlinear process in (randomly oriented) gaseous systems [170, 213]. At solid surfaces, odd as well as even harmonics of the fundamental laser frequency are produced due to symmetry breaking at the plasma-vacuum interface [170, 213].

The HHG spectrum generated from gaseous media has particular salient features which are illustrated in figure 3.6.

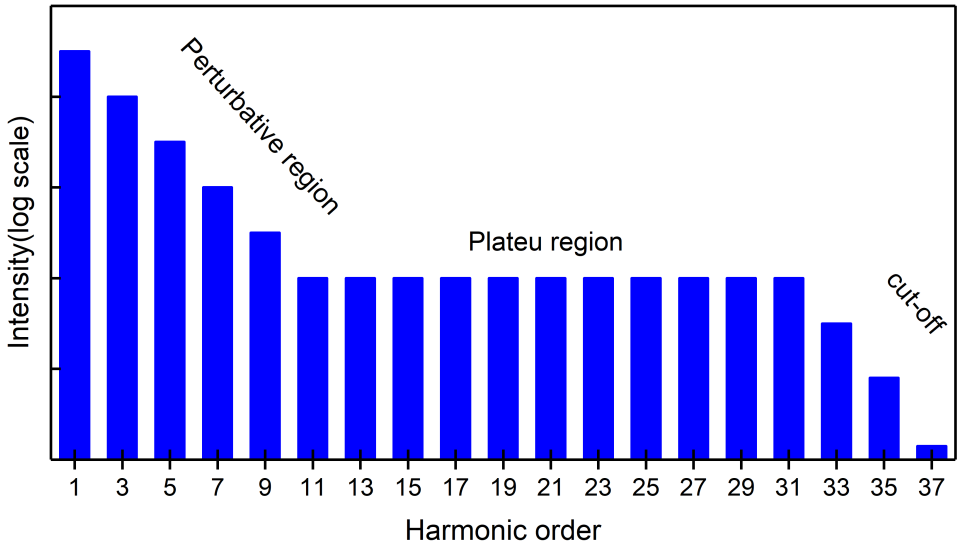

Figure 3.6: A schematic illustration of the HHG spectrum. In the perturbative regime, at lower harmonic orders, the HHG spectrum has a negative slope. The plateau region, extends over the range of intermediate orders and is terminated at the cut-off energy point, which determines the highest harmonic orders. The decrease of the harmonic peak intensities after the cut-off point is also shown. Only odd harmonic orders of the fundamental frequency can be produced in an isotropic gas-phase medium.

At the first few lower order harmonic frequencies, an intensity pattern dominates in which the intensity of harmonics has a negative slope and decreases rapidly with the increase of the harmonic orders. This is followed by a non-perturbative plateau region. In the plateau region, the harmonics have roughly the same intensity up to high harmonic orders. Eventually, the

plateau region is terminated, at which point, the harmonic intensity drops rapidly. This point is well-defined as a cut-off frequency. An important aspect of the HHG spectrum is that it is not what is expected from perturbative nonlinear optics, which would predict a decrease in intensity with the increase of the harmonic orders [186].

In 1993 Kulander [214] and Corkum [186] provided a theoretical description of the mechanism of the gas-phase HHG process. The basic features of HHG can be clearly explained in terms of the semiclassical three-step model. Remarkably, in atomic systems, this model provides predictions which are supported by a more elaborate direct solution of the time-dependent Schrodinger equation (TDSE) [186, 215].

As shown in the figure 3.7, the semi-classical three-step model can be summarized as follows:

1. **Tunnel ionization:** The electron is in a ground state and bound to the parent atom by the Coulomb potential. When a strong laser field interacts with the atom, the Coulomb potential barrier is deformed and an electron can tunnel through the barrier potential and escape from the atom with zero initial kinetic energy.

2. **Acceleration:** The ionized electron, with zero initial kinetic energy in the continuum, is accelerated away from the parent atom by a laser field. When the field changes its sign, a portion of the electrons are accelerated and coherently driven back toward the parent ion.

3. **Recombination:** Finally, the returning electron recombines with the parent ion and releases the energy absorbed by emitting a high-energy photon.

The three-step model can quite accurately describe the experimental results when rare gas atom media are considered and provide a reasonable explanation of the HHG emission. The goal of the model is to characterize the behavior of the atomic or molecular system under the influence of the intense laser field and to visualize the ionization process of the electron, acceleration, and recombination with its parent ion. In the following, these processes are described in detail.

- **Ionization:**

Initially, the electron is in the ground state of the atom or molecule. In the presence of a strong electric field which is introduced by the incident laser, the potential barrier of the atom can be distorted, allowing ionization to produce an electron with near zero kinetic energy via tuning process. This process is called tunnel or strong-field ionization. It can take place at peak intensities above 10^{14} W/cm^2 [216, 217] and leads to the atoms (or molecules) of a gas being ionized at roughly the peak of an optical cycle, as illustrated in figure 3.7a.

It is sufficient to know at this point that there are different regimes for non-resonant optical photoionization processes: multiphoton ionization, tunneling ionization, and above-barrier ionization [218]. The strength and the intensity of the laser field compared to the atomic potential

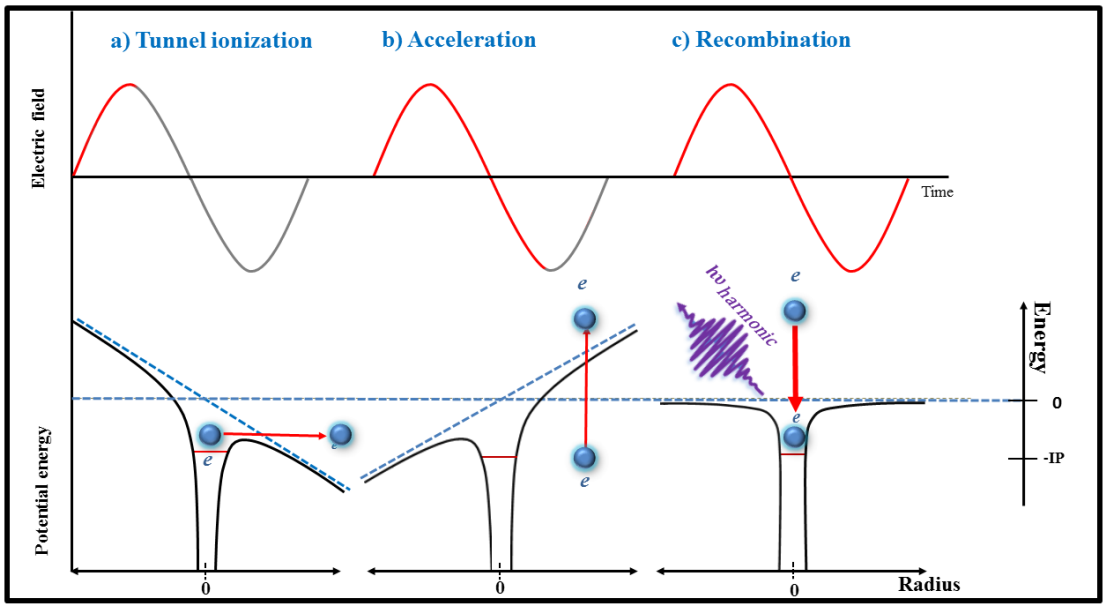

Figure 3.7: The three-step model of HHG a) Initially, the electron is bounded by the Coulomb potential of the atom, the electron is pulled away from the field-dressed atom by the influence of the incident laser near the peak of the optical field. b) In the second step, the released electron (with near zero kinetic energy) is accelerated away from the parent atom by the effect of the laser field. c) When the laser field changes the sign, some of the generated electrons are accelerated back toward the parent atom and, as the third step, recombines with the parent ion leading to the emission of a photon with a high energy.

can be used to distinguish between these regimes of ionization. The ionization mechanism for any process can be characterized by the parameter defined by Keldysh [219–221]:

$$\gamma = \sqrt{\frac{I_p}{2U_p}}, \tag{3.26}$$

where U_p: is the ponderomotive energy which is defined as:

$$U_p = \frac{e^2E^2}{4m_e\omega^2} = \frac{e^2I}{2m_e\omega^2\varepsilon_o c} \propto I\lambda^2, \tag{3.27}$$

Here e is the electron charge, E_o is the amplitude of electric field, ω is the angular frequency of the driving laser, ε_o is the permittivity of free space, and c is the speed of light.

The ponderomotive energy is the mean kinetic energy which can be gained by an electron in an oscillating electric field. From equation 3.27, one can see that the energy is proportional to the square of the ionizing wavelength, λ, and to the intensity, I, of the incident laser radiation. Considering equation 3.26, the ionization regime can be classified according to the Keldysh parameter as follows:

Situation where the single-photon energy is lower than the ionization potential are consid-

ered. When $\gamma >> 1$, multiphoton ionization is the dominant ionization mechanism. In this case, the ionization potential of the atom is greater than the ponderomotive energy. This process occurs at relatively high laser frequencies or lower intensities. The physical picture of ionization can be understood as the absorption of multiple photons by a system to reach an energy level higher than the ionization potential. At low intensities, when the ionization process can be described in terms of perturbation theory, the electrons are produced with relatively little kinetic energy [222, 223].

When the laser field becomes strong enough, the perturbation regime breaks down and many photons are absorbed in addition to the minimum number of photons required for ionization. $\gamma < 1$ defines the associated tunnel ionization regime. Tunnel ionization takes place on a time scale which is much shorter than the optical period of the electrical field of the laser pulse. The laser electric field strongly distorts the Coulomb potential of the atom to form a potential barrier, through which the initially bound electron penetrates (see figure3.7 a). To enhance the tunnel ionization rate, the field strength should be nearly constant during the tunneling process [222, 223].

The above barrier regime takes place when $\gamma << 1$. In this case, the perturbed electron will be able to escape from the atomic system even without passing through the barrier formed by the Coulomb potential of the atom [222, 223].

Of these three cases, the tunnel regime is the mechanism which facilitates the production of HHG light.

- **Acceleration:**

In the second step of the model, the ionized electron is accelerated by the driving laser field and in the presence of the ionic Coulomb field, gaining kinetic energy. Whilst the tunneling mechanism can only be depicted as a quantum mechanical process, the propagation of the free electron in the continuum can be well described classically. Since the Coulomb force on the electron by the ion can be treated as negligible, the motion of the free electron in the presence of the field of the laser pulse can be described by Newtons equations of motion [224]:

$$\ddot{x} = E_o cos(\omega t), \tag{3.28}$$

$$\dot{x} = \frac{E_o}{\omega} sin(\omega t) - \frac{E_o}{\omega} sin(\omega t_o), \tag{3.29}$$

$$x = \frac{E_o}{\omega} cos(\omega t) - (t - t_o)\frac{E_o}{\omega} sin(\omega t_o) - \frac{E_o}{\omega^2} cos(\omega t) \tag{3.30}$$

According to the electron trajectories calculated using equation 3.30, a free electron may or may not be driven back to the ion core, the result depends on the time of tunnel ionization with respect to the phase of the incident laser field. Figure 3.8 illustrates the electron trajectories for different tunneling times of birth t_o. Depending on t_o, the electron can either be driven back to

the ion or it may move away while oscillating and spreading in the electric field. Electrons that return to the ion at $t > t_o$ contribute to the HHG yield via recombination.

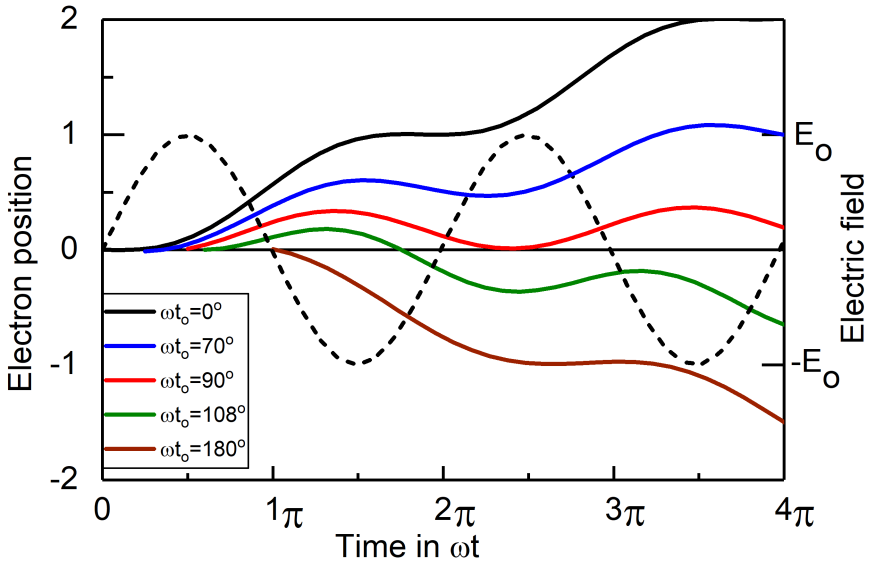

Figure 3.8: Time-dependent electron trajectories in a laser field for different phases of birth. Electrons ionized at different phases of the ionizing electric field follow different trajectories and only certain phases of birth result in the electron returning to the nucleus. The vertical scale represents the distance between the electron and the nucleus. The black dashed line represents the electric field in arbitrary units.

- **Recombination:**

The moment that the field changes sign, the electron may be accelerated back to its parent ion. The electron re-collision event may result in either elastic/inelastic collisions or electron recombination with the parent ion. If the electron recombines with its parent ion, reforming the initial neutral ground state, a photon with an energy equal to the sum of the ionization potential of the atom, I_P, and the kinetic energy of the returning electron (third step of the model) may be released from the system.

It is possible to calculate the kinetic energy of the electron when it returns to the core, allowing the HHG photon energy to be readily calculated. Classically this can be achieved by finding the roots of x(t)=0 for different values of t_o and computing the kinetic energy at the instant of return using the following relation:

$$E_{kinetic} = \frac{1}{2} m\dot{x}(t)^2 \tag{3.31}$$

From the analysis of the electron trajectories, the maximum photon energy (cut-off energy) is given by [186, 215]:

$$E_{cutoff} = \hbar\omega_{max} = I_p + 3.17U_p, \tag{3.32}$$

where ω_{max} is the maximum angular frequency of XUV light.
Hence, ω_{max}=q_{max} ω_o, where q_{max} is the cutoff harmonic order, therefore

$$q_{max} = \frac{I_p + 3.17U_p}{\hbar\omega_o}, \tag{3.33}$$

The term $3.17U_P$ is the maximum kinetic energy for the electron returning to the atom. One can find that, for various electric field phases of electron birth, the maximum kinetic energy of the returning electrons occurs at a phase of approximately $\varphi \approx 18°$, as shown in figure 3.9 [225].

Based on equation 3.32, the energy cutoff of the HHG process can be extended by increasing the ponderomotive energy, which can be achieved by applying a laser field with a lower frequency or higher intensity. Due to the quadratic scaling of the cut-off with λ or $1/\nu$, the use of longer wavelength drivers is promising due to increasing the cut-off energy [226]. At this point, one could say that the harmonic order can be increased by increasing the laser intensity to a certain point determined by the saturation intensity of ionization. Increasing the intensity of the laser field further leads to over the barrier ionization and a reduction of the HHG yield. Extension of the cutoff is also possible to a certain degree by using an atomic system with higher ionization potential. Noble gases are conventionally used for HHG production due to their high ionization potentials, chemical inertness, and ready availability from gas cylinders.

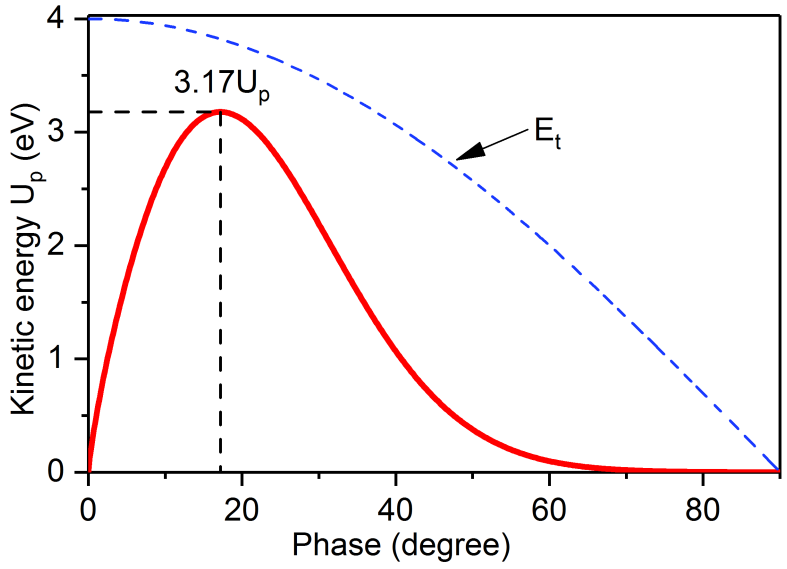

Figure 3.9: Electron kinetic energy upon return to the nucleus as a function of the phase of the driving laser field, E_t, at which the ionization occurs. The maximum of the kinetic energy is obtained at approximately 18°, where the kinetic energy upon return reaches $3.17U_p$.

3.4.3 Phase Matching in HHG

In order to obtain strong harmonic emission in the generating medium, phase-matching needs to be considered and optimized. In general, the phase fronts of the fundamental laser and the generated harmonics must be in phase when they propagate through the medium. In such a case, constructive interference between the produced harmonics occurs, leading to a coherent buildup of harmonic emission. Otherwise, a phase-lag between the fundamental and harmonic beams will accumulate upon propagation through the generation medium. This phase mismatch can be expressed as the difference between the propagation wave vectors of the fundamental laser field and generated harmonic fields:

$$\Delta k_q = q k_o - k_q, \tag{3.34}$$

where q is the harmonic order, k_q is the wave vector of the q^{th} harmonic and k_o is the wave vector of the fundamental beam. In a perfectly phase-matched HHG process, the phase mismatch of the fundamental laser and produced harmonic beam is equal to zero, i.e. Δk_q=0 [225, 227]

The intensity, I, of the generated harmonic at the end of the nonlinear medium, neglecting absorption, is given by [170]:

$$I = L[\frac{sin(\Delta k_q L/2)}{(\Delta k_q L/2)}]^2, \tag{3.35}$$

where L is the length of the medium. In general, the wave vector (k) of a driving laser or high harmonic propagating in an atomic gas medium is given by [225]:

$$k = \frac{2\pi}{\lambda} + \frac{2\pi N_a n(\lambda)}{\lambda} - N_e r_e \lambda \tag{3.36}$$

Here N_a is the atom density, N_e is the free electron density in the medium, $n(\lambda)$ is the wavelength-dependent refractive index per unit neutral atom density for the wavelength λ, and r_e is the classical electron radius. On the right hand side of equation 3.36, the first term represents the dispersion of the vacuum, the second term is the dispersion of the gas and the third term results from the dispersion of the driving-laser-induced plasma.

In general, due to the propagation of different frequencies with different phase velocities in the material, the dispersion associated with the nonlinear medium destroys phase matching. For low harmonics (such as SHG, THG), phase matching is achieved using a birefringent crystal (see section 3.3.1). Such birefringent crystals would be destroyed by the strong-driving laser fields used for HHG and would be non-transmissive for the high photon energy harmonics produced. Accordingly, isotopic noble gases are commonly used as nonlinear media for the (gas-phase) HHG process. Minimization of the phase mismatch in such cases is performed by trying to balance the dispersion effects of the neutral and plasma in HHG (see equation 3.36). Additionally, since the wavelength-dependent index of refraction of the neutral and plasma determine the phase-matching, control of the driving laser focus and variation of the intensity

of the fundamental laser across the focus represent ways to achieve good phase-matching of high harmonic orders. In general, the phase mismatch can be expressed as the sum of four terms [227, 228]:

$$\Delta k_q = \Delta k_M + \Delta k_P + \phi_G + \Delta k_A \tag{3.37}$$

In equation 3.37, the first term, Δk_M, is due to the medium dispersion and the second term, Δk_P, is related to the plasma dispersion. The third term, ϕ_G, is caused by the geometric dispersion that arises primarily from the Gouy phase shift when the generating beam propagates freely (i.e. unguided). The last term, Δk_A, in the equation is the atomic phase mismatch. The phase matching can be optimized by balancing the different terms presented in equation 3.37.

- **Medium (neutral gas) phase mismatch:**

The contribution of neutral gas phase-mismatch is due to the difference between the refractive indices of the gas per unit atmosphere at the fundamental and harmonic wavelengths. This phase mismatch contribution is given by [227, 228]:

$$\Delta k_M = \frac{2\pi q}{\lambda}(n_\omega - n_{q\omega}), \tag{3.38}$$

where λ is the wavelength of the fundamental laser, and $(n_q - n_{q\omega})$ is the difference of the refractive indices of the gas per unit atmosphere at the fundamental and harmonic wavelengths of order q, respectively. The refractive index of the noble gas is close to unity (under non-resonant conditions), depends on the incident frequency and is proportional to the gas pressure. Applying a fundamental laser with a high peak intensity leads to ionization of the gas medium, where the fraction of ionization is defined as:

$$\eta = \frac{N_e}{N_a}, \tag{3.39}$$

where N_e and N_a are the electron and atomic number density, respectively. By setting $\delta_n = (n_q - n_{q\omega})$, equation 3.38 can be written as:

$$\Delta k_M = \frac{2\pi q}{\lambda} P\delta_n(1-\eta), \tag{3.40}$$

where P is the gas pressure.

- **Plasma dispersion phase mismatch:**

Interaction of an intense laser beam with a gas medium leads to the generation of free electrons via a strong-field ionization processes. These free electrons and the associated ions cause plasma dispersion, which potentially reduces the coherence length, and thus, the harmonic yield. The phase mismatch due to plasma dispersion is described by the expression [228, 229]:

$$\Delta k_q = \eta P N_{atm} r_e \lambda (q - \frac{1}{q}) \tag{3.41}$$

where p and η are the gas pressure and ionization fraction, respectively, N_{atm} is the atomic number density at 1 atm, and r_e is the classical electron radius which is given by:

$$r_e = \frac{1}{4\pi\varepsilon_o}\frac{e^2}{mc^2}, \tag{3.42}$$

To produce a higher order harmonic, a high intensity of the fundamental laser needs to be applied. In such a case, the ionization rate and the free electron densities are increased i.e. the plasma-associated phase mismatch between the driver and high-harmonic becomes more important. The contribution from the phase mismatch due to plasma dispersion is negative, whilst the contribution from the phase mismatch due to neutral gas dispersion is positive. Thus, variation of the laser intensity allows us to adjust the fraction of ionization and the total phase mismatch.

- **Geometrical phase mismatch:**

The geometric term is produced when a focused Gaussian beam propagates in a gas cell with the geometric phase of a freely propagating beam flipping around the focal point. This shift is called the Gouy phase shift [230, 231]. Along its propagation direction, a Gaussian beam acquires a phase deviation which is caused by the difference between the plane wave of the Gaussian beam and the phase front of a plane wave with the same optical frequency. This Gouy shift is given by:

$$\phi_G(Z) = \arctan\frac{Z}{Z_R} \tag{3.43}$$

where $Z_R = \pi\omega_o/\lambda$ is the laser Rayleigh length, ω_o is the beam waist radius (at $1/e^2$), and Z is the distance from the beam focus along the axis of propagation.

The coherence length of the q^{th} high harmonic can then be written as:

$$L_{G,coh.}(Z) = \frac{\pi(Z_R + \frac{Z^2}{Z_R})}{q} \tag{3.44}$$

According to equation 3.44, $L_{G,\,coh.}(Z)$ is proportional to Z. Thus, the effect of the Gouy phase shift can be controlled by placing the focus of the laser beam at a different position with respect to the gas medium [232]. When the laser is focused before or after the gas medium, efficient phase matching is achieved. When the focus is at the center of the medium, the intensity of the generated harmonic is low due to sub-optimal phase matching.

- **The atomic phase mismatch:**

The last term of equation 3.37 is due to atomic dipole phase mismatch. Since the atomic dipole phase varies with the intensity of the applied laser field, this can lead to a decrease in the harmonic emission. This effect can be reduced by finding situations in which the net phase of

the geometrical and atomic dipole phase mismatch are played against each other in order to achieve good phase matching.

The phase mismatch of the atomic dipole originates from the trajectory of the emitted electron which leads to the generation of the q^{th} harmonic from the continuum state. This phase varies linearly with the laser intensity. Since laser intensity can vary in both the longitudinal and radial directions, therefore, the atomic dipole phase also varies axially as well as radially. In this case, reduction of harmonic emission as well as strong spatial distortion take place [232]. To reduce of this effect, situations are sought in which the atomic dipole phase mismatch can play against the geometrical phase mismatch in order to improve overall phase matching. One way to minimize the phase mismatch is to minimize the variation of the harmonic phase with propagation. This can be achieved when the laser is focused before the gas cell, i.e. the harmonic phase variation is minimized, and thus the phase mismatch is also minimized [232].

A Gaussian laser beam with intensity I_o along the direction of propagation z can be described as:

$$I(z) = \frac{I_o}{[1+(\frac{2Z}{Z_R})^2]} \tag{3.45}$$

The contribution of the dipole phase to the phase mismatch of the qth harmonic can then be expressed as [233, 234]:

$$\Delta k_A = \frac{8Z}{{Z_R}^2[1+(\frac{2Z}{Z_R})^2]^2}\alpha_q I_o \tag{3.46}$$

where α_q is a coefficient related to the electron trajectories and Z_R is the Rayleigh length.

The atomic dipole phase mismatch allows a high plasma dispersion to be compensated because it acts as an additional time dependent wave vector. The dipole phase and the phase gradient of the dipole phase helps to reduce the phase mismatch at a high intensity region of the driving laser beam and thus to enhance the HHG efficiency [234].

3.4.4 Space Charge Effect

The space charge effect (SCE) is an important issue that one should consider in photoelectron spectroscopy experiments. The SCE originates from the interaction between the charged particles generated at a sample to form a charge cloud or plasma. The SCE changes the physical characteristics of the emitted charged particles, such as their angular distribution and kinetic energy. In PES experiments, where the detected charged particles are electrons, the SCE should be considered since it may distort the information acquired from the detected photoelectrons. The SCE has a significant effect on the measured PES when an intense laser field is applied to a condense phase sample [235, 236]. Once ionization processes are initiated, the photoemitted electrons form an electron cloud of potentially high electron density. This gives rise to Coulomb interactions between the emitted electrons as well as between the electrons and positive ions which are left in the sample. As a result, the SCE leads to a redistribution of the photoelectrons in the continuum spectrum, causing gain or loss of a fraction of the kinetic energy of

the charged particles due to attractive or repulsive forces. Due to the field gradient generated by the time-evolving charged particle population density, the electron velocity distribution is invariably broadened by the SCE.

In the time-resolved photoelectron spectroscopy (TRPES) technique, the SCE becomes prominent when a solid or liquid sample is used [236–239]. The SCE effect in liquid solution was first reported by my group [239] and has been an essential consideration for the study of aqueous electron dynamics using time-resolved photoelectron spectroscopy technique. In this case, where two laser beams with a different photon energy interact with the sample, two electron clouds are created at different times. Since the mutual Coulomb interaction depends on the density of the time-evolving charged particle distribution and the distance between the two clouds, thus, the time-delay between pump and probe pulses and the pump- and probe- intensity play important roles in determining the strength of the SCE.

When a pump pulse with a sufficient intensity interacts with the sample, photoelectrons are produced due to the direct ionization processes initiated by the multiphoton absorption. The photo-emitted electrons form a time-evolving charge cloud, and the intensity of the pump pulse determines the electronic density of the formed cloud (see the upper part (panel a) of figure.3.10).

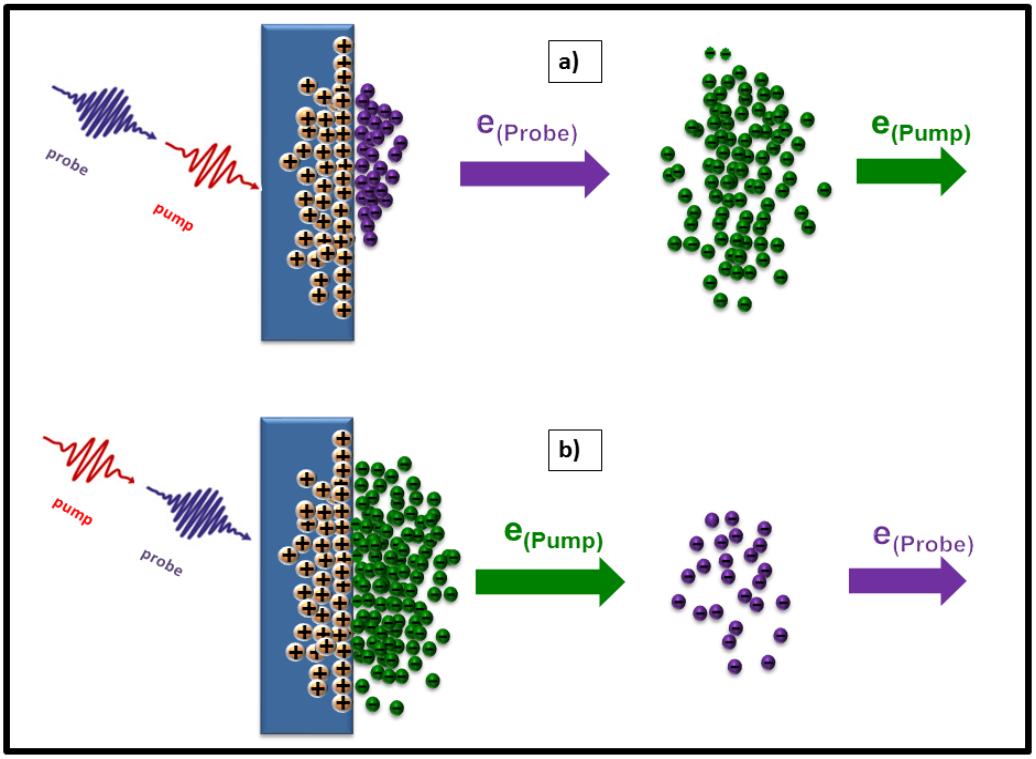

Figure 3.10: Space-charge effect: (a) Pump pulse arrives first at the sample, (b) Probe pulse arrives before pump pulse at the sample.

After the excitation with the pump pulse, a probe pulse may be applied to the sample, potentially creating another cloud of photoemitted electrons. When the time delay between the

pump and probe pulses is short, the distance between the two clouds is small and thus, the effect of the mutual Coulomb interaction between the two clouds will be at its strongest. The charge cloud formed by a high harmonic probe beam generally has a low density due to its relatively low intensity with respect to the applied pump pulses. With a low photon energy pump pulse and a high photon energy probe beam, the photo-emitted electrons associated with each laser pulse will interact on the way to the detector. Upon application of sufficiently intense pump/probe pulses, the electrons in the two clouds will strongly interact, leading to an exchange of their kinetic energy due to mutual Coulomb repulsion. Considering a high photon energy high-harmonic probe pulse and a low photon energy pump pulse, the probe pulse photoelectrons will pass through the photoemitted electron cloud of the pump beam before arriving at the detector. This interaction leads to positive SCE at the earliest pump-probe time delays, which can be seen in the photoelectron spectrum as a negative energy shift on the kinetic energy scale.

In addition, in the case of neutral or positively charged samples, the intense pump pulses produce a high density of confined positive ions, distributed over the pump-sample interaction region. The cloud of electrons created by the probe pulse and the positive ions produced at the surface of the sample by the pump pulse interact with each other. As a result, the kinetic energies of the photoelectrons created by the probe pulse are reduced at intermediate pump-probe delays. The superposition of the positive and negative components of the SCE leads to spectral shifts and broadening of the peaks in the photoelectron spectrum.

When the probe pulse interacts with the sample first (see the lower part (panel b) of figure 3.10), the reverse situation takes place. In this case, the high kinetic energy cloud of photoelectrons created by the probe pulse is formed earlier than those associated with the pump pulse. Here, a positive SCE occurs because of the attraction between probe-generated ions and the photoelectrons emitted by the pump pulse whilst the negative SCE occurs because of the repulsion between the photoemitted pump and probe electron clouds. In the probe-pump case, the superposition of the positive and negative components of the SCE always has a positive sign, implying a positive kinetic energy shift of the probe pulse generated electrons. This has been demonstrated in Ref. [239].

As an example of the time-dependent SCE, figure 3.11 shows the dependence of the probe electron kinetic energy shift as a function of the pump-probe delay. One can see from figure 3.11 that the energy shift can exceed a few eV, which is a significant value for valence PES experiments. Here, the SCE was measured using a liguid jet sample (see section 4.5)

The superposition of the two laser pulses at zero time delay creates a strong SCE due to the small distance between the interacting charge particles clouds. Nevertheless, a number of effects appear in the electron spectra at time zero such as the free-free electron transitions, which makes distinguishing features specifically associated with SEC difficult.

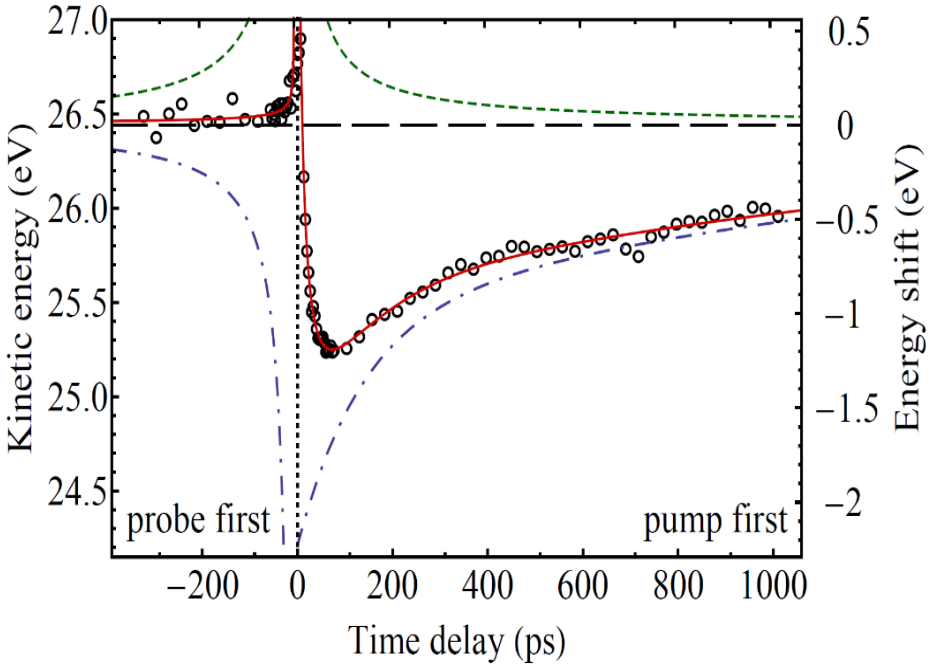

Figure 3.11: Energy shift of the Fe-3d(t_{2g}) ionization peak, recorded with an aqueous ferrocyanide liquid jet, as a function of time delay between the a third harmonic pump, with photon energy of 4.55 eV and ∼55 fs duration, and the XUV probe, 21st harmonic with 32.6 eV photon energy and ∼50 fs duration, probe pulses. The experimental data are shown by circles while the dashed horizontal line denotes the peak position obtained when applying the XUV pulse only. The spectral energy shift due to the space-charge effect is presented on a kinetic energy scale. The analytical model of the results is shown as a red (solid) curve. The calculated specific contributions from the negative and positive space charge effects are shown in the figure as green dashed lines and blue dotted-dashed line, respectively, see reference [239] for details.

3.4.5 Laser-Assisted Effect in Pump-Probe PES Experiments

The tremendous development of ultrashort pulse laser systems and the associated widespread access to intense laser fields has led to far-ranging studies of nonlinear, strong laser field light-matter interactions. Such developments have simultaneously given access to the ultrafast timescale, allowing a range of femtosecond-time-resolved spectroscopy techniques such as time-resolved photoelectron spectroscopy and UV/Vis transient absirption spectroscopy to be developed [212, 240, 241].

In the presence of a strong laser field (in the TRPES experiments), electrons emitted to the vacuum can be accelerated or decelerated by the influence of the applied laser field. This is associated with absorption or emission of laser photons by the electron in the combined ion Coulomb-laser field, leading to the appearance of sidebands in the XUV photoemission spectrum with these sidebands having an energy separation equal to the photon energy of the applied laser radiation. This effect is known as laser-assisted photoemission (LAPE) [181, 242].

The LAPE effect was first investigated in Argon atoms in the presence of a strong CO_2 pulsed laser field [242]. Later this effect was observed by Glover *et al*, in the photoelectron spectrum of gaseous helium ionized by ultrashort soft x-ray pulses [243]. Also, the LAPE effect has been successfully observed by combining femtosecond extreme-ultraviolet pulses from a free-electron laser with intense light pulses from a synchronized neodymium-doped yttrium lithium fluoride laser [244]. In these early works, the LAPE effect was studied by means of photoelectron spectroscopy, applied to condensed matter samples and using attosecond laser pulses [245]. Later studies show that the physics of the laser-assisted photoelectric effect can be extended to solid-state systems [181,246]. Recently, the LAPE effect has also been observed in the liquid phase by using the TRPES technique [247]. In principle, the concept of the LAPE effect is the same for the gas, solid or liquid phase. It can be described in terms of free-free electron transitions in the continuum [181].

The basic principle of laser-assisted photoemission processes can be presented in two steps. First, the system, initially in the ground state, is excited above the vacuum ionization threshold upon absorption of a high energy photon, photo-oxidizing the sample and producing a free electron in the ionization continuum. Here we consider ionization by an ultrashort XUV pulse [243, 246]. In the second step, the emitted photoelectron interacts with the superimposed high intensity (assisting) laser pulse. If the released electron is still close to the oxidized parent system and is still effected by the interaction potential of the core when the pump pulse arrives, it can absorb or emit one or several photons from the intense, superimposed field . This effect gives rise to sidebands in the XUV photoemission spectrum, which are separated on the kinetic energy scale by the photon energy associated with the superimposed, intense field. At different time delays between the XUV and intense (assisting) laser pulses, side-band-generating pulses (LAPE effect) appear when the two pulses overlap in time. Figure 3.12 schematically illustrates the LAPE effect.

The LAPE effect is useful tool for time-resolved photoemission experiments as it provides information on timing synchronization between pump and probe pulses. The LAPE effect gives rise to a photoelectron signal which represents the cross-correlation of the pump and probe processes in the TRPES spectra. This facilitates the determination of the time-zero and the temporal resolution of pump-probe experiments. By measuring the kinetic energy spectra of electrons produced in the LAPE process of the two pulses, a clear cross-correlation effect will appear in the PES spectra. As discussed above, the cross-correlation process can be measused in the absence of any resonant states. In any pump-probe PES experiment, the kinetic energy of the photoemitted electrons can be written as [243, 248, 249]:

$$E_{Kin} = N\hbar\omega_1 + M\hbar\omega_2 + I_p \tag{3.47}$$

where ω_1 and ω_2 are photon energies of the first and second laser pulses, respectively. I_p represents the ionization potential of the atom or molecule, N is the number of involved first

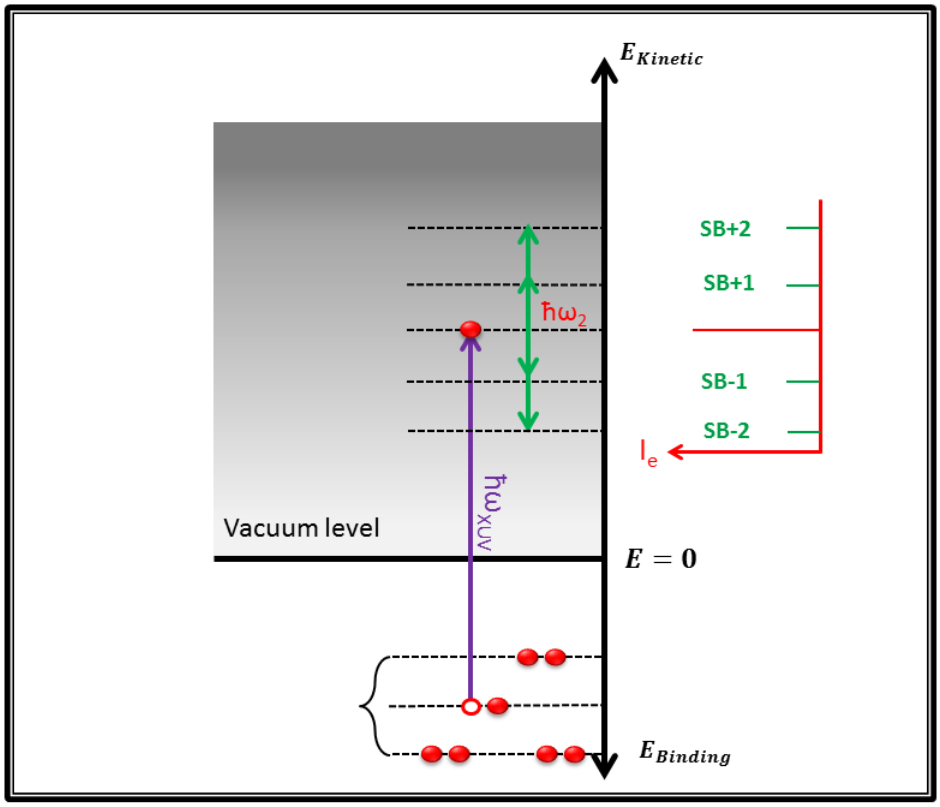

Figure 3.12: Schematic illustration of the laser-assisted photoemission (LAPE) process. An electron in the ground state of a sample is emitted above the vacuum threshold by absorption of an XUV photon from the probe beam. The released electron absorbs or emits one or several photons from the intense, assisting laser field laser.

pulse (probe) photons, and M is the number of second pulse (pump) photons. Here the sign of M can be positive or negative for ionization channels corresponding to the absorption or emission of second pulse (pump) photons, respectively. In the case of a weak ω_1 field with sufficient photon energy to directly ionize the sample, the ionization yield $S_M(\tau)$ in the emission bands at a given time delay τ can be represented by the convolution integral [181]:

$$S_M(\tau) \approx \int_{-\infty}^{\infty} I_1(t) I_2^M(t-\tau) dt \tag{3.48}$$

where I_1 and I_2 are intensities of first and second laser pulses, respectively.

Assuming that, the first and second beams have Gaussian temporal profiles, the duration of the cross-correlation signal can be calculated from equation 3.48 as [249]:

$$\tau_{cc}^2 = \tau_1^2 + \frac{\tau_2^2}{|M|} \tag{3.49}$$

Here τ_{cc} is the temporal width of the cross-correlation signal, and τ_1, τ_2 are the temporal widths of the first (XUV probe) and second (pump) pulses, respectively.

3.5 UV/VIS Transient Absorption Spectroscopy

Time-resolved transient absorption spectroscopy (TAS) is a powerful technique that has been used to study many photo-generated species which are of interest in the physical and material sciences [16]. It is capable of providing information about the kinetics of the excited states by measuring the time-dependent absorption signal. TAS is a typical pump-probe method in which the pump pulse is employed to populate an excited state and the probe pulse is applied to measure the changes to the absorption spectrum caused by the transient species as a function of time delay between the pulses. The evolution of the absorption spectrum as a function of time delay contains information on the dynamic processes that occur in the molecular or material system under investigation, such as excited state populations and decay, energy migration, electron transfer, isomerization, and intersystem crossing.

3.5.1 Principles of Time-Resolved Transient Absorption Spectroscopy

In TAS, a fraction of molecules is promoted to an electronically excited state (A1) from the ground state (A0) by applying a relatively high intensity pump pulse (see figure 3.13). A probe pulse, which has low intensity, is sent through the sample with a time delay (Δt) with respect to the pump pulse. The probe pulse should have a weak intensity in order to avoid multiphoton processes during probing. The pump and probe beams are spatially overlapped on the sample. The pump beam is usually blocked after the sample, whereas the probe beam passes through the sample to a detector to measure the transmitted light intensity. The excitation process induces changes to the absorption spectrum of the molecular system under investigation, which can be monitored at many wavelengths simultaneously using a white light super-continuum probe. The probe spectrum is recorded, e.g., by the combination of a spectrograph and camera. A controlled delay stage is used to adjust the arrival time between pump and probe pulses to the sample. By changing the time delay, Δt, between the pump and the probe pulses and measuring the transmittance spectrum at each time delay, an informative 2-dimensional map of the signal as a function of time delays and absorption wavelengths of the interrogated system is produced. By comparing the transmitted intensity of the probe pulse with and without the effect of the pump pulse, the transient absorption signal can be determined as a function of wavelengths and time delays. According to the Beer-Lambert law, the expression of the optical density (OD) is [250]:

$$I_{po}(\lambda) = I_o(\lambda)10^{-OD(\lambda)}, \tag{3.50}$$

$$OD(\lambda) = LC\varepsilon(\lambda), \tag{3.51}$$

where $I_o(\lambda)$ and $I_{po}(\lambda)$ are the intensities of the probe beam before and after interaction with the sample, respectively, L is the path length of the sample, C is the concentration of the investigated molecule in the solution and $\varepsilon(\lambda)$ is the wavelength-dependent molar extinction coefficient, which provides a measure of the strength of optical absorption of the material under

investigation.

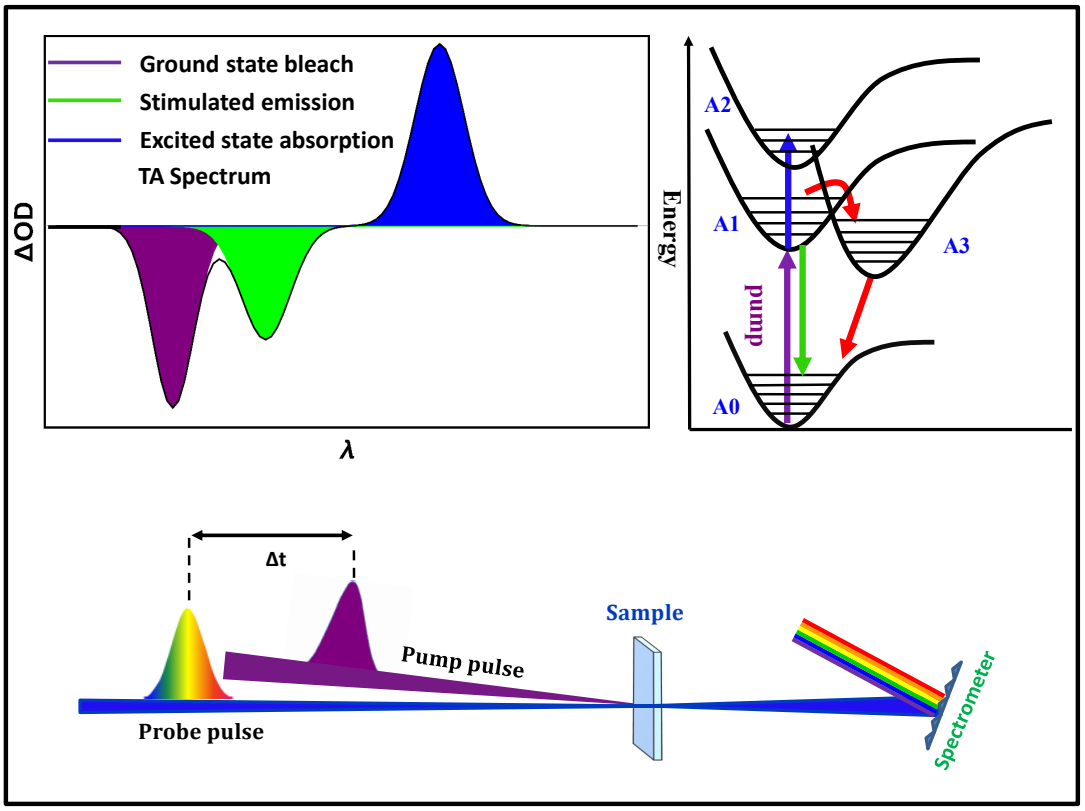

Figure 3.13: A schematic of the TAS experiment. In an ultrafast TAS experiment, a sample of interest is excited by a pump pulse. The probe pulses are analyzed by the spectrometer. The TAS signal is recorded as the change in optical density, $\Delta OD(\lambda)$, in the case where the pump pulse is present and where it is not. When the detected transmittance increases upon optical excitation, i.e. a negative $\Delta OD(\lambda)$ is measured, this usually corresponds to a ground state, A0, bleach or stimulated emission signal. The population of states A1$-$A3 is typically accompanied by excited-state absorption, leading to positive $\Delta OD(\lambda)$ values.

Changes in state populations result in changes of the effective concentration, and thus in a changing OD:

$$I_{pp}(\lambda) = -I_o(\lambda)10^{-[OD(\lambda)+\Delta OD(\lambda)]}, \tag{3.52}$$

$$\Delta OD(\lambda) = log[\frac{I_{po}}{I_{pp}}], \tag{3.53}$$

where the po and pp subscripts denote the attenuated (transmitted) intensity of the probe beam in the probe-only and pump-probe cases, respectively.

In general, contributions from different processes can be found in the transient absorption spectrum. These contributions can be distinguished via the spectral positions at which they appear and the associated signs of the ΔOD. It is important to understand the physical processes associated with the signals in the TA spectrum. The contributions that can be observed are:

ground state bleach, excited state absorption, stimulated emission, and photoproduct absorption.

- **Ground state bleach:**

This bleach is due to the promotion of a fraction of the molecules from the ground state, A0, to an excited state, A1, via absorption of photons of the pump pulse (see the upper right panel of figure 3.13). The concentration of the ground state has been decreased due to pump photon absorption, leading to a ground state signal depletion. As a consequence, the ground-state absorption after the excitation process is less than that in the non-excited molecules. This leads to $OD_{pump} < OD_{probe}$ and the observed ΔOD signal in the wavelength region of the ground state absorption become negative. This is schematically indicated in the upper left panel of figure 3.13 where the TA spectrum shows a negative signal (purple area).

- **Stimulated emission:**

Stimulated emission can occur when the probe beam passes through the excited sample. During this time, a photon from the probe pulse can induce a radiative transition of an excited electron to a lower-lying state, potentially producing the ground state. The emitted photon propagates in the same direction as the probe photon, and then both will be detected. This leads to a relative increase in the intensity of the probe beam at the detector. Therefore, the apparent OD_{pump} will be lower than the OD_{probe}, and thus, the ΔOD appears with a negative sign in the spectrum, as schematically shown in the upper left panel of figure 3.13 (green area).

- **Excited state absorption:**

This process can take place when the excited states absorb a photon from the probe beam and are thus promoted to higher excited states (see the upper right panel of figure 3.13). This leads to a positive ΔOD signal which appears in the wavelength region of excited-state absorption as shown in the upper left panel as a blue area with a positive ΔOD signal in the TA spectrum.

- **Photoproduct absorption:**

A positive signal may occur in the TA spectrum after excitation of a photosynthetic system. This signal is due to a photo-reaction in the sample leading to a transient state, such as metastable states, charge-separated states, isomerization states, or photochemical reaction products. The positive signal associated with such a species appears at the specific region where the product absorption bands are located.

3.6 Polarization Effect of the Pump Beam

In the present study, experiments were performed with different alignments of the linear pump polarization by setting its polarization axis to be parallel, perpendicular, or at magic angle

(54.7°) with respect to the linearly polarized probe pulses. Here, absorption by polarized pump pulses generates a transient anisotropy in the electron density distribution and nuclear geometry distribution, which may be used to provide new insights into the resulting electronic dynamics of molecules, when polarized probe pulses are applied [251–253]. Information on the energy dependent dynamics, the angular distribution of the photoelectrons, the electronic relaxation processes, and resonant states, can be provided with bi-chromatic laser fields where probe pulses can directly ionize, via one-photon transitions, valence and/or inner-shell electrons.

Excitation by the pump pulses may lead to the formation of nonuniform electron density distributions in atomic/molecular systems, i.e. the formation of electronic anisotropy. In particular, application of pump pulses of linear polarization leads to preferential electronic excitation of molecules along the transition dipole moment, μ, and the angular-dependent probability $P(\vartheta)$ to excite a molecule can be expressed as [254]:

$$p(\vartheta) \propto \langle (\overrightarrow{E} \quad \overrightarrow{\mu})^{2n} \rangle \propto cos^{2n}\vartheta, \tag{3.54}$$

where $\overrightarrow{E}$ is the electrical field vector along the z-axis in the laboratory frame, n is the number of photons absorbed in the excitation process, and ϑ is the angle between the z-axis and the transition dipole moment.

Different relative polarization states of the pump and probe pulses probe the pump-generated anisotropy differently. This is due to the sensitivity of the bound-bound or bound-free (ionizing) transitions to the electronic polarization of the sample. Exploiting this effect, the transient anisotropy of the sample and the associated populated electronic states can be recorded with time-delayed, polarized probe pulses. The rotational behavior of molecules (a nuclear anisotropy created by the pump pulses), which often occurs on a picosecond-nanosecond time scale [252], the internal vibrational relaxation in molecules, and electronic resonance and energy transfer processes are examples of processes that may take place in the liquid phase and display a transient anisotropy [252].

The total anisotropy can be expresses in terms of the average orientation of the transition dipole moments of the photoexcited molecules. The anisotropy can be probed by measuring the signal when the polarization of probe pulses is set either parallel or perpendicular with respect to the pump pulse polarization. Thus, the time-dependent anisotropy parameter can be defined by [251, 254, 255]:

$$r(\Delta t) = \frac{S_{\parallel}(\Delta t) - S_{\perp}(\Delta t)}{S_{\parallel}(\Delta t) + 2S_{\perp}(\Delta t)}, \tag{3.55}$$

Here, $S_{\parallel}(\Delta t)$ and $S_{\perp}(\Delta t)$ are the total photoemission yields (or absorption signal) which is recorded for pulses being polarized parallel or perpendicular with respect to each other over the time delay (Δt) between the pump and probe pulses, respectively. In the PES experiments, the above anisotropy definition requires detection of photoelectrons in all directions. However, the spectrometer which is used in the PES experiments of this work, only collects a portion

of the emitted electrons with a maximum acceptance angle of ± 15°. The measurement of photoelectron angular distribution (PAD), which defines as the dependence of the distributions of electron ejected from the system to the polarization alignments of the applied laser pulses, is difficult in the present PES experiment.

The anisotropy becomes irrelevant, when the mutual alignment of the pump and probe polarization axes is set at magic angle (54.7°). For absorption or florescence transient spectroscopy experiments, the anisotropy for the case of one-photon pump and one-photon probe process is written as [251, 254]:

$$r(\Delta t) = \frac{2}{5}\langle P_2(\mu_{pump}(\Delta t = 0)\mu_{probe}(\Delta t))\rangle = \langle \frac{2}{5} P_2 cos(\theta)\rangle = \langle \frac{1}{5}(3cos^2(\theta) - 1)\rangle \tag{3.56}$$

where P_2 is the second Legendre polynomial, μ_{pump} and μ_{probe} are the transition dipoles of the pump and probe transitions, respectively, and the brackets mean the expectation value.

One can easily find that $r(\Delta t) = 0$ at $\theta = 54.7^o$. Therefore, in the transient absorption experiments, it is common to apply pump and probe polarization aligned at magic angle.

The magic angle arises similarly in PES experiments. Considering the case of ionization with a single photon of linearly polarized light, the PAD has the form [256]:

$$I(\theta) \propto 1 + \beta_2 P_2(cos(\theta)) \tag{3.57}$$

where β is the conventional anisotropy or asymmetry parameter. The term $\beta_2 P_2(cos(\theta))$ in the equation 3.57 is zero when the angle θ equals to 54.7°. Therefore, when the angle between the pump and the probe polarization is set at the magic angle (54.7°) the intensity of $S_{\parallel}$ and $S_{\perp}$ only depend on the cross section.

The general formula describing the photoelectron angular distribution in l+1́(pump-probe) photo-ionization of a molecular system is more complex than equation 3.57 and can be expressed as [256]:

$$I(\theta, \phi) \propto \sum_{L=0}^{L_{max}} \sum_{M=-L}^{L} B_{LM} Y_{LM}(\theta, \phi) \tag{3.58}$$

Here the PAD is considered with respect to an axis in the molecule, $Y_{LM}(\theta, \phi)$ is a spherical harmonic function, (θ, ϕ) are measured with respect to a molecular z axis, and B_{LM} are coefficients that describe the contribution of each partial wave to the PAD and thus, their values define the interference of partial waves [256, 257]. The B_{LM} coefficients depend on the molecular alignment prepared by the pump pulse, i.e. the molecular geometry and electronic structure, the dynamics of photoionization, the experimental geometry, the orbital from which the electron is ejected, and the photoionization energy [256]. The sum term, L, is the rank of the spherical harmonic and is related to the angular momentum quantum number. In the case of an isotropically distributed electron density, this parameter is equal to 2n, where n is the number of photons involved in the ionization process. M is related to the angular momentum

projection quantum number, and its value is limited by -$L_{max} \leq M \leq L_{max}$. The values of L and M depend on the angular momentum and symmetry restrictions, which depend on both the properties of the atom/molecule under study and the experimental geometry [258]. The simplification of equation 3.58 is performed in the dipole approximation, allowing values of L to be determined to be l-1 and l+1, where l is the initial angular momentum quantum number of the photoelectron.

Equation 3.58 is usually determined by relatively small values of L and M. The first coefficient, B_{00}, is proportional to the angle-integrated photoelectron intensity. The subsequent coefficients describe the anisotropy of the PAD, and are normally divided by B_{00} to give a normalized coefficient to compare with other measurements [256].

For different polarization alignment of the pump and probe laser field, differential PADs with different values of the asymmetry parameters B_{LM} can be derived from equation 3.58. Three specific cases are presented below:

- **Parallel polarization alignments of the pump and probe pulses**

In the case when both the excitation and ionization laser beams are linearly polarized along the same laboratory z axis and only one photon from each laser beam is absorbed, the PAD for parallel relative polarization becomes cylindrically symmetric, i.e. independent of ϕ and equation 3.58 becomes [256]:

$$I(\theta) \propto B_{00}Y_{00}(\theta,\phi) + B_{20}Y_{20}(\theta,\phi) + B_{40}Y_{40}(\theta,\phi), \tag{3.59}$$

- **Perpendicular polarization alignments of the pump and probe pulses**

If the polarization vectors of the excitation and ionization light beams are both linearly polarized but are perpendicular to each other, the cylindrical symmetry may be broken and terms with $M \neq 0$ appear. The PAD equation is given by [256]:

$$I(\theta,\phi) \propto B_{00}Y_{00}(\theta,\phi) + \sum_{L=2,4} (B_{L-2}Y_{L-2}(\theta,\phi) + B_{L0}Y_{L0}(\theta,\phi) + B_{L+2}Y_{L+2}(\theta,\phi)) \tag{3.60}$$

where the z axis is along the polarization vector of the ionizing light.

- **Magic angle polarization alignments of the pump and probe pulses**

In the time-resolved PES experiments with two linearly polarized light beams whose polarization vectors are aligned at the magic angle (54.7°), the angular distribution is given by [256]:

$$I(\theta,\phi) \propto \sum_{L=0,2} B_{L0}Y_{L0}(\theta,\phi) + \sum_{L=2,4} (B_{L\pm1}Y_{L\pm1}(\theta,\phi) + B_{L\pm2}Y_{L\pm2}(\theta,\phi)) \tag{3.61}$$

where the z axis is along the polarization vector of the ionizing light.

The effect of polarization of the applied laser pulses in the pump-probe experiments is very clear. At short time delays, the transition dipole moments of the molecules, which absorbed a single photon, are aligned to the pump laser polarization with a $\cos^2(\theta)$ probability distribution. In particular, if the alignment is created by a linear transition, the principal axis of the excited molecule can be aligned preferentially parallel or perpendicular to the pump laser polarization, depending on the transition dipole moment. By applying probe pulses with linear polarization, at short time delays, the PAD generally shows a characteristic nonuniform distribution. At longer time delay (in non-isolated systems), the alignment parameter decreases, so the ensemble of molecules moves toward a random alignment in space. At even longer delay time, the characteristic features of anisotropy completely vanish.

A further consideration in PAD measurements is the collection volume of the spectrometer. In the case of the THEMIS time-of-flight-spectrometer discussed here, the collection volume depends on the lens mode utilized and spans the sub-millisteradian to hundred-millisteradian solid angle collection ranges. This effect must be considered and deconvolved from any PAD data measured with such a spectrometer to facilitate the interrogation of the ionization dynamics. In the case of magic-angle polarization alignments, however, the angular selectivity of the spectrometer simply reduces its overall collection efficiency, preserving the relative photoelectron peak intensities and the inherent ionization signal levels.

Concluding this discussion, the appearance of transient spectra in PES experiments can be different for specific alignments of the pump and probe polarization axes. The polarization effect can lead to the increase or decrease of the photoemission contribution from a given excited state, when photoelectrons are detected in a particular direction in the laboratory frame instead of measuring the total emission yield. It can also result in a strong suppression of the contribution from a state, depending on the asymmetry parameters and the mutual angle of polarization axes. Therefore, application of the magic angle between pump and probe polarization is of special interest in time-resolved spectroscopy experiments. In this case every populated state contributes to the transient signal according to its population, the corresponding transition cross section with the asymmetry parameters becoming irrelevant.

In the present work, we extend the previous study on the excited state dynamics of ferricyanide by using the magic-angle configuration of polarization alignment of the pump and probe pulses. It provides complementary results which we use to identify the relaxation mechanism of this molecule. For the sake of comparison, the PES study was performed with the perpendicular polarization alignment as well.

3.7 Data Analysis Procedure (Global Fitting)

A global fit analysis was used to numerically solve the nonlinear system which represents the state population dynamics of the studied liquid samples, providing important information including the time-dependent changes in the electronic structure of the photo-excited states fol-

lowing optical excitation. The mechanisms of intramolecular electron transfer of a molecular or material system can be obtained from time-resolved measurements once the data has been analyzed with an appropriate model. A global fit based on such a kinetic model can be used to analyze the time-resolved data presented here. This section includes the analysis procedure of the transient spectra that is used to extract the ultrafast kinetics of the observable spectroscopic changes. In both experiments (TRPES and TAS), the goal of using a global-fit approach was to estimate the expected parameter values (such as state amplitudes, time constants) of each observation, including the temporal signal behavior and associated energetically dispersed spectra of the evolved state. Spectrally dispersed time-resolved measurements yield multidimensional data sets $D_{exp.}(s,t)$, where one dimension (t) is given by the delay time and the other dimension (s) is the spectral term. In this study, the latter is either the binding energy of the emitted electrons (in PES spectra) or the wavelengths of the probe light (in TAS spectra). In the global fit analysis, the two-dimensional spectra are modeled by the spectral components of each time-dependent state, $D_{mod.}(s,t)$. Throughout this work, we assume that the spectral features of the involved states are not time-dependent. Thus, the model data matrix can be expressed as a matrix multiplication [259, 260]:

$$D_{\text{mod.}} = A(s)\,T(t). \tag{3.62}$$

Here, the columns of A(s) represent the amplitude spectra of the involved state, while the rows of T(t) contain their respective normalized population densities.

The optimization problem in the global fitting procedure is the computation of the best-fit parameters by minimizing the sum of squares of the difference between the data set and the model. This is performed by minimizing the objective function [259, 260]:

$$\chi^2 = \left|\left| \frac{D_{\text{exp.}}(s,t) - D_{\text{mod.}}(s,t)}{k(s,t)} \right|\right|^2, \tag{3.63}$$

where k denotes the standard deviation of the respective data points. Since the photoelectron signal measured with the TOF spectrometer displays Poisson statistics, we assume the standard deviation to be the square root of the data value, i.e., $k(s,t) = \sqrt{(D_{exp}(s,t)}$. For TAS, the respective Gaussian standard deviation is obtained from the statistics of the repeated spectral measurements. Confidence intervals of the fit parameters are determined by numerically calculating the Hessian of the objective function.

In the following, we will explain the structures of the kinetic and spectral matrices, as well as the specifics of the PES and TAS analysis, in more detail.

- **Kinetic matrix**

The time-dependent evolution can be introduced as a sum of the differential kinetic equations that represents the transient population of the electronic states and the dynamics of the states

decays in the interrogated system. The initial condition at negative time delays always assumes the full population of the electronic ground state [GS]=1, while all other states are unpopulated. Solving the kinetic equations results in a population-density matrix T(t), wherein the rows contain the normalized time-dependent population densities of the real states. Specifically considering aqueous samples, we account for the contribution of the solvent signal by assuming a constant population density of unity for the ground state of the water molecules.

A particular rate equation model is proposed to represent the time-dependent dynamics of the resonant states in the molecular system. Solving the model differential equations is performed numerically or analytically using a closed solution of the equation.

Applying the respective solution of the rate equations for the model in a global-fit-analysis reveals kinetic parameters (i.e., rate constants), as well as spectra associated with the involved states. For all the states involved, the corresponding spectra are represented as columns of the amplitude matrix. The pump intensity is considered to have a Gaussian temporal envelope of unit amplitude, which is described as:

$$I_{\text{pump}}(t) = \exp\left[\frac{-(t-t_0)^2}{2\sigma_{\text{pump}}^2}\right], \tag{3.64}$$

where σ_{pump} is the Gaussian width of the pump intensity profile.

In the PES spectra, the time-dependent cross-correlation (CC) signal is represented by an amplitude-normalized Gaussian, i.e., identical to the pump intensity. The signals from the CC and solvent are described and appended as an additional separated vector to the population-density matrix. The photoemission spectra of the solvent and resonance states, which are obtained from the fit, are strictly positive, whereas the CC signal may also assume negative values. The negative CC amplitudes account for the bleaching arising from the depletion of the solute and solvent states caused by the pump pulse. In this way, bleaching does not imply negative population densities of the electronic states, rather a transient reduction of population.

In the TA spectra, the CC is visible as a cross-phase modulation where the spectral contributions are already included in equation (3.24). An additional row, which describes the cross-phase modulation signal, is appended to the time-dependent matrix.

To obtain the actually observable kinetic matrix, T(t), the rows of the population-density matrix of the real states are convolved with the area-normalized Gaussian probe-pulse envelope intensity. The equation of the probe pulse time envelope is written as:

$$I_{\text{probe}}(t) = \frac{1}{\sqrt{2\pi}\sigma_{probe}} \exp\left[\frac{-(t-t_0)^2}{2\sigma_{\text{probe}}^2}\right], \tag{3.65}$$

where σ_{probe} is the Gaussian width of the probe pulse.

The convolution is especially applied in the PES spectra, while in the TAS spectra, the convolution of the states and CC are included already in the solution to the model equations.

Due to the supercontinuum probe generation mechanism, the TA spectra exhibit a chirp effect, whereas the temporal chirp effect is significantly less in the PES experiments and is assumed to be negligible on the timescales considered in this thesis. For optimal time resolution, the chirp effect has to be compensated. This can either be done with pre-compression of the pump and probe pulse chirp or by post-processing the acquired data. In the TA spectra, the chirp effect on the XPM and resonantly populated state signals are modeled and accounted for in the data analysis. In this case, the compensation of the chirp is performed by finding the time zero for each energy bin vector and temporally shifting all associated time traces to the correct time zero.

- **Spectral matrices**

Each transient spectrum can either be introduced explicitly as a sum of Gaussian components or can be implicitly derived from the least squares algorithm. In the explicit case, the Gaussian sum method is employed in the global fitting to represent the spectra obtained from the experiment. With the spectra of states being decomposed into a sum of Gaussian profiles:

$$A_i(E) = \sum_{j=1}^{n_i} A_{ij} \exp\left[-4\ln(2)\frac{(E-E_{ij})^2}{w_{ij}^2}\right]. \tag{3.66}$$

where A_{ij}, E_{ij}, w_{ij} are the amplitude, position and width of a given state i. The number of Gaussian terms n_i is specific for each state and was defined in the course of the global fit analysis. The minimum number of Gaussian terms was utilized in order to minimize the weighted residual obtained from the fit.This method is used in the PES analysis to estimate energetic positions of the real states in the spectra.

In the implicit case, the least squares method is used in the global fitting to represent the spectra. Under this condition, the shape of the spectra can be written in the form [261]:

$$A = D_{exp.} T^T (T.T^T)^{-1} \tag{3.67}$$

where T is the time-dependent matrix which results from solving the kinetic equations, $()^{-1}$ denotes the matrix pseudoinverse which is used to solve the linear equation system, and T^T is the transpose of the time-dependent matrix. The implicit method is applied separately for each spectral bin in the TAS spectra.

Chapter 4

Experimental Setups

This chapter is dedicated to describe the experimental setups which were used for transient XUV photoelectron spectroscopy (PES) and transient absorption spectroscopy (TAS) measurements.

Section 4.1 contains a description of the femtosecond titanium:sapphire (Ti:Sa) laser system, which is used to generate 800 nm central wavelength ultrashort laser pulses. The same Ti:Sa laser system was applied to generate the pump and probe pulses for the TRPES and TAS experiments. In order to investigate the electronic dynamics of the molecular system, ultrashort pump pulse are employed, either the second harmonic of the laser fundamental or a specific wavelength generated from an optical parametric amplifier (OPA) system. The second harmonic and optical parametric amplifier setups are presented in sections 4.2 and 4.3, respectively. Section 4.4 starts with an overview of the time-resolved photoelectron spectroscopy (TRPES) experimental setup, and then a detailed description of the high harmonic generation (HHG) setup is presented. Sections 4.5 highlights fundamental aspects and perspectives for time-resolved PES experiments on highly volatile liquid microjets in high/ultrahigh vacuum environment required for electron detection. The detection of the photoemitted electrons using a time-of-flight (TOF) electron spectrometer is described in section 4.6. Finally, section 4.7 presents the overview of the time-resolved transient absorption spectroscopy setup.

4.1 Femtosecond Laser System

For the experiments discussed in this thesis, a mode-locked seed laser oscillator (Ti:Sa COHERENT Vitara, Coherent Inc.), operating at a repetition rate of 80 MHz, is pumped by a CW laser (Coherent-Verdi-G5, Coherent Inc.) at 532 nm with 5 W of average power. The CW laser at 532 nm is efficiently absorbed by the Ti:Sa crystal, indirectly resulting in a broadband light emission in the near-infrared (NIR) region. The oscillator gives approximately 10 nJ pulses at a central wavelength of 800 nm with a pulse duration of typically 8–10 fs at FWHM. As the ultrashort pulse produced from the mode-locked oscillator is not very intense, thus, it should be amplified. Stretching the pulses before injection into an amplifier cavity is necessary in order

to avoid damage of the optical components due to the very high peak intensity of the amplified femtosecond pulses. Accordingly, the generated femtosecond pulses from the oscillator have to pass through three steps, i) a stretcher which temporally elongates the input pulse from femtosecond to picosecond duration, ii) a regenerative amplification cavity where the actual amplification happens, iii) a single-pass Ti:sapphire amplifier and iv) a compressor to return the pulse duration back to a tens of femtosecond (see figure 4.1). Such amplification scheme is known as chirped-pulse amplification (CPA). In the first step, an all-reflective, grating pulse stretcher is adopted. When the femtosecond pulses are injected in the stretcher, the ultra-short pulse is spectrally dispersed. Due to the configuration of the stretcher, the short wavelength component travels further through the stretcher than the long wavelength components. Therefore, prolongation of the pulse takes place. After that, the chirped pulse, with 80-100 ps of pulse duration, is introduced into the regenerative amplifier (COHERENT, Legend Elite Duo, Coherent Inc.) using a Pockels cell operating at 5 MHz, reducing the pulse repetition rate from 80 MHz, which is the second step of amplification of the produced laser beam. The regenerative amplifier cavity is made up of a second Ti:Sa crystal, placed in an optical resonator. The amplifier is pumped by an Nd:YLF pulsed laser (COHERENT Evolution, Coherent Inc.) at 527 nm wavelength with a pump power of 75 W. The incident pulse in the resonator cavity makes several round trips through the Ti:Sa crystal. On each pass in the cavity, the pulse gains energy from the pumped crystal. In the end, the amplified pulse with high energy is switched out of the cavity using a second Pockels cell operates at 5KHz. In the last step, the amplified pulses are compressed by a dual grating compressor, which operates to chirp the pulse in the opposite direction of the stretcher and amplification optics, providing an output of approximately 2.5 mJ pulse energy with 25 fs pulse duration at a center wavelength of 800 nm and a repetition rate of 5 kHz.

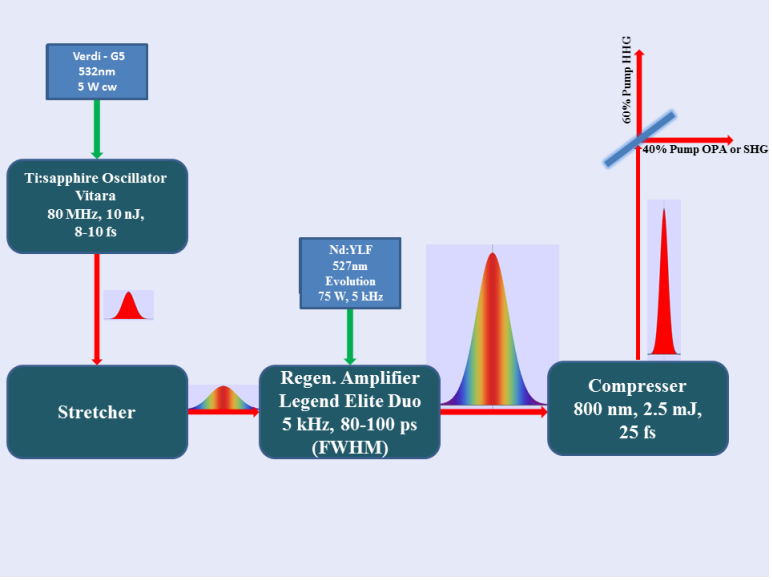

Figure 4.1: Schematic view of the femtosecond laser system. A detailed description is provided in the text.

4.2 Second Harmonic Generation (SHG)

In some of the experiments discussed here, the second harmonic (SH) of the Ti:Sa laser is used as a pump pulse to excite ground state molecules to electronically excited states. Afterward the HHG pulse is applied to monitor electrons in the ground and excited states. The choice of the SH as a pump source depends on the energy gap between the ground and excited states of chromophore in the molecules under investigation. The second harmonic generation (SHG) setup is depicted schematically in figure 4.2. After splitting the laser output into two branches, one of them is used to generate the SH pump beam, in a β-Barium Borate (BBO) crystal. BBO crystals have a high second-order non-linear susceptibility and NIR damage thresholds, leading to a high potential efficiency of SHG at the Ti:S a fundamental wavelength of 800 nm. The orientation of the BBO crystal axis with respect to the linear horizontal polarization of the incident laser pulse is an important parameter for efficient SHG. The angle between the fundamental beam and the crystal axis influences the phase matching conditions. A maximum efficiency of the SHG process can be achieved with a perpendicular orientation of the BBO crystal optic axis to the polarization alignment of the fundamental laser pulse. The conversion efficiency of the SHG process can be adjusted by rotating the polarization axis of the fundamental beam with respect to the crystal axis. This is achieved using an 800 nm half-wave plate positioned in front of the BBO crystal. Thus, the SHG intensity can be set to a specifically chosen value between the maximum and minimum depending on the alignment of the polarization direction and the crystal axis. Control over the alignment of the polarization axis orientation of the SH is important for polarization-state and time-resolved experiments (see chapter 6).

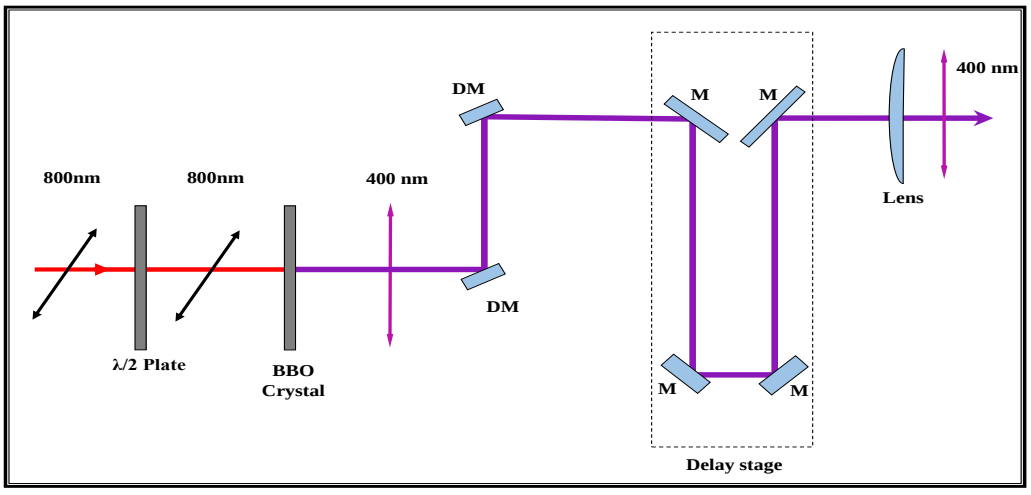

Figure 4.2: Schematic illustration of the second harmonic generation setup.

In such experiments, the wave plate also needs to be adjusted to achieve a desired intensity of the SH pulses. Since the fundamental beam has a horizontally polarized output, and the crystal axis is set vertically, the generated SH would have a vertical polarization axis. In order to rotate the polarization axis of the SHG pulses by 90°, the crystal should be rotated by 90°

degrees and the wave plate by 45°. For a specific SHG linear polarization direction, a similar procedure can be used to adjust the polarization axis of the generated SH to any other alignment. The generated SH can be separated from the residual 800 nm pump beam using dichroic mirrors (DM). A pair of dichroic mirrors is placed after the crystal to reflect the SHG beam and reject the fundamental beam (see figure 4.2). After the separation of the generated SH light, the beam is sent to a delay stage. The travel time of the SHG beam in the delay stage was adjusted in order to control the relative time delay between the pump and probe pulses. Afterward, the SH beam enters the interaction region through a thin optical window.

4.3 Optical Parametric Amplifier (OPA)

In birefringent nonlinear optical crystals, different nonlinear processes such as SHG, SFG, and DFG can be used to convert the wavelength of the incident light to another wavelength, giving the possibility to readily extend the range of available laser wavelengths which can be used in experiments (see section 3.3.1). A generally applicable way of obtaining a tunable output of the laser in the UV/Visible/IR spectral domain is to use the optical parametric amplification process [262]. In the present work, a commercial optical parametric amplifier (OPA, OPerA-Solo, Coherent Inc.) is used to provide a wide range of wavelengths (240–2600 nm). The OPA system generates an ultra-short pulse at a specific central optical frequency like the SHG process described in the previous sub-section, which is used as a pump beam to excite the molecular system under investigation. The optical parametric amplification system is built upon the second, $\chi^{(2)}$, and third-order susceptibility, $\chi^{(3)}$, of select nonlinear media. First, a white light supercontinuum is generated in a sapphire crystal ($\chi^{(3)}$ medium, see section 3.3.2 for a description of the process), producing a broadband, low-pulse-energy, chirped seed for the OPA process. Subsequently, these low energy pulses are amplified at specific frequencies in $\chi^{(2)}$ non-linear media. In such nonlinear materials, which lack inversion symmetry, two photons can be generated from a single photon or vice versa. In the OPA system, the initially weak seed beam with the frequency of ω_S (signal) and an intense beam with the frequency of ω_P (pump), where $\omega_P > \omega_S$, propagate together through a first BBO nonlinear crystal. Due to the parametric amplification process, a specific example of DFG, two intense beams with frequencies ω_S and ω_I=ω_P-ω_S can be generated. The generated beam with the frequency ω_I is referred to as the idler, and the other generated beam with frequency ω_S is is referred to as the signal. In this case, the photon energy of the pump, ω_P, wave is converted with the sum of the lower photon energies of the signal and idler beams, equaling the photon energy of the pump. The ω_S and ω_I frequencies and efficiency of the amplification process are set by energy ω_P=ω_I+ω_S and momentum k_P=k_S+k_I conservation, so that, the phase matching conditions Δk=k_S+k_I-k_P needs to be fulfilled. Typically, dense, solid birefringent materials are used to satisfy the phase matching conditions in order to increase the efficiency of the nonlinear process. Phase matching in a birefringent crystal can be satisfied by adjusting the angle of the crystal axis with respect to

the polarization of the incident beam, selecting an appropriate pump intensity, and using nonlinear crystals of an appropriate length similarly to the SHG process previously described. In the present OPA system, a pair of BBO crystals are used for two stages of parametric amplification of a temporally gated component of the white light seed. The amplified component is selected by setting the appropriate delay between the pump and seed/signal and adjusting the phase-matching angle of the crystal. Most of the parameters such as the orientation of the crystal axis and the beam path are monitored and controlled by computer software. In summary, the OPA system has different stages to generate and amplify a broad range of frequencies. It includes a white-light continuum generation (WLC) stage, a pre-amplifier or the first amplification stage, and a power amplifier or the second amplification stage.

Femtosecond laser pulses of 800 nm wavelength with 1 mJ energy are used to pump the OPA system. The tuning range of generated frequencies can be extended using optional wavelength extensions. SHG, SFG and DFG processes can be used to extend the tuning range into the ultraviolet, visible or infrared spectral region, depending on the required wavelength. The combination of the SFG process and the tunable OPA signal allows a tuning range of 475-540 nm to be covered. In the present study, 500 nm is used for pumping the sodium nitroprusside (SNP) aqueous solution sample.

4.4 Overview of the Time-Resolved Photoelectron Spectroscopy (TRPES) Setup

The UV- or visible-pump and XUV-probe pulses are generated using a commercial Ti:Sa laser system, delivering pulses of 25 fs duration at an 800 nm central wavelength, with 2.5 mJ pulse energies at a repetition rate of 5 kHz. The laser output is split by a beam splitter, so that $\sim$ 1.0 mJ of the pulse energy is dedicated to pumping either an optical parametric amplifier OPA (see section 4.3) or a SHG setup (see section 4.2), depending on the absorption spectrum of the studied chromophore. The rest of the pulse energy of 1.5 mJ is used to pump a monochromatized high-harmonic-generation (HHG) beam line to produce ultrashort XUV light pulses for TRPES experiments. The XUV setup consists of an argon gas cell, where the fundamental laser beam is focused just before the cell to efficiently generate odd-order harmonics. A reflection zone-plate monochromator was used to separate the chosen harmonic and to focus it at a slit plane for spectral selection [263, 264]. After that, the selected harmonic is reflected to the TRPES interaction region using a grazing-incidence toroidal gold mirror. The HHG setup will be discussed later in this section. The experimental setup is illustrated in figure 4.3. After the generation of the pump and probe beams, both beams are sent to the interaction region. There, the pump and probe pulse are spatially overlapped at the sample. The relative angle between the incident pump and probe beams at the interaction region is 1°. Such a small angle facilitates a good spatial overlap of the two beams close to the micro-jet nozzle in front of the spectrometer ori-

fice and high temporal resolution. The pump-probe time delay was adjusted by an optical delay stage (Newport, FMS300CC) in the pump beam line, allowing for a time-step resolution of 1.6 fs and a maximum delay range of 2 ns. At the available XUV photon energies 26.4, 32.6, and 38.8 eV, the electron attenuation length is close to the minimum. Here, electrons are collected from a liquid sample in approximately 20-30 Å range of the surface, making our experiments highly surface sensitive [265, 266].

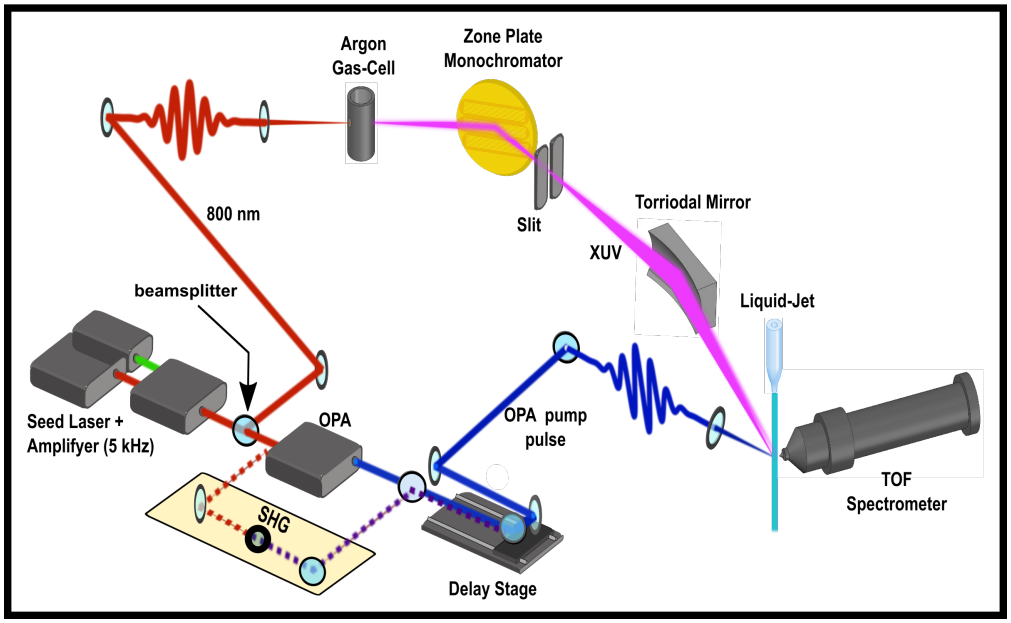

Figure 4.3: Schematic of the pump-probe photoelectron setup. The output of the commercial Ti:Sa laser is split into two branches. One branch is used to generate and monochromatize the HHG probe beam whereas another branch is employed to pump an optical parametrical amplifier (OPA) or to generate the second harmonic of the fundamental wavelength beam shown as dashed lines of the SHG setup. The pump and probe beams are overlapped onto the micro-jet sample. The emitted photoelectrons are recorded by means of a time-of-flight (TOF) spectrometer.

The volatile sample solution is injected into the interaction region using the liquid micro-jet technique [265, 267, 268]. The liquid sample is pushed through a quartz nozzle with the use of a syringe pump at a flow rate of 0.5 ml/min. A commercial quartz nozzle (Micro liquids GmbH) with an approximate 24 μm orifice diameter is typically used in our setup. The nozzle is mounted to a manipulator on the top flange of the interaction chamber which can be easily positioned with a 0.1 μm precision in three-dimensions. The liquid jet remains laminar over a distance of a few millimeters from the nozzle tip [267]. After the laminar region, the liquid flow breaks up into droplets, which are collected in a liquid nitrogen cooled trap. This trap is made from stainless steel and is coled from the atmospheric side, facilitating freezing of the liquid filament streams as it hits the trap walls. A vacuum environment is created and maintained

by pumping the stainless steel chamber with a series of connected pumps. The interaction chamber has two liquid nitrogen-cooled traps, one to freeze out the liquid droplets and one to trap the water vapor produced by the aqueous microjet. A membrane pump and turbo molecular pump is used to ensure a working pressure below 2×10^{-5} mbar in the interaction chamber for an adequate electron mean free path before transfer to a differentially pumped photoelectron spectrometer.

The liquid jet is centered at a distance of less than 1 mm in front of the skimmer orifice ($d \approx 400\mu m$) of a commercial time-of-flight (TOF) electron spectrometer (SPECS, THEMIS 600). The TOF spectrometer consists of a drift tube with a set of electrostatic lenses to guide the electrons to a delay-line detector located at the end of the tube. The vacuum system of the spectrometer is separated from the interaction chamber by a valve and is differentially pumped by three turbo-molecular pumps to create an high vacuum environment for photoelectron detection (see section 4.6).

Regarding the XUV setup, the fundamental laser beam which is used to generate the XUV light is focused into an argon gas cell using a lens of 600 mm focal length. A schematic of the XUV experimental setup is depicted in figure 4.4. The focusing lens (L) is mounted on a translation stage in order to adjust the position of the pump laser focus in front of the argon gas cell. By placing a half wave plate (Z) and a polarizer (PL) before the focusing lens (see figure 4.4), the intensity of the pump beam which is focused into the gas cell, could be regulated. Reducing the pulse energy allows the adjustment of the pump beam intensity to achieve optimum phase-matching in the argon gas and generate plasma. A peak intensity of the order of 10^{14} W/cm^2 at the laser focus is found to be optimum for XUV light generation. The gas cell is a cylindrical tube of 16 mm length and has holes which are sealed with aluminum foil. This cell is filled with argon gas via a gas feed-through to the vacuum chamber. The entrance and exit apertures are produced by the focused pump laser that drills through the aluminum foil. The HHG light is produced in the cell when the pump light interacts with the argon gas. The argon gas pressure in the gas cell was adjusted by using a dosing valve to optimize the XUV photon flux. The gas pressure of the argon and the position of the focused pump beam in the gas cell are very important parameters which influence the HHG efficiency [232]. During the operation of HHG source, it was found that a pressure of 20 mbar with a focus position directly before the gas cell (in the beam propagation direction) is the best condition to achieve a good output of HHG light. The beam of the 21st harmonic (photon energy of 32.6 eV) is selected using an off-axis reflection zone plate (ZP) and an adjustable slit. The ZP consists of three gold-coated zone structures fabricated on a single silicon substrate with a 50 mm diameter [249]. The working principle is based on the two-dimensional diffraction of different harmonics of the incident beam at different angles and focal length, resulting in their focus onto spatially separated points. In this setup, the monochromator was used to select the 17th, 21st or 25th harmonic using the different zone structures. In order to adjust the position and reflection angles of the zone plate, the substrate of the ZP is mounted on a set of motorized stages. The optic can

accordingly be adjusted in three translational and three rotational directions with a precision of 0.1 μm and 2 μrad, respectively.

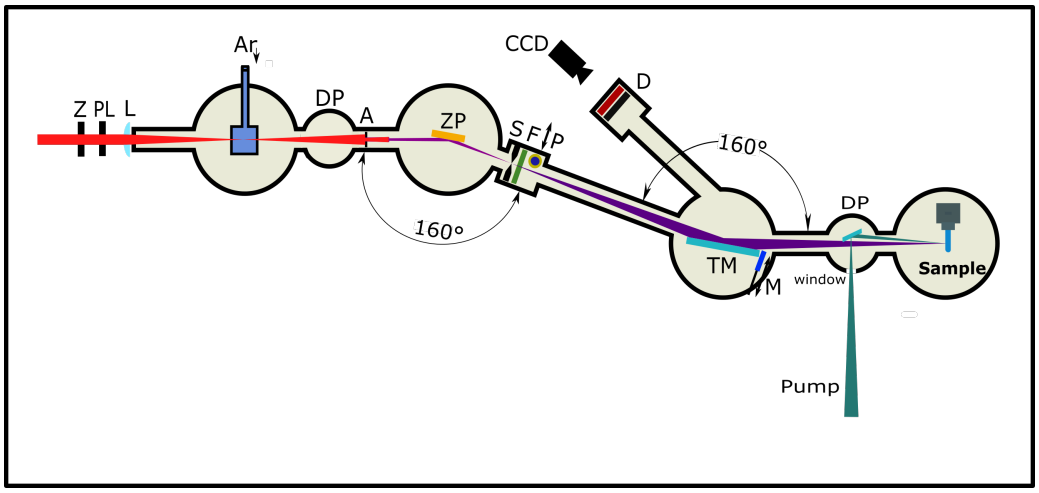

Figure 4.4: Schematic view of the XUV experimental setup. Notations:(Z) wave plate, (PL) polarizer, (L) lens, (DP) differential pumping stage, (A) aperture, (ZP) zone plate, (S) slit, (F) aluminum foil, (P) movable photodiode, (TM) toroidal mirror, (M) movable plane mirror, (D) position-sensitive detector.

To minimize absorption of the high harmonics and protect thr monochromator optics, a differential pumping stage (DP) is used between the HHG and ZP chambers allowing the maintenance of a low pressure of 10^{-8} mbar in the ZP chamber during the experiment. The adjustable slit (S), with a few tenths of a millimeter width, was placed at the ZP focal plane to select the desired harmonic. In order to filter out the rest of the IR beam that propagates with the harmonic beam, a thin aluminum foil (F) of 300 nm thickness was located behind the ZP chamber. An aperture (A) of 2 mm diameter is placed before the ZP chamber to block the main part of the more divergent high harmonic pump beam and thus, to avoid potential melting of the aluminum foil which is placed after the ZP chamber. The HHG flux was detected by a removable photodiode (P) placed behind the monochromator and after the aluminum filter.

A gold-coated toroidal mirror (TM) was used to refocus the selected harmonic beam into the interaction chamber to a typical focal spot size of 50 μm . In order to minimize the focus aberrations of the XUV spot, the focal length of the toroidal mirror was designed to refocus the beam without magnification at the distance of 1200 mm, which is the distance between the mirror and the slit.

This mirror was mounted on a movable stage inside a vacuum chamber with three translational and three rotational dimensions of freedom. Another planar mirror (M) can be inserted into the path of the refocused beam to redirect and monitor the XUV beam focus spot with a home-built position sensitive detector (D). By controlling the position of the toroidal mirror, it is possible to adjust the intersection of the HHG beam with the sample at a specific point in front of the spectrometer orifice.

In the actual experiment, the spot size of the HHG probe beam at the liquid jet was approximately 60 μm as measured with a translatable knife edge and photodiode. The photon flux of the XUV light was calculated to be 10^6 photons per pulse in the interaction region, based on the current measured by a calibrated photodiode.

4.5 Volatile Liquid Micro-Jet in Vacuum

Many chemical transformation occur in aqueous solution, including many biological phenomena. Liquid solutions are also ideal environments efficient for chemistry with their high densities and therefore, it provides the ideal conditions for understanding many of the important chemical, physical, biological and electronic processes take place in nature. Accordingly, much of the terrestrially and industrially important chemistry occurs in liquids. Therefore, chemists and physicists are interested in the physicochemical properties of solutions and solvents under different conditions. The enabling concept of most of the experiments performed in this dissertation is application of the PES technique to valance liquid samples. As stated before, the basic idea of a PES experiment is that photons of a defined energy are absorbed and electrons are ejected and analyzed with information about molecular or material systems of interest being extracted based on the properties of the ejected electrons. For a meaningful measurement, the electron kinetic energy should be measured with a high accuracy. In order not to distort the information carried by the emitted electrons, they must travel from the interaction region to the detector without colliding with residual gas particles. Therefore, a high vacuum environment is required in PES experiments. For condensed phase samples, collisions within and scattering from the sample must also be considered to interpret PES experimental results and extract as much information from the measurements as possible.

In the present study, aqueous solutions of the chosen samples are introduced to the laser interaction region using the liquid micro-jet technique [265, 267, 268]. This technique provides the possibility of introducing a free-flowing (clean) liquid surface while preserving high vacuum conditions.

In 1930, Bailey performed the first experiments on a low-vapor pressure liquid in vacuum using a mercury drop at the end of a capillary [269]. Photoelectron spectra of flowing, low vapor pressure liquids were measured for the first time in 1973 by Siegbahn, using a liquid jet of 0.2 mm diameter [270]. In the late 1980s, Faubel studied collision-free evaporation from steady-state and temperature-controlled liquid surfaces [271, 272]. Later, the micro-jet technique was established and applied in PES experiments, allowing such experiments to be performed with volatile, free flowing (clean) liquid samples in vacuum [265, 268, 273].

Photoelectrons emitted from highly volatile solutions can encounter elastic and inelastic collisions within the sample and with gas molecules evaporated from the sample. These collisions distort the kinetic energy of the photoelectrons. The path length of the emitted electron can travel without colliding with surrounding molecules, defines the electron mean free path λ_e.

The mean free path in the gas phase at thermal equilibrium is given by [271]:

$$\lambda_e = \frac{A}{n_v}, \tag{4.1}$$

where n_v is the equilibrium vapor pressure and A is given by:

$$A = \frac{KT}{\sqrt{2}\rho_v}. \tag{4.2}$$

Here K is Boltzmann's constant; T is the temperature and ρ_v is the molecular collision cross-section. For a sufficiently thin liquid jet streaming in a vacuum, the liquid evaporates radially from the surface and forms a vapor surrounding the jet. The evaporated gas has a cylindrical distribution of vapor around the surface of the jet. In this geometry, the gas density falls off as the inverse of the distance from the jet, $\frac{r_o}{r}$ [271], where r_o is the radius of the micro-jet. By reducing the radius of the liquid jet, r_o, the evaporation surface area decreases. In this case, the vapor density decreases quickly along the radial coordinate (r), therefore, the electron mean free path increases. For typical experimental conditions employing water as a micro-jet, λ_e is on the order of 0.7 mm [267].

Differential pumping and sub-millimeters transfer lengths from the liquid jet to the time of flight spectrometer are used to achieve such conditions in PES experiments. By transferring the electrons from high to ultrahigh vacuum environment within millimeters of their birth and decreasing the density of the vapor, an effective mean free path up to 1 m, is achieved.

In the present experiment, the liquid jet is formed by injecting liquid samples into the interaction chamber through a quartz nozzle with a diameter of 24 μm (micro Liquids GmbH). A syringe pump (HPLC pump Techlab Economy 2ED, Techlab GmbH) is used to push the liquid sample into the vacuum with a chosen flow rate. The liquid micro-jet remains laminar over a distance of a few millimeters from the nozzle tip. The inner diameter of the quartz nozzle capillary and the applied flow rate of the sample determine the length of this laminar region. The laminar-jet region is smooth and can be considered as being of cylindrical shape. A few millimeters beyond the nozzle tip, the liquid microjet will break into droplets, eventually being collected by collect in a liquid nitrogen cooled trap.

The region of laminar flow represents the laser-sample interaction region, providing a continuously refreshed liquid sample with a defined surface and minimal local vapor pressure. The typical flow rate of the micro-jet is 0.5 mL/min, which corresponds to an approximate jet flow velocity of 25 m/s. At this flow velocity and with a 5 kHz laser repetition rate, the investigated liquid sample is renewed with every laser shot. Thus, accumulated sample damage is prohibited. In order to minimize the effects of streaming potential on the liquid jet [274], a low-concentration salt was added to aqueous samples to increase their conductivities. 0.02 mol/L concentration of NaCl were generally prepared and mixed with the sample aqueous solution under investigation to facilitate such studies [274].

4.6 Time-of-Flight Electron Spectrometer

Electrons are detected using a commercially available THEMIS 600 (SPECS GmbH) photoelectron spectrometer. The spectrometer consists of the differentially-pumped time of flight (TOF) tube, an electrostatic lens system, and the delay-line detector (DLD). The main purpose of the time of flight tube is to guide the photo-emitted electrons from the interaction region to the detector and allow photoelectrons of different kinetic energies to disperse along the flight path. In our experiments, the liquid microjet is located in front of the skimmer at a distance of approximately 0.5 mm. A conical skimmer with an aperture of about 400 μm forms the entrance and differential pumping aperture to the spectrometer region. Such a small orifice of the skimmer acts as a gas pressure barrier between the main chamber and the drift tube and facilitates the maintenance of a low pressure in the spectrometer tube during liquid jet operation. In order to ensure and maintain a low residual gas pressure of below 10^{-6} mbar in the spectrometer, three turbo-molecular pumps with a pumping speed of 300 L/s are used to pump the spectrometer unit. A valve is located directly behind the skimmer to temporarily close the spectrometer aperture. A closing mechanism is desirable to preserve the vacuum conditions in the spectrometer flight tube in case the experimental chamber has to be vented, for example when introducing the liquid jet nozzle into the chamber or to clean the delivery nozzle if the capillary becomes blocked. The TOF tube is built of a stainless steel housing which is wrapped with two magnetically isolating layers of μ-metal. The magnetic shielding decreases the effect of external magnetic fields (including the Earth's magnetic field) down to an uncritical level. Three pairs of Helmholtz coils are located in front of the spectrometer entrance to compensate magnetic fields in the laser-liquid jet interaction region. A schematic view of the spectrometer is shown in figure 4.5. The electrostatic lenses in the drift tube allow the spectrometer to be operated in different operation acquisition modes. These modes are characterized by specific energy resolutions, acceptance angles, and ranges of determined electron kinetic energies. The electrostatic lens system consists of ten cylindrical lenses which are labeled T1–T10 (see figure 4.5).

The acceptance angle of the electron trajectories depends on the lens mode and can be set in the range between $\pm$ 1° and $\pm$ 15°. All lens-system modes are controlled electronically in the computer software. The 3D-DLD is positioned at the end of the 758 mm drift tube (see figure 4.5). The 3D-DLD directly measures the arrival time and the position of each electron flying, with the arrival time referenced to the laser arrival time at the sample. The arrival time and position of electrons depend on the electron initial kinetic energy E_{kin} and the emission angle. Using an inversion routine provided by SPECS, full information about the polar emission angle, azimuthal emission angle, and kinetic energy of the electrons can be obtained in parallel. Two different operational modes of the spectrometer were exclusively used in the present work, Drift Mode (DM) and Wide Angle Mode (WAM). In the drift mode, the lenses are switched off and the spectrometer corresponds to a conventional field-free design, with an acceptance angle of

1°. Moreover, the DM provides the highest kinetic energy resolution of all spectrometer modes, corresponding to an energy resolution of 25 meV at 20 eV. In WAM mode, the electrostatic lens system is operated in a way that allows the largest collection angle of ±15° and thus, WAM provides the highest collection efficiency of all spectrometer modes. In this case, the energy resolution is decreased to 0.1 eV and the kinetic energy range is restricted so that it is used for a certain range (±10%) around the chosen pass energy.

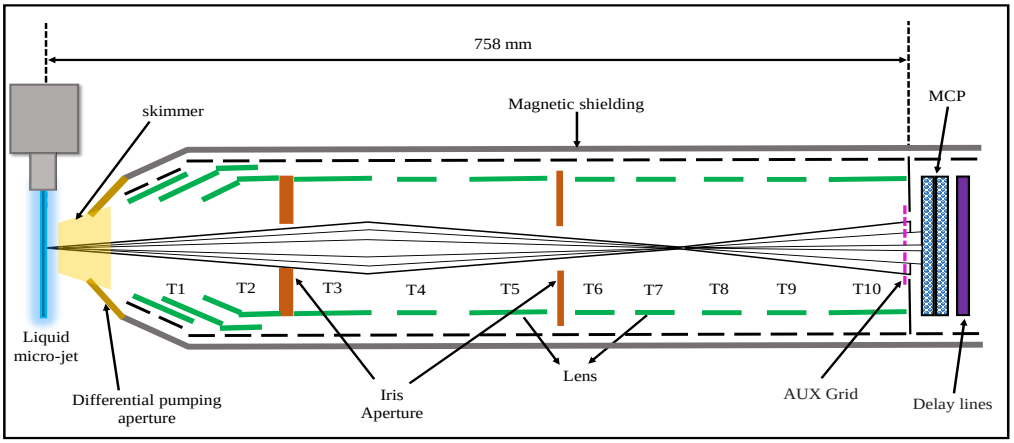

Figure 4.5: Schematic view of the SPECS Themis 600 time-of-flight spectrometer (TOF). Electron trajectories are emitted from the micro-jet and guided by the static electric field to the multi-channel plate (MCP) DLD detection unit. Operating the electrostatic lenses in different modes allows finding a compromise between high transmission and high energy resolution. The AUX grid in front of the detector is used as a filter of slow electrons allowing to avoid saturation of the detector.

The detector consists of two MCPs in a Chevron arrangement for pulse amplification and an in-vacuum readout unit consisting of crossed delay lines (see figure 4.6). The image is sampled by the DLD readout electronics. The position-sensitive detection involves measuring the coordinate of electron when it arrives in each individual delay line, which is encoded by the arrival times of the signal at opposite ends of the given delay line. Each delay line is connected to a constant fraction discriminator for pulse shaping and accurate arrival timing and a time-to-digital converter for arrival time tracking. The arrival time of the electrons is measured with respect to the arrival time of the laser pulse in the interaction region. This is facilitated by triggering the DLD electronic system synchronously with the laser pulses. The trigger signal is provided by the electronic synchronization unit of the laser system. The DLD signals are fed into a PC and data acquisition and processing software. To convert the measured position and arrival time of the electrons to their angular and kinetic energy distribution in the interaction region, the program simulates a large number of electron trajectories to compose a transformation matrix. With this transformation matrix and an appropriate electron generation

time-zero calibration, it is possible to convert the raw data to a photoelectron kinetic energy spectrum and angular distribution.

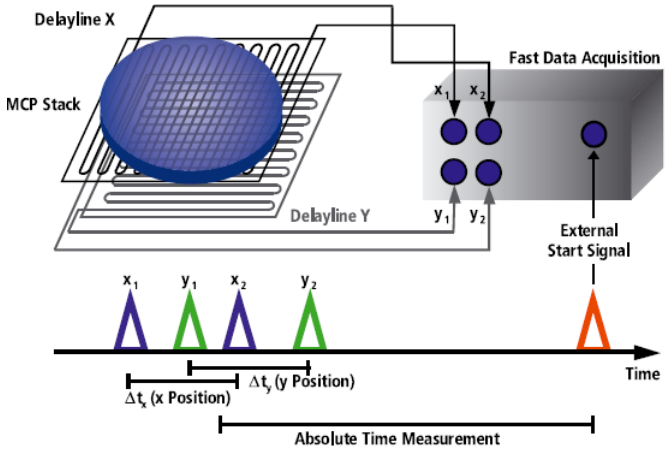

Figure 4.6: Schematic of the delay line detector (reprinted from the Journal of Electron Spectroscopy and Related Phenomena, with permission from Elsevier) [275]. When the amplified electron cloud hits the two delay line stack at a certain position, the pulsed signal is transmitted along each delay line to its opposite ends. The four measured arrival times, caused by a single electron hitting the pair of grids and referenced to the trigger signal from the laser system, are amplified and accurately time-stamped using the fast data acquisition electronics. The temporal structure of the recorded electrical signals are shown in the lower panel of the figure.

4.7 Overview of the Transient Absorption Spectroscopy Setup

The TAS setup allows us to investigate liquid media in a transmission geometry. A scheme of the utilized setup is shown in figure 4.7. The light source for the TA setup is the same regeneratively amplified femtosecond Ti:Sa laser as described in detail in section 4.1. In the TAS experiments, about 0.25 mJ were split off from the fundamental 800 nm beam and used for generating pump and probe light pulses. The fundamental laser beam is further divided into two beams using a beam splitter (BS) providing beams with 0.21 mJ (85 %) and 37.5 μJ (15 %) pulse energy in each arm. After the beam splitter, a fraction of the beam (85%) is directed toward a BBO crystal to generate pump light at 400 nm via second-harmonic generation (for more details see section 4.2). The SH intensity is controlled using a half wave plate and the SHG process. A set of dichroic mirrors is located after the BBO crystal to remove the 800 nm residual beam, reflecting the SH and transmitting the residual 800 nm beam. The polarization of the SH pump light is adjusted using a $\lambda/2$ wave plate just before focusing the pulses into the interaction region. At the sample locus, about 1.3 μJ pump pulses were focused to a spot size of about 600 μm with pulse intensity of 1.5×10^{10} W/cm^2.

A visible supercontinuum (SC), which is generated in a c-cut sapphire crystal, is used as

probe light in the TAS measurements. This allows us to probe a spectral range of 450-1000 nm when pumping the WLC stage with the fundamental wavelength. This nicely coincides with the measurement range of the applied Si-CCD detector. To ensure linear polarization of the SC probe light, a thin-film, broad-band polarizer is inserted directly after the SC generation. Care was taken to maintain a substantially smaller probe spot ($\approx 250\ \mu$m) than the pump spot ($\approx 600\ \mu$m), so that a uniform excitation of the sample over the probe region is ensured.

The pump and probe beams are spatially overlapped at the sample. The temporal overlap is adjusted by roughly varying the path length for the SH pump pulse to approximately match the path length of the probe beam in the experiment. It was found that the common method of delaying the pump pulse lead to intolerable pointing instabilities and intensity fluctuations. Therefore, we chose to delay the fundamental pulse of the probe beam before generating the SC light. In this case, observation of a very good pointing as well as spectral and power stability of the probe pulses is achieved. A 300 mm motorized delay stage (Newport, FMS300PP) equipped with a hollow-cube retroreflector (Newport, UBBR2.5-1UV) with UV enhanced aluminum coating is utilized to vary the path distance of the probe beam in small steps in order to get an adjustable and accurate time delay between the pump and probe pulses. The delay stage is capable of changing the path length of the probe beam up to a possible maximum delay of 2 ns with a minimum incremental motion of 3.3 fs. A chopper is positioned in the path of the generated SH pump beam. A photodiode is positioned after the chopper to detect the presence of pump pulses at a given time. This arrangement allows for proper synchronization of pump-probe cycles, thus suppressing the flip-over-effect encountered when the pump and probe phases are accidentally mixed up.

The pump and probe beams are focused onto the sample and aligned to have the best spatial overlap between the beams at the sample surface. After passing through the sample, the probe beam is routed to a parabolic mirror that focuses the beam onto the entrance slit of the spectrograph. A set of filters are located before the slit of the spectrograph in order to reduce the intensity of the probe beam to avoid the saturation of the charge couple device (CCD) camera, as well as to suppress residual pump light.

The Czerny-Turner spectrograph (Andor Shamrock 303i) consists of two concave mirrors and a diffraction grating. The first mirror is used to collimate the incident light from the entrance slit and then to direct the collimated beam onto the diffraction grating. Once the probe beam has been separated into its chromatic components by the grating, the second mirror is used to focus the dispersed probe beam onto the detector plane. The resulting spectrum is detected using a CCD camera (Andor Newton du 920 p). Since the chopper is synchronized with the detector by computer software, it enables registration of the intensity by the computer during periods when the pump beam is present and when it is blocked by the chopper. For every measurement, the spectrally dispersed, transmitted probe spectrum is measured. In the pump-probe acquisition, the excited and ground state spectra are measured. This spectrum is compared to the un-pumped (probe only) ground state spectrum recorded in a subsequent acquisition.

The applied detector allows spectra to be recorded at rates up to 200 Hz, thus one has to either reduce the repetition rate or integrate several subsequent probe-only/pump-probe spectra. We chose the latter approach, summing around 60 probe-only, then 60 pump-probe shots, and calculating the ΔOD signal from these data using equation 3.53. The supercontinuum is found to be stable enough that using the described scheme, a shot-to-shot referencing method yields a reasonable detection sensitivity of about 10^{-3} OD upon recording 100 pump-probe cycles, i.e., in < 3 s of measurement time. All measurement devices (spectrograph, detectors, chopper, delay stage) are controlled by a custom-written computer program developed in the group. The computer program controls the experiment and shows the ΔOD as a function of delay times and wavelength. All measurements are stored as raw data sets, including the measured spectra (integrated over 60 shots) and every shot energy. The sample solutions were contained in a 1 mm thick fused silica cuvette in a conventional transmission geometry.

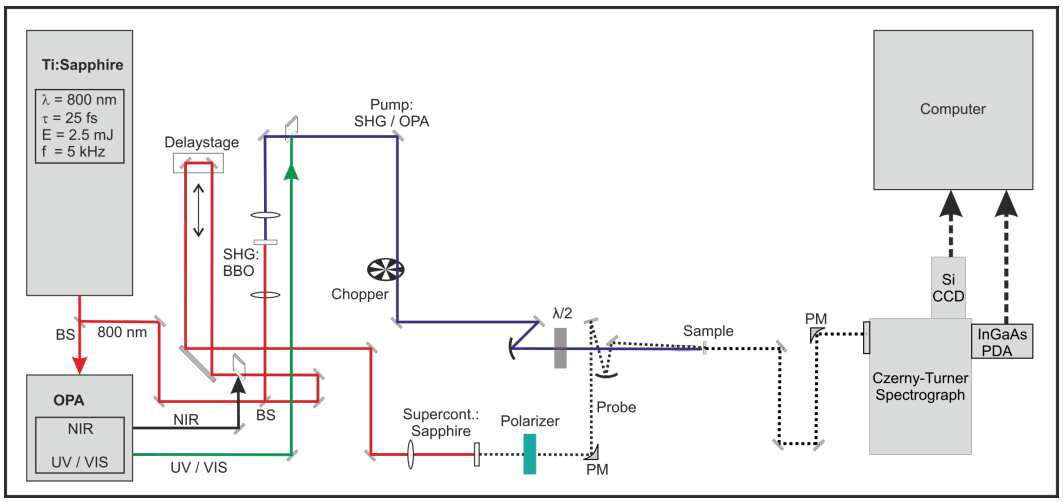

Figure 4.7: Sketch of the TA experimental setup. OPA: optical-parametric amplifier, BS: beam splitter 800 nm, SHG: second-harmonic generation, BBO: β - BaB_2O_4, PM: off-axis parabolic mirror.

Additionally, pump or probe pulses can be generated by an OPA (see section 4.3). The SFS or SH of the signal or idler OPA output can be utilized as tunable TA pump source in the UV or Visible range. The signal or idler pulses can also be used to generate TA probe pulses via WLC. Although technically more challenging than using the fundamental output of the laser, allows for broadband detection between 450 nm and 1800 nm and also helps to mitigate problems due to interactions of the strong residual SC pump light with the TA pump pulses.

Chapter 5

Photoinduced Isomerization Dynamics of Sodium Nitroprusside (SNP)

A part of the results presented in this chapter has been published in the following article: "Ultrafast kinetics of linkage isomerism in $Na_2[Fe(CN)_5NO]$ aqueous solution revealed by time-resolved photoelectron spectroscopy". A. A. Raheem, Martin Wilke, Mario Borgwardt, Nicholas Engel, Sergey I. Bokarev, Gilbert Grell, Saadullah G.Aziz, Oliver Kühn, Igor Yu. Kiyan, Christoph Merschjann, and Emad F. Aziz. Structural Dynamics 4, 044031 (2017); doi: 10.1063/1.4990567.

Authors contributions:

A.A. Raheem carried out the experiment, analyzed the data, interpreted the results, wrote the following parts of the manuscript (introduction, experimental setup and material, results and discussion and conclusion and outlook). **MartinWilke, Mario Borgwardt and Nicholas Engel** contributed to the preparation of the experiments and data collection. **Sergey I. Bokarev, Gilbert Grell, Saadullah G.Aziz and Oliver Kühn** performed the theoretical calculations and described and documented the computational details. **Igor Yu. Kiyan** worked out of the technical details of the experiment, helped supervise the project, and approved the final version of the manuscript to be submitted. **Christoph Merschjann** supervised the project, contributed to the development of the analysis and interpretation of the results, contributed to the writing of the following parts (results and discussion and conclusion and outlook) and approved the final version of the manuscript to be submitted. **Emad F. Aziz** co-supervised the research and funded the project.

This chapter describes two different experiments to follow the excited state dynamics leading to photoisomerization process of SNP. To our knowledge these experiments are the first examples of ultrafast isomerization dynamics being treated in the liquid phase using the TR-PES techniques.

Depending on the initial electronic transition, two different isomerization processes can be induced in SPN molecule. The molecular orbital configuration of the SNP ground state can be described as $1a_1^2\,1e^4\,1b_2^2\,2a_1^2 3a_1^2\,2e^4\,1b_1^2\,2b_1^2\,3e^4\;4a_1^2\,1a_2^2\,4e^4\,5e^4\,6e^4\,2b_2^2\,7e^0\,3b_1^0\,5a_1^0\,8e^0$. Accordingly, SNP has singlet ground state. The first excited singlet state of SNP is accessed via the $2b_2 \longrightarrow 7e$ transition and corresponds to the population of the first ^{1}MLCT state. Here we trigger this transition at 500 nm wavelength to form the side-on configuration MS2 state on ultrafast timescale. The second excited singlet state of SNP is accessed via the $6e \longrightarrow 7e$ transition and corresponds to population of the second ^{1}MLCT state. The excitation wavelength of this transition is at 400 nm to produce the MS1 state, i.e., the differences between the transitions from the $6e$ and $2b_2$ configurations are most easily distinguishable when considering the isomerization mechanism of the NO ligand after exciting an electron to the $7e(\pi^*_{NO})$ orbitals.

5.1 XUV-Photoelectron Spectrum of SNP, $[Fe(CN)_5NO]^{2-}$, Aqueous Solution

The steady-state photoelectron spectrum of a 500 mM aqueous sodium nitroprusside (SNP) (to which sodium chloride was added to a concentration of 15 mM) was recorded by applying XUV pulses with a 32.6 eV photon energy. Figure 5.1 shows spectral peaks arising from ionization of SNP as well as from liquid and gaseous water. The spectrum was recorded in the drift operational mode of the spectrometer. For the purpose of maintaining stable conditions, the spectrum was recorded in a sequence of measurements with equally short acquisition times. For photoionization from water and SNP, the binding energy was calculated as the difference between the XUV photon energy (32.6 eV) and the kinetic energy. The photoemission spectrum in 5.1 is presented in a wide range of binding energies from 5 to 30 eV, enabling investigation of electronic structural features of water and SNP as well. The photoelectron spectrum of the SNP aqueous solution contains contributions from ionization of the liquid $1b_1, 3a_1$ and $1b_2$ and gas-phase $1b_1$ water molecular orbitals.

Since the binding energies can be related to a reference peak, the absolute ionization potentials can be derived by calibration using species with known binding energies. In the present case, a photoelectron spectrum from argon gas in the absence of the liquid jet is used for a spectrometer arrival time and, hence, energy calibration. The electron time of flight is converted to electron kinetic energy by the software directly, as previously discussed. After the calibration procedure and switching from an effusive Argon source to an aqueous liquid microjet, the width and energy position of each peak of water are in a good agreement with the photoelectron spectra of water presented in references [276, 277]. In the spectrum, the rather large gas peak is due to the larger focal size of the XUV spot ($\sim 60\ \mu$m) as compared to the micro-jet diameter (24 μm), which leads to a larger interaction volume of XUV photons with gas-phase water in comparison to references [276, 277]. A part of the spectrum above 20 eV binding energy also

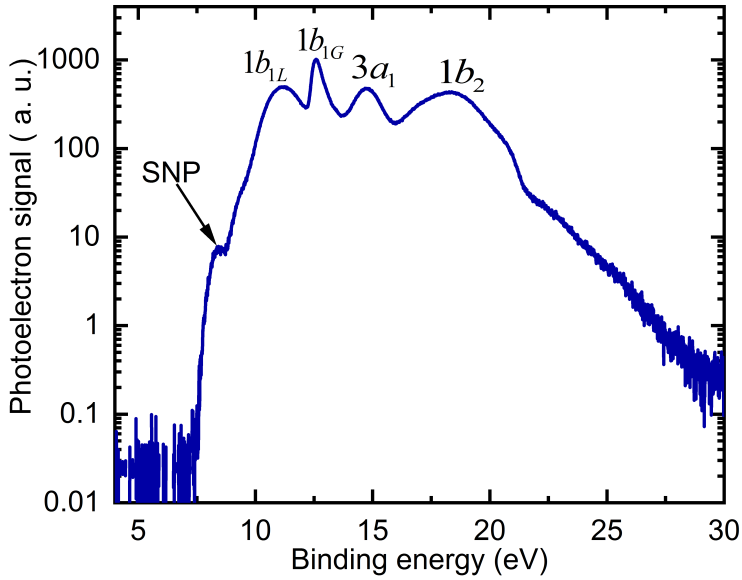

Figure 5.1: Photoemission spectrum of sodium nitroprusside (SNP) aqueous solution obtained using the XUV probe beam alone. Spectral peaks are attributed to ionization from the $1b_1$, $3a_1$, and $1b_2$ orbitals of water molecules and the observable iron-center-localized Fe (3d) (HOMO) orbitals. The signal is presented on a semi-logarithmic scale.

contains secondary electron and electron scattering contributions which arise as an unstructured background. The chloride counter ion is not apparent here due to the low concentration of sodium chloride.

An SNP ionization signal is clearly observed as a shoulder of the $1b_1$ peak of liquid water. This peak is mainly assigned to emission from the iron center ion as supported by theoretical calculations (see figure 2.2 for details).

By measuring the water ionization yield without SNP under the same conditions, a comparison between the photoelectron spectrum of water and SNP aqueous solution can be made to isolate the contributions of SNP which are covered by the water peaks.

Figure 5.2 a) shows the comparison of steady-state XUV photoemission spectra of the solvent (green) and the SNP aqueous solution (red) in a chosen range of the spectrum where the ionization yield of SNP is present. One can clearly observe the contributions of SNP in the region below 11 eV binding energy. In this region, the signal is associated with the electron yield from the Fe(3d) orbital of SNP and from the ligands, which can barely be observed in the spectrum as shown in figure 5.2 (a). To reveal the SNP photoemission spectrum, the solvent signal is subtracted from the SNP spectrum and treated as a background.

In the right panel (b) of figure 5.2, the contributions of SNP after subtraction of the water background spectrum are shown in more detail. From this figure, the electronic ground state configuration of SNP has three distinguishable spectral bands, centered at binding energies of 8.31 $\pm$ 0.05 eV, 9.62 $\pm$ 0.05 eV, and 10.46 $\pm$ 0.04 eV. The energy positions are obtained by fitting the background-subtracted signals to a superposition of three Gaussian peaks. The fit

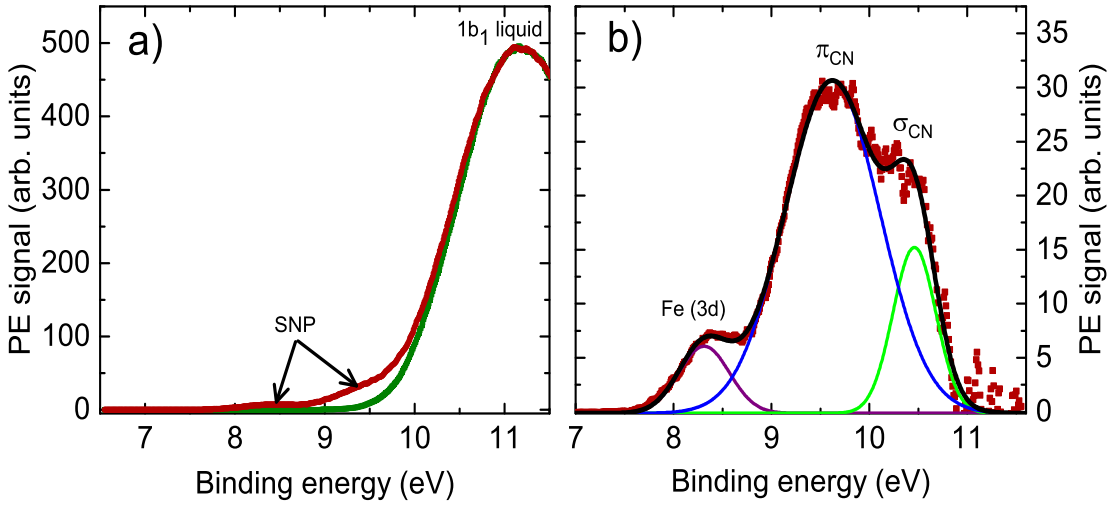

Figure 5.2: (a) Steady-state XUV photo-emission spectra, recorded in a drift mode, of pure water (green) and SNP dissolved in water (red). (b) Difference spectrum showing the SNP spectral components in more detail. A superposition of three Gaussian profiles, depicted as solid curves, was used to fit the data. The individual bands at 8.31 eV, 9.62 eV, and 10.46 eV are primarily attributed to ionization from Fe(3d), π_{CN} orbitals, and σ_{CN} ligand orbitals, respectively.

result is presented by the black curve, the individual Gaussian peaks are also shown in figure 5.2 (b). These three Gaussian peaks arise from two different molecular orbital configurations, which are attributed to ionization of the iron center and the ligands molecular orbital. According to the TDDFT calculations and assignments of the XPS/UPS spectrum [120, 278], the band with the lowest binding energy in the range of approximately 8-9 eV is primarily attributed to ionization from the Fe(3d) orbitals, whereas the other spectral peaks lying above 9 eV have dominant contributions from the CN ligands. In particular, the band at approximately 9.6 eV corresponds predominantly to ionization from π_{CN} orbitals, those at $\geq$ 10 eV stem from σ_{CN} orbitals. Interestingly, photoionization from the NO^+ (HOMO-1) ligand does not contribute to the ionization cross section in this energy range. Additionally, the kinetic energy distribution of the iron peak does not provide any information about the d-orbital splitting of the iron contributions to ground state, i.e. both the $2b_2$ and 6e ionizing transitions contribute to the peak at 8.31 eV .

5.2 Ultrafast Kinetics of SNP Following 500 nm Photo-excitation

Irradiation of SNP aqueous solution with blue-green light (450-560 nm) leads to electronic excitation from the singlet ground state (GS) into the lowest-lying singlet metal-to-ligand charge

transfer (MLCT) state. Such promotion of electrons can be described as a transition from the highest occupied molecular orbital (HOMO) Fe($3d_{xy}$) to the lowest unoccupied orbital (LUMO) π^*_{NO} [90]. This transition triggers the geometrical reorganization of the Fe–NO bond towards an almost orthogonal (Fe–N–O $\approx 77°$) side-on, metastable configuration of NO, which is named MS2 [101, 104, 105]. In the first set of the experiments focused on the photoisomerization of SNP, 500 nm wavelength (2.48 eV photon energy) pump pulses were applied to produce the side-on configuration, MS2, of SNP. After such excitation, the photoelectron yield upon probing with extreme ultraviolet (XUV) photons with 32.6 eV photon energies provides information about the lifetime of the ES (^{1}MLCT) state, as well as the population dynamics of the MS2 state, while yielding the time-dependent electronic binding energies.

The spot size of the HHG probe beam at the liquid jet in these experiments was 60 μm. The XUV photon flux in the interaction region was approximately 10^6 photons per pulse, as measured using a calibrated photodiode. The spot size of the 500 nm pump beam was 200 μm, with a maximum pulse energy of 1.5 μJ, corresponding to 3.8×10^{12} photons per pulse. The pump pulse duration of 55 fs (FWHM) was determined using an optical autocorrelation system (ape GmbH, pulse check Type 2), leading to pulse intensity of 1.7×10^{11}. The pump and probe beam polarizations were parallel to each other and the spectrometer TOF axis and the beams were spatially overlapped at the sample. The pump-probe delay time was adjusted by an optical delay line in the pump beam line to track the excited states dynamics on the femtosecond to nanosecond timescale. The wide-angle operation mode of the spectrometer was used to measure the transient signal which could be recorded with a reasonably short acquisition time, providing PE spectra within 10 second at each time delay between the pump and probe puses.

Reducing the pump pulse intensity was necessary to suppress excessive multiphoton ionization of the sample by the pump pulse alone and, thus, to avoid sample degradation and to relatively enhance pump-probe signals. At optimum pump intensities, a small amount of slow electrons are produced by the pump pulse and their contribution to the XUV spectrum is negligible. Reducing the pump intensity also decreases the spectral shifts due to the space charge effect [239]. Varying the pump intensity to optimize the experimental conditions was achieved using a filter in the pump beam path or by changing the pump beam diameter by shifting focal position of the pump beam.

By comparing the pump-probe spectra recorded at negative time delays (when the probe pulse arrives before the pump pulse at the sample) with the pump-probe spectra recorded at positive time delays, the contributions from the cross-correlation (CC) signal can be seen, as shown in figure 5.3. Figure 5.3 (a) shows PE spectra at three chosen time delays (Δt) between the pump and probe pulses. The signal at Δt = -200 fs reveals the contributions from the ground state of the SNP aqueous solution, which is used as a background measurement in the analysis of transient spectra. The PE spectrum at Δt = 0 fs is dominated by the cross-correlation signal. At zero-time delay, the energetic position of the CC signal extends over

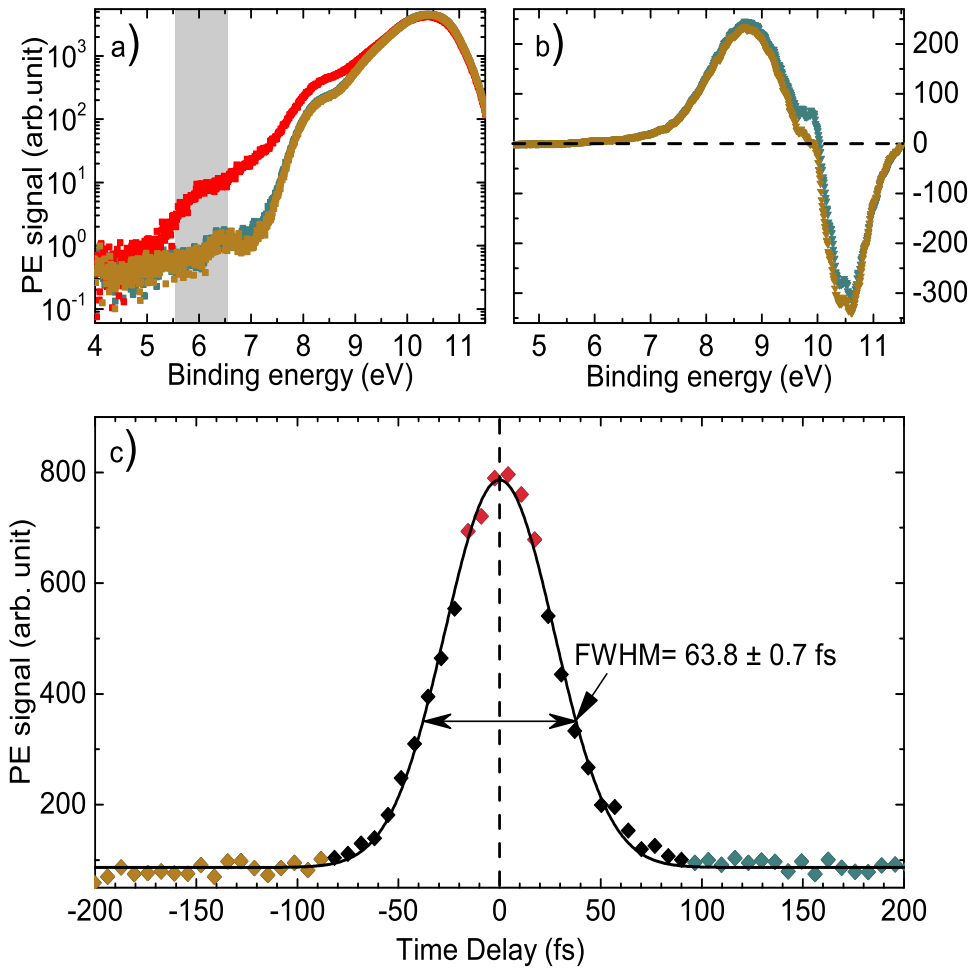

Figure 5.3: a) Transient PE spectra of SNP, measured at time delays of -200 fs (brown), 0 fs (red), and +200 fs (blue). b) Difference between the spectra obtained at zero-time delay and -200 fs (brown), and +200 fs (blue), respectively. c) Transient signal in the time-domain, integrated between 5.55 eV and 6.55 eV [gray area in panel (a)]. The pump-probe cross-correlation trace was fit using a Gaussian temporal profile with a FWHM of 63.8 $\pm$ 0.7 fs and is shown as a black line.

a range from 4 eV up to 9 eV binding energy. At positive delay, Δt =+200 fs, the CC signal vanishes and just the transient signal in the binding energy range between 6.5 and 11 eV remains. This signal is associated with electronic rearrangements, including the production of the MS2 configuration. In figure 5.3 (a), the signal is presented on top of the steady-state background signal. Figure 5.3 (b) shows the subtle differences observable in figure 5.3 (a) after background subtraction. The transient signal, arising around 10 eV, is highlighted and indicates the appearance of transient states. Clear differences are observed in the subtracted spectra between zero-time delay and negative (brown curve) and positive (blue curve) time delay. In addition to the CC signal, the pump-probe signal is observable in the binding energy region between 8-11 eV. The negative signal in the binding energy range of 9.5-11 eV provides information about

the depletion of the sample at time zero, highlighting the effect of laser-assisted photoemission of the SNP sample and $1b_1$ peak of water. Integration of the time-resolved PES signal of the SNP solution in the range between 5.55 eV and 6.55 eV (gray area in figure 5.3 (a)), yields the temporal profile shown in figure (5.3 c). In this region, the transient signal contains only the CC yield, without emission contributions from the excited states. A Gaussian fit was used to determine the full width at half maximum (FWHM) of the CC peak. The time resolution of the pump-probe measurements is defined by the width of the cross-correlation trace. The duration of the CC was deduced to be (63.8 $\pm$ 0.7) fs (at FWHM). Such a short CC width provides a sufficiently high time resolution for revealing short-lived transient electronic states which are populated following pump excitation of the sample.

5.2.1 Transient Photoemission Spectra of SNP Aqueous Solution

A series of scans in the pump-probe time delay range from -230 fs to +330 fs were performed. While combining the series, the data sets were corrected for the delay-dependent energy shift and the drift of the zero-time delay. The energy shift is caused by the pump-probe-delay-dependent space-charge effect induced by the pump beam in the liquid sample [239]. Therefore, the energy scale in each spectrum of a given series needed to be corrected separately. The ionization signal from the Fe 3d ($2b_2$,6e) orbital, giving rise to a well-distinguished energy peak at 8.31 eV in each XUV spectrum, was used as an energy reference in wide-angle mode operational system of TOF and the transient data treatment. The drift of the time zero was caused by changes in the environmental conditions in the laboratory and could reach a value of approximately 120 fs over the course of a day. This drift was corrected according to the center position of the cross-correlation signal imprinted in each time-delay scan. The pump-probe signal for different time delays was recorded in the wide-angle mode of the spectrometer to provide a high collection/detection efficiency of photoelectrons in the energy range of interest. The results of the time-resolved PE measurements are presented in figure 5.4, which shows dependence of the recorded electron binding energies on the pump-probe time delay. Negative time delays are associated with the XUV probe pulses arriving first at the interaction region. For a better visibility of the transient signal at positive time delays, the averaged spectra recorded at very early negative delays (from -230 fs to -200 fs) have been subtracted as a background. The background consists of a superposition of the photoemission spectra of the SNP and water ground state (GS) (see figure 5.1). This leads to a negative signal in the vicinity of zero time delay and at binding energies between 10 and 11 eV, where the photoemission yields of the $1b_1$ orbital of liquid water and of the SNP ground state are decreased due to electron density redistribution in the process of cross-correlation between the pump and probe pulses [247].

The CC also gives rise to a prominent positive signal between 7.3 and 9.5 eV, which is assigned to the respective photoemission bands of water and SNP, resulting from absorption of one XUV photon and one visible pump photon. Regarding this first-order sideband of the

laser-assisted XUV ionization, its spectral yield can be simply represented by the steady-state XUV photoemission spectrum, shifted on the energy axis by the pump photon energy (2.48 eV) towards lower binding energies. This CC signal can be utilized to determine the time response of the setup, as well as to pin down the exact position of the origin of the delay-time axis, as has been shown in the reference [279]. The presence of the CC signal with a short duration in the measurement enables us to determine time zero intrinsically and with high precision. Thus, it facilitates the identification of ultrafast contributions to the kinetics with time constants even below the time response of the system. On such timescales, the short-lived signals appear with a shift and asymmetric broadening as compared to the CC-dominated kinetics [279]. Besides the strong CC and short-lived signals, there is a clear evidence (see figure 5.4) for the enhanced photoemission at positive delays, especially between 9.5 and 10.5 eV binding energy. These features emerge during the first 300 fs and persist beyond the maximum time delay of the current investigation (+330 fs). Therefore, the long-lived features are assigned to MS2, in accordance with previous reports [100, 108, 125, 280].

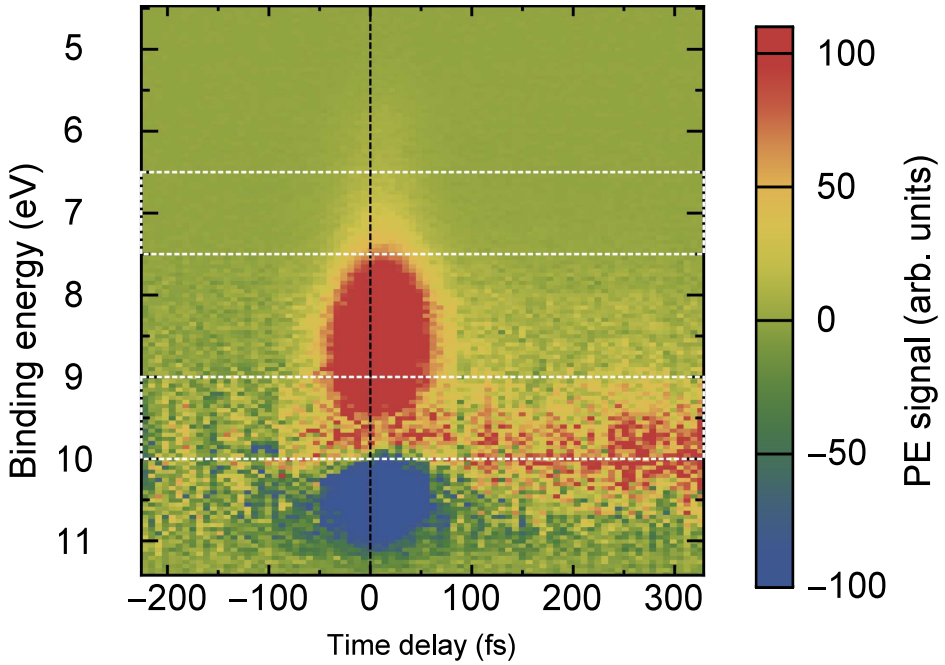

Figure 5.4: A series of 500 nm pump-XUV probe photoelectron spectra of SNP aqueous solution plotted versus binding energy obtained in pump-probe time delays range from -230 to +330 fs. For a better visibility, the averaged spectra recorded at negative delays (-230 to -200 fs) have been subtracted as a background. The spectra show a prominent cross-correlation signal located at the region 9.5-7.3 eV which decreases at lower binding energies. The fast decaying bleach signal in the region $>$ 10 eV is associated with the CC signal. The asymmetry of the photoemission yield in the vicinity of zero-time delay is due to the emission contribution from the excited transient states superimposed with the CC signal. The marked spectral range between 9.5-10.5 eV contains a signal that originates from ionization of the MS2 state.

It is noted that, the spectral shape and position of the emerging MS2 PE signal appears similar to that of the SNP ground state. This fact is also supported by the theoretical calculation of PES spectra for GS and MS2 states as will be discussed later.

It is important to point out that the population of the MS1 state is not considered in the case where the 500 nm is used as a pump wavelength. The reason for that is the photon energy necessary to trigger the photoisomerization toward MS1, 3.1 eV, via a charge transfer 6e$\longrightarrow$7e, is larger than the photon energy used in this case, 2.4 eV (see figure 2.2) [90, 93, 100, 124]. Therefore, even with two-photon excitation, which is unlikely in the experiments, the photoinduced MS1 state signal will have small contributions in the measured PES transient spectra. On the other hand, irradiation in the spectral range of 400 – 470 nm leads to a 40–50% population of the MS1 state [93, 100, 105, 124]. Nevertheless, in the spectral range of 500–580 nm only MS2 can be populated [93, 100, 124]. In addition, increasing the temperature of the sample, which is room temperature in the present experiments, leads to transfer the molecules from MS1 state into MS2 state (see sec. 2.2.1 and sec. 2.2.2 for more details). In this case, 35% of MS1 state can be transferred to the MS2 state [93, 100, 124]. In spite of that, if there are contributions from the MS1 state in the pump-probe spectra, these contributions will be small and they should be neglectable in the data analysis.

5.2.2 Kinetic Model

The initial photo-excitation step leading to the formation of the side-on configuration involves the population of the lowest singlet excited state, ^{1}ES, corresponding to the lowest-lying ^{1}MLCT state. Based on previous studies [108, 281, 282] as well as the results from the theoretical calculations [120], there is an additional state which can possibly be populated during the early photodynamics. This state lies close in energy to the ground state barrier between the ^{1}GS and ^{1}MS2 configurations and should be considered as an intermediate state on the way to populating the ^{1}MS2 state. In more details, the nitroprusside molecule has previously been investigated using picosecond transient infrared spectroscopy [108]. The analysis of the measured spectra predicts that the pathway to the photoinduced MS2 state includes an additional electronic state, which decays on $<$ 20 fs timescales [108]. So far, the low experimental time-resolution ($\sim$1 ps) of transient infrared experiment has not allowed the associated state life time or ultrafast kinetics to be precisely determined. Therefore, the second model, which is adopted in the present work, is proposed to investigate the ultrafast dynamics (time constant and binding energy) in the time range of $<$ 100 fs. The description of the second model is based on involving an additional electronic state. This state represents an intermediate state, where the retained electrons reside to prepare the electronic state and molecular configuration for NO-rotation. The consideration of the second model is necessary due to the indication of presence of the ultrafast transient signal in the measured PES spectra and depending on the previous study [108]. In addition, involvement of the triplet, ^{3}ES (^{3}MLCT), states might be possible during the early photodynamics, as will be

discussed later. Based on these considerations as well as on the kinetic schemes utilized earlier in the literature, two different kinetic models have been applied in the data analysis. The first model (model 1) includes three states (GS, ES, and MS2). This model was previously adopted in references [100, 125] to estimate the mechanism of build-up of the MS2 configuration of SNP. Here, a direct population of MS2 and the GS from the ES (^{1}MLCT) state is assumed. The model 2 assumes the presence of an additional intermediate state referred to as X. The models 1and 2 are schematically depicted in figure 5.5. The respective rate equation system for model 1 can be written as follows:

$$\begin{aligned}
\frac{\mathrm{d}[\mathrm{GS}_{(0)}]}{\mathrm{d}t} &= -aI_{\mathrm{pump}}(t)[\mathrm{GS}] + k_{10}[\mathrm{ES}] + k_{20}[\mathrm{MS2}] \\
\frac{\mathrm{d}[\mathrm{ES}_{(1)}]}{\mathrm{d}t} &= +aI_{\mathrm{pump}}(t)[\mathrm{GS}] - k_{10}[\mathrm{ES}] - k_{12}[\mathrm{ES}] \\
\frac{\mathrm{d}[\mathrm{MS2}_{(2)}]}{\mathrm{d}t} &= +k_{12}[\mathrm{ES}] - k_{20}[\mathrm{MS2}]
\end{aligned} \tag{5.1}$$

Here $[\xi]$ denotes the population of state ξ and the corresponding rate constants are denoted by k_{if}, where i and f are the initial and final states for a given transition, respectively. The parameter (a) describes the time-dependent excitation transition rate.

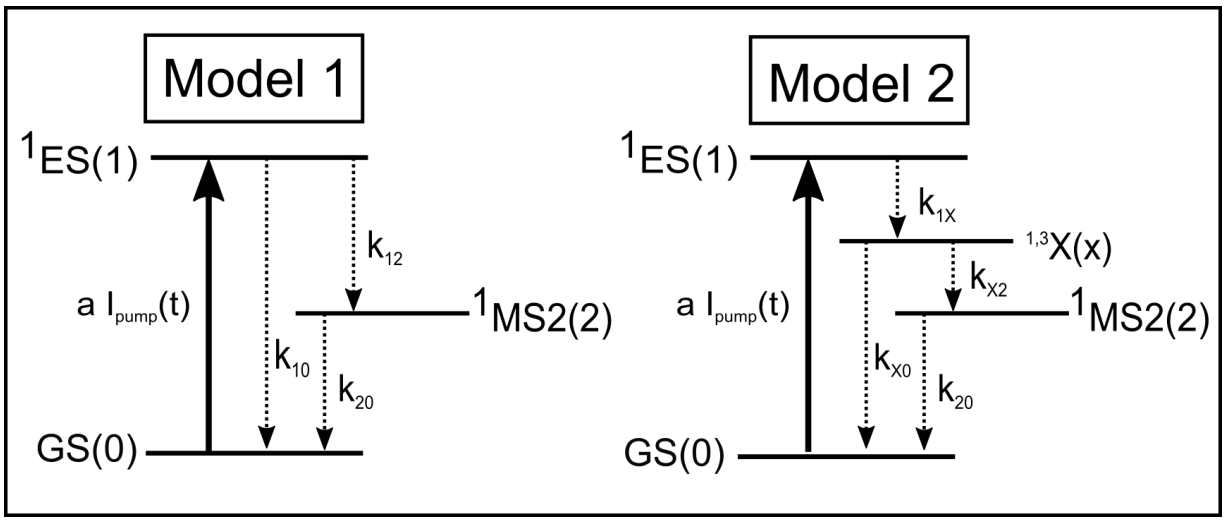

Figure 5.5: Schematic depiction of the SNP excited state relaxation processes in aqueous SNP following excitation at 500 nm. The relevant rate parameters used in equations (5.1) and (5.2) are used to label the diagram.

The second model (model 2) incorporates an additional intermediate state, X, which, according to Lynch *et al* [108], is populated from the ES on an ultrafast timescale and from where the subsequent parallel relaxation to either MS2 or GS takes place. The nature of this X state in the model 2 will be discussed later. The population dynamics of the short-lived X state should

lead to characteristic binding energy shifts in the transient photoemission signal on a few-10-femtosecond timescale [279]. The rate equations associated with model 2 can be written as follows:

$$\begin{aligned}
\frac{\mathrm{d}[\mathrm{GS}_{(0)}]}{\mathrm{d}t} &= -a\,I_{\mathrm{pump}}(t)[\mathrm{GS}] + k_{\mathrm{X0}}[\mathrm{ES}] + k_{20}[\mathrm{MS2}] \\
\frac{\mathrm{d}[\mathrm{ES}_{(1)}]}{\mathrm{d}t} &= +a\,I_{\mathrm{pump}}(t)[\mathrm{GS}] - k_{1X}[\mathrm{ES}] \\
\frac{\mathrm{d}[\mathrm{X}_{(x)}]}{\mathrm{d}t} &= +k_{1\mathrm{X}}[\mathrm{ES}] - k_{\mathrm{X0}}[\mathrm{X}] - k_{\mathrm{X2}}[\mathrm{X}] \\
\frac{\mathrm{d}[\mathrm{MS2}_{(2)}]}{\mathrm{d}t} &= +k_{X2}[\mathrm{X}] - k_{20}[\mathrm{MS2}]
\end{aligned} \tag{5.2}$$

5.2.3 Global Fit Analysis

The observation of changes in the photoelectron spectrum after excitation with a femtosecond laser field can be quantified using a global-fit analysis for the measured multidimensional data. This section includes the analysis procedure of the transient spectra that reveals the ultrafast kinetics during the emergence of the MS2 conformer. This analysis is based on solving the kinetic equations of both models using a matrix based approach. The time-dependent CC signal is represented by an amplitude-normalized Gaussian, i.e., that represents the convolution of the pump and probe pulse intensity profiles. The signals from the CC and solvent are appended as additional rows to the population-density matrix.

The respective best fits and corresponding residuals for model 1 and model 2 are shown in figure 5.6. Analogously to the measured data, the photoemission spectra of the SNP ground state and water, as obtained from the respective fit, have been subtracted from the modeled transient spectra. The kinetic fit parameters are presented in table 5.1 and the parameters for the Gaussian deconvolution of the fitted XUV photoemission spectra are listed in table 5.2.

It is noted that, in the figure 5.6, the CC behavior contains positive and negative signal. Figure 5.7 shows the CC spectra obtained from the fits to the two-color spectrum. The results associated with models 1 and 2 are shown as the black and dashed red lines, respectively. Both models yield similar CC signal behavior and are in good agreement with the experimental results (see figure 5.3 (b)).

One can see from figure 5.6 that there is no clear superiority of either model in the description of our experimental data. Further, the rate parameters extracted from both models are in overall good agreement. To compare Models 1 and 2 in more detail, figures 5.8 (a)–(d) show the decomposition of the transient signal into individual contributions from the involved ground and excited states, as well as the CC signal. This decomposition is presented for two energy ranges, 6.5-7.5 eV [(a) and (b)] and 9.0-10.0 eV [(c) and (d)], where the respective photoemission yields of ^{1}ES and ^{1}MS2 are maximal, according to the global fit results. Again, these cuts

show that both models provide fit results of similar quality.

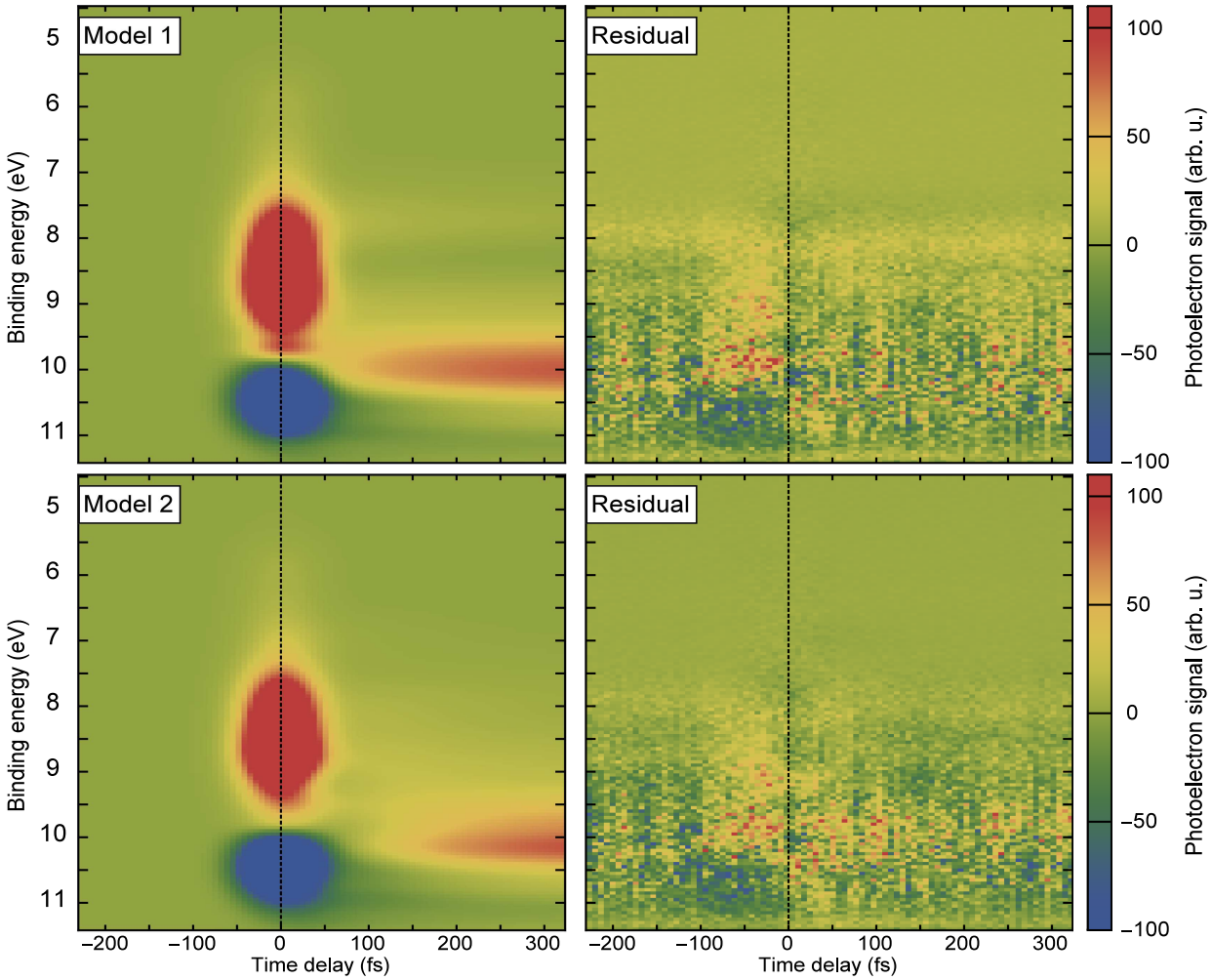

Figure 5.6: Global fit results and residuals for Model 1 (upper panels) and Model 2 (lower panels), respectively.

It is interesting to note that the ionization yield of ^{1}ES in model 2 has a maximum at approximately (20 fs). Such a short-time maximum was expected, as suggested in the calculations discussed in section 5.2.4 and the references [108, 120] (also see figure 2.4 in chapter 2). The decomposed amplitude associated with the ^{1}ES contribution is significant, which supports the presence of an intermediate state X. Before turning to a more detailed discussion about the existence of the X state in SNP, we highlight the extracted transfer time for population of the MS2 state at ambient temperature: $k_{12}^{-1} = 253 \pm 19$ fs for model 1, and $k_{1X}^{-1} + k_{X2}^{-1} = 234 \pm 39$ fs for model 2.

It is also found that competing process, $^1\text{ES} \longrightarrow {}^1\text{GS}$, occurs on a similar timescale, actually slightly faster than the population of MS2. Hence, slightly less than 50% of the originally excited molecules are inferred to produce the MS2 configuration, whereas the over-all switching ratio (i.e., with respect to the total number of molecules) is $\approx 10\%$, which was determined from

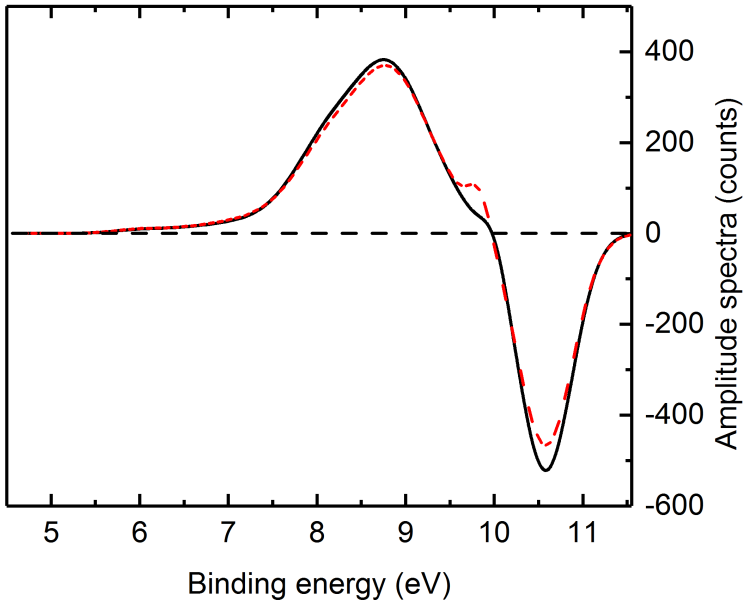

Figure 5.7: Cross-correlation spectra extracted from global fits with models 1(black curve) and 2 (dashed red curve).

the global fit results, corresponding to the conversion of the sample under the pump conditions (see blue curves in the panels (e) and (f) of figure 5.8). Both values are in good agreement with the data of reference [100], irrespective of the presence of an intermediate state. The de-excitation of the ^{1}ES(^{1}MLCT) state, as considered in models 1 and 2, involves channels of a different nature. Another reference suggested that the ^{1}ES$\longrightarrow{}^1$GS transition (model 1) leads to the population of highly excited vibrational levels of the GS state, whose thermalization then proceeds on a timescale of a few picoseconds [125]. Such a decay channel is not considered in model 2. Instead, the de-excitation proceeds via population of the X state, which can be the same singlet excited adiabatic state,^{1}ES, where the NO ligand is slightly rotated toward its side-on orientation via potential barrier. On the one hand, the fast decay time (33 ± 2 fs) of the ^{1}ES signal, which is much faster than the transition to ^{1}MS2 (k_{12}) (see table 5.1) or back relaxation to ^{1}GS (k_{10}), supports changes of the geometric configuration or even of the electronic state. A possible candidate for such a transient electronic state is the first excited triplet state. On the other hand, the timescale of this transition appears to be quite fast for both NO rotation and intersystem crossing (ISC), because of the large mass of the NO ligand and the expected low magnitude of the spin-orbit coupling matrix elements. As a very rough estimate of the time needed for geometric reorganization, one can consider the 24 fs half-period of the 708 cm^{-1} ground state Fe-NO bending normal mode in the limit of small vibrational levels, which is closest to the NO rotational motion (see figure 2.4 in chapter 2). In addition, a special comment should be added concerning the multiplicity of the X state. Although the potential energy surfaces of the first excited singlet and triplet states are almost parallel along the NO rotation coordinate, the analysis of the vibronic coupling suggests a crossing of singlet and triplet states

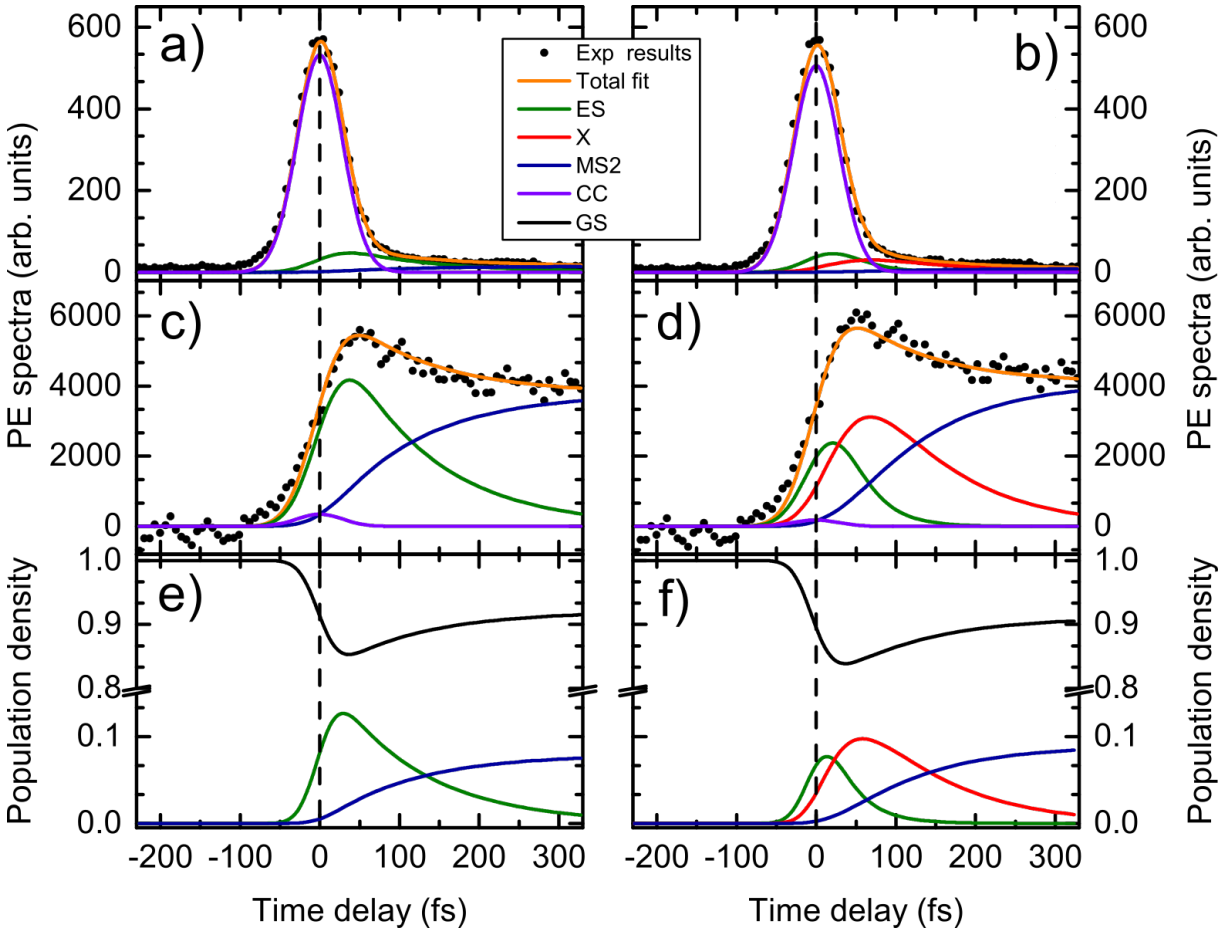

Figure 5.8: Comparison of global-fit results for Models 1 (left column) and Model 2 (right column). a), b) Energy-integrated kinetic traces, global fit result and its decomposition into specific state contributions in the region 6.5 to 7.5 eV. (c) and (d) Same as a), b), but for the region 9.0 to 10.0 eV. e), f) Transient population densities obtained from the fits for the GS and excited states of SNP.

along the totally symmetric stretching Fe-NO tuning mode, with a ground state frequency of 818 cm^{-1}, corresponding to a half-period of 21 fs. Notably, another group reported a mode at 662 cm^{-1}, corresponding to half-period of 25 fs [100]. This may make the ISC efficient and, thus, the photochemical pathway from ^{1}ES to ^{1}MS2 may be accompanied by an ultrafast double ISC ($^1\text{ES}\longrightarrow{}^3\text{X}\longrightarrow{}^1\text{MS2}$), representing relaxation dynamics involving both NO rotation and Fe-NO stretching nuclear motions. However, the probability of such an ultrafast double should ISC be lower than that of the internal conversion (IC) pathway, $^1\text{ES}\longrightarrow{}^1\text{X}\longrightarrow{}^1\text{MS2}$ or ^{1}GS. Note that unravelling the competition between multiple ISC and IC channels in transition-metal complexes is a non-trivial task, as recent investigations show [73]. For simplicity, one might consider that singlet and triplet MLCT states form a joint band and ^{1}ES and ^{3}ES as well as ^{1}X and ^{3}X signals should be treated together in the global fit analysis. Finally, one should note that besides the ultrafast transition $^1\text{ES}\longrightarrow{}^1\text{X}$, Lynch *et al* suggested a parallel ultrafast (10 fs)

back relaxation ^{1}ES$\longrightarrow{}^1$GS, which was assigned to a stimulated emission process [108]. From our data analysis, we cannot find evidence for such a transition. In fact, both models 1 and 2 yield time constants of 200 ± 21 fs for the back transition toward GS. Further, to the best of our knowledge, there have been no reports so far on the luminescent properties of SNP, *et al* one stimulated emission. This suggests that any relaxation processes are of non-radiative nature. As considered by Gallé *et al*, the transition ^{1}ES$\longrightarrow{}^1$GS results in a highly excited vibrational state of the GS, whose thermalization proceeds on a timescale of a few picoseconds [125]. Based on these findings, we consider that a back relaxation ^{1}ES$\longrightarrow{}^1$GS on a 10 fs timescale is very unlikely, leaving either the scenario of Refs. [247] and [100] (model 1), or the indirect singlet path way of model 2.

Table 5.1: Kinetic fit parameters for Model 1 and Model 2, respectively.

parameter	Model 1	Model 2	unit
a	4.00 ± 0.30	4.00 ± 0.57	molecule^{-1} ps^{-1}
$1/k_{10}$	200^{+23}_{-19}		fs
$1/k_{12}$	235^{+20}_{-17}		fs
$1/k_{1X}$		$33.3^{+1.6}_{-1.5}$	fs
$1/k_{X0}$		$200.5^{+2.6}_{-2.6}$	fs
$1/k_{X2}$		200^{+45}_{-31}	fs
$1/k_{20}$	110	110	ns
σ_{pump}	19.60 ± 0.89	19.60 ± 0.82	fs
σ_{probe}	20.5 ± 1.2	20.5 ± 1.8	fs

Furthermore, to provide a reliable comparison between model 1 and model 2, the F-statistics were calculated. This criterion is well satisfied when comparing the two models depending on the reduced χ^2 values obtained from the fit of both models. The reduced χ^2 values of model 1 (simple) and model 2 (extended) determine the goodness of fit of the model, where the smaller χ^2 value of the extended model is statistically significant only if the F statistic exceeds a critical value F_c defined by the F-distribution function. Once the criterion $F_c < F$, where $F_c = F(p_e\text{-}p_s; n\text{-}p_e)$, is fulfilled, the simple model can be excluded. Where p_s and p_e are the corresponding numbers of fit parameters of the simple and extended model, respectively, and n is the number of data points on the energy and time scale. The F-statistics formula is written as [283–286]:

$$F = \frac{(\chi_s^2 - \chi_e^2)}{\chi_e^2} \frac{(n - p_e)}{(p_e - p_s)} \tag{5.3}$$

where χ_s^2 and χ_e^2 are the residual sums of squares obtained from the fit of the model 1(simple) and model 2 (extended), respectively. The corresponding numbers of fit parameters are χ_s^2,

χ^2_e, p_s, p_e, and n are 0.12, 0.10, 92, 108 and 85×140, respectively. Using these numbers, we achieve F = 147.40 for the F statistic. In the present case, we have Fc = 2.78. Thus, the F statistic significantly exceeds the critical value and the simple model can be rejected with confidence larger than 99.99%. Accordingly, the consideration of the simple model (model 1) is inadequate to reproduce the PES transient signal. This means that the simple model can be excluded with high confidence and the extended model (model 2), which describes better the measured transient signal, should be considered instead.

Table 5.2: Fit parameters of Gaussian peaks used to describe the amplitude spectra for Models 1 and 2, respectively. Position values denote binding energy.

Peak	State	Model 1			Model2		
		position / eV	FWHM / meV	amplitude / cts	position / eV	FWHM / meV	amplitude / cts
1	GS	11.196 ± 0.055	465 ± 70	365 ± 77	11.20 ± 0.13	465 ± 60	365 ± 30
2	GS	10.11 ± 0.21	859 ± 33	2581 ± 88	10.11 ± 0.19	859 ± 94	2580 ± 250
3	GS	9.46 ± 0.16	955 ± 70	916 ± 65	9.46 ± 0.15	955 ± 95	921 ± 25
4	GS	8.434 ± 0.073	800 ± 74	181 ± 15	8.421 ± 0.065	801 ± 53	180 ± 19
1	ES	11.2 ± 1.7	300 ± 21	260 ± 21	10.4 ± 1.6	750 ± 210	1100 ± 260
2	ES	10.3 ± 1.9	590 ± 130	1194 ± 44	10.0 ± 1.9	598 ± 66	2150 ± 130
3	ES	9.9 ± 2.5	760 ± 29	2100 ± 130	9.6 ± 1.7	555 ± 73	1500 ± 320
4	ES	9.35 ± 0.72	800 ± 100	790 ± 51	8.9 ± 1.6	493.7 ± 9.1	332 ± 35
5	ES	9.04 ± 0.95	903 ± 36	89.9 ± 7.8	7.08 ± 0.82	495 ± 55	70.0 ± 4.3
6	ES	8.5 ± 1.4	895.4 ± 6.6	120.5 ± 6.2			
7	ES	8.05 ± 0.48	895 ± 50	155 ± 13			
8	ES	7.5 ± 1.3	809.6 ± 8.5	10.0 ± 1.5			
1	X				11.2 ± 1.9	301 ± 19	260 ± 13
2	X				10.3 ± 2.6	596 ± 60	1140 ± 220
3	X				9.9 ± 1.5	750 ± 53	1870 ± 140
4	X				9.35 ± 0.56	796 ± 61	862 ± 93
5	X				9.0 ± 1.1	905 ± 28	130 ± 12
6	X				8.6 ± 4.5	900 ± 73	82 ± 14
7	X				8.33 ± 0.81	802 ± 71	260 ± 19
8	X				7.33 ± 0.56	850 ± 41	20.0 ± 1.6
1	MS2	11.0 ± 1.8	810 ± 170	425 ± 78	11.00 ± 0.44	805 ± 31	425 ± 39
2	MS2	10.4 ± 2.1	550 ± 35	1110 ± 180	10.4 ± 1.4	550 ± 92	1390 ± 370
3	MS2	10.0 ± 2.4	710 ± 20	2950 ± 200	10.0 ± 1.9	708 ± 42	2610 ± 130
4	MS2	9.7 ± 1.6	734 ± 31	1200 ± 230	9.6 ± 1.4	734 ± 50	1280 ± 80
5	MS2	9.20 ± 0.58	663 ± 49	533 ± 42	9.2 ± 2.9	662 ± 43	500 ± 29
6	MS2	8.7 ± 3.3	705 ± 72	161 ± 11	8.7 ± 1.9	700 ± 110	170 ± 46
7	MS2	8.15 ± 0.53	960 ± 58	120 ± 10	8.35 ± 0.65	960 ± 100	170.1 ± 5.4
1	H_2O	10.80 ± 0.23	533 ± 36	1300 ± 260	10.80 ± 0.23	533 ± 20	1300 ± 130
2	H_2O	10.50 ± 0.25	721 ± 49	2430 ± 150	10.50 ± 0.25	721 ± 36	2430 ± 220
1	CC	10.6 ± 2.1	720 ± 180	−470 ± 230	10.6 ± 2.7	700 ± 170	−520 ± 120
2	CC	9.8 ± 3.6	301 ± 36	80.9 ± 3.9	10.0 ± 3.3	301 ± 34	52 ± 2
3	CC	9.4 ± 1.3	760 ± 160	67 ± 7	9 ± 2	760 ± 180	62.1 ± 2.6
4	CC	8.8 ± 1.2	881 ± 30	307 ± 50	8.84 ± 0.91	880 ± 100	316 ± 14
5	CC	8.15 ± 0.41	955 ± 70	190 ± 35	8.15 ± 0.28	955 ± 43	205 ± 25
6	CC	7.27 ± 0.59	913 ± 47	26.0 ± 1.5	7.3 ± 0.7	910 ± 130	21.7 ± 1.5
7	CC	5.95 ± 0.51	605 ± 71	7.00 ± 0.49	5.95 ± 0.55	605 ± 46	6.00 ± 0.51
8	CC	6.57 ± 0.56	900 ± 82	10.62 ± 0.61	6.57 ± 0.56	900 ± 60	10.92 ± 0.46

5.2.4 Comparison with Theory

Theory calculations were performed using the DFT approach [120]. For $[Fe(CN)_5NO]^{2-}$, the GS, MS1, and MS2 minima of the singlet ground state potential energy surface have been obtained as well as the adiabatic minimum energy path along the NO rotation coordinate. Five excited singlet states have been calculated along this ground state path at the level of time-dependent DFT (TDDFT) as well as one triplet state at the level of unrestricted DFT (UDFT). The solvent environment was accounted for by using the polarizable continuum model which is essential to stabilize the complex. To interpret the experimental data, the photoelectron probe spectra have been computed for the ground and lowest excited singlet and triplet states at the GS and MS2 molecular geometry as well as at a slightly skewed geometry with the angle (Fe–N–O = 135°), denoted as the X geometry. The theory qualitatively reproduces the spectral band structure originating from ionization channels leading to the formation of the SNP ion with different electronic configurations. The photoemission spectra of the ground state, as well as the excited states for both models inferred from the fit, are compared with the corresponding spectra predicted by the theory in figure 5.9. In this figure, the right column shows XUV photoemission spectra calculated using TDDFT for the states $GS^{1;3}ES^{1;3}X$, and MS2. The solid curves have been obtained by convolution of the stick spectra (blue) with Gaussian functions of width w= 0.28 eV. The inaccuracy of the theoretical method leads to shifts in the energy of the calculated photoelectron features of the order of 0.5 eV [287, 288]. Thus, the theoretical results presented in figure 5.9 demonstrate a reasonable compromise between the stability and the accuracy of the reference theoretical data. The left panel of figure 5.9 represents the photoelectron spectra obtained from the global fit results with the use of the models described before. One can see that the results of the TDDFT calculations agree reasonably well with the spectra obtained from the fit results of SNP in the measured energy region. The fit results for the Gaussian deconvolution of the photoelectron spectra are listed in table 5.2. One should note that the PE spectra originating from different electronic states at different geometric configurations are quite similar to each other with an exclusion being the spectrum of ^{1}ES. This fact, which is probably intimately connected to the weakness of the NO^+ photoionization yield in the investigated PES energy region, does not allow us to unambiguously assign the transient signal to the triplet electronic state. Therefore, further experiments are needed to clarify the multiplicity of the X state. Nevertheless, the calculated potential energy curves and the fast decay of the unique transient signal assigned to ^{1}ES strongly suggest the involvement of the intermediate state ^{1,3}X, the state 1 being either singlet or triplet.

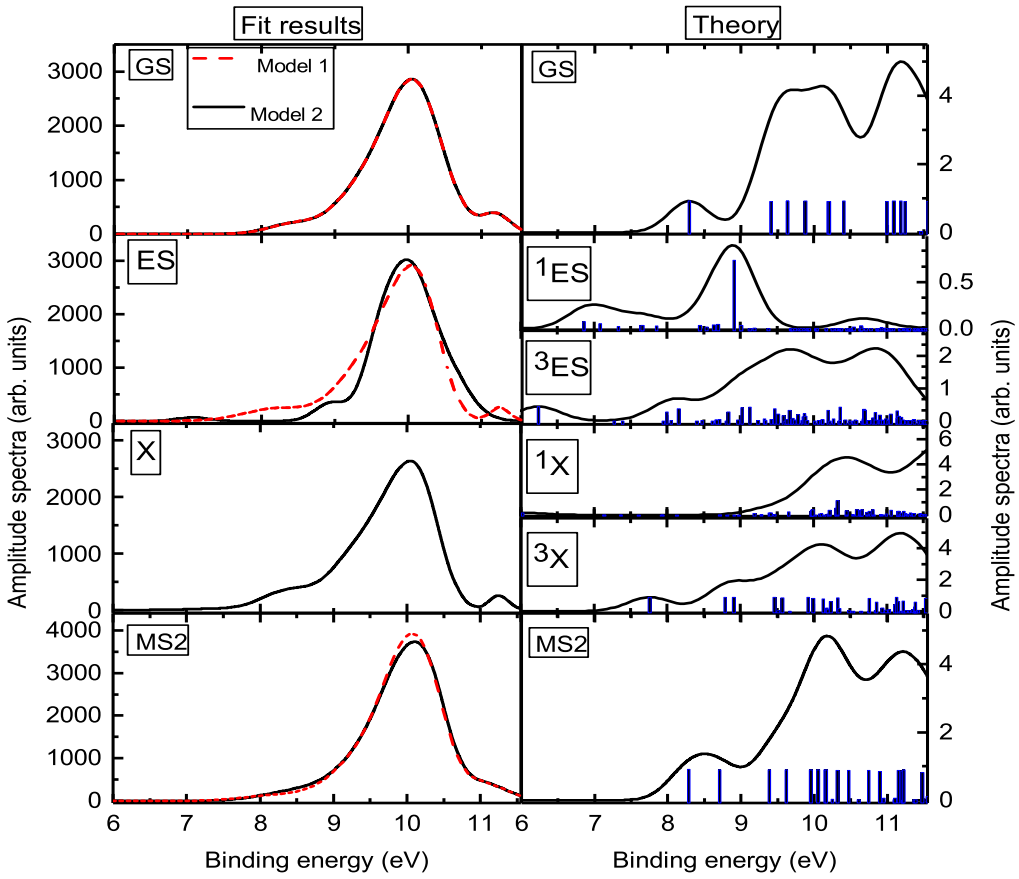

Figure 5.9: Comparison between PES amplitude spectra of SNP, as obtained from the global fits of Models 1 and 2, respectively (left column). The right column shows XUV photoemission spectra calculated using TDDFT for the states GS, ^{1,3}ES, ^{1,3}X, and MS2. The solid curves have been obtained by convolution of the stick spectra (blue) with Gaussian functions of width $w = 0.28\,\text{eV}$ [see equation (3.66)].

5.3 Ultrafast Kinetics of SNP Following 400 nm Photoexcitation

In the previous sections, we studied the dynamics of formation MS2 state in SNP via excitation at 500 nm wavelength. An additional process can be initiated in SNP using the shorter wavelength for the excitation. Pumping SNP with a 3.1 eV photon energy (400 nm) leads to the electronic excitation from the 6e(xz,yz) to $7e(\pi^*_{NO})$-character molecular orbitals, resulting in the formation of the isonitrosyl (Fe–O–N) metastable configuration, which is named MS1. In this case, the angle of the NO ligand rotation is 180° with respect to the ground state configuration (see figure 2.4).

5.3.1 Pump-Probe Photoelectron Spectra

In order to understand the generation of the isonitrosyl configuration state, MS1, the processes following the electronic excitation have been investigated using the femtosecond pump-probe photoelectron spectroscopy method at ambient temperature. An optical pulse of 400 nm wavelength was applied as the pump beam. The spot size of the 400 nm pump beam at FWHM, was approximately 250 μm, with a maximum pulse energy of 1.6 μJ. The pulse duration was estimated to be 80 fs, leading to a pump pulse peak intensity of 1.1×10^{11} Wcm^{-2}. Utilizing the PES experimental setup and high harmonic monochromator, the 21^{st} harmonic of 800 nm, 38.0 nm (32.6 eV) was used as the probe beam. The polarization of the pump and probe pulses were mutually parallel and parallel to the spectrometer time-of-flight axis.

Series of pump-probe measurements with a 500 mM SNP sample concentration were recorded for delay times in the range from -434 fs up to 1540 fs with 13 fs delay steps. Comparing the pump-probe spectra recorded at early negative time delay (-400 fs) with the spectra measured at chosen positive time delays (+200,+500,+1000 fs), one can verify that the spectral shift due to the space charge effect of the ionized aqueous sample is negligible. Thus, the transient PE spectra were recorded as many temporal scans corrected for the zero-time delay shift throughout the measurements, that were subsequently scanned. The measured pump-probe spectra are presented in figure 5.10 on the binding energy scale for different time delays in the range mentioned above. An average of a few spectra recorded at negative time delays was subtracted from the pump-probe spectra to reveal the transient signal which may be buried under the water peaks.

The transient signal shown in the figure 5.10 includes a strong feature at the zero-time delay. This feature was unequivocally attributed to the cross-correlation signal from the SNP aqueous solution. The CC component highlights the time resolution of the experiment in situ. Notably, there is no shift or asymmetry in the CC signal at lower binding energy. This indicates that any associated transient signal has a negligible lifetime compared to the CC width in this energy region. Furthermore, the clear appearance of an additional long-lived signal in the energy range of 7.5-10.5 eV is observed. This component grows rapidly within the experimental time resolution and after that, the signal remains constant until the maximum time delay applied in the measurement. In addition, this feature has highest intensity in the energy position containing emission contributions from the ligands ground state. Such a long-lived feature appearing in the metal-ligand binding energy region of SNP highlights that the transient signal of SNP localizes at binding energies where direct ground state emission is prevalent (although the ground state signal has been subtracted here). This resembling the results of the 500 nm excitation energy study on the generation of MS2 state. Therefore, the rising, long-lived signal confirms that the transient signal occurs on the range of binding energies above 8 eV is due to the population dynamics of the MS1 state. The MS1 signal originates from the rearrangement of the NO ligand configuration and from Fe^{2+} metal center interactions with the ligand.

In SNP, the electronic transition driven by 400 nm photo-excitation produces a second excited MLCT state, involving the transfer of electronic density that was primarily localized on the Fe^{2+} metal center to the ligands. It is difficult to isolate signals associated with different energetically separated states based on figure 5.10 alone. Hence, a more detailed comparison of the PE spectra measured at different chosen positive time delays is needed to determine whether there is more than one excited state which can be populated over the 1.5 ps delay range.

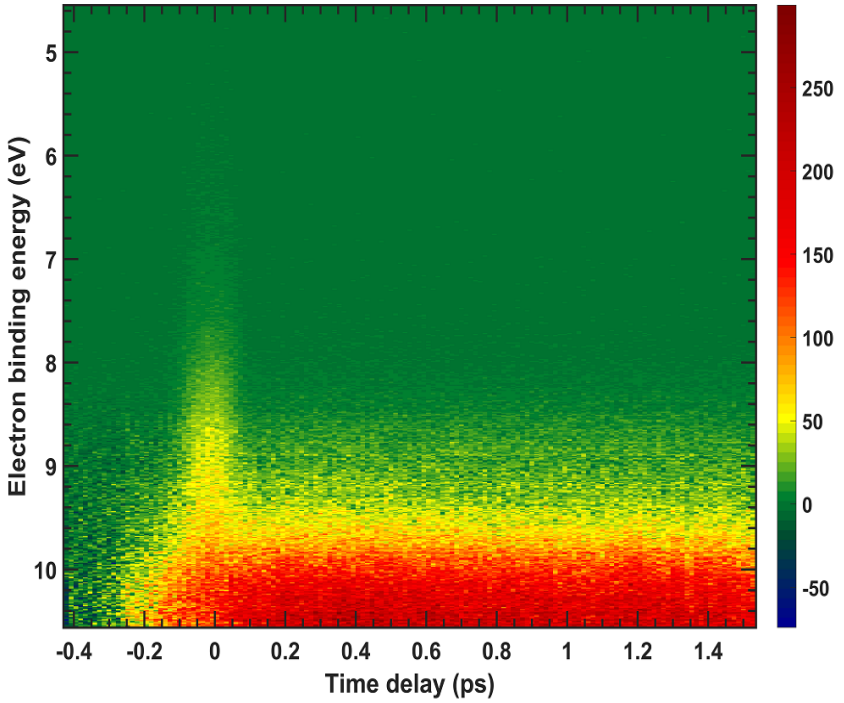

Figure 5.10: The transient signal of 0.5 M SNP aqueous solution measured after 400 nm photo-excitation recorded using the spectrometer's wide-angle-mode. The background of SNP at negative time delay is subtracted from the pump-probe measurements. A strong CC signal with a 120 ± 3 fs width at FWHM arises at the zero-time delay which defines the resolution of the experiment. The transient feature which is apparent at binding energies of 8.5-10.5 eV is assigned as a signature of the MS1 excited state of SNP.

A detailed comparison of transient spectra recorded at different delays is shown in figure 5.11. In this figure, the pump-probe photoelectron spectra of 500 mM aqueous SNP upon photo-excitation with a 400 nm pulse at time delays of 0, -400, +200, +500 and +1500 fs corresponding to the red, black, green, orange and blue curves, respectively, are presented. The upper left panel of the figure 5.11 a) shows the spectra over the entire range of binding energies measured in the experiment (4-10 eV). The signal components associated with excited states and processes can be estimated from these spectra. The contributions of the CC can be seen to lie in the range from 4.5 to 9.5 eV in the spectrum recorded at zero-time delay (red curve). The CC contributions arise from the photoemission bands of water and SNP as well. By taking the photon energy of the pump pulse (3.1 eV) into account, we observe that the maximum

appearance of the CC contributions is shifted from the original ground state peaks of SNP and water by the energy of the pump photons (3.1 eV), indicating the absorption of a single pump photon (see figure 5.11 a, main panel).

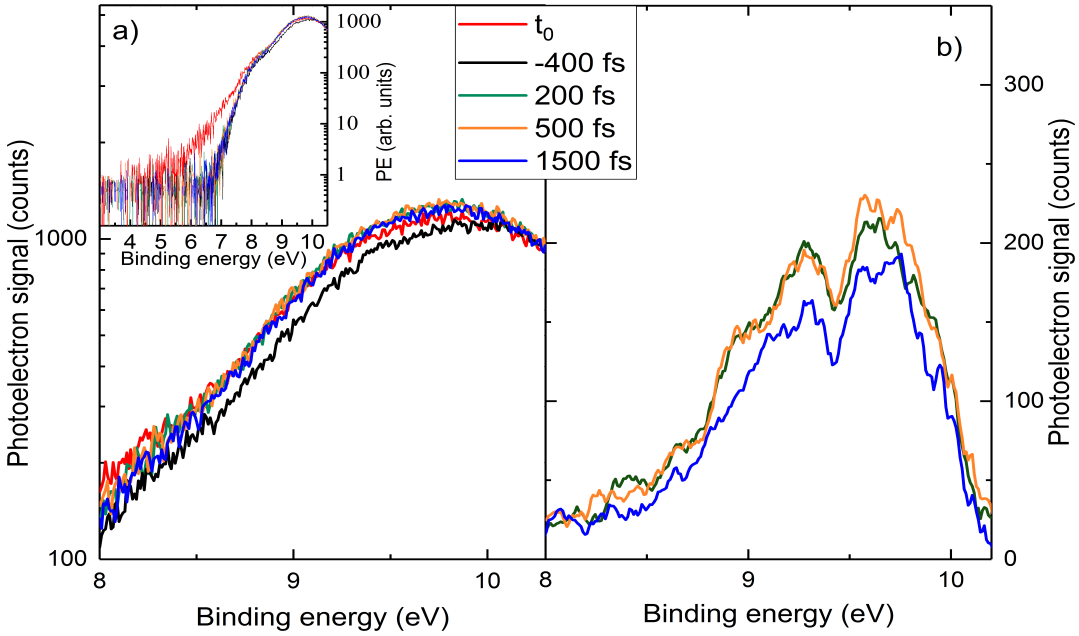

Figure 5.11: a) Comparison of transient spectra measured after 400 nm excitation of SNP aqueous solution at different time delays. The left panel shows spectra at -400 fs (black curve), +200 fs (green curve), +500 fs (orange curve), +1500 fs (blue curve), and zero-time delay (red curve) in the binding energy range of 8-10.5 eV. The right panel shows the transient spectra in the entire range of binding energies of 4-10 eV recorded in the measurement. Panel b) shows the smoothed (rebinned) difference of the spectrum at a negative time delay of -400 fs and the spectra recorded at time delays of +200 fs (green curve), +500 fs (orange curve) and +1500 fs (blue curve).

The left panel of figure 5.11 a) shows a comparison between the spectra of SNP aqueous solution in the 8-10 eV binding energy range. In this figure, the spectrum at a negative time delay of -400 fs (black curve), at zero-time delay (red curve) and at three different positive time delays are displayed. The spectra recorded at delays of +200 fs (green curve), +500 fs (orange curve), and +1500 fs (blue curve) provide evidence of the transient state signal. One can observe that the spectral shape appears to be very similar at each time delay and the maximum signal arises in a binding energy range of 8.5-9.5 eV. In addition, figure 5.11 b) illustrates the photoelectron spectra obtained as a difference between the negative-delay spectrum (-400 fs) and the spectra at different positive time delays. From this figure, it is straightforward to see that there is a transient signal which has a maximum at a binding energy of 9.5 eV. Likewise, there is no difference between the spectra at +200 and +500 fs time delay in the binding energy range where the transient signal is observed. However, there is a slight difference in the relative

amplitude at the +1500 fs time delay. This suggests that the PE spectra at positive time delays are associated with one excited state.

5.3.2 Results of the Fitting Analysis and Discussion

Typically, photo-excitation dynamics in molecular systems can be induced via resonant electronic excitation. After that, the transitions between the excited states relax intramolecularly and potentially itromolecularly, under going a cascade of transitions from a state lying at highest energy to lower-energy states, before eventually reaching the ground state configuration. In SNP, the production of MS1 follows after the 400 nm excitation and the initial population of the second ^{1}MLCT state. Thus, the electron population dynamics of the MS1 state can be described by a sequential model as:

$$GS \xrightarrow{P(t)} MLCT \xrightarrow{k_1} ES \xrightarrow{k_2} MS1$$

Here GS represents the ground state, ES denotes an intermediate transient excited state which can be populated on the way to generating the MS1 state, P(t) is the time-dependent population rate which is proportional to the time-dependent pump pulse intensity and k_1, k_2 are the decay rates from the MLCT to the ES and from the ES to the MS1 states, respectively. One should note that the lifetime of MS1state is much longer than the timescale of the measured data. This lifetime was reported in previous studies to be around 100 ns [108,125], which cannot be followed in the present measurement because of the limits of the maximum accessible time delay between the pump-probe pulses in these measurements (2 ns). Thus, the decay process of MS1 is not considered in the further analysis. The signal attributed to ionization from the MS1 state is not included in the model used to fit the PES data. The MS1 signal should appear immediately after the depopulation of ES state. Since the transient signal was measured with a short time delay compared to the lifetime of the ES state, thus the signal originating from MS1 cannot be distinguished and isolated. In addition, due to the signals associated with both states (ES and MS1) seemingly occurring in the same electron binding energy region and the expected long lifetime of the MS1 state, only an approximate growth time constant of the MS1 state can be measured with such a short time delay scan. Nevertheless, including a signal from MS1 state is possible with the use of a global fitting procedure and the measured data. However, as will be demonstrated from the data analysis below, the transient signal in the binding energy range of 7.5-10.5 eV has a lifetime of $\approx$ 8.7 ps. In contrast, the typical life times of the MLCT states of the SNP sample, lie in the tens of femtoseconds range [51, 72, 289]. Therefore, based on the existing SNP excited state dynamic literature, the transient spectra shown in the figure 5.11 should be assigned to population of an intermediate ES state. The system of differential equations applied to describe the relaxation processes of SNP in the present study are as follows:

$$\frac{d[MLCT]}{dt} = P(t)[GS] - k_1[MLCT]$$
$$\frac{d[ES]}{dt} = k_1[MLCT] - k_2[ES], \tag{5.4}$$

with the initial condition [MLCT] = 0 and [ES] = 0 at $t \longrightarrow -\infty$. Considering that the pump pulse has a Gaussian time envelope of width σ_{pump}, the population rate of the MLCT state can be described as:

$$P(t) = \rho_I \exp\left[\frac{-t^2}{2\sigma^2_{\text{pump}}}\right], \tag{5.5}$$

Where ρ_I represents a product of the photo-transition cross section and the peak intensity of the laser pump pulse. The differential equation (5.4) can be solved analytically:

$$ES(t) = A\left[\exp\frac{(k_2^2 - k_1^2)\sigma^2_{pump}}{4}(erf(\frac{t}{\sigma_{pump}} - \frac{\sigma_{pump} * k_2}{2}) + 1)\right]$$
$$\left[\exp(-k_1 t)(erf(\frac{t}{\sigma_{pump}} - \frac{\sigma_{pump} * k_1}{2}) + 1)\right], \tag{5.6}$$

where erf(x) is the error function and A is a numerical coefficient.

Figure 5.12 shows the integrated transient photoelectron signal as a function of the time delay. The main figure shows the integrated signal over the binding energy range of 7.5-8.5 eV, corresponding to the region of appearance of the pump-probe transient. This region includes the population of the MLCT state at early delay times and the ES excited state at later times. Figure 5.12 highlights two different features: the cross-correlation trace and a relatively long-lived species. The inset shows the integrated PES signal in the region of 4.5-5.5 eV, where the cross-correlation contribution dominates. A Gaussian profile is used to fit the cross-correlation signal. A temporal width of the CC signal is found to be 120 $\pm$ 3 fs (FWHM), as obtained from the fit. This width prevents the isolation of excited states with a lifetime shorter than a few tens of femtosecond. In particular, the peak centered at zero-time delay and the symmetry of this cross-correlation peak (see the main panel of figure 5.12) imply that there is no superimposed excited state with a lifetime comparable to the width of the CC signal .

One can see that the long-lived excited state contribution appears immediately after the CC trace and does not relax to the ground state within the maximum time delay of the measurement. The analytical solution of the rate equations is used to fit this signal (see equation (5.6)). The results of the fit are summarized in table 5.3. The total signal is decomposed into two exponential decays with time constants of 74 $\pm$ 28 fs and 8.7 $\pm$ 2.3 ps, corresponding to the inverse rates $\frac{1}{k1}$ and $\frac{1}{k2}$, respectively.

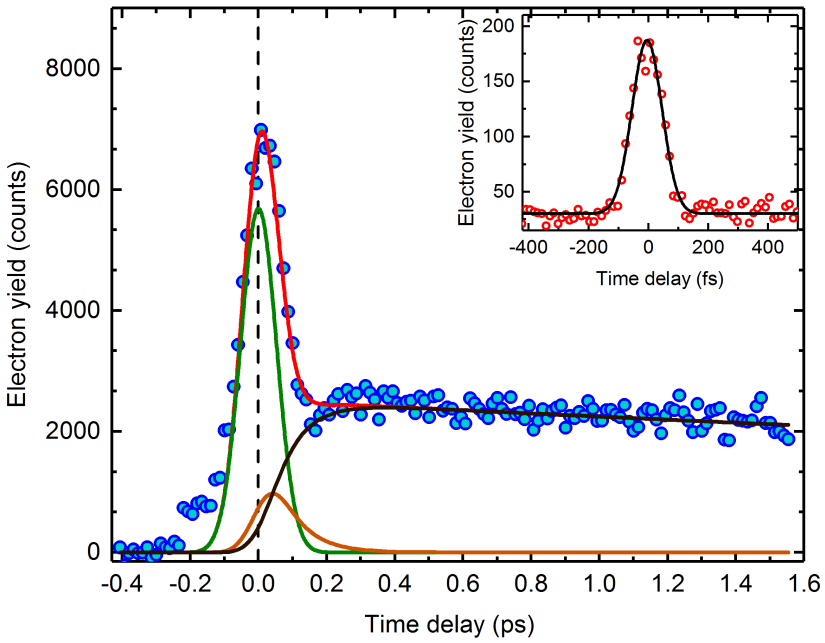

Figure 5.12: Integrated transient photoelectron signal of SNP aqueous solutions over the binding energy window 7.5 to 8.5 eV, corresponding to the population dynamics of the MS1 state. The red solid line represents the fit result of the model described by equation (5.6), to the experimental data (shown by the blue circles). Using the fit, the overall signal is decomposed in the individual ionization yields of the MLCT and ES states, shown by the orange and black lines, respectively. Inset: Integrated transient photoelectron signal in the binding energy range 4.5 to 5.5 eV, where the cross-correlation signal dominates. The results from the fit to Gaussian envelopes are presented by green solid line. The FWHM of CC peak is 120 $\pm$ 3 fs.

Table 5.3: Fit results of the kinetic model of SNP excited at 400 nm.

parameter	Results	unit
A_{cc}	7400 $\pm$ 1700	Molecule^{-1}fs^{-1}
σ_{pump}	40 $\pm$ 18	fs
σ_{probe}	33.0 $\pm$ 3.8	fs
$1/k_1$	74 $\pm$ 28	fs
$1/k_2$	8.7 $\pm$ 2.3	ps

The results from the femtosecond TRPES experiments demonstrate that the photoinduced isomerization dynamics of aqueous SNP can be interrogated on ultrafast times scales and on

an absolute energy scale. The data analysis facilitates a full description of the generation of isonitrosyl from SNP. One could say that irradiation with light of 400 nm induces a charge-transfer transition from the non-bonding $3d_{(xy,yz)}$ orbital to the unoccupied anti-bonding π_{NO} orbital. In this case, the system symmetry changes from a $^1A_1$ state to a doubly degenerate ^1E state [281, 290]. According to the Jahn–Teller theorem, the degeneracy of the twofold ^1E state will act as a driving force for the NO ligand rotation and isomerization [125, 281, 291]. The transition from ^1E (MLCT) to ES might occur directly after photo-excitation to the ^1E state on a timescale below our time resolution. The double exponential decay dynamics extracted in the fit results show that after the initial $^1A_1 \longrightarrow {}^1E$ excitation, the transition into the intermediate state ES, occurs within a 74 $\pm$ 28 fs lifetime. Since the rotation of NO to generate the MS1 isomer occurs on a picosecond time scale [100], this process can be associated with the decay time constant of approximately 8.7 $\pm$ 2.3 ps obtained from our fit results. Thereby, it is logical to consider that within the 8.7 $\pm$ 2.3 ps time-constant state extracted from the experimental data, the MS1 state is populated as a result of electronic relaxation from ES. Finally, the MS1 state decays back to the GS within 100 ns at room temperature [108]. The observation of signatures of the MLCT state and ^{1}ES allows us to present a more detailed picture of the processes leading to the photo-induced isomerization of SNP to produce MS1. In the first step, the excitation from the GS to the MLCT state takes place, described as a $3d_{xz,yz} \longrightarrow \pi_{NO}$ transition. This represents the HOMO-1 to LUMO transition with an excitation energy of 3.1 eV. An important observation is that immediately after the illumination with 400 nm light, the ES is populated within tens of fs. It should be mentioned that the MS1 state can be populated only after the depopulation of the ES. This explains the absence of any MS1 contribution in our data, since the 8.7 $\pm$ 2.3 ps decay time of ES defines the time scale of the MS1 population, i.e. much longer than our measurement time scale. It is clear from the binding energy range of generation that the MS1 electronic configuration of producing the isomerism (Fe-N-O) is linked to the GS configuration of SNP, which is in agreement with the results reported in the reference [108]. Figure 5.13 schematically summarize the processes leading to the generation of the MS1 and MS2 states.

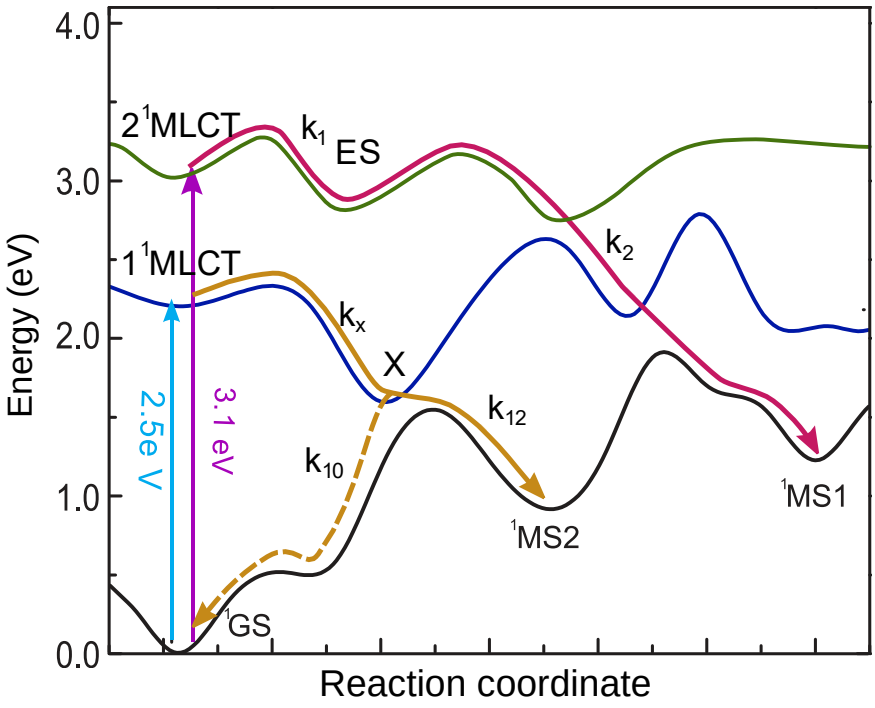

Figure 5.13: Schematic of the proposed excited state relaxation and simultaneous photo-formation mechanism of the MS1 and MS2 states in SNP.

Chapter 6

The Electron Dynamics of Ferricyanide Studied with Variable Pump Pulse Polarizations

This chapter is partly based on the article: N. Engel, S. I. Bokarev, A. Moguilevski, A. A. Raheem, R. Al-Obaidi, T. Möhle, G. Grell, K. R. Siefermann, B. Abel, S. G. Aziz, O. Kühn, M. Borgwardt, I. Kiyan and E. Aziz, "Light-induced relaxation dynamics of the ferricyanide ion revisited by ultrafast xuv photoelectron spectroscopy," Physical Chemistry Chemical Physics, vol. 19, no. 22, pp. 14 248–14 255, 2017 doi:10.1039/C7CP01288H.

Authors contributions:

N. Engel carried out the experiment, analyzed the data, interpreted the results and wrote the manuscript (introduction and experimental parts) with input from all authors. **S. I. Bokarev, T. Möhle, G. Grell, S. G. Aziz and O. Kühn** performed the theoretical calculations and wrote the computational and theory part. **A. Moguilevski, A. A. Raheem, R. Al-Obaidi** carried out the experiment, contributed the interpretations of the results and approved the final version to be submitted. **K. R. Siefermann** contributed to the experiments at the first stage of the measurements. **B. Abel** approved the final version to be submitted. **M. Borgwardt** contributed to development of the analysis and designed the figures. **I. Kiyan** supervised the research, contributed to develop the analysis and interpretation of the results, contributed to the writing draft (result and discussion part) and approved the final version to be submitted. **Emad F. Aziz** co-supervised and funded the project.

Additionally, subsequent TRPES experiments (not reported in the aforementioned article) were performed with different pump-probe relative polarization (magic angle and perpendicular) states by **A. A. Raheem** (carried out the experiment, analyzed the data, interpreted the results, wrote the description of results and discussion, and conclusion and outlook), and **Igor Kiyan** (worked out of the technical details of the experiment, helped supervise the project, and approved the final version of the description of the results). Also the TAS work described in

section 6.2 were performed with magic angle pump-probe relative polarization states by **A. A. Raheem** (carried out the experiment, analyzed the data, interpreted the results, wrote the description of results and discussion, and conclusion and outlook), **Nataliia Kuzkova** (contributed to the preparation of the experiments) and **Christoph Merschjann** (supervised the project, contributed to the development of the analysis and interpretation of the results, worked out of the technical details of the experiment, and approved the final version of the description of the results.)

6.1 Transient PES Study of Ferricyanide Aqueous Solution

In the previous PES study, which I contributed to in our lab, the early electron dynamics of ferricyanide in aqueous solution were probed with parallel relative polarization alignments of the pump and probe pulses [132]. The PES results provided information on excited state nonadiabatic and spin crossover transitions which occur on a sub-picosecond timescale. In these experiments, we showed that the initial doublet-quartet intersystem crossing takes place on a 176^{+50}_{-32} fs timescale and is followed by a slower 749^{+129}_{-96} fs intersystem crossing process. (Note that these time constant have been extracted from improved fits to the data reported in reference [132] and that error bounds on these numbers are reported here for the first time). Ojeda *et al* subsequently investigated the photophysics of ferricyanide aqueous solution following LMCT transitions using PES spectroscopy with parallel polarization alignment of the pump and probe pulses [154]. The PES results indicated a prompt reduction of the Fe^{3+} transition metal center to Fe^{2+} and a back electron transfer in 475 $\pm$ 130 fs. In this chapter, additional PES recorded with magic angle and perpendicular alignments of the pump and probe pulses are presented. These results allows us to further investigate the ultrafast dynamics of ferricyanide in aqueous solution.

Ligand-to-metal-charge-transfer (LMCT) transitions can be induced in ferricyanide ions, $[Fe^{III}(CN)_6]^{3-}$, by applying a laser pulses in the visible/ultraviolet optical range, promoting electrons from the ground state and increasing electron density at the Fe^{3+} center. In the present work, pump pulses of 400 nm wavelength (3.1 eV) were applied to induce doublet LMCT transitions in aqueous ferricyanide solutions. The pump pulses were generated via second harmonic generation of the 800 nm fundamental laser. After excitation, the electron density distribution was probed at well-defined delay times using an XUV probe beam, the 21^{st} harmonic order of the laser fundamental at 32.6 eV photon energy, as generated via HHG. The focal spot size of the 3.1 eV pump beam at the sample was approximately 100 μm (at $1/e^2$). The focal spot size of the HHG beam in the interaction region was 60 μm (at $1/e^2$). The peak intensity of the pump beam was attenuated to approximately 3.4×10^{11} W/cm^2 to minimize multiphoton ionization of the sample. The 3.1 eV photon energy pump pulses had durations of approximately 75 fs with

pulse energy of 1 μJ, corresponding to 2.0×10^{12} photon per pulse. The polarization of the pump beam was applied in two addition different configurations in the measurements reported here: i) at magic angle and ii) perpendicular to the probe beam polarization. A 400 nm half wave-plate optic was used to control the pump beam polarization. The probe beam polarization remained parallel to the TOF spectrometer axis during the measurements. In combination with the previously reported results [132], these measurements constitute a full set of polarization-state and time-resolved PES measurements.

6.1.1 Ground-State XUV Spectrum of Ferricyanide Aqueous Solution

The sample was prepared from an aqueous 0.5 M ferricyanide solution by adding sodium chloride to 10 mM levels. The PE spectrum of ferricyanide $[Fe^{III}(CN)_6]^{3-}$ was measured by applying the XUV probe beam alone. Figure 6.1 shows spectral peaks arising from ionization of liquid and gaseous water and $[Fe^{III}(CN)_6]^{3-}{}_{(aq)}$. These features are assigned in the figure. The PE spectrum was obtained by adding many spectra of equal acquisition time, recorded in the drift operational mode of the spectrometer. The electron binding energy scale in figure 6.1 was calculated as the difference between the XUV photon energy and the kinetic energy of the detected photoelectrons. The spectral peak positions displayed in figure 6.1 were calibrated using the known binding energy of the liquid water $1b_1$ peak at 11.16 ± 0.04 eV [267, 292].

The peaks in the spectrum are marked according to the water and ferricyanide molecular orbitals from which the electrons are thought to be predominantly emitted. Namely, ionization contributions from molecular orbitals $1b_{1,L}$, $1b_{1,G}$, $3a_1$ and $1b_2$ of water as well as of the Fe(3d) orbitals of ferricyanide and its counter ion $K^+(3p)$ are indicated in figure 6.1, where the L and G substrates denote liquid- and gas-phase peaks, respectively. This designation is in an agreement with the electronic structure of ferricyanide given in the literature [267, 292]. The energy positions of the water peaks in figure 6.1 are in good agreement with the binding energy positions obtained from soft x-ray photoelectron spectroscopy [277]. Fits to the water-background subtracted data are shown in the figure inset. A well-resolved electron yield from the Fe(3d) orbitals of ferricyanide is determined at 8.04 ± 0.03 eV and 9.36 ± 0.02 eV binding energy from the fits shown in the inset. These central positions of the aqueous Fe(3d) peaks are in excellent agreement with the reported experimental and theoretical values [132, 139]. In the previous reported results of the iron PE signal recorded at the BESSYII synchrotron, contributions of three peaks, at 8.71, 9.63 and 7.52 eV, were observed [139]. Due to the broad-band width, lower flux and acquisition rate associated with the HHG beam line, we observed two broadened peaks centered at the weighted average position of these three peaks, i.e. at 8.04 eV and 9.36 eV. Thus, both peaks in the inset are assigned to the ground state (HOMO) of the iron central metal, Fe(3d), in ferricyanide molecule.

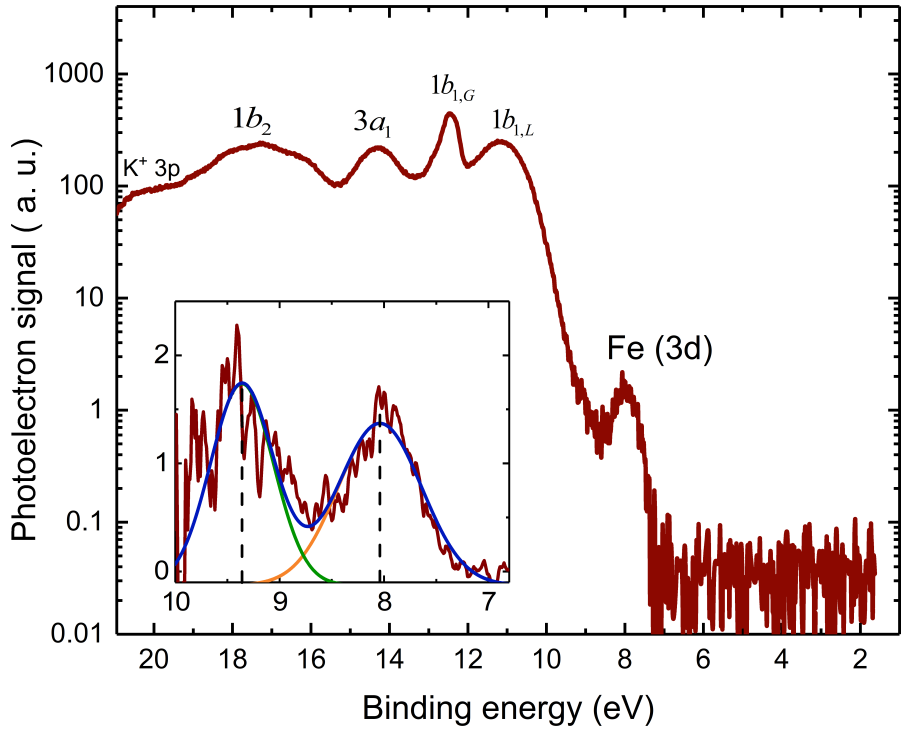

Figure 6.1: The PE spectrum of ferricyanide aqueous solution obtained by applying the XUV pulse only. Spectral peaks are attributed to ionization contributions of the iron-center-localized Fe(3d) molecular orbitals, the K^+ ion, and the $1b_1$ (liquid, L, and gaseous, G), $3a_1$ and $1b_2$ water molecular orbitals. The inset shows the same data over a reduced binding energy range after subtraction of the solvent water background along with a multi-peak fits to the associated data.

6.1.2 Transient Photoemission Spectra of Ferricyanide $[Fe^{III}(CN)_6]^{3-}$ Aqueous Solution Obtained with Different Pump Polarizations

The transient PES technique was used to study the dynamics of ferricyanide aqueous solution following 3.1 eV photo-excitation. Figures 6.2, panels a) and b), show the transient signal from 0.5 M ferricyanide aqueous solution, as a function of binding energy and time delay between the pump and probe pulses for two applied polarization directions. To enhance visibility of the transient signal, the XUV emission spectrum of the unpumped sample (recorded at maximum negative time delays) was subtracted as a background spectrum at each time delay. This background signal was obtained by averaging the first ten negative-time-delay spectra. The color bar in the figures represents the magnitude of the photoemission yield. The effects of space charge, as well as the shift of the time zero during the measurement, are corrected for all measured spectra. Due to these corrections, the binding energy and delay time axes are slightly different in the two measurements. These results performed with magic angle relative polarization alignments of the pump and probe pulses complement previous studies [132], which utilized parallel relative polarization alignments of the pump and probe pulses. The magic angle polarization combination was utilized in these measurements in order to obtain more specific information

on the excited state dynamics with elimination of any polarization dependence, i.e. to get closer to extracting the state population dynamics. A perpendicular polarization alignment was also implemented in the pump-probe experiments in an effort to extract valuable information about the investigated molecules and their ionization dynamics through comparison of the results extracted from different polarization alignment data sets.

Figure 6.2, panel a), shows the photoemission spectra of the ferricyanide sample at magic angle relative alignment of the pump and probe beam polarization. Here, the binding energy range is from 5.4 to 9.1 eV. The time delay axis spans the range between -312 fs up to a delay of 1728 fs. The utilized delay time value is sufficient to reveal the early-time population dynamics of different excited states. The negative values associated with the background-subtracted signal in the electron binding energy range of 6.8-7.4 eV and >8.5 eV are due to the depletion of the molecular orbitals primarily associated with Fe(3d) and the CN ligand orbitals, respectively, as induced by the pump beam. One can notice a distinct feature in the spectra measured when the pump and probe pulses are temporally overlapped. This signal is attributed to the first and second positive sidebands of the cross-correlation of the water peaks, that can be used to obtain an accurate value for the zero-time delay.

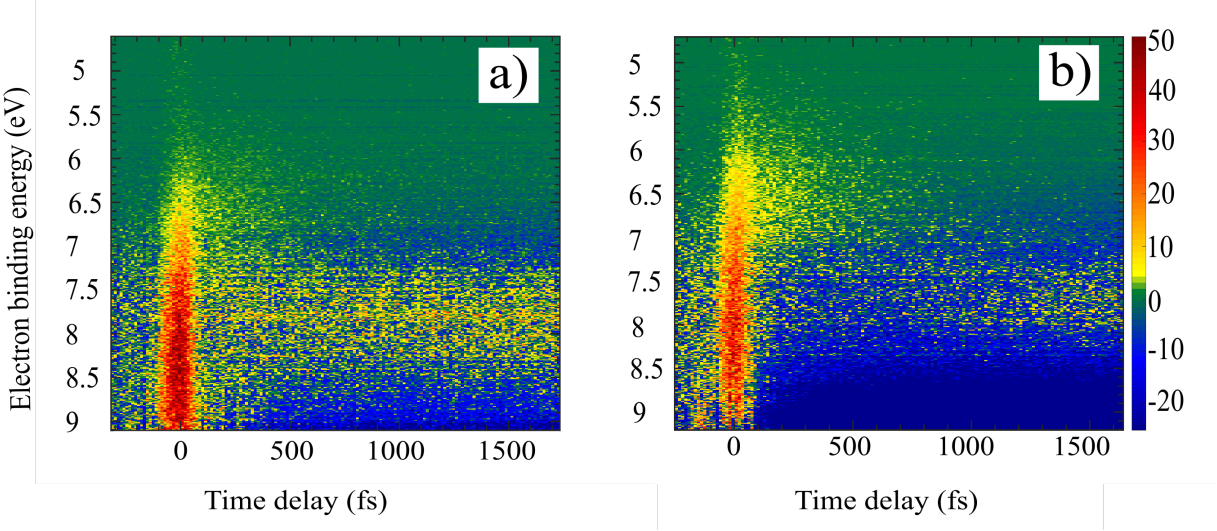

Figure 6.2: Time-resolved photoelectron signal of ferricyanide aqueous solution as a function of the electron binding energy and delay time between the pump and probe laser pulses. Panel a) shows the photoemission spectra recorded at the magic angle relative alignment of the pump and probe polarization. The spectrum is presented in the binding energy range of 5.4-9.1 eV and in the pump-probe time delay ranges of -312 fs to +1728 fs. Panel b) shows the transient photoemission signal in the binding energy range of 5.3-9.2 eV and the time delay between -246 fs up to +1635 fs as recorded with the polarization axes of pump and probe pulses set perpendicularly to each other.

The predominant cross-correlation signal is located in the binding energy range of 6.0-9.1

eV, with the signal decreasing at lower electron binding energies. There is a clearly visible positive transient signal which appears at positive time delays in different binding energy ranges. The interesting feature of the transient signal arises immediately after the time zero delay of the pump-probe pulses in two binding energy regions, 5.8-6.8 eV and 7.2-8.3 eV. In the lower binding energy range, the transient signal dissipates within the first picosecond. In contrast, the transient signal in the higher binding energy range is present at much longer time delays.

Figure 6.2 panel b), shows an analogous data set obtained for the perpendicular relative alignment of the pump and probe polarization direction. The transient photoemission spectra were measured in the range of time delays between -246 fs to +1635 fs. The background subtracted spectra are presented over the binding energy range of 5.3-9.2 eV. Analogously to the data obtained at the magic angle direction of the pump and probe polarization, there is a short-lived pump-probe signal appearing in the binding energy ranges 5.8-6.8 eV, which decays within 1 ps. Another prominent transient signal appears in the binding energy range of 7.3-8.1 eV. At long time delays (even longer than the maximum time delay displayed in figure 6.2), the transient signal can still be clearly observed. In general, the total transient signal measured with the perpendicular alignment of the pump and probe beam polarizations is lower in magnitude compared to the transient signal recorded for the same acquisition time in the magic angle case.

Moreover, one can observe that the bleach signal, which appears as blue areas in figure 6.2 panel b) due to depletion of the ground state, is clearly visible as a broad-band in the spectra at higher electron binding energies. The extension of this bleaching signal to lower electron binding energies is not as clearly observed for the magic angle case as in the case of perpendicular polarization alignment. One can conclude that the relative bleaching signal is substantially affected when changing the polarization direction of the pump beam.

For comparison data recorded with parallel relative pump-probe polarizations and associated with reference [132] is shown in figure 6.3. One can clearly see the transient signal that appears immediately after time zero in the 6.0-6.8 eV binding energy range and disappears on a picosecond time scale. Moreover, the negative value of the signal in the binding energy range between 7 and 8 eV is due to the depletion of the Fe(3d) orbital induced by the pump beam.

As will be demonstrated later, the transient signal which appears at lower binding energies is due to the population of the LMCT state, as reported in the previous study using parallel alignment of the pump polarization [132]. In contrast, the long-lived transient signal observed at higher binding energy is due to the buildup of a long-lived excited state, labeled ES.

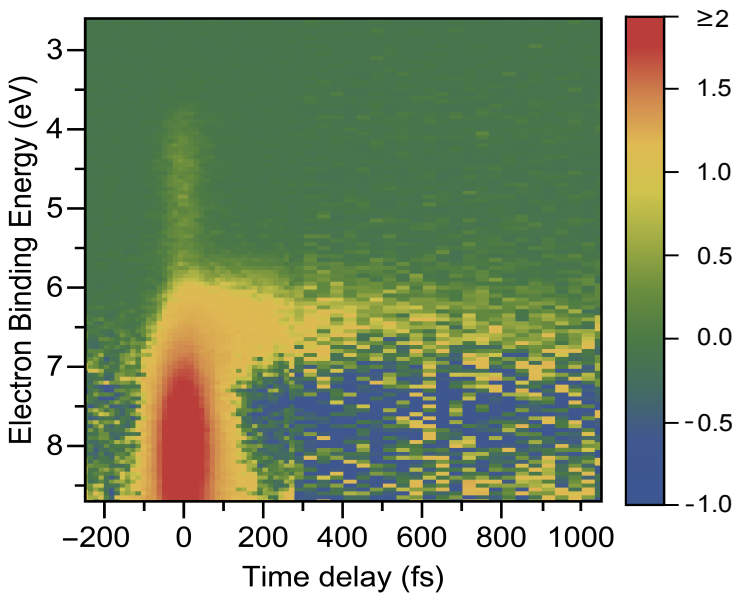

Figure 6.3: Time-resolved photoelectron signal of ferricyanide aqueous solution as a function of the electron binding energy and delay time between the pump and probe laser pulses recorded with a 400 nm pump beam and at the parallel relative alignment of the pump-probe polarization [132].

6.1.3 Kinetic Model

To unravel the processes underlying the observable spectroscopic changes and make a detailed description of the electronic dynamics, a model-based analysis of the measurements is mandatory. In the present work, the transient spectra measured for different polarization angles of the pump beam and with a sufficient time resolution to resolve the underlying dynamics show interesting features in two separate ranges on the binding energy scale. To interpret these features, the spectra were analyzed in terms of a global fit to a kinetic model which describes the population of electronic states and takes into account certain transition channels. The kinetic model presumes that the optical excitation with a 400 nm wavelength leads to electron transfer from the doublet ground state to a doublet excited ligand-to-metal charge transfer (^{2}LMCT) state, corresponding to excitation from a ligand centered-orbital to a metal-localized d-orbital.

The prepared excited ^{2}LMCT state undergoes subsequent electronic relaxation via an ISC process leading to the formation of the quartet ligand-field state (^{4}LF). The ^{4}LF state was previously shown to decay on a sub-picosecond time scale based on the data recorded with parallel relative polarizations that accompanies the magic angle and perpendicular relative polarization data sets primarily discussed here [132]. In the magic angle and perpendicular data shown in figure 6.2, the transient signal at low binding energies similarly decays within the first picosecond after the zero-time delay. Thus, this signal can also be attributed to the sequential population

of the ^{2}LMCT and ^{4}LF states. However, the results of both measurements with different pump polarization alignments reveal the presence of a long-lived state strongly contributing to the emission signal in the binding energy range between 7 and 8 eV. The decay time of this state is longer than the maximum of the time delay applied in the present experiment ($\sim$1.7 ps). To include this long-lived state in the analysis, an additional state (ES) is introduced in the kinetic model, assuming that it is populated via decay of the ^{4}LF excited state. An ionization scheme corresponding to the model of $[Fe^{III}(CN)_6]^{3-}$ relaxation following 400 nm excitation is shown in figure 6.4.

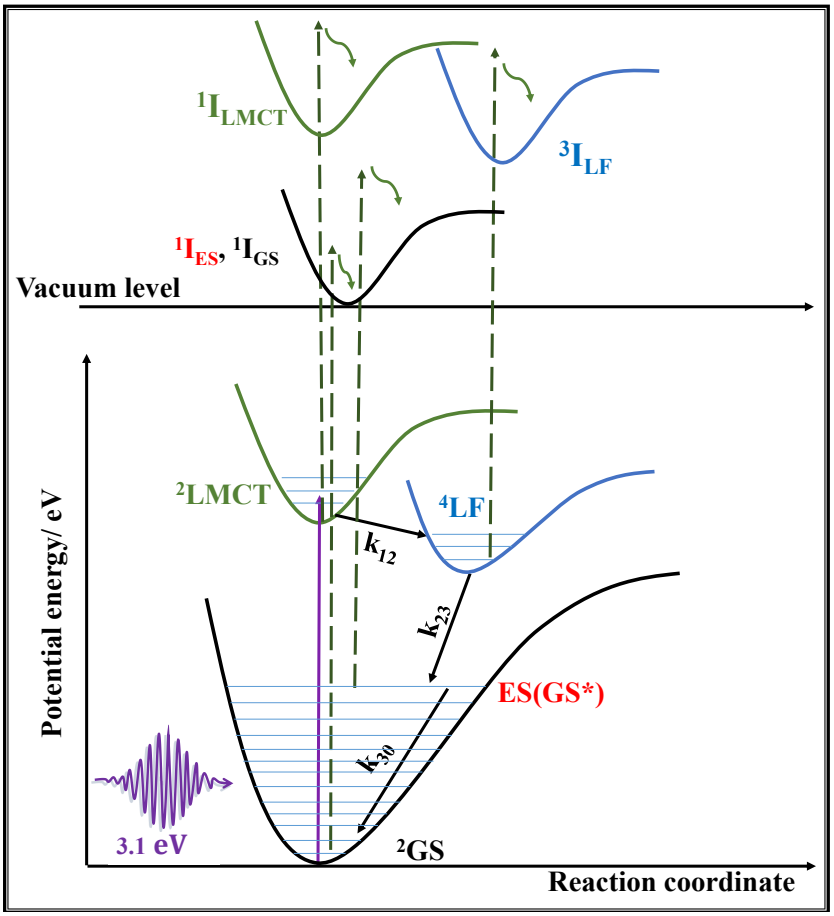

Figure 6.4: Schematic of the photochemical cycle of $[Fe^{III}(CN)_6]^{3-}$ described in a simplified energy level diagram. Absorption at 400 nm (3.1 eV) results in rovibronic excitation from the ground state to an excited ^{2}LMCT state (purple arrow), where it undergoes ultrafast decay into the ^{4}LF state. The ^{4}LF state decays to the 'ES' state and then to the rovibronic ground state with a relatively long time decay constant compared to those associated with the other states. The dashed green arrows represent the ionization above the vacuum level and to form different neutral correlated ion states that result different electron kinetic energies.

With the previous information, the kinetic rate equations, describing transitions between the electronic states, can be written as:

$$\begin{aligned}
\frac{\mathrm{d}[\mathrm{GS}]}{\mathrm{d}t} &= -a\,I_{\mathrm{pump}}(t)[\mathrm{GS}] + k_{30}[\mathrm{ES}] \\
\frac{\mathrm{d}[\mathrm{LMCT}]}{\mathrm{d}t} &= +a\,I_{\mathrm{pump}}(t)[\mathrm{GS}] - k_{12}[\mathrm{LMCT}] \\
\frac{\mathrm{d}[\mathrm{LF}]}{\mathrm{d}t} &= +k_{12}[\mathrm{LMCT}] - k_{23}[\mathrm{LF}] \\
\frac{\mathrm{d}[\mathrm{ES}]}{\mathrm{d}t} &= +k_{23}[\mathrm{LF}] - k_{30}[\mathrm{ES}]
\end{aligned} \tag{6.1}$$

Here $[\zeta]$ denotes the normalized population density of electronic state ζ and the parameter (a) represents the time-dependent excitation transition rate.

The corresponding transition rate constants between the states are denoted by k_{ij}, where i and j are the initial and final states for a given transition, respectively.

6.1.4 Population Dynamics of Electronically Excited Ferricyanide in Aqueous Solution

The reproduced PES transient spectra of ferricyanide, which are obtained from the global fit results with the use of the model described in equation 6.1, are shown in figure 6.5. The modeled spectra are presented after subtraction of the ground state spectrum of the sample (solute) and solvent at negative time delay. These background subtracted spectra are reproduced by the fit results. Panels a) and b) show the experimental data recorded with magic angle and perpendicular relative alignment of the pump polarization, respectively, in order to compare with the fit results. Figure 6.5 panels c) and d) show the photoemission spectra of ferricyanide aqueous solution obtained from the global fit. In panels e) and f), the difference between the measured PES data and the fit results (the residuals) are shown, demonstrating that the fit results match well with the corresponding measured spectra.

The two transient signals in the PES spectra are well separated in binding energy, i.e. the kinetics of the electronic population can be presented separately for each of the two spectral components. The transient signal at lower binding energy has previously been assigned to the intersystem-crossing transition from the photoexcited ligand-to-metal charge transfer state(s), ^{2}LMCT, to the ligand field state(s), ^{4}LF, in a few-hundred femtosecond(s), which subsequently decay within 1 ps [154,293]. The transient signal at higher binding energy is observed up to and presumably beyond the end of the measured pump-probe delay time, indicating that the excited state has a significantly longer lifetime at this binding energy position. These binding energy regions are highlighted in figure 6.5 a) and b) with dashed white lines. In order to investigate these lifetimes further, the electron yields of the entire PE bands corresponding to the LMCT state and the subsequently populated states are integrated to yield the data shown in figure 6.6.

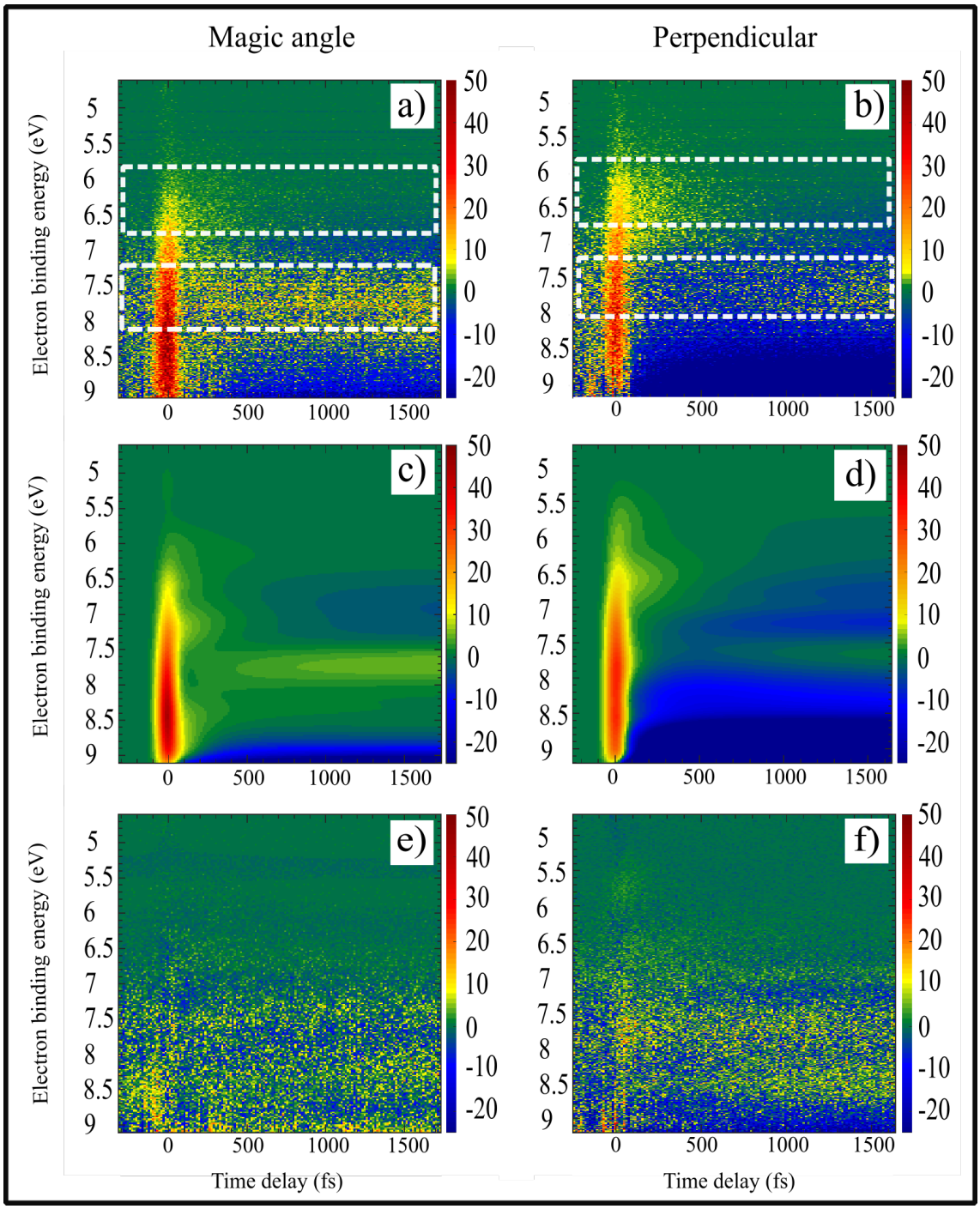

Figure 6.5: Global fit reproduction of the experimental data for the magic angle and perpendicular relative polarizations by the kinetic model described in the main body of the text and by equation 6.1. Panels a) and b) again show the PES data from figure 6.2, in this case with white line overlays to highlight the binding energy integration regions used to produce the temporal cuts shown in figure 6.6. Panels c) and d) show the modeled PES spectra of the ferricyanide aqueous solution obtained from the global fit procedure. Panels e) and f) show the residuals determined via subtraction of the experimental photoemission spectra and the corresponding fit results for both polarization cases.

These integrated traces are analyzed in the following. The electron count rate of the transient signal is affected by the bleaching of the ground state sample signal for the magic angle alignment of the pump polarization and even more so for the perpendicular case, as depicted in figure 6.5. Thus, a mechanism to disentangle the bleaching effect from the transient excited state PE signal is necessary. This can be achieved by subtracting the ground state signal of the sample. There are two specific ways to show the transient signal without the effect of the bleach, depending on the subtraction procedure adopted with the ground state spectrum. The first way is to subtract the static PES spectrum at negative time delay from the PES spectra for all time delays. Another way is to subtract the time-dependent ground state signal of the sample dynamically from the PE spectra for each binding energy bin, leaving only the net excited state transient signal that evolves during the measured time. In the latter case, the ground state spectrum was taken from the global fit result at each time delay and subtracted from the corresponding PES spectrum at each binding energy bin.

The transient photoelectron yields, which are obtained by binding energy integration of the measured PE spectra and from the fit results for a given delay time are presented in figure 6.6 for magic angle and perpendicular alignment of the pump polarization. The associated relaxation time constants of the excited states are presented in table 6.1.

In figure 6.6, panels a) and b) represent the dynamic signals associated with the cross-correlation signal and the evolution of the ground state population of the sample over the measured pump-probe time delay range. For the magic angle and perpendicular alignment cases, the fit yields relatively similar values for the lifetime constants of the transient states. Panels c) and d) in figure 6.6 present the transient signal integrated over the 5.8-6.8 eV binding energy range for the magic angle and perpendicular case, respectively. The time-independent ground state signal associated with the sample at a negative time delay is subtracted from the PES spectra in these figures. Panels e) and f) show the transient signal over the same region with the subtraction of the dynamic ground state signal from the PE spectra for the relative alignments of the magic angle and perpendicular pump polarization, respectively. Within these binding energy ranges, figure 6.5 shows a transient signal, which has completely decayed within an approximately 1 ps time scale for magic angle and perpendicular relative polarizations. For the integrated electron yield in the binding energy range of 5.8-6.8 eV for magic angle and perpendicular polarizations, the maximum of the integrated PE signal is shifted to positive time delay, indicating that there is a short-lived transient state with a lifetime comparable to the FWHM of the cross-correlation. In the energy integrated PES signal, one can see that, after the pronounced cross-correlation signal (purple), there are two components representing the ^{2}LMCT (green) and ^{4}LF (blue) states. The ^{2}LMCT state has a decay time of 171^{+27}_{-20} fs for magic angle and 178^{+26}_{-20} fs for the perpendicular alignments of the pump and probe pulses. While the ^{4}LF state has a decay time of 692^{+77}_{-63} fs and 627^{+108}_{-80} fs for magic angle and perpendicular relative polarizations, respectively. In addition, the orange line shows a slight contribution of the long-lived state, ES, at this range of binding energy that decays with 18^{+12}_{-17} ps and $19.0^{+5.0}_{-3.3}$ ps for the two polarization cases, respectively.

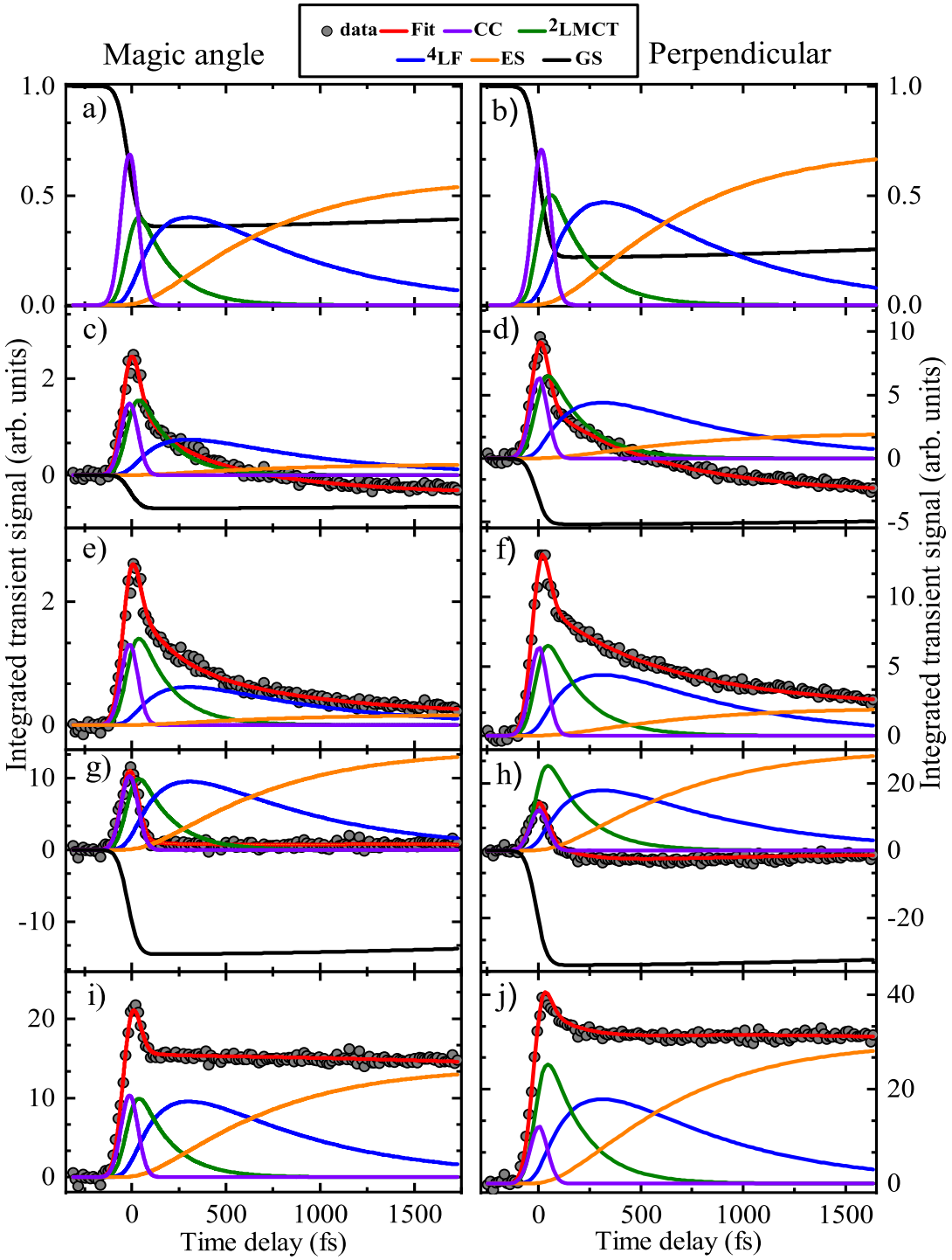

Figure 6.6: The global fit results for the magic angle and perpendicular relative directions of the pump pulse polarization. Panels a) and b) show transient population densities obtained from the global fits. Panels c) and d) respectively represent the binding energy integrated kinetic traces and the corresponding fit result, and its decomposition into specific state contributions in the binding energy ranges of 5.8-6.8 eV for magic angle and perpendicular relative polarizations. Panels e) and f) are the same as c) and d) with dynamic subtraction of the ground state signal extracted from the global fits. Panels g), h), i), j) are the analogous results for the binding energy ranges of 7.2-8.3 eV and 7.3-8.1 eV for the two polarization geometries, respectively.

Panels g) and h) in figure 6.6, show the electron yield of the subtracted transient signal at binding energy ranges of 7.2-8.3 eV and 7.3-8.1 eV for the magic angle and perpendicular case, respectively. The intensity of the transient signal is clearly affected by the bleach of the PE spectra at this region. The negative signal in the electron yield at this region can be excluded completely from the spectra by subtracting the fit component associated with ground state dynamically, as shown in panels i) and j) figure 6.6 for the magic angle and perpendicular case, respectively. At this binding energy region, a very clear contribution of the long-lived excited state, ES, can be recognized. The character of this state will be discussed later.

Table 6.1: Kinetic global (3D) fit parameters for magic angle and perpendicular alignments of the pump polarization relative to the probe polarization.

Parameter	Magic angle	Perpendicular	Unit
aI_{pump}	0.131 ± 0.011	0.20 ± 0.03	$Molecule^{-1}ps^{-1}$
$1/k_{12}$ (^{2}LMCT)	171^{+27}_{-20}	178^{+26}_{-20}	fs
$1/k_{23}$ (^{4}LF)	692^{+77}_{-63}	627^{+108}_{-80}	fs
$1/k_{30}$ (ES)	18^{+12}_{-17}	$19.0^{+5.0}_{-3.3}$	ps
σ_{pump}	31.3 ± 3.3	30.8 ± 2.4	fs
σ_{probe}	31.9 ± 2.5	29.5 ± 2.2	fs

The magic angle and perpendicular relative polarization state data sets have been similarly plotted and fit in order to compare with the data sets that were reported in reference [132] for the parallel relative pump-probe polarization. In the parallel polarization case, the transient signal integrated over the energy range between 6.0 and 6.8 eV encompasses the LMCT band.

Similar energy ranges were taken after subtracting the bleach contribution from the magic angle and perpendicular relative polarization state data sets. 2D fitting is performed to similarly extract the time constants for these three polarization alignments. The reproduced time evolution of the transient signal recorded for parallel polarization alignments of pump and probe pulses is shown in figure 6.7 and the results are summarized in table 6.2. A model incorporating two states (^{2}LMCT and ^{4}LF) was utilized to fit the parallel polarization state data set, while an additional state (ES) was included for the magic angle and perpendicular polarization states. Time constants of 176^{+50}_{-32} fs, 176^{+31}_{-23} fs, and 179^{+173}_{-59} fs were determined for the ^{2}LMCT state time constant for parallel, magic angle and perpendicular polarization states, respectively.The lifetime of the ^{4}LF state(s) was extracted from the fit to be 749^{+129}_{-96} fs, 740^{+240}_{-150} fs, 714^{+309}_{-166} fs for parallel, magic angle and perpendicular polarization states, respectively. The lifetimes of ES state in the magic angle and perpendicular polarization alignments were $30.4^{+11.8}_{-6.6}$ ps and $17.7^{+9.6}_{-4.6}$ ps, respectively as extracted from the 2D fit procedure. The results extracted from thethree data sets using 2D fit routine are in good agreement with the results that have been

extracted from the 3D fit procedure and enable a more consistent comparison between these three different cases.

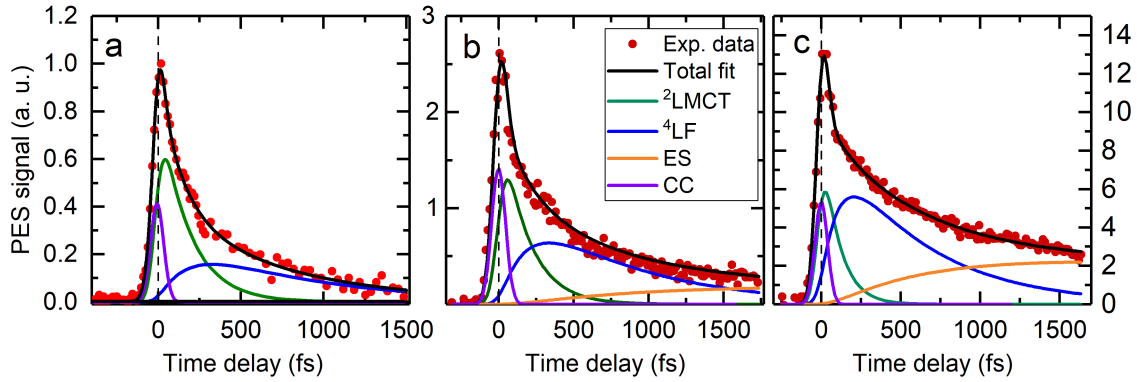

Figure 6.7: Transient binding energy integrated signal for a) parallel, b) magic angle, and c) perpendicular relative alignment of pump and probe pulse polarizations. The overall signals are decomposed to the individual ionization yields of the ^{2}LMCT, ^{4}LF, and ES states and the cross-correlation signal as shown by the green, blue, orange, and purple lines, respectively. The parallel data set is adequately fit with two state components, whereas the magic angle and perpendicular data sets require pre-treatment of the ground state bleach signal and the inclusion of additional state, ES.

Table 6.2: The results extracted from the 2D fit routine for parallel, magic angle, and perpendicular relative alignments of the pump and probe pulse polarizations.

Parameter	Parallel	Magic angle	Perpendicular	Unit
aI_{pump}	0.069 ± 0.016	0.099 ± 0.043	0.027 ± 0.011	Molecule^{-1}ps^{-1}
$1/k_{12}$ (^{2}LMCT)	176^{+50}_{-32}	176^{+31}_{-23}	179^{+173}_{-59}	fs
$1/k_{23}$ (^{4}LF)	749^{+129}_{-96}	740^{+240}_{-150}	714^{+309}_{-166}	fs
$1/k_{30}$ (ES)	$---$	$30.4^{+11.8}_{-6.6}$	$17.7^{+9.6}_{-4.6}$	ps
σ_{pump}	37.5 ± 6.7	35 ± 3.6	29.0 ± 4.8	fs
σ_{probe}	26.00 ± 0.89	29.9 ± 5.7	28.0 ± 5.9	fs

Using different alignments of the pump pulse polarization leads to a change in the relative strength of the transient state signals. The appearance of the transient signals are affected due to a polarization-dependent sensitivity of the ionizing transitions and spectrometer collection efficiency. This dependence was clearly observed in the PE spectra as a different behavior of the ground state bleaching in the transient state regions. Both the ^{2}LMCT and/or ^{4}LF states signal can also be expected to display such polarization sensitivity. As ionization channels will produce different time-dependent PADs depending on the relative polarization geometries,

the angularly selectivity of the photoelectron spectrometer is expected to result in somewhat polarization-sensitive time- constants, as observed in the TRPES measurements.

Despite the slightly different electron kinetic energy ranges analyzed from the different relative pump-probe polarization data sets, the obtained binding energies and lifetimes of the ^{2}LMCT and ^{4}LF excited states determined with magic angle and perpendicular relative polarizations, using both 2D and 3D fit routines, are in agreement with previous studies of ferricyanide aqueous solution [132, 154]. Additionally, the formation of a long-lived state, here referred to as ES, was not considered in reference [132]. In this previous time-resolved PE spectroscopy study, the energetic regions associated with population of the long-lived state was not taken into account in the fitting routine. The polarization dependence of the aqueous ferricyanide TRPES data is now considered. The polarization alignment of the applied pump pulses, transient asymmetries of the photoexcited molecules, the relative polarization alignment of the probe pulses, and associated different sensitivities to the excited state dynamics will result in somewhat different photoelectron peak magnitudes and lifetimes being extracted from the data sets recorded with different pump-probe polarization states. In this situation, the symmetry of the photoexcited species and the transition dipole moment associated with pump-photon excitation results in an initial molecular- and lab-frame alignment of the molecular axis distribution [162, 253]. The initial lab frame alignment varies as we alter the pump polarization alignment. Furthermore, due to the bandwidth and ultrashort nature of the pump-pulses, a range of rovibrational states are coherently excited to produce a time-evolving rovibrational wave packet upon excitation that results in a pump-polarization- and time-dependent laboratory frame alignment. In the pump-probe experiment, the photoelectron distribution produced by ultrashort XUV illumination of the pump-aligned excited state distribution varies depending on the pump polarization alignment. Similarly, the relative alignment of the spectrometer collection axis with respect to the 3D photoelectron distribution varies with pump polarization. Hence, pump polarization state dependent pohotoelectron peak magnitudes and lifetimes are expected. The difference between the determined excited state lifetime values are presented in table 6.2 with the state-associated signal magnitude variation shown in figure 6.7. The trend of the time-constant with polarization is highlighted in the former. One can see that the most probable lifetime of the ^{4}LF state decreases when we change the polarization alignment from parallel to perpendicular via magic angle. The lifetime of the ^{2}LMCT state is so short that a clear difference in the time constant values are not observed. In addition, the error ranges extracted from the data sets at the three different alignments of the polarization of pump pulses are large. Accordingly, definitive time constant differences and associated information about the excited state and ionization dynamics (especially for the ^{2}LMCT lifetime) is difficult to extract from the current data. Reduction of these error values could potentially be achieved by collecting more pump-probe data, to significantly improve the signal-to-noise levels. However, due to the limited pump pulse intensities that can be applied in the single-photon-absorption regime, this could only be achieved with a higher repetition rate laser source than that employed here. Fi-

nally, it is restated that the magic angle data set yields the most accurate state lifetime results for the aqueous ferricyanide, and other, samples due to this geometry's insensitivity to molecular axis alignment and the PADs formed upon photoionization following photoexcitation.

The important experimental observations in the present study were the identification of two short- and one relatively long-lived state. By combining the analysis of the experimental data and theoretical calculations from reference [132], the interpretations of the photophysical dynamics will be explored in greater detail. The electronic symmetry of the ground state of the ferricyanide molecule is $^2A_{1g}$ (see figure 6.8), with an electronic configuration of $(t_2g)^5((d_{x^2-y^2})^2(dxy)^2(d_{z^2})^1(d_{xz})^0(d_{yz})^0)$ (for more details about the molecular energy levels of ferricyanide, see section 2.3.2). There are two low-lying electronic states 0.22 eV above the $^2A_{1g}$ ground state with E_g symmetry, where either of the degenerate e_g orbitals ($d_{x^2-y^2}$ or d_{xy}) are singly occupied. Due to the energy gap between these two states, the ground state is predominantly populated at room temperature. Due to symmetry selection rules, the electric dipole-allowed transitions from the ground $^2A_{1g}$ state imply that only ^{2}LMCT or ^{2}MLCT states should be observed in the absorption spectrum while the local ligand-field d-d transitions are forbidden [132]. The ultrafast photophysical processes in $[Fe^{III}(CN)_6]^{3-}$ are initiated by 3.1 eV photoexcitation, leading to the initial population of the $^2A_{2u}$ state via Franck-Condon transitions [132]. Interestingly, the initial excitation is not only to the $^2A_{2u}$ state, where the probability of population is 0.67. The ^2E_u states are also populated with a 0.33 probability according to the calculated oscillator strengths. Since both states are non-adiabatically coupled via the pseudo-Jahn–Teller mechanism, involving the Fe-CN stretching (374 cm^{-1}) and NC-Fe-CN deformation (447 cm^{-1}) vibrational modes of e_g symmetry, the population of the ^2E_u state should quickly decay (on a timescale shorter than the cross-correlation width of the PES experiments presented here) to the $^2A_{2u}$ state. (Note that the ^2E_u state is not explicitly included in our kinetic model due to our expected inability to detect its signatures with our experimental time resolution). Due to the Franck-Condon region occurring close to a crossing point between the potential curves of the primarily directly populated $^2A_{2u}$ state and the lowest-lying quartet state, $^4B_{1g}$, there is almost no intersection barrier between the potential energy surfaces of these states (see figure 6.8). This leads to an ultrafast spin crossover between the $^2A_{2u}$ (^{2}LMCT) and $^4B_{1g}$ (^{4}LF) states, which takes place within >200 fs, as observed in the experimental data. Additionally, the potential energy surfaces of the ^{2}LMCT ($^2A_{2u}$ and ^2E_u) states also cross two ^{2}LF states (denoted as black lines in the figure 6.8). Both processes occur with a reorganization of charge from the metal-center back to the CN ligands. Due to the relatively small size of the molecule, vibrational cooling occurs on longer, multi-picosecond timescales and an excess of vibrational energy remains following repopulation of the $^2A_{1g}$ ground state [294, 295].

The decay of the low-lying quartet ligand-field, ^{4}LF, state leads to repopulation of the CN ligand-centered t_{1u} molecular orbital in the electronic ground state (see figure 2.6) [154]. This state decays within the first picosecond following photoexcitation. The respective transition represents the deactivation channel assigned to the second measured time constants of 749^{+129}_{-96}

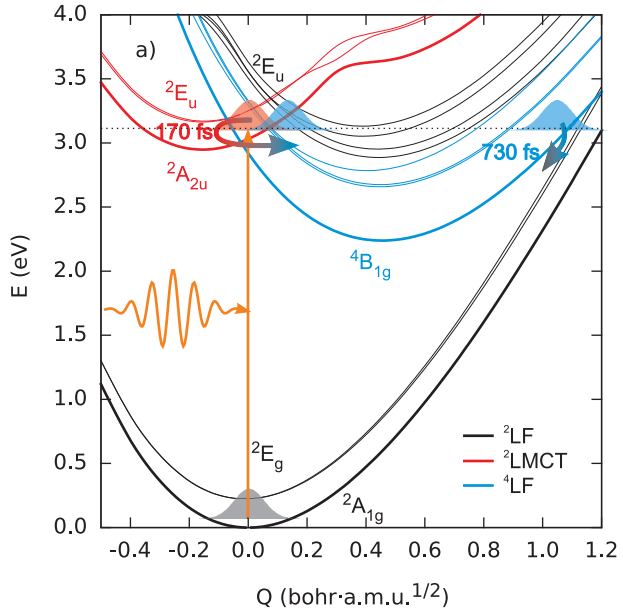

Figure 6.8: Calculations of the potential energy surfaces along the a_{1g} Fe-CN stretching mode of the lowest doublet and quartet electronic states of $[Fe^{III}(CN)_6]^{3-}$ reproduced from reference [132]. The grey lines represent the $^2A_{1g}$ ground state and low-lying ^2E_g state. The black lines represent the doublet ligand-field states (^{2}LF), red lines correspond to doublet charge-transfer states (^{2}LMCT) populated by the pump pulse (orange arrow) with energy marked by the horizontal dashed line, and the cyan lines represent quartet ligand-field states (^{4}LF).

fs, 692 $^{+77}_{-63}$ fs and 627 $^{+108}_{-80}$ fs for parallel [132], magic angle and perpendicular relative polarizations, respectively. The production of an intermediate state, ES, in the kinetic model is necessary to explain the long-lived signal in the PES spectra. This excited state has been observed in reference [154] and referred to as t_{1u} molecular orbital population, i.e., being due to reformation of the electronic ground state and vibrational cooling, which occurs on a multi-picosecond time scale (10 ps). Notably, Yu *et al* observed similar dynamics with 0.9 ± 0.1 ps and 7.3 ± 0.2 ps time constants following excitation with mid-infrared pulses at a center frequency of 2050 cm^{-1} [296]. The associated intermediate obseved here appears to undergo relaxation to the vibronic ground state within 18^{+12}_{-17} ps and $19.0^{+5.0}_{-3.3}$ ps for the magic angle and perpendicular relative alignment of the pump polarization, respectively, in good agreement with precious work. However, the accuracy of the picosecond time constants associated with this 'ES' state could likely be significantly improved by increasing the temporal span of TRPES data or by adopting a different time-resolved spectroscopic technique to probe the longer term relaxation behavior, as will be discussed later .

6.1.5 The Transient State Photoemission Spectra of Ferricyanide Aqueous Solution

Figure 6.9, panels a) and b) show the state-associated spectra extracted from global fits to the photoemission spectra produced with different relative polarization geometries, fit results for magic angle and perpendicular relative polarizations, respectively. While panel c) shows the calculated photoelectron spectra for different electronic states of $[Fe^{III}(CN)_6]^{3-}$ [132]. By comparing the photoemission spectra extracted from the experimental data fit results (panels a) and b)) with the theory in panel (c), one can see a reasonably good agreement between the photoemission spectra of ferricyanide.

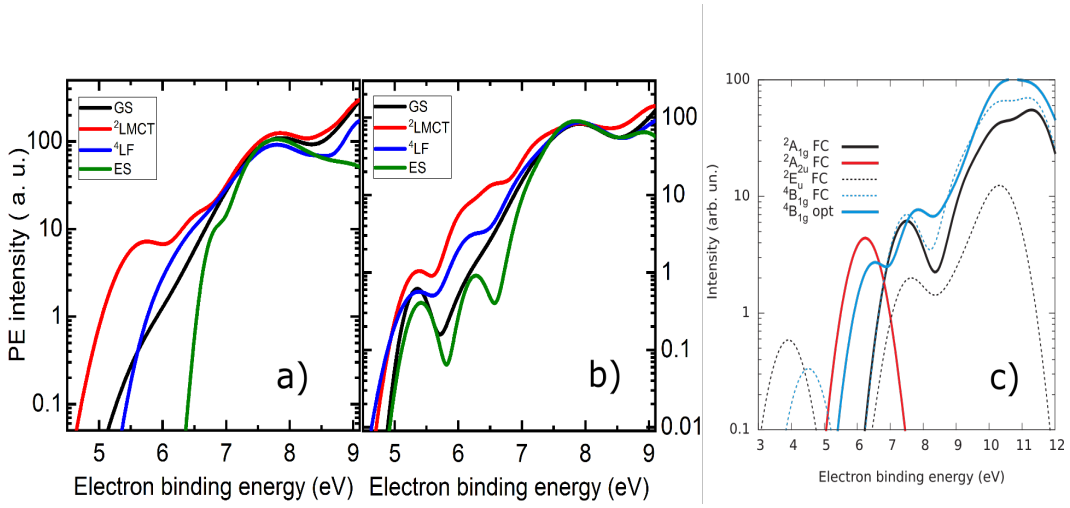

Figure 6.9: Transient energy spectra of state-associated photoelectrons from ferricyanide aqueous solution following excitation at 3.1 eV. (a) Results extracted from the global fits to the photoemission spectra recorded with magic angle relative alignments of the polarization of the pump and probe pulses. (b) Results extracted from the global fits to the photoemission spectra recorded with a perpendicular alignment of the polarization of the pump and probe pulses. c) Calculated PES associated with different electronic states taken from reference [132].

The theoretical analysis allows us to assign the spectral features in the spectra shown in figure 6.9. The ground state structure (black line) of the theoretical calculations is primarily produced through ionization of the occupied iron 3d-orbitals with binding energies at approximately 7.4 eV. The broad spectral feature above 8.5 eV is associated with ionizing transitions from a combination of iron and ligand orbitals. The photoemission spectra produced from global fits gives the ionization of the Fe(3d) at approximately 7.9 eV in both cases. The energy region below 8 eV is the region where most of the transient signals from different excited states can be extracted and which is of most interest in the present study. The pump photon energy leads to most of the excited state features occurring at lower binding energies compared to the ground state features by 3.1 eV. Accordingly, a spectral band of the ^{2}LMCT state should appear at binding energies of approximately 5-6 eV, as observed in the experimental data. The

PES spectrum of the ^{2}LMCT states is notably different from that of the ^{4}LF states and more pronounced at lower binding energies. The time-resolved data shows that at lower binding energies, excited states with short (sub-picosecond) lifetimes are dominant, while the long-lived transient component is almost absent. Similarly, the ^{4}LF state also has a sub-picosecond lifetime with the associated spectrum spanning the binding energy range between 5.5-7.0 eV. It is noted that, the calculated ^{4}LF state spectrum is not reproduced over the complete energy profile of the experimental signal. The shape of the photoemission spectra of this state was found to sensitively depend on the theory method used to calculate the transient state energies. The green curves in panels a) and b) highlight the long-lived state contributions, which are not considered in the calculated spectra in panel c). This state has a lifetime of 18-19 ps, according to the aforementioned fits of the experimental data and depending on the alignment of the polarization of the pump pulse (see table 6.1). This range of the decay time has been previously reported to be in the range of 10 ps in references [107, 154, 296] using different time-resolved techniques. The energetic parameters of the photoemission spectra extracted from global fit results are summarized in table 6.3.

Table 6.3: Fit parameters of Gaussian peaks used to describe the amplitude spectra for magic angle and perpendicular relative alignment of the polarization of the pump pulses in the ferricyanide experiments. Position values denote binding energies.

Peak	State	Magic angle			Perpendicular		
		amplitude / cts	position / eV	FWHM / eV	amplitude / cts	position / eV	FWHM /eV
1	GS	900 ± 450	10.6 ± 7.9	0.65 ± 0.33	834 ± 67	10.6 ± 4.4	0.96 ± 0.31
2	GS	830 ± 190	9.9 ± 4.0	0.699 ± 0.081	958 ± 67	10.1 ± 2.5	1.10 ± 0.18
3	GS	154.0 ± 8.8	9.61 ± 0.87	1.56 ± 0.12	283.4 ± 9.2	9.6 ± 1.5	1.56 ± 0.17
4	GS	76 ± 11	7.53 ± 0.31	0.92 ± 0.15	88.0 ± 7.9	8.3 ± 2.5	0.992 ± 0.066
5	GS	12.48 ± 0.67	7.20 ± 0.27	0.857 ± 0.078	20.1 ± 1.9	7.3 ± 2.2	1.22 ± 0.19
6	GS	1.21 ± 0.22	6.4 ± 1.1	0.80 ± 0.13	0.71 ± 0.11	6.1 ± 1.4	1.002 ± 0.052
7	GS	0.609 ± 0.092	5.3 ± 1.2	0.38 ± 0.12			
1	^{2}LMCT	90 ± 11	9.1 ± 2.8	0.66 ± 0.04	311 ± 37	9.1 ± 8.0	0.71 ± 0.21
2	^{2}LMCT	41.0 ± 9.4	9.0 ± 6.4	0.835 ± 0.060	55.0 ± 6.6	8.5 ± 2.4	0.52 ± 0.05
3	^{2}LMCT	39.0 ± 9.6	8.5 ± 2.6	0.768 ± 0.097	90.0 ± 3.9	8.0 ± 1.4	0.913 ± 0.047
4	^{2}LMCT	52.3 ± 6.5	8.0 ± 2.4	0.852 ± 0.073	63 ± 14	7.6 ± 1.4	0.70 ± 0.12
5	^{2}LMCT	38.5 ± 4.7	7.6 ± 1.9	0.793 ± 0.050	25.5 ± 2.4	7.1 ± 3.1	0.609 ± 0.022
6	^{2}LMCT	27.0 ± 4.7	7.1 ± 1.1	0.602 ± 0.021	14.0 ± 2.1	6.5 ± 3.3	0.70 ± 0.13
7	^{2}LMCT	12.0 ± 2.5	6.51 ± 0.70	0.512 ± 0.027	7.00 ± 0.62	5.6 ± 3.4	0.81 ± 0.15
8	^{2}LMCT	5.9 ± 0.4	6.0 ± 1.3	0.503 ± 0.064			
9	^{2}LMCT	1.02 ± 0.22	5.3 ± 1.1	0.518 ± 0.072			
1	^{4}LF	60.6 ± 1.3	9.3 ± 2.4	0.54 ± 0.18	153 ± 22	9.1 ± 3.5	0.544 ± 0.076
2	^{4}LF	54 ± 13	8.9 ± 1.4	0.72 ± 0.16	30.1 ± 1.3	8.9 ± 6.5	0.506 ± 0.028
3	^{4}LF	29.1 ± 5.6	8.4 ± 2.4	0.702 ± 0.072	49.1 ± 9.9	8.5 ± 3.3	0.56 ± 0.14
4	^{4}LF	60.0 ± 6.9	7.9 ± 1.1	0.76 ± 0.02	50.1 ± 2.6	7.6 ± 1.9	0.64 ± 0.13
5	^{4}LF	28.0 ± 3.1	7.55 ± 0.69	0.88 ± 0.17	63.0 ± 3.7	7.6 ± 3.1	0.657 ± 0.087
6	^{4}LF	13.87 ± 0.92	7.06 ± 0.43	0.76 ± 0.11	28 ± 4	7.15 ± 0.20	0.703 ± 0.091
7	^{4}LF	2.81 ± 0.36	6.15 ± 0.37	0.603 ± 0.032	9.01 ± 0.66	6.5 ± 3.1	0.707 ± 0.090
8	^{4}LF	0.554 ± 0.075	5.28 ± 0.87	0.610 ± 0.077	1.76 ± 0.29	6.0 ± 4.9	0.647 ± 0.089
1	ES	49 ± 12	8.9 ± 1.3	0.65 ± 0.20	30.1 ± 6.3	9.1 ± 3.2	0.794 ± 0.075
2	ES	21.87 ± 0.63	8.5 ± 1.9	0.940 ± 0.068	25.08 ± 0.50	8.6 ± 1.2	0.960 ± 0.057
3	ES	48.2 ± 3.2	7.95 ± 0.74	0.979 ± 0.027	22.0 ± 3.5	8.3 ± 4.2	0.963 ± 0.072
4	ES	46.0 ± 2.6	7.65 ± 0.57	0.70 ± 0.13	53.00 ± 0.14	7.8 ± 2.1	0.911 ± 0.084
5	ES	6.53 ± 0.57	7.06 ± 0.61	0.433 ± 0.034	40.0 ± 5.5	7.6 ± 2.0	0.7 ± 0.1
6	ES	1.008 ± 0.069	6.20 ± 0.75	0.410 ± 0.060	22.52 ± 0.48	7.3 ± 3.3	0.605 ± 0.041
7	ES	0.409 ± 0.092	5.34 ± 0.20	0.410 ± 0.063	7.05 ± 0.47	6.8 ± 2.8	0.324 ± 0.040
1	H_2O	807 ± 35	10.7 ± 4.7	0.95 ± 0.25	810 ± 300	10.7 ± 5.7	0.950 ± 0.048
2	H_2O	500 ± 110	10.1 ± 4.7	0.90 ± 0.19	498 ± 69	10.1 ± 1.6	0.90 ± 0.33
1	CC	21.1 ± 6.9	8.9 ± 3.4	0.82 ± 0.32	25.5 ± 9.3	8.8 ± 5.2	0.67 ± 0.19
2	CC	35.1 ± 6.0	8.4 ± 4.6	0.82 ± 0.18	36.2 ± 9.1	8.2 ± 6.8	0.83 ± 0.15
3	CC	41.0 ± 1.8	7.8 ± 2.6	0.96 ± 0.35	19.4 ± 2.3	7.6 ± 4.0	0.73 ± 0.12
4	CC	4.0 ± 1.0	7.2 ± 4.3	0.75 ± 0.24	23.2 ± 4.0	7.0 ± 5.5	0.751 ± 0.049
5	CC	10.0 ± 1.6	6.75 ± 0.90	0.86 ± 0.14	5.0 ± 1.3	6.2 ± 4.6	0.88 ± 0.24
6	CC	1.33 ± 0.58	5.1 ± 6.5	0.80 ± 0.11			

6.2 Time-Resolved Transient Absorption Study of Ferricyanide Aqueous Solution

The relaxation of the long-lived ES state to the ground state and/or other states cannot be reliably determined in the PES experiment. This restriction is directly related to the limited time delay range of the data reported here and to a low signal-to-noise ratio in PES experiments using a photon-limited high-harmonic XUV probe. In order to clarify the nature of the long-lived ES state and to give a more complete description of the photocycle, a femtosecond time-resolved transient absorption (TA) spectroscopy study was conducted.

6.2.1 Transient Absorption Spectra of Ferricyanide $[Fe^{III}(CN)_6]^{3-}$

The sample used in the experiment was an aqueous solution with a concentration of 8 mM held within a glass cuvette with an optical path length of 1 mm. The TA spectra were collected using 400 nm pump light (produced by SHG of the fundamental beam, as described in Chapter 4) and a white light supercontinuum (WLC, also discussed in chapter 4) as the probe. The relative polarization of the probe and pump pulses was set to the magic angle of 54.7°. The results observed at the magic angle relative polarizations of the pump and probe pulses give the time-constants and energies more representative of the state dynamics. In this case, the transient signals are independent of the effect of the transition dipole moment alignment and coherent molecular rotation dynamics introduced by the pump pulses. The pump beam was focused into the sample with a spot diameter of 600 μm at $1/e^2$, with estimated pump pulse duration of 60 fs and a pump pulse energy of 1.3 μJ, corresponding to a 2.6×10^{12} photon per pulse irradiation and a peak intensity of 1.5×10^{10} W/cm^2. The focused spot size of the WLC probe beam was 250 μm ($1/e^2$) at the sample cuvette. The associated pulse duration, probe pulse energy and peak intensity are estimated to be 65 fs, 2 nJ and 1.3×10^8 W/cm^2, respectively. For each time delay, 200 pump-probe spectra were collected to evaluate the transient absorption spectra and the spectrally-resolved probe pulse intensities were compared when the pump pulse was ON or OFF, i.e. with the pump applied or not.

Figure 6.10 a) illustrates typical raw and chirp-corrected TA spectra for an aqueous ferricyanide sample. The first four time-delay spectra were averaged and subtracted from the TA spectra over all measured time delays. The TA spectra were recorded from -9 to 500 ps with three step ranges. The first range is a linearly decreasing scale from -9 to -1 ps with a step size of 1.14 ps, the interval between -1 to 1 ps has constant time steps of 20 fs, and the interval between 1 to 500 ps is logarithmically increasing with a starting value of 31 fs. In figure 6.10, panel a), one can observe changes in optical density at various spectral positions between 530-750 nm. The color bar represents the magnitude of the absorption change, where red corresponds to an increase in the absorption and blue to a decrease in absorption. In the short-delay range, a clear transient signal can be distinguished. A positive band in the 530-650 nm region forms within

the width of the instrument response, which is 89 $\pm$ 3 fs. Moreover, the transient signal further reduces as the time delay is increased here, in particular after about 1 ps. After that the transient signal reaches a steady-state and the spectrum of the ground state is reproduced within the maximum time delay used in the experiment.

In order to understand the physical processes behind these changes of the optical density, an analysis of the TA spectra using a global fit was required. Based on the known information from the PES results, the model described by equation 6.1 is applied to simulate the time-dependent spectral changes. Figure 6.10, panel c) shows the TA spectra of ferricyanide, resulting from the fit routine. The model reproduces the time evolution of TA spectra during the photo-excitation. The residual spectra between the experiment and fit results, which are shown in figure 6.10 panel e), indicate that there is a good agreement between the experimental data and global fit results.

6.2.2 Zero-time and Chirp Correction

As a result of the temporal chirp of the WLC probe, the time-zero in the TA experiments is wavelength dependent. This can be seen in the raw 2D transient absorption spectrum (see figure 6.10 (a)) as a strong curvature at the onset of the transient signal. In the present analysis, chirp correction is carried out simultaneously to extraction of the kinetic information from the TA spectra e.g. by global analysis methods.

Correction for chirp can be made in the analysis, by applying temporal offsets such that the zero position is set correctly at every wavelength. In more detail, the peak positions (in time) of all wavelength components in the fit are shifted using a second order polynomial equation describing the explicit wavelength-dependence of the time-zero offset. The resulting time- and wavelength-dependent population densities are then fit to the experimental data in the usual optimization process, according to Chapter 3 section 3.7. After the fit, the resulting optimized chirp polynomial can be used to correct for the time-zero shift of both the original data and fit results. Thus, subsequently the TA map shows sharp bands at one time zero for all wavelengths and for all measured spectra. The corrected TA experimental data and the fit results, as well as the fit-data residual are shown in figure 6.10, panels b), d), and, f), respectively.

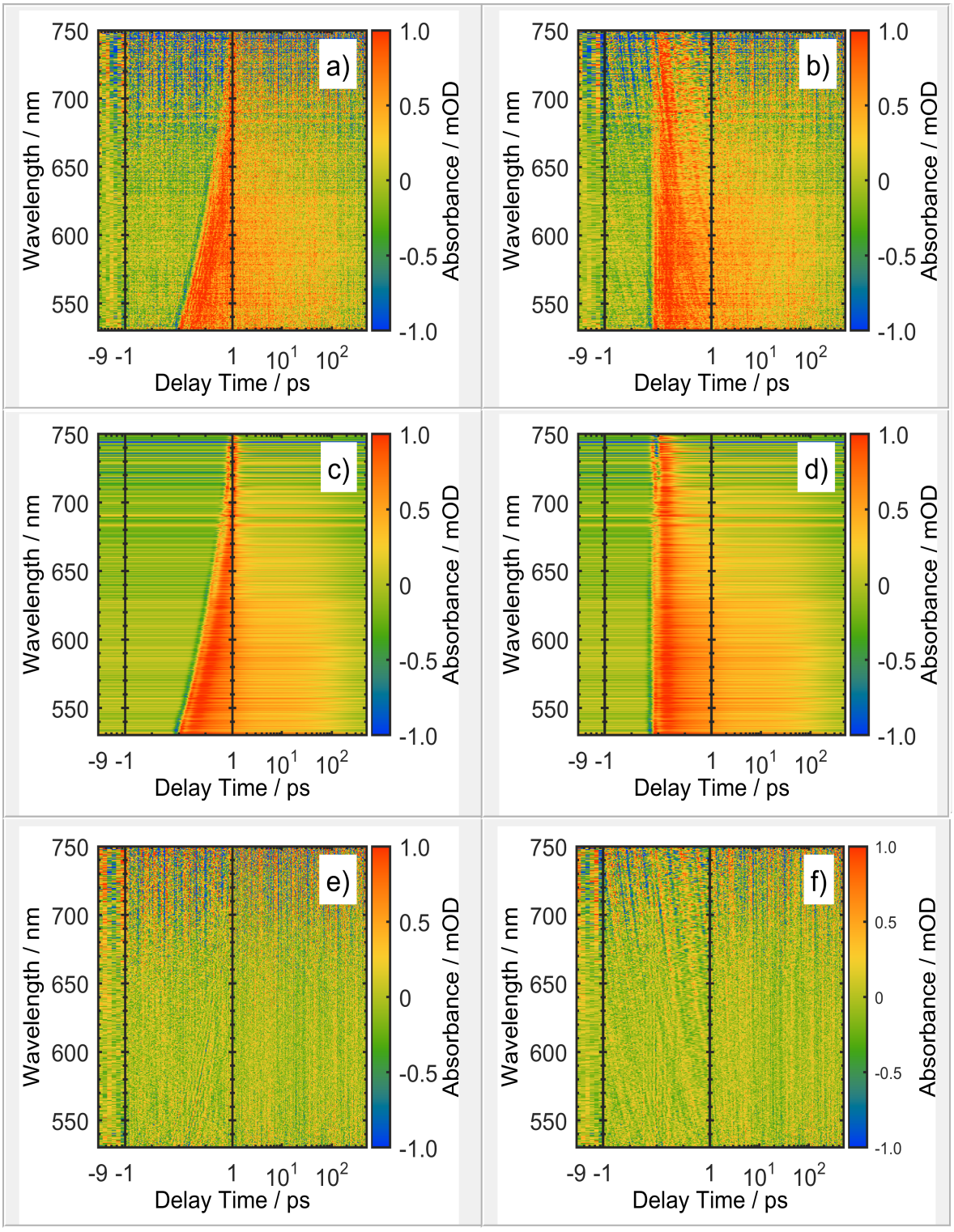

Figure 6.10: Three-dimensional TA spectra recorded as a function of wavelength and pump-probe delay time. a) and b) represent the raw (chirped) and chirp-corrected (un-chirped) TA spectra. The color bar represents the mOD scale. c) and d) are the reproduction of the chirped and un-chirped TA spectra from the fit results using the model described by equation 6.1, respectively. e) and f) show the difference between the experiment and fit results for the raw and chirp-corrected results, respectively.

6.2.3 Population Dynamics and Global Fit Results

Figure 6.11 shows the species-associated spectra obtained from the fit results.

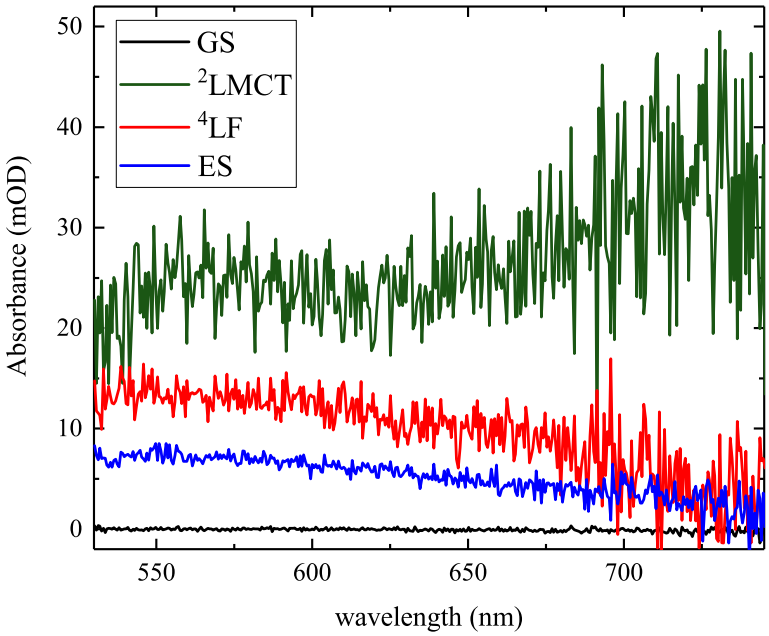

Figure 6.11: The species-associated TA spectra obtained from the fit results for different excited states as well as for the ground state of the aqueous ferricyanide sample.

Time-dependent absorbance changes of the excited states and their lifetimes, i.e. the time scales of electronic configuration change, can be determined from femtosecond-time-resolved TAS experiments. From figure 6.11, one can see that the spectral distribution of different electronically excited state signals overlap with each other. The signals associated with the population dynamics of the individual electronic states cannot be spectrally separated. In particular, in the spectral range > 630 nm, an obvious signal for the spectra of all states is observed. This can also be seen clearly in figure 6.10, where the spectral evolution has a broad absorption band spanning the visible region. Thus, this spectral range was taken into account in the following analysis in order to investigate the lifetimes of the excited states. The excited state lifetimes, as extracted using the global fit, are reported in table 6.4.

Figure 6.12 a) shows the kinetic traces integrated between 550 nm and 630 nm. At earlier time delays, the signal evolution can be described by two processes assigned to short and long lifetime contributions to the excited state populations. These lifetimes correspond to the population of the ^{2}LMCT excited states following electronic excitation from the ground state and the subsequent electronic rearrangement and formation of the ^{4}LF state, respectively. Three time constants were extracted from the global fit to the TA data for the relaxation process of the photo-excited ferricyanide liquid sample. The first one has a lifetime of about 173^{+16}_{-14} fs

Table 6.4: Fit results of the kinetic model of ferricyanide.

parameter	Results	unit
$1/k_{12}$	173^{+16}_{-14}	fs
$1/k_{23}$	864^{+41}_{-38}	fs
$1/k_{30}$	$136^{+2.8}_{-2.6}$	ps
σ_{pump}	60.3 ± 1.2	fs
σ_{probe}	65.5 ± 1.6	fs

and corresponds to the ^{2}LMCT state lifetime, in accordance with the results from the PES experiment (171^{+27}_{-20} fs for magic angle) and from the related results reported in reference [132]. The second slower component of 864^{+41}_{-38} fs (associated with the 692^{+77}_{-63} fs time constant from the magic angle PES results), which corresponds to the extracted lifetime of the ^{4}LF state. The latter lifetime is equivalent to and even slower than, the second lifetime determined from the global fit results in the PES data. Thus, the initial positive TA band signal in the 550-630 nm region corresponds to a ^{2}LMCT state signature and the associated subsequent decay as the ^{4}LF state is populated. On the longer time delay scale, the population dynamics of the undetermined excited state, ES, is described by a third lifetime of $136^{+2.8}_{-2.7}$ ps. This latter finding is in contrast to the PES results of this work, as well as to the reports from the literature [107,154,296], where additional transient species with time-constants of $<$20 ps were identified.

It is has been found from PES measurements of ferricyanide as well as from transient vibrational spectroscopy [154, 156] studies that a long-lived excited state is formed with a time-constant $<$20 ps. Here, significantly longer lifetimes were extracted from TA experiments with respect to the signal attributed to the unidentified ES state in the PES experiments. The TA signal that may be ascribed to the ES state can be seen in the figure 6.12. The TA signal may either be attributed to the same state probed in the short timescale PES experiments, to a signal from an additional electronic state, to a multi-pump-photon excited state signal, or potentialy to photochemical degradations of the sample over time in the static cell TA measurements. The longer timescale measurements reported in the TA experiments with respect to the PES measurements are clearly more appropriate for determining many-picosecond lifetimes signal decays. Significant errors (beyond the fitting errors) are expected in the TRPES data recorded out to $\sim$ 2 ps delays. However, differing contributions from different ^{2}LF/^{4}LF states to the TRPES and TA data sets may also lead to different lifetimes being extracted using these two techniques. An alternative explanation for the time constant differences is that another excited state should be included in the TA kinetic analysis. Finally, photodecomposition of ferricyanide should also be considered. This is a complicated process that is known to occur upon irradiation in the UV spectral range [21]. At 355 nm and 266 nm excitation may lead to release of CN^- ions, i.e. to produce $[Fe(CN)_5OH_2]^{2-}$ following photoaquation [21]. This process was studied with pi-

cosecond time-resolution by Reinhard *et.al.*, although the low temporal resolution of the pump laser (10 ps at FWHM) and x-ray probe pulses (70 ps) in this experiment prevented the intermediately formed compound, $[Fe(CN)_5OH_2]^{3-}$, from being observed [21, 280]. Accordingly, the intermediates and reaction mechanism associated with this process are still unclear. In the present study, the femtosecond pump pulse durations enhances two-pump-photon processes, potentially leading to $[Fe(CN)_5OH_2]^{2-}$ formation following two-photon-absorption at 400 nm. Furthermore, due to the static absorption cell used in the TA experiments, cumulative photodissociation may occur over the time of the measurements, resulting in appreciable photoproduct concentrations. Thus, two-photon absorption of the pump (3.1 eV) may lead to photoaquation of $[Fe(CN)_5OH_2]^{2-}$ and longer hundred-picosecond time constants being extracted from the TA data.

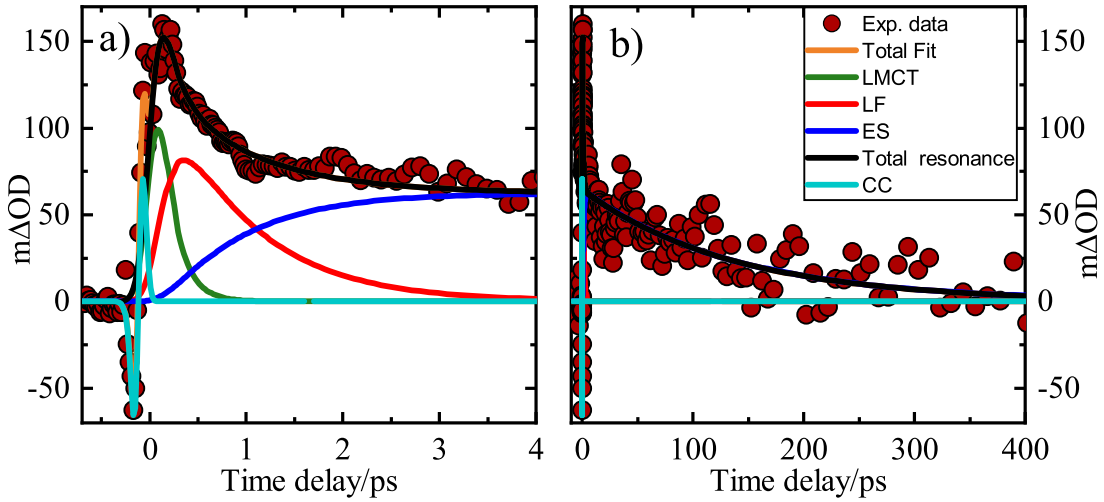

Figure 6.12: The time-dependent absorption signal traces of aqueous ferricyanide following 3.1 eV, ^{2}LMCT, excitation. The signals for the full delay range can be described by the black curve that consists of three exponential growth and decay components. Panel a): the transient signal is shown for delays of up to 4 ps and over the 550-630 nm wavelength range. In this figure, the shorter time scale is shown to visualize the first excited state behaviors and their decay within the first 1 ps. Panel b) represents the transient traces over the -9 to 400 ps range. In this panel, the 'ES' contribution underlies the black 'Total resonance' curve.

In all cases, further experiments would be needed to clarify the time-constants differences between the TA and TRPES data and to learn more about the relaxation dynamics of aqueous ferricyanide. For example, by ensuring that a refreshed sample is present for each interaction with the laser pulses in the TA experiment and by increasing the temporal range probed in the TRPES work. In general, in both the PES and TA experiments, the lifetimes of the ^{2}LMCT and ^{4}LF states have been confirmed and the presence of one or more long-lived states with life times in the tens to hundreds of picosecond range has been observed in both sets of experiments.

The ultrafast photophysical processes in ferricyanide, following photoexcitation at a 400 nm wavelength, can be summarized using the joint analysis of the experimental (PES and TA)

results and theoretical calculations. In the TRPES experiments, the initially excited ^{2}LMCT states gives rise to the transient signal in the lower binding energy range. The potential energy curves of the ^{2}LMCT and ^{4}LF states are very close to each other and close to the Franck-Condon point (see figure 6.8). Furthermore, the Franck–Condon region has a relatively small gradient and the initially excited wave packet slowly moves away from this point. This leads to an ultrafast spin crossover between these two states. The lifetime of the ^{2}LMCT state is found using PES experiments to be 176^{+50}_{-32} fs, 171^{+27}_{-20} fs and 178^{+26}_{-20} fs for parallel, magic angle and perpendicular alignments of the pump and probe pulses, respectively. The TA spectroscopy experiments confirm this lifetime with 173^{+16}_{-14} fs extracted from the associated magic angle data. Following excitation, the wave packet quickly reaches a ^{2}LMCT-^{4}LF crossing point, resulting in population of the ^{4}LF state. The lifetime of the ^{4}LF state is found from the PES experiments to be 749^{+129}_{-96} fs, 692 $^{+77}_{-63}$ fs and 627 $^{+108}_{-80}$ fs with the relative polarizations of the probe and pump beams aligned parallel [132], at magic angle and perpendicular, respectively. A similar value to these lifetimes of 864^{+41}_{-38} fs was extracted for the ^{4}LF state in the TA experiments.

In addition, a long-lived transient signal has been reported in different experiments. In the PES experiments, lifetimes of 18^{+12}_{-17} ps and $19.0^{+5.0}_{-3.3}$ ps for the magic angle and perpendicular cases have been respectively extracted from early-time (<2 ps delay) data sets. Whilst, in the TA experiments, a longer lifetime was measured of $136^{+2.8}_{-2.6}$ ps at magic angle relative alignments of the pump and probe pulses polarizations. Ojeda *et. al.* were able to establish that the back electron transfer time from the iron center to the ligand occurs within approximately 0.5 ps following photo-excitation [154]. Furthermore, using infrared TA spectroscopy, it was found that the formed highly vibrationally excited states completely decay to the ground vibronic state with two time constants of 1.1 ps and 10 ps [154]. Another group, Sando *et al*, measured the vibrational relaxation time decay for high frequency modes of aqueous ferricyanide following excitation with mid-IR at 5 μm using ultrafast infrared spectroscopy [107]. The measured signal time decay was determined to be 7.0 $\pm$ 1.0 ps [107]. Additionally, Yu *et al* have applied IR absorption, transient IR pump-probe, and waiting-time-dependent two-dimensional (2D) IR measurements on ferricyanide ions solvated in water to measure the associated structural and relaxation dynamics following mid-infrared excitation at a center frequency of 2050 cm^{-1} [296]. They extracted vibrational excited state lifetimes using double exponential functions with time constants of 0.9 ± 0.1 ps and 7.3 ± 0.2 ps [296]. Hence, multiple studies have attributed picosecond timescale signal lifetimes to vibrational cooling dynamics in aqueous ferricyanide and the picosecond time constants extracted from the TRPES and TA results reported here are similarly assigned.

A complete summary of the time constants extracted from 400 nm irradiated aqueous ferricyanide samples using different spectroscopic techniques is provided in table 6.5

Table 6.5: A summary of the time constants extracted from different experiments upon 400 nm excitation of aqueous ferricyanide.

Experiment	$1/k_1$	$1/k_2$	$1/k_3$
Parallel (PES)	176^{+50}_{-32} fs	749^{+129}_{-96} fs	– – –
Magic angle (PES)	171^{+27}_{-20} fs	692^{+77}_{-63} fs	18^{+12}_{-17} ps
Perpendicular(PES)	178^{+26}_{-20} fs	627^{+108}_{-80} fs	$19.0^{+5.0}_{-3.3}$ ps
Magic angle (TA)	173^{+16}_{-14} fs	864^{+41}_{-38} fs	$136^{+2.8}_{-2.6}$ ps
Ojeda *et. al.*-Ref. [154]	475 $\pm$ 130 fs	1.1 ps	10 ps

Chapter 7

Conclusions

A methodology to perform femtosecond-time-resolution and polarization dependent TRPES experiments with aqueous samples has been developed and demonstrated. Accordingly, five femtosecond TRPES experiments from aqueous TM complexes have been reported in this thesis, in one case with direct comparison to femtosecond time-resolved UV/Vis TA data. An analysis package was produced that allows the early-time dynamics of different molecular systems to be characterized on the basis of transient photoemission and absorption spectra obtained with a time-resolution comparable to the time scale of the observed kinetic process itself.

Excited state dynamics experiments were performed to track the isomerization processes occurring in aqueous SNP using the TRPES technique. For the case where the side-on configuration of SNP is produced via pumping at 500 nm (excitation leading to MS2), TRPES is a well-suited technique. The temporal resolution of the experiment is sufficient to observe ultrafast photo-excitation and subsequent relaxation processes, allowing the indirect population of the metastable MS2 state to be observed with a time constant less than 240 fs. The present investigations corroborated the results of previous reports concerning the excitation and relaxation kinetics using time-resolved infrared spectroscopy and transient absorption spectroscopy [93, 108, 125]. With the aid of TD-DFT calculations, the absolute binding energies of the involved electronic ground and excited states were further identified, indicating the presence of a short-lived intermediate state in the relaxation pathway to the metastable isomerized state, MS2. However, further investigations are needed to identify the multiplicity of this state. Based on these findings, investigations of the early-time kinetics of novel linkage isomerization of solution phase species by means of transient PES have demonstrably become feasible.

As for producing the isonitrosyl configuration (Fe–O–N) of aqueous SNP after excitation at 400 nm, the PES experiment tracked the light-induced population of the MS1 state, allowing us to propose a population mechanism. Excitation at a 3.1 eV photon energy leads to an excited state from which the transition into MS1 occurs within 8.7 ± 2.3 ps. The rotation of the NO ligand to 180° proceeds with this time constant. Here, the experiment offers the possibility to probe the potential energy surface of the initial excited state which precedes the production of the MS1 state. The results clearly show that a second, so far undetermined excited state, 'ES',

is populated via the initially excited MLCT state within the time resolution of our experiment. Its lifetime was determined to be 74 ± 28 fs from the fit analysis. A more detailed analysis of the parameters of the involved photo-excited states and how they lead to MS1 population could be achieved using a global fitting procedure, although this would be complicated by the overlap of the transient signals with the solvent peaks.

The excited state dynamics of aqueous ferricyanide have also been investigated, in this case using time-and polarization-resolved TRPES as well as femtosecond-resolution UV/Vis transient absorption spectroscopy. The population dynamics occurring after optical excitation with a 400 nm pump wavelength was specifically studied. Different alignments of the pump polarization (magic angle and perpendicular) were used in these experiments and compared with previously recorded parallel data [132]. To evaluate the data with high precision and extract comprehensive information, a global fit analysis based on an appropriate model of the PES signal as well as the changes in the TA spectrum was employed. The joint analysis of photoemission and UV/Vis transient absorption data represent a powerful tool for studying ultrafast electron dynamics of the ferricyanide transition-metal complex in aqueous solution. The collective photoemission spectra are in good agreement with the previous PES results recorded in our lab and reported in reference [132]. The results demonstrate that changing the polarization alignment of the pump pulses do change the relative ionization signals of the photoexcited electronic states. Doublet metal-to-ligand-charge-transfer, ^{2}LMCT, states were populated via photoexcitation from the doublet ground state. Relaxation from the ^{2}LMCT states to one or more quartet ligand field states, ^{4}LF, occurs quickly via intersystem crossing within 171^{+27}_{-20} fs and 178^{+26}_{-20} fs for magic angle and perpendicular polarization relative directions of the pump and probe pulses, respectively, which is near-identical to the time-constants extracted from the parallel relative polarization data set (176^{+50}_{-32} fs). Subsequently, the doublet-quartet intersystem crossing is followed by slower intersystem crossing to a lower-lying excited state with lifetimes of 749^{+129}_{-96} fs, 692 $^{+77}_{-63}$ fs and 627 $^{+108}_{-80}$ fs for parallel, magic angle and perpendicular polarization directions, respectively. Based on the results reported here and the current scientific literature, the decay signal is likely associated with population of vibrationally excited levels of the electronic ground state. The population dynamics of the initially populated states was confirmed by TA experiments where similar population dynamics were observed. The lifetime of the transient signal, here attributed to the ^{2}LMCT and ^{4}LF states, was reported based on analysis of the TA data to be 173^{+16}_{-14} fs and 864^{+41}_{-38} fs, respectively.

Additionally, the generation of a long-lived state was also detected. According to the limited time-span PES results (<2 ps delay), the depopulation of a long-lived state occurs on a 18^{+12}_{-17} ps and $19.0^{+5.0}_{-3.3}$ ps time scale for magic angle and perpendicular polarization directions, respectively. However, a long-lived state was detected in the TA spectra with a lifetime of $136^{+2.8}_{-2.6}$ ps. The results from the PES experiments were focused on the dynamics that take place at short time delay, which was short compared to the life time of long-lived excited state signal extracted from the TA data, resulting in additional uncertainty in this time-constant determina-

tion. A further reason for the differing TRPES and TA time-constants may be their differing sensitivity to dynamics in the vibrationally excited ground electronic state. The reason for the difference in the lifetime of the long-lived state may also be related to photochemical product formation by single or multi-pump-photon excitation or excited state decomposition pathways where the photo-products contribute to the absorption bands attributed to the ferricyanide liquid sample. An alternative possibility is that the long-lived signal is associated with dynamics in cumulatively produced photoproducts in the static absorption cell. Therefore, longer time delay TRPES experiments and a refreshed sample in the TA experiments should be employed in follow-up studies to those presented here to facilitate extraction of the definitive lifetime of this state, the origin of the long-lived signal and to determine whether the long-lived states observed in the PES and TA experiments have similar origins. Despite this, this work successfully highlighted the long-lived excited state signal and further confirmed the transient signals, attributed to two or more excited states with a lifetimes less than 1 ps.

Finally, these experiments cumulatively demonstrate our ability to follow electronic dynamics of complex molecules in the solution phase/in strongly-interacting environments in order to understand the behavior of the materials on the microscopic level. These abilities, applied to increasingly complicated systems, may be seen as a promising route to find better ways to employ such complexes and associated materials for the benefit of humanity.

Reference

[1] Volkhard May and Oliver Kühn. *Charge and energy transfer dynamics in molecular systems*. John Wiley & Sons, 2008.

[2] Shaul Mukamel. *Principles of nonlinear optical spectroscopy (Oxford Series in Optical and Imaging Sciences)*, volume 29. Oxford university press New York, 1995.

[3] A Maciejewski, R Naskrecki, M Lorenc, M Ziolek, J Karolczak, J Kubicki, M Matysiak, and M Szymanski. Transient absorption experimental set-up with femtosecond time resolution. femto-and picosecond study of DCM molecule in cyclohexane and methanol solution. *Journal of Molecular Structure*, 555(1-3):1–13, 2000.

[4] Munira Khalil, Matthew A Marcus, Amanda L Smeigh, James K McCusker, Henry HW Chong, and Robert W Schoenlein. Picosecond X-rayabsorption spectroscopy of a photoinduced iron (II) spin crossover reaction in solution. *The Journal of Physical Chemistry A*, 110(1):38–44, 2006.

[5] David Glijer, Johan Hebert, Elzbieta Trzop, Eric Collet, Loïc Toupet, Hervé Cailleau, GS Matouzenko, HZ Lazar, Jean-François Létard, S Koshihara, et al. Photoinduced phenomena and structural analysis associated with the spin-state switching in the $[Fe_{II}(DPEA)(NCS)_2]$ complex. *Physical Review B*, 78(13):134112, 2008.

[6] Ian A Howard and Frederic Laquai. Optical probes of charge generation and recombination in bulk heterojunction organic solar cells. *Macromolecular Chemistry and Physics*, 211(19):2063–2070, 2010.

[7] Gerhard Stock and Wolfgang Domcke. Detection of ultrafast molecular-excited-state dynamics with time-and frequency-resolved pump-probe spectroscopy. *Physical Review A*, 45(5):3032, 1992.

[8] Niels E Henriksen and Volker Engel. Femtosecond pump-probe spectroscopy: A theoretical analysis of transient signals and their relation to nuclear wave-packet motion. *International Reviews in Physical Chemistry*, 20(2):93–126, 2001.

[9] Grazyna Palczewska, Patrycjusz Stremplewski, Susie Suh, Nathan Alexander, David Salom, Zhiqian Dong, Daniel Ruminski, Elliot H Choi, Avery E Sears, Timothy S Kern,

Maciej Wojtkowski, and Krzysztof Palczewski. Two-photon imaging of the mammalian retina with ultrafast pulsing laser. *JCI insight*, 3(17), 2018.

[10] Devens Gust, Thomas A Moore, and Ana L Moore. Molecular mimicry of photosynthetic energy and electron transfer. *Accounts of Chemical Research*, 26(4):198–205, 1993.

[11] Gábor Benkö, Jani Kallioinen, Jouko EI Korppi-Tommola, Arkady P Yartsev, and Villy Sundström. Photoinduced ultrafast dye-to-semiconductor electron injection from non-thermalized and thermalized donor states. *Journal of the American Chemical Society*, 124(3):489–493, 2002.

[12] Samir Kumar Pal and Ahmed H Zewail. Dynamics of water in biological recognition. *Chemical Reviews*, 104(4):2099–2124, 2004.

[13] Ahmed H Zewail. Femtochemistry: Atomic-scale dynamics of the chemical bond using ultrafast lasers (nobel lecture). *Angewandte Chemie International Edition*, 39(15):2586–2631, 2000.

[14] S Lochbrunner, JJ Larsen, JP Shaffer, M Schmitt, Thomas Schultz, JG Underwood, and Albert Stolow. Methods and applications of femtosecond time-resolved photoelectron spectroscopy. *Journal of Electron Spectroscopy and Related Phenomena*, 112(1-3):183–198, 2000.

[15] Yu-San Huang, Takeshi Karashima, Masayuki Yamamoto, and Hiro-o Hamaguchi. Molecular-level investigation of the structure, transformation, and bioactivity of single living fission yeast cells by time-and space-resolved raman spectroscopy. *Biochemistry*, 44(30):10009–10019, 2005.

[16] Rudi Berera, Rienk van Grondelle, and John TM Kennis. Ultrafast transient absorption spectroscopy: principles and application to photosynthetic systems. *Photosynthesis research*, 101(2-3):105–118, 2009.

[17] Gavin D Reid and Klaas Wynne. Ultrafast laser technology and spectroscopy. *Encyclopedia of Analytical chemistry*, 35(4), 2000.

[18] Biman Bagchi. Dynamics of solvation and charge transfer reactions in dipolar liquids. *Annual Review of Physical Chemistry*, 40(1):115–141, 1989.

[19] Ch Bressler, C Milne, V-T Pham, Amal ElNahhas, Renske M van der Veen, Wojciech Gawelda, S Johnson, Paul Beaud, Daniel Grolimund, Maik Kaiser, et al. Femtosecond XANES study of the light-induced spin crossover dynamics in an iron (II) complex. *Science*, 323(5913):489–492, 2009.

[20] A Cannizzo, CJ Milne, C Consani, W Gawelda, Ch Bressler, F Van Mourik, and M Chergui. Light-induced spin crossover in Fe (II)-based complexes: The full photocycle unraveled by ultrafast optical and X-ray spectroscopies. *Coordination Chemistry Reviews*, 254(21-22):2677–2686, 2010.

[21] M Reinhard, TJ Penfold, FA Lima, J Rittmann, MH Rittmann-Frank, R Abela, I Tavernelli, U Rothlisberger, CJ Milne, and M Chergui. Photooxidation and photoaquation of iron hexacyanide in aqueous solution: A picosecond X-ray absorption study. *Structural Dynamics*, 1(2):024901, 2014.

[22] BJ Powell. Theories of phosphorescence in organo-transition metal complexes–from relativistic effects to simple models and design principles for organic light-emitting diodes. *Coordination Chemistry Reviews*, 295:46–79, 2015.

[23] Antonín Vlček. Ultrafast excited-state processes in Re (I) carbonyl-diimine complexes: from excitation to photochemistry. In *Photophysics of Organometallics*, pages 115–158. Springer, 2009.

[24] Arvind Kumar, Shih-Sheng Sun, and Alistair J Lees. Photophysics and photochemistry of organometallic rhenium diimine complexes. In *Photophysics of Organometallics*, pages 37–71. Springer, 2009.

[25] Devens Gust, Thomas A Moore, and Ana L Moore. Solar fuels via artificial photosynthesis. *Accounts of Chemical Research*, 42(12):1890–1898, 2009.

[26] Carsten Deibel, Thomas Strobel, and Vladimir Dyakonov. Role of the charge transfer state in organic donor–acceptor solar cells. *Advanced Materials*, 22(37):4097–4111, 2010.

[27] Arianna Marchioro, Joël Teuscher, Dennis Friedrich, Marinus Kunst, Roel Van De Krol, Thomas Moehl, Michael Grätzel, and Jacques-E Moser. Unravelling the mechanism of photoinduced charge transfer processes in lead iodide perovskite solar cells. *Nature Photonics*, 8(3):250, 2014.

[28] Gary F Moore and Gary W Brudvig. Energy conversion in photosynthesis: a paradigm for solar fuel production. *Annu. Rev. Condens. Matter Phys.*, 2(1):303–327, 2011.

[29] Claudio Garino and Luca Salassa. The photochemistry of transition metal complexes using density functional theory. *Phil. Trans. R. Soc. A*, 371(1995):20120134, 2013.

[30] Nicola J Farrer, Luca Salassa, and Peter J Sadler. Photoactivated chemotherapy (pact): the potential of excited-state d-block metals in medicine. *Dalton Transactions*, (48):10690–10701, 2009.

[31] Dennis EJGJ Dolmans, Dai Fukumura, and Rakesh K Jain. Photodynamic therapy for cancer. *Nature Reviews Cancer*, 3(5):380, 2003.

[32] Albert Ruggi, Fijs WB van Leeuwen, and Aldrik H Velders. Interaction of dioxygen with the electronic excited state of Ir (III) and Ru (II) complexes: principles and biomedical applications. *Coordination Chemistry Reviews*, 255(21-22):2542–2554, 2011.

[33] Michael Grätzel. Dye-sensitized solar cells. *Journal of Photochemistry and Photobiology C: Photochemistry Reviews*, 4(2):145–153, 2003.

[34] André Sarto Polo, Melina Kayoko Itokazu, and Neyde Yukie Murakami Iha. Metal complex sensitizers in dye-sensitized solar cells. *Coordination Chemistry Reviews*, 248(13-14):1343–1361, 2004.

[35] Simona Fantacci and Filippo De Angelis. A computational approach to the electronic and optical properties of Ru (II) and Ir (III) polypyridyl complexes: applications to DSC, OLED and NLO. *Coordination Chemistry Reviews*, 255(21-22):2704–2726, 2011.

[36] Thomas S Teets and Daniel G Nocera. Photocatalytic hydrogen production. *Chemical Communications*, 47(33):9268–9274, 2011.

[37] Tom Bitterwolf. Photochemistry of transition metal complexes. *Encyclopedia of Inorganic and Bioinorganic Chemistry*, 2011.

[38] Vanesa Fernandez-Moreira, Flora L Thorp-Greenwood, and Michael P Coogan. Application of d6 transition metal complexes in fluorescence cell imaging. *Chemical Communications*, 46(2):186–202, 2010.

[39] Philip Coppens, Irina Novozhilova, and Andrey Kovalevsky. Photoinduced linkage isomers of transition-metal nitrosyl compounds and related complexes. *Chemical Reviews*, 102(4):861–884, 2002.

[40] Norman N Greenwood and A Earnshaw. Chemistry of the elements, Butterworth Heinemann. *Oxford, ISBN*, 80379419:795, 1997.

[41] John Burgess and Martyn V Twigg. Iron: inorganic & coordination chemistry. *Encyclopedia of Inorganic Chemistry*, 2006.

[42] W Chadwick Ellis, Neal D McDaniel, Stefan Bernhard, and Terrence J Collins. Fast water oxidation using iron. *Journal of the American Chemical Society*, 132(32):10990–10991, 2010.

[43] Felix Gärtner, Albert Boddien, Enrico Barsch, Koichi Fumino, Sebastian Losse, Henrik Junge, Dirk Hollmann, Angelika Brückner, Ralf Ludwig, and Matthias Beller. Photocatalytic hydrogen generation from water with iron carbonyl phosphine complexes:

improved water reduction catalysts and mechanistic insights. *Chemistry–A European Journal*, 17(23):6425–6436, 2011.

[44] O Kahn and C Jay Martinez. Spin-transition polymers: from molecular materials toward memory devices. *Science*, 279(5347):44–48, 1998.

[45] Philipp Gütlich, Harold A Goodwin, and Kamel Boukheddaden. *Spin crossover in transition metal compounds III*. Springer Science & Business Media, 2004.

[46] Sidney Francis Alan Kettle. *Physical inorganic Chemistry: a Coordination Chemistry Approach*. Springer, 2013.

[47] John Stanley Griffith. *The theory of transition-metal ions*. Cambridge University Press, 1964.

[48] Andreas Hauser, Cristian Enachescu, Max Lawson Daku, Alfredo Vargas, and Nahid Amstutz. Low-temperature lifetimes of metastable high-spin states in spin-crossover and in low-spin Iron (II) compounds: The rule and exceptions to the rule. *Coordination Chemistry Reviews*, 250(13-14):1642–1652, 2006.

[49] Kuppuswamy Kalyanasundaram. Photophysics, photochemistry and solar energy conversion with Tris (Bipyridyl) Ruthenium (II) and its analogues. *Coordination Chemistry Reviews*, 46:159–244, 1982.

[50] Steven M Fatur, Samuel G Shepard, Robert F Higgins, Matthew P Shores, and Niels H Damrauer. A synthetically tunable system to control mlct excited-state lifetimes and spin states in Iron (II) Polypyridines. *Journal of the American Chemical Society*, 139(12):4493–4505, 2017.

[51] Majed Chergui. Ultrafast photophysics of transition metal complexes. *Accounts of Chemical Research*, 48(3):801–808, 2015.

[52] Ariana Rondi, Yuseff Rodriguez, Thomas Feurer, and Andrea Cannizzo. Solvation-driven charge transfer and localization in metal complexes. *Accounts of Chemical Research*, 48(5):1432–1440, 2015.

[53] Arnd Vogler and Horst Kunkely. Photoreactivity of metal-to-ligand charge transfer excited states. *Coordination Chemistry Reviews*, 177(1):81–96, 1998.

[54] Peter C Ford, David Wink, and John Dibenedetto. *Mechanistic aspects of the photosubstitution and photoisomerization reactions of d^6 metal complexes*. John Wiley & Sons, 2009.

[55] F Scandola, CA Bignozzi, and MT Indelli. Intramolecular energy and electron transfer in polynuclear metal complexes. In *Photosensitization and Photocatalysis Using Inorganic and Organometallic Compounds*, pages 161–216. Springer, 1993.

[56] James K McCusker. Femtosecond absorption spectroscopy of transition metal charge-transfer complexes. *Accounts of Chemical Research*, 36(12):876–887, 2003.

[57] Devens Gust, Thomas A Moore, and Ana L Moore. Mimicking photosynthetic solar energy transduction. *Accounts of Chemical Research*, 34(1):40–48, 2001.

[58] O Sato, T Iyoda, A Fujishima, and K Hashimoto. Photoinduced magnetization of a cobalt-iron cyanide. *Science*, 272(5262):704–705, 1996.

[59] Alan F Heyduk and Daniel G Nocera. Hydrogen produced from hydrohalic acid solutions by a two-electron mixed-valence photocatalyst. *Science*, 293(5535):1639–1641, 2001.

[60] Suzanne Ferrere and Brian A Gregg. Photosensitization of TiO_2 by [Fe^{II} (2, 2‘-bipyridine-4, 4‘-dicarboxylic acid)$_2$(CN)$_2$]: band selective electron injection from ultra-short-lived excited states. *Journal of the American Chemical Society*, 120(4):843–844, 1998.

[61] Brian N Figgis. Ligand field theory. *Comprehensive Coordination Chemistry*, 1:213–279, 1987.

[62] JS Griffith and LE Orgel. Ligand-field theory. *Quarterly Reviews, Chemical Society*, 11(4):381–393, 1957.

[63] Peter Atkins and Tina Overton. *Shriver and Atkins' inorganic chemistry*. Oxford University Press, USA, 2010.

[64] James Franck and EG Dymond. Elementary processes of photochemical reactions. *Transactions of the Faraday Society*, 21(February):536–542, 1926.

[65] Chantal Daniel. Photochemistry and photophysics of transition metal complexes: Quantum chemistry. *Coordination Chemistry Reviews*, 282:19–32, 2015.

[66] Chantal Daniel. Electronic spectroscopy and photoreactivity in transition metal complexes. *Coordination Chemistry Reviews*, 238:143–166, 2003.

[67] Chantal Daniel. Absorption spectroscopy, emissive properties, and ultrafast intersystem crossing processes in transition metal complexes: TD-DFT and spin-orbit coupling. In *Density-Functional Methods for Excited States*, pages 377–413. Springer, 2015.

[68] Chantal Daniel and Christophe Gourlaouen. Chemical bonding alteration upon electronic excitation in transition metal complexes. *Coordination Chemistry Reviews*, 344:131–149, 2017.

[69] Hartmut Yersin, Andreas F Rausch, Rafał Czerwieniec, Thomas Hofbeck, and Tobias Fischer. The triplet state of organo-transition metal compounds. triplet harvesting and singlet harvesting for efficient OLEDs. *Coordination Chemistry Reviews*, 255(21-22):2622–2652, 2011.

[70] Paul S Wagenknecht and Peter C Ford. Metal centered ligand field excited states: Their roles in the design and performance of transition metal based photochemical molecular devices. *Coordination Chemistry Reviews*, 255(5-6):591–616, 2011.

[71] Gleb Baryshnikov, Boris Minaev, and Hans Ågren. Theory and calculation of the phosphorescence phenomenon. *Chemical Reviews*, 117(9):6500–6537, 2017.

[72] Wenkai Zhang, Roberto Alonso-Mori, Uwe Bergmann, Christian Bressler, Matthieu Chollet, Andreas Galler, Wojciech Gawelda, Ryan G Hadt, Robert W Hartsock, Thomas Kroll, Kasper S. Kjær, Katharina Kubiček, Henrik T. Lemke, Huiyang W. Liang, Drew A. Meyer, Martin M. Nielsen, Carola Purser, Joseph S. Robinson, Edward I. Solomon, Zheng Sun, Dimosthenis Sokaras, Tim B. van Driel, György Vankó, Tsu-Chien Weng, Diling Zhu, and Kelly J. Gaffney. Tracking excited-state charge and spin dynamics in iron coordination complexes. *Nature*, 509(7500):345, 2014.

[73] Gerald Auböck and Majed Chergui. Sub-50-fs photoinduced spin crossover in $[Fe(bpy)_3]^{2+}$. *Nature Chemistry*, 7(8):629, 2015.

[74] Pavlo O Dral, Mario Barbatti, and Walter Thiel. Nonadiabatic excited-state dynamics with machine learning. *The Journal of Physical Chemistry Letters*, 9(19):5660–5663, 2018.

[75] Christian Bressler and Majed Chergui. Ultrafast X-ray absorption spectroscopy. *Chemical Reviews*, 104(4):1781–1812, 2004.

[76] Ph Wernet, Kristjan Kunnus, Ida Josefsson, Ivan Rajkovic, Wilson Quevedo, Martin Beye, Simon Schreck, Sebastian Grübel, Mirko Scholz, Dennis Nordlund, et al. Orbital-specific mapping of the ligand exchange dynamics of $Fe(CO)_5$ in solution. *Nature*, 520(7545):78, 2015.

[77] Kozo Sone and Yutaka Fukuda. Solvatochromism of transition metal complexes with organic ligands in donor and acceptor solvents. *Reviews in Inorganic Chemistry*, 11(2-4):123–154, 1990.

[78] Alistair J Lees. The luminescence rigidochromic effect exhibited by organometallic complexes: rationale and applications. *Comments on Inorganic Chemistry*, 17(6):319–346, 1995.

[79] Karen C Timberlake. *Chemistry: an introduction to general, organic, and biological chemistry*. Pearson, 2015.

[80] Subhas Samanta, Andrew A Beharry, Oleg Sadovski, Theresa M McCormick, Amirhossein Babalhavaeji, Vince Tropepe, and G Andrew Woolley. Photoswitching azo compounds in vivo with red light. *Journal of the American Chemical Society*, 135(26):9777–9784, 2013.

[81] Estíbaliz Merino and María Ribagorda. Control over molecular motion using the cis–trans photoisomerization of the azo group. *Beilstein Journal of Organic Chemistry*, 8(1):1071–1090, 2012.

[82] Martin Klok, Nicola Boyle, Mary T Pryce, Auke Meetsma, Wesley R Browne, and Ben L Feringa. Mhz unidirectional rotation of molecular rotary motors. *Journal of the American Chemical Society*, 130(32):10484–10485, 2008.

[83] Xiaojuan Pang, Xueyan Cui, Deping Hu, Chenwei Jiang, Di Zhao, Zhenggang Lan, and Fuli Li. "watching" the dark state in ultrafast nonadiabatic photoisomerization process of a light-driven molecular rotary motor. *The Journal of Physical Chemistry A*, 121(6):1240–1249, 2017.

[84] Raquel Travieso-Puente, Simon Budzak, Juan Chen, Peter Stacko, Johann TBH Jastrzebski, Denis Jacquemin, and Edwin Otten. Arylazoindazole photoswitches: Facile synthesis and functionalization via SNAr substitution. *Journal of the American Chemical Society*, 139(9):3328–3331, 2017.

[85] Xiaojuan Pang, Chenwei Jiang, Yongnan Qi, Ling Yuan, Deping Hu, Xiuxing Zhang, Di Zhao, Dongdong Wang, Zhenggang Lan, and Fuli Li. Ultrafast unidirectional chiral rotation in the Z–E photoisomerization of two azoheteroarene photoswitches. *Physical Chemistry Chemical Physics*, 20(40):25910–25917, 2018.

[86] Kazuhiro Ookubo, Yoshiyuki Morioka, Hiroshi Tomizawa, and Eiichi Miki. Vibrational spectroscopic study of light-induced metastable states of ethylenediaminenitrosylruthenium (II) complexes. *Journal of Molecular Structure*, 379(1-3):241–247, 1996.

[87] Thomas E Bitterwolf. Photochemical nitrosyl linkage isomerism/metastable states. *Coordination Chemistry Reviews*, 250(9-10):1196–1207, 2006.

[88] Dominik Schaniel and Theo Woike. Necessary conditions for the photogeneration of nitrosyl linkage isomers. *Physical Chemistry Chemical Physics*, 11(21):4391–4395, 2009.

[89] Dmitry V Fomitchev and Philip Coppens. Light-induced metastable linkage isomers of transition metal nitrosyls. *Comments on Inorganic Chemistry*, 21(1-3):131–148, 1999.

[90] Periakaruppan Thangiah Manoharan and Harry B Gray. Electronic structure of Nitroprusside ion. *Journal of the American Chemical Society*, 87(15):3340–3348, 1965.

[91] Periakaruppan Thangiah Manoharan and Harry B Gray. Electronic structures of metal pentacyanonitrosyls. *Inorganic Chemistry*, 5(5):823–839, 1966.

[92] MJ Clarke and JB Gaul. Chemistry relevant to the biological effects of nitric oxide and metallonitrosyls. In *Structures and Biological Effects*, pages 147–181. Springer, 1993.

[93] D Schaniel, Th Woike, C Merschjann, and M Imlau. Transient kinetics of light-induced metastable states in single crystals and aqueous solutions of $Na_2[Fe(CN)_5NO].2H_2O$. *Physical Review B*, 72(19):195119, 2005.

[94] Ulrich Hauser, Volker Oestreich, and Heinz Dieter Rohrweck. On optical dispersion in transparent molecular systems. *Zeitschrift für Physik A Atoms and Nuclei*, 280(1):17–25, 1977.

[95] Th Woike, M Imlau, V Angelov, J Schefer, and B Delley. Angle-dependent mössbauer spectroscopy in the ground and metastable electronic states in $Na_2[Fe(CN)_5NO].2H_2O$ single crystals. *Physical Review B*, 61(18):12249, 2000.

[96] D Schaniel, Th Woike, L Tsankov, and M Imlau. Evidence of four light-induced metastable states in iron-nitrosyl complexes. *Thermochimica Acta*, 429(1):19–23, 2005.

[97] D Schaniel, J Schefer, B Delley, M Imlau, and Th Woike. Light-induced absorption changes by excitation of metastable states in $Na_2[Fe(CN)_5NO].2H_2O$ single crystals. *Physical Review B*, 66(8):085103, 2002.

[98] Anthony R Butler and Ian L Megson. Non-heme iron nitrosyls in biology. *Chemical Reviews*, 102(4):1155–1166, 2002.

[99] Dominik Schaniel, Mirco Imlau, Thomas Weisemoeller, Theo Woike, Karl W Krämer, and H-U Güdel. Photoinduced nitrosyl linkage isomers uncover a variety of unconventional photorefractive media. *Advanced Materials*, 19(5):723–726, 2007.

[100] Dominik Schaniel, Matthieu Nicoul, and Theo Woike. Ultrafast reversible ligand isomerisation in $Na_2[Fe(CN)_5NO].2H_2O$ single crystals. *Physical Chemistry Chemical Physics*, 12(31):9029–9033, 2010.

[101] MD Carducci, MR Pressprich, and P Coppens. Diffraction studies of photoexcited crystals: Metastable nitrosyl-linkage isomers of sodium nitroprusside. *Journal of the American Chemical Society*, 119(11):2669–2678, 1997.

[102] Th Woike, W Krasser, PS Bechthold, and S Haussühl. Investigation of the metastable state of $Na_2[Fe(CN)_5NO].2H_2O$ by optical spectroscopy I. comparison of the raman spectra of the ground and metastable state. *Solid State Communications*, 45(6):499–502, 1983.

[103] Th Woike, W Krasser, PS Bechthold, and S Haussühl. Extremely long-living metastable state of $Na_2[Fe(CN)_5NO].2H_2O$ single crystals: Optical properties. *Physical Review Letters*, 53(18):1767, 1984.

[104] Dominik Schaniel, Th Woike, Jürg Schefer, V Petříček, KW Krämer, and Hans-Ulrich Güdel. Neutron diffraction shows a photoinduced isonitrosyl linkage isomer in the metastable state S I of $Na_2[Fe(CN)_5NO].2D_2O$. *Physical Review B*, 73(17):174108, 2006.

[105] D Schaniel, Th Woike, J Schefer, and V Petříček. Structure of the light-induced metastable state SII in $Na_2[Fe(CN)_5N\ O].2H_2O$. *Physical Review B*, 71(17):174112, 2005.

[106] Jennifer F Brookes, Karla M Slenkamp, Michael S Lynch, and Munira Khalil. Effect of solvent polarity on the vibrational dephasing dynamics of the nitrosyl stretch in an FeII complex revealed by 2D IR spectroscopy. *The Journal of Physical Chemistry A*, 117(29):6234–6243, 2013.

[107] Gerald M Sando, Q Zhong, and JC Owrutsky. Vibrational and rotational dynamics of cyanoferrates in solution. *The Journal of Chemical Physics*, 121(5):2158–2168, 2004.

[108] Michael S Lynch, Mark Cheng, Benjamin E Van Kuiken, and Munira Khalil. Probing the photoinduced metal- nitrosyl linkage isomerism of sodium nitroprusside in solution using transient infrared spectroscopy. *Journal of the American Chemical Society*, 133(14):5255–5262, 2011.

[109] B Delley, J Schefer, and Th Woike. Giant lifetimes of optically excited states and the elusive structure of sodiumnitroprusside. *The Journal of Chemical Physics*, 107(23):10067–10074, 1997.

[110] Darío A Estrin, Luis M Baraldo, Leonardo D Slep, Beatriz C Barja, Jose A Olabe, Luca Paglieri, and Giorgina Corongiu. Theoretical and experimental study of medium effects on the structure and spectroscopy of the $[Fe(CN)_5NO]^{2-}$Ion. *Inorganic Chemistry*, 35(13):3897–3903, 1996.

[111] V Rusanov, H Paulsen, LH Böttger, H Winkler, JA Wolny, N Koop, Th Dorn, C Janiak, and AX Trautwein. Mössbauer, nuclear inelastic scattering and density functional studies on the second metastable state of $Na_2[Fe(CN)_5NO].2H_2O$. *Hyperfine Interactions*, 175(1-3):141–150, 2007.

[112] Ulrich Hauser, Volker Oestreich, and Heinz Dieter Rohrweck. On optical dispersion in transparent molecular systems. *Zeitschrift für Physik A Atoms and Nuclei*, 284(1):9–19, 1978.

[113] Herbert Winnischofer, Fábio M Engelmann, Henrique Eisi Toma, Koiti Araki, and Hercilio R Rechenberg. Acid–base and spectroscopic properties of a novel supramolecular porphyrin bonded to four pentacyanoferrate (II) groups. *Inorganica Chimica Acta*, 338:27–35, 2002.

[114] Daisuke Asakura, Masashi Okubo, Haoshen Zhou, Kenta Amemiya, Kozo Okada, Per-Anders Glans, Catherine A Jenkins, Elke Arenholz, and Jinghua Guo. Anisotropic charge-transfer effects in the asymmetric $Fe(CN)_5NO$ octahedron of sodium nitroprusside: a soft X-ray absorption spectroscopy study. *Physical Chemistry Chemical Physics*, 16(15):7031–7036, 2014.

[115] Volker Dieckmann, Sebastian Eicke, Kristin Springfeld, and Mirco Imlau. Transition metal compounds towards holography. *Materials*, 5(6):1155–1175, 2012.

[116] M Imlau, Th Woike, R Schieder, and RA Rupp. Holographic recording with orthogonally polarized waves in centrosymmetric $Na_2[Fe(CN)_5NO].2H_2O$. *EPL (Europhysics Letters)*, 53(4):471, 2001.

[117] JA Güida, OE Piro, and PJ Aymonino. Infrared absorption spectra of sodium pentacyanonitrosylosmate (II) dihydrate in two excited electronic metastable states. *Inorganic Chemistry*, 34(16):4113–4116, 1995.

[118] ME Chacón Villalba, JA Güida, EL Varetti, and PJ Aymonino. Infrared evidence of NO linkage photoisomerization in $Na_2[Fe(CN)_5NO].2H_2O$ at low temperature: experimental and theoretical (DFT) isotopic shifts from $^{15}N(O)$, ^{18}O and ^{54}Fe species. *Spectrochimica Acta Part A: Molecular and Biomolecular Spectroscopy*, 57(2):367–373, 2001.

[119] H Zöllner, W Krasser, Th Woike, and S Haussühl. The existence of light-induced long-lived metastable states in different $X_n[Fe(CN)_5NO]yH_2O$ crystals, powders and solutions. *Chemical Physics Letters*, 161(6):497–501, 1989.

[120] Azhr A Raheem, Martin Wilke, Mario Borgwardt, Nicholas Engel, Sergey I Bokarev, Gilbert Grell, Saadullah G Aziz, Oliver Kühn, Igor Yu Kiyan, Christoph Merschjann, et al. Ultrafast kinetics of linkage isomerism in $Na_2[Fe(CN)_5NO]$ aqueous solution revealed by time-resolved photoelectron spectroscopy. *Structural Dynamics*, 4(4):044031, 2017.

[121] Th Woike, W Krasser, H Zöllner, W Kirchner, and S Haussühl. Population dynamics of the two light induced metastable states in $Na_2[Fe(CN)_5NO].2H_2O$ single crystals. *Zeitschrift für Physik D Atoms, Molecules and Clusters*, 25(4):351–356, 1993.

[122] V Rusanov, Sv Stankov, and AX Trautwein. Photoswitching of nitroprussides. *Hyperfine Interactions*, 144(1-4):307–323, 2002.

[123] Philipp Gütlich, Yann Garcia, and Theo Woike. Photoswitchable coordination compounds. *Coordination Chemistry Reviews*, 219:839–879, 2001.

[124] Th Woike, W Kirchner, G Schetter, Th Barthel, Kim Hyung-sang, and S Haussühl. New information storage elements on the basis of metastable electronic states. *Optics Communications*, 106(1-3):6–10, 1994.

[125] Geoffrey Gallé, Matthieu Nicoul, Theo Woike, Dominik Schaniel, and Eric Freysz. Unraveling the mechanism of NO ligand photoisomerism by time-resolved infrared spectroscopy. *Chemical Physics Letters*, 552:64–68, 2012.

[126] T Ressler. Solid-state kinetics and catalytic behavior of selective oxidation catalysts from time-resolved XAFS investigations. *Catalysis Today*, 145(3-4):258–266, 2009.

[127] Frederico A Lima, Thomas J Penfold, Renske M van der Veen, Marco Reinhard, Rafael Abela, Ivano Tavernelli, Ursula Rothlisberger, Maurizio Benfatto, Christopher J Milne, and Majed Chergui. Probing the electronic and geometric structure of ferric and ferrous myoglobins in physiological solutions by Fe K-edge absorption spectroscopy. *Physical Chemistry Chemical Physics*, 16(4):1617–1631, 2014.

[128] James Barber. Photosynthetic energy conversion: natural and artificial. *Chemical Society Reviews*, 38(1):185–196, 2009.

[129] Pingwu Du and Richard Eisenberg. Catalysts made of earth-abundant elements (Co, Ni, Fe) for water splitting: recent progress and future challenges. *Energy & Environmental Science*, 5(3):6012–6021, 2012.

[130] Arnd Vogler and Horst Kunkely. Photochemistry induced by metal-to-ligand charge transfer excitation. *Coordination Chemistry Reviews*, 208(1):321–329, 2000.

[131] Hui Xu, Runfeng Chen, Qiang Sun, Wenyong Lai, Qianqian Su, Wei Huang, and Xiaogang Liu. Recent progress in metal–organic complexes for optoelectronic applications. *Chemical Society Reviews*, 43(10):3259–3302, 2014.

[132] Nicholas Engel, Sergey I Bokarev, Alexandre Moguilevski, Azhr A Raheem, Ruba Al-Obaidi, Tobias Möhle, Gilbert Grell, Katrin R Siefermann, Bernd Abel, Saadullah G Aziz, Oliver Kühn, Mario Borgwardt, Igor Yu. Kiyan, and Emad F. Aziz. Light-induced relaxation dynamics of the ferricyanide ion revisited by ultrafast XUV photoelectron spectroscopy. *Physical Chemistry Chemical Physics*, 19(22):14248–14255, 2017.

[133] Andre D Miller, Ilia Bezel, Kelly J Gaffney, Sean Garrett-Roe, Simon H Liu, Paul Szymanski, and Charles B Harris. Electron solvation in two dimensions. *Science*, 297(5584):1163–1166, 2002.

[134] Wenkai Zhang, Minbiao Ji, Zheng Sun, and Kelly J Gaffney. Dynamics of solvent-mediated electron localization in electronically excited hexacyanoferrate (III). *Journal of the American Chemical Society*, 134(5):2581–2588, 2012.

[135] RW Parsons and HG Drickamer. Effect of pressure on the spectra of certain transition metal complexes. *The Journal of Chemical Physics*, 29(4):930–937, 1958.

[136] John J Alexander and Harry B Gray. Electronic structures of hexacyanometalate complexes. *Journal of the American Chemical Society*, 90(16):4260–4271, 1968.

[137] CS Naiman. Interpretation of the absorption spectra of $K_3Fe(CN)_6$. *The Journal of Chemical Physics*, 35(1):323–328, 1961.

[138] John J Alexander and Harry B Gray. Molecular orbital theory for metal complexes: ferrocyanide and cobalticyanide ions. *Coordination Chemistry Reviews*, 2(1):15–28, 1967.

[139] Robert Seidel, Stephan Thürmer, Jan Moens, Paul Geerlings, Jochen Blumberger, and Bernd Winter. Valence photoemission spectra of aqueous $Fe^{2+/3+}$ and $[Fe(CN)_6]^{4-/3-}$ and their interpretation by DFT calculations. *The Journal of Physical Chemistry B*, 115(40):11671–11677, 2011.

[140] Drew A Meyer, Xuena Zhang, Uwe Bergmann, and Kelly J Gaffney. Characterization of charge transfer excitations in hexacyanomanganate (III) with Mn K-edge resonant inelastic X-ray scattering. *The Journal of Chemical Physics*, 132(13):134502, 2010.

[141] BN Figgis and MA Hitchman. Ligand field theory and its applications 2000.

[142] Katrin R Siefermann, Yaxing Liu, Evgeny Lugovoy, Oliver Link, Manfred Faubel, Udo Buck, Bernd Winter, and Bernd Abel. Binding energies, lifetimes and implications of bulk and interface solvated electrons in water. *Nature Chemistry*, 2(4):274, 2010.

[143] Jose M Leal, Begoña Garcia, and Pedro L Domingo. Outer-sphere hexacyanoferrate (III) oxidation of organic substrates. *Coordination Chemistry Reviews*, 173(1):79–131, 1998.

[144] George I.H. Hanania, Dennis H Irvine, William A Eaton, and Philip George. Thermodynamic aspects of the potassium hexacyano-ferrate (III)-(II) system. II. reduction potential. *The Journal of Physical Chemistry*, 71(7):2022–2030, 1967.

[145] Harry B Gray and NA Beach. The electronic structures of octahedral metal complexes. I. Metal hexacarbonyls and hexacyanides. *Journal of the American Chemical Society*, 85(19):2922–2927, 1963.

[146] Mihial Atanasov, Peter Comba, Claude A Daul, and Andreas Hauser. DFT-based studies on the Jahn- Teller effect in 3d hexacyanometalates with orbitally degenerate ground states. *The Journal of Physical Chemistry A*, 111(37):9145–9163, 2007.

[147] Gobinda Basu and R Linn Belford. Nature of the visible charge-transfer bands of $K_3Fe(CN)_6$. *The Journal of Chemical Physics*, 37(9):1933–1935, 1962.

[148] SC Jain, AVR Warrier, and HK Sehgal. Electronic and vibrational spectra of ferricyanide ions doped in NaCl and KCl crystals. *Journal of Physics C: Solid State Physics*, 6(1):193, 1973.

[149] Dimitri E Khoshtariya, Reinhard Meusinger, and Roland Billing. Optical and thermal outer-sphere electron self-exchange reaction of the Hexacyanoferrate (II/III) couple: Comparative analysis of band-shape and activation parameters and large solvent kinetic isotope effect. *The Journal of Physical Chemistry*, 99(11):3592–3597, 1995.

[150] Nicholas Engel, Sergey I Bokarev, Edlira Suljoti, Raul Garcia-Diez, Kathrin M Lange, Kaan Atak, Ronny Golnak, Alexander Kothe, Marcus Dantz, Oliver Ku+hn, et al. Chemical bonding in aqueous ferrocyanide: experimental and theoretical X-ray spectroscopic study. *The Journal of Physical Chemistry B*, 118(6):1555–1563, 2014.

[151] Kristjan Kunnus, Wenkai Zhang, Mickaël G Delcey, Rahul V Pinjari, Piter S Miedema, Simon Schreck, Wilson Quevedo, Henning Schröder, Alexander Föhlisch, Kelly J Gaffney, et al. Viewing the valence electronic structure of ferric and ferrous hexacyanide in solution from the Fe and cyanide perspectives. *The Journal of Physical Chemistry B*, 120(29):7182–7194, 2016.

[152] Rosalie K Hocking, Erik C Wasinger, Frank MF de Groot, Keith O Hodgson, Britt Hedman, and Edward I Solomon. Fe L-edge XAS studies of $K_4[Fe(CN)_6]$ and $K_3[Fe(CN)_6]$: a direct probe of back-bonding. *Journal of the American Chemical Society*, 128(32):10442–10451, 2006.

[153] Miriam Shirom and Gabriel Stein. Excited state chemistry of the ferrocyanide ion in aqueous solution. I. formation of the hydrated electron. *The Journal of Chemical Physics*, 55(7):3372–3378, 1971.

[154] José Ojeda, Christopher A Arrell, Luca Longetti, Majed Chergui, and Jan Helbing. Charge-transfer and impulsive electronic-to-vibrational energy conversion in ferricyanide: Ultrafast photoelectron and transient infrared studies. *Physical Chemistry Chemical Physics*, 19(26):17052–17062, 2017.

[155] Hans Jakob Wörner, Christopher A Arrell, Natalie Banerji, Andrea Cannizzo, Majed Chergui, Akshaya K Das, Peter Hamm, Ursula Keller, Peter M Kraus, Elisa Liberatore,

et al. Charge migration and charge transfer in molecular systems. *Structural Dynamics*, 4(6):061508, 2017.

[156] M Chergui. Ultrafast photophysics and photochemistry of iron hexacyanides in solution: Infrared to X-ray spectroscopic studies. *Coordination Chemistry Reviews*, 372:52–65, 2018.

[157] Giacomo Prampolini, Pengyun Yu, Silvia Pizzanelli, Ivo Cacelli, Fan Yang, Juan Zhao, and Jianping Wang. Structure and dynamics of ferrocyanide and ferricyanide anions in water and heavy water: An insight by MD simulations and 2D IR spectroscopy. *The Journal of Physical Chemistry B*, 118(51):14899–14912, 2014.

[158] A Mokhtari, P Cong, JL Herek, and AH Zewail. Direct femtosecond mapping of trajectories in a chemical reaction. *Nature*, 348(6298):225, 1990.

[159] Ahmed H Zewail. Femtochemistry: recent progress in studies of dynamics and control of reactions and their transition states. *The Journal of Physical Chemistry*, 100(31):12701–12724, 1996.

[160] Ingolf V Hertel and Claus-Peter Schulz. *Atoms, molecules and optical physics*. Springer, 2015.

[161] Claude Rulliere. *Femtosecond laser pulses*. Springer, 2005.

[162] Albert Stolow, Arthur E Bragg, and Daniel M Neumark. Femtosecond time-resolved photoelectron spectroscopy. *Chemical Reviews*, 104(4):1719–1758, 2004.

[163] David E Spence, P Np Kean, and Wilson Sibbett. 60-fsec pulse generation from a self-mode-locked Ti: sapphire laser. *Optics Letters*, 16(1):42–44, 1991.

[164] G Cerullo, Sandro De Silvestri, Vittorio Magni, and L Pallaro. Resonators for kerr-lens mode-locked femtosecond Ti: sapphire lasers. *Optics Letters*, 19(11):807–809, 1994.

[165] Peter F Moulton. Spectroscopic and laser characteristics of $Ti:Al_2O_3$. *Journal of the Optical Society of America B*, 3(1):125–133, 1986.

[166] W Sibbett, AA Lagatsky, and CTA Brown. The development and application of femtosecond laser systems. *Optics Express*, 20(7):6989–7001, 2012.

[167] RL Fork, OE Martinez, and JP Gordon. Negative dispersion using pairs of prisms. *Optics Letters*, 9(5):150–152, 1984.

[168] Edward Miesak and Raluca Negres. Alignment procedure for a dual grating pulse compressor. *Applied Optics*, 37(34):8146–8146, 1998.

[169] Rick Trebino. *Frequency-resolved optical gating: the measurement of ultrashort laser pulses*. Springer Science & Business Media, 2012.

[170] Robert W Boyd. *Nonlinear optics*. Elsevier, 2003.

[171] SA Kovalenko, AL Dobryakov, J Ruthmann, and NP Ernsting. Femtosecond spectroscopy of condensed phases with chirped supercontinuum probing. *Physical review A*, 59(3):2369, 1999.

[172] V Blanchet, S Lochbrunner, M Schmitt, JP Shaffer, JJ Larsen, MZ Zgierski, T Seideman, and A Stolow. Towards disentangling coupled electronic–vibrational dynamics in ultrafast non-adiabatic processes. *Faraday Discussions*, 115:33–48, 2000.

[173] Douglas R Cyr and Carl C Hayden. Femtosecond time-resolved photoionization and photoelectron spectroscopy studies of ultrafast internal conversion in 1, 3, 5-hexatriene. *The Journal of Chemical Physics*, 104(2):771–774, 1996.

[174] Thomas Schultz and Ingo Fischer. Time-resolved photoelectron spectroscopy of the allyl radical: The lifetimes of the ultraviolet bands. *The Journal of Chemical Physics*, 109(14):5812–5822, 1998.

[175] Carolyn P Schick, Scott D Carpenter, and Peter M Weber. Femtosecond multiphoton ionization photoelectron spectroscopy of the S2 state of phenol. *The Journal of Physical Chemistry A*, 103(49):10470–10476, 1999.

[176] R. Haight, J. Bokor, J. Stark, R.H. Storz, R.R. Freeman, and P.H. Bucksbaum. Picosecond time-resolved photoemission study of the InP (110) surface. *Physical Review Letters*, 54(12):1302, 1985.

[177] Albert Stolow and Jonathan G Underwood. Time-resolved photoelectron spectroscopy of non-adiabatic dynamics in polyatomic molecules. In *Advances in Chemical Physics*, pages 497–584. John Wiley& Sons, Ltd, 2008.

[178] Toshinori Suzuki. Time-resolved photoelectron spectroscopy of non-adiabatic electronic dynamics in gas and liquid phases. *International Reviews in Physical Chemistry*, 31(2):265–318, 2012.

[179] Ute B Cappel, Stefan Plogmaker, Joachim A Terschlüsen, Torsten Leitner, Erik MJ Johansson, Tomas Edvinsson, Anders Sandell, Olof Karis, Hans Siegbahn, Svante Svensson, Nils Mårtensson, Håkan Rensmo, and Johan Söderström. Electronic structure dynamics in a low bandgap polymer studied by time-resolved photoelectron spectroscopy. *Physical Chemistry Chemical Physics*, 18(31):21921–21929, 2016.

[180] Akari Takayama. *High-Resolution Spin-Resolved Photoemission Spectrometer and the Rashba Effect in Bismuth Thin Films*. Springer, 2014.

[181] G Saathoff, L Miaja-Avila, M Aeschlimann, MM Murnane, and HC Kapteyn. Laser-assisted photoemission from surfaces. *Physical Review A*, 77(2):022903, 2008.

[182] Maciej Lewenstein, Ph Balcou, M Yu Ivanov, Anne L'huillier, and Paul B Corkum. Theory of high-harmonic generation by low-frequency laser fields. *Physical Review A*, 49(3):2117, 1994.

[183] Shambhu Ghimire, Anthony D DiChiara, Emily Sistrunk, Pierre Agostini, Louis F DiMauro, and David A Reis. Observation of high-order harmonic generation in a bulk crystal. *Nature Physics*, 7(2):138, 2011.

[184] Anthony D DiChiara, Emily Sistrunk, Terry A Miller, Pierre Agostini, and Louis F DiMauro. An investigation of harmonic generation in liquid media with a mid-infrared laser. *Optics Express*, 17(23):20959–20965, 2009.

[185] Heiko G Kurz, Daniel S Steingrube, Detlev Ristau, Manfred Lein, Uwe Morgner, and Milutin Kovačev. High-order-harmonic generation from dense water microdroplets. *Physical Review A*, 87(6):063811, 2013.

[186] Paul B Corkum. Plasma perspective on strong field multiphoton ionization. *Physical Review Letters*, 71(13):1994, 1993.

[187] A L'Huillier, KJ Schafer, and KC Kulander. Higher-order harmonic generation in xenon at 1064 nm: The role of phase matching. *Physical Review Letters*, 66(17):2200, 1991.

[188] Anne L'Huillier, Philippe Balcou, Sebastien Candel, Kenneth J Schafer, and Kenneth C Kulander. Calculations of high-order harmonic-generation processes in xenon at 1064 nm. *Physical Review A*, 46(5):2778, 1992.

[189] eg PA Franken, Alan E Hill, CW el Peters, and G Weinreich. Generation of optical harmonics. *Physical Review Letters*, 7(4):118, 1961.

[190] GHC New and JF Ward. Optical third-harmonic generation in gases. *Physical Review Letters*, 19(10):556, 1967.

[191] DI Metchkov, VM Mitev, LI Pavlov, and KV Stamenov. Fifth harmonic generation in sodium vapor. *Optics Communications*, 21(3):391–394, 1977.

[192] JOHN Reintjes, Chiao-Yao She, and R Eckardt. Generation of coherent radiation in xuv by fifth-and seventh-order frequency conversion in rare gases. *IEEE Journal of Quantum Electronics*, 14(8):581–596, 1978.

[193] J Bokor, PH Bucksbaum, and RR Freeman. Generation of 35.5-nm coherent radiation. *Optics Letters*, 8(4):217–219, 1983.

[194] A McPherson, G Gibson, H Jara, U Johann, Ting S Luk, IA McIntyre, Keith Boyer, and Charles K Rhodes. Studies of multiphoton production of vacuum-ultraviolet radiation in the rare gases. *Journal of the Optical Society of America B*, 4(4):595–601, 1987.

[195] XF Li, A L'Huillier, M Ferray, LA Lompré, and G Mainfray. Multiple-harmonic generation in rare gases at high laser intensity. *Physical Review A*, 39(11):5751, 1989.

[196] Kenzo Miyazaki and Hirofumi Sakai. High-order harmonic generation in rare gases with intense subpicosecond dye laser pulses. *Journal of Physics B: Atomic, Molecular and Optical Physics*, 25(3):L83, 1992.

[197] Anne L'Huillier and Ph Balcou. High-order harmonic generation in rare gases with a 1-ps 1053-nm laser. *Physical Review Letters*, 70(6):774, 1993.

[198] Thomas Brabec and Ferenc Krausz. Intense few-cycle laser fields: Frontiers of nonlinear optics. *Reviews of Modern Physics*, 72(2):545, 2000.

[199] Philippe Antoine, Anne L'huillier, and Maciej Lewenstein. Attosecond pulse trains using high–order harmonics. *Physical Review Letters*, 77(7):1234, 1996.

[200] Pascal Salieres and Maciej Lewenstein. Generation of ultrashort coherent XUV pulses by harmonic conversion of intense laser pulses in gases: towards attosecond pulses. *Measurement Science and Technology*, 12(11):1818, 2001.

[201] Matthias Uiberacker, Th Uphues, Martin Schultze, Aart Johannes Verhoef, Vladislav Yakovlev, Matthias F Kling, Jens Rauschenberger, Nicolai M Kabachnik, Hartmut Schröder, Matthias Lezius, et al. Attosecond real-time observation of electron tunnelling in atoms. *Nature*, 446(7136):627, 2007.

[202] Alexandre Moguilevski, Martin Wilke, Gilbert Grell, Sergey I Bokarev, Saadullah G Aziz, Nicholas Engel, Azhr A Raheem, Oliver Kühn, Igor Yu Kiyan, and Emad F Aziz. Ultrafast spin crossover in $[Fe^{II}(bpy)_3]^{2+}$: Revealing two competing mechanisms by extreme ultraviolet photoemission spectroscopy. *ChemPhysChem*, 18(5):465–469, 2017.

[203] Oren Cohen, Amy L Lytle, Xiaoshi Zhang, Margaret M Murnane, and Henry C Kapteyn. Optimizing quasi-phase matching of high harmonic generation using counterpropagating pulse trains. *Optics Letters*, 32(20):2975–2977, 2007.

[204] SL Voronov, I Kohl, JB Madsen, J Simmons, N Terry, J Titensor, Q Wang, and J Peatross. Control of laser high-harmonic generation with counterpropagating light. *Physical Review Letters*, 87(13):133902, 2001.

[205] William T Silfvast. *Laser fundamentals*. Cambridge university press, 2004.

[206] Jorge J Rocca. Table-top soft X-ray lasers. *Review of Scientific Instruments*, 70(10):3799–3827, 1999.

[207] David Attwood, Klaus Halbach, and Kwang-Je Kim. Tunable coherent X-rays. *Science*, 228(4705):1265–1272, 1985.

[208] Kwang-Je Kim and Andrew Sessler. Free-electron lasers: present status and future prospects. *Science*, 250(4977):88–93, 1990.

[209] Donna Strickland and Gerard Mourou. Compression of amplified chirped optical pulses. *Optics Communications*, 55(6):447–449, 1985.

[210] Sterling Backus, Charles G Durfee III, Margaret M Murnane, and Henry C Kapteyn. High power ultrafast lasers. *Review of Scientific Instruments*, 69(3):1207–1223, 1998.

[211] J Zhou, J Peatross, MM Murnane, HC Kapteyn, and IP Christov. Enhanced high-harmonic generation using 25 fs laser pulses. *Physical Review Letters*, 76(5):752, 1996.

[212] Zenghu Chang, Andy Rundquist, Haiwen Wang, Margaret M Murnane, and Henry C Kapteyn. Generation of coherent soft X-rays at 2.7 nm using high harmonics. *Physical Review Letters*, 79(16):2967, 1997.

[213] Geoffrey New. *Introduction to nonlinear optics*. Cambridge University Press, 2011.

[214] KC Kulander, KJ Schafer, and JL Krause. Theoretical model for intense field high-order harmonic generation in rare gases. *Laser Physics*, 3(2):359–364, 1993.

[215] Jeffrey L Krause, Kenneth J Schafer, and Kenneth C Kulander. High-order harmonic generation from atoms and ions in the high intensity regime. *Physical Review Letters*, 68(24):3535, 1992.

[216] David N Fittinghoff, Paul R Bolton, Britton Chang, and Kenneth C Kulander. Observation of nonsequential double ionization of helium with optical tunneling. *Physical Review Letters*, 69(18):2642, 1992.

[217] Barry Walker, Eric Mevel, Baorui Yang, Pierre Breger, Jean-Paul Chambaret, Andre Antonetti, Louis F DiMauro, and Pierre Agostini. Double ionization in the perturbative and tunneling regimes. *Physical Review A*, 48(2):R894, 1993.

[218] Jozsef Seres, V.S. Yakovlev, E. Seres, Ch. Streli, Peter Wobrauschek, Ch. Spielmann, and Ferenc Krausz. Coherent superposition of laser-driven soft-X-ray harmonics from successive sources. *Nature Physics*, 3(12):878, 2007.

[219] LV Keldysh et al. Ionization in the field of a strong electromagnetic wave. *Sov. Phys. JETP*, 20(5):1307–1314, 1965.

[220] SV Popruzhenko. Keldysh theory of strong field ionization: history, applications, difficulties and perspectives. *Journal of Physics B: Atomic, Molecular and Optical Physics*, 47(20):204001, 2014.

[221] Nikolaj B Delone and Vladimir Pavlovich Kraĭnov. *Atoms in strong light fields*, volume 28. Springer-Verlag, 1985.

[222] Steeve Augst, David D Meyerhofer, Donna Strickland, and See-Leang Chin. Laser ionization of noble gases by coulomb-barrier suppression. *Journal of the Optical Society of America B*, 8(4):858–867, 1991.

[223] JH Posthumus. The dynamics of small molecules in intense laser fields. *Reports on Progress in Physics*, 67(5):623, 2004.

[224] Stefan Hüfner. Band structure and angular-resolved photoelectron spectra. In *Photoelectron Spectroscopy*, pages 411–500. Springer, 2003.

[225] Carsten Winterfeldt, Christian Spielmann, and Gustav Gerber. Colloquium: Optimal control of high-harmonic generation. *Reviews of Modern Physics*, 80(1):117, 2008.

[226] Tenio Popmintchev, Ming-Chang Chen, Dimitar Popmintchev, Paul Arpin, Susannah Brown, Skirmantas Ališauskas, Giedrius Andriukaitis, Tadas Balčiunas, Oliver D Mücke, Audrius Pugzlys, et al. Bright coherent ultrahigh harmonics in the kev x-ray regime from mid-infrared femtosecond lasers. *science*, 336(6086):1287–1291, 2012.

[227] Alessandro Averchi, Daniele Faccio, Ricardo Berlasso, Miroslav Kolesik, Jerome V Moloney, Arnaud Couairon, and Paolo Di Trapani. Phase matching with pulsed bessel beams for high-order harmonic generation. *Physical Review A*, 77(2):021802, 2008.

[228] T Pfeifer, Ch Spielmann, and G Gerber. Femtosecond x-ray science. *Reports on Progress in Physics*, 69(2):443, 2006.

[229] JT Verdeyen and JB Gerardo. Application of the laser to plasma refractive index determination. *Annals of the New York Academy of Sciences*, 122(2):676–684, 1965.

[230] Karsten Rottwitt and Peter Tidemand-Lichtenberg. *Nonlinear optics: principles and applications*. CRC Press, 2014.

[231] Charles G Durfee III, Andy R Rundquist, Sterling Backus, Catherine Herne, Margaret M Murnane, and Henry C Kapteyn. Phase matching of high-order harmonics in hollow waveguides. *Physical Review Letters*, 83(11):2187, 1999.

[232] Pascal Salieres, Anne L'Huillier, and Maciej Lewenstein. Coherence control of high-order harmonics. *Physical Review Letters*, 74(19):3776, 1995.

[233] Mette Borg Gaarde, F Salin, E Constant, Ph Balcou, KJ Schafer, KC Kulander, and Anne L'Huillier. Spatiotemporal separation of high harmonic radiation into two quantum path components. *Physical Review A*, 59(2):1367, 1999.

[234] T Auguste, B Carré, and P Salières. Quasi-phase-matching of high-order harmonics using a modulated atomic density. *Physical Review A*, 76(1):011802, 2007.

[235] S Passlack, S Mathias, O Andreyev, D Mittnacht, M Aeschlimann, and M Bauer. Space charge effects in photoemission with a low repetition, high intensity femtosecond laser source. *Journal of Applied Physics*, 100(2):024912, 2006.

[236] Annette Pietzsch, Alexander Föhlisch, Martin Beye, Martin Deppe, Franz Hennies, Mitsuru Nagasono, E Suljoti, W Wurth, C Gahl, K Döbrich, et al. Towards time resolved core level photoelectron spectroscopy with femtosecond x-ray free-electron lasers. *New Journal of Physics*, 10(3):033004, 2008.

[237] LP Oloff, M Oura, K Rossnagel, A Chainani, M Matsunami, R Eguchi, T Kiss, Y Nakatani, T Yamaguchi, J Miyawaki, et al. Time-resolved haxpes at sacla: probe and pump pulse-induced space-charge effects. *New Journal of Physics*, 16(12):123045, 2014.

[238] P Siffalovic, Markus Drescher, and Ulrich Heinzmann. Femtosecond time-resolved core-level photoelectron spectroscopy tracking surface photovoltage transients on p–GaAs. *Europhysics Letters*, 60(6):924, 2002.

[239] R Al-Obaidi, M Wilke, M Borgwardt, J Metje, A Moguilevski, N Engel, D Tolksdorf, A Raheem, T Kampen, S Mähl, I. Yu. Kiyan, and E. F. Aziz. Ultrafast photoelectron spectroscopy of solutions: space-charge effect. *New Journal of Physics*, 17(9):093016, 2015.

[240] Ch Spielmann, NH Burnett, S Sartania, R Koppitsch, M Schnürer, C Kan, M Lenzner, P Wobrauschek, and F Krausz. Generation of coherent X-rays in the water window using 5-femtosecond laser pulses. *Science*, 278(5338):661–664, 1997.

[241] Henry C Kapteyn, Margaret M Murnane, and Ivan P Christov. Extreme nonlinear optics: coherent x rays from lasers. *Phys. Today*, 58(3):39–46, 2005.

[242] A Weingartshofer, JK Holmes, G Caudle, EM Clarke, and H Krüger. Direct observation of multiphoton processes in laser-induced free-free transitions. *Physical Review Letters*, 39(5):269, 1977.

[243] TE Glover, RW Schoenlein, AH Chin, and CV Shank. Observation of laser assisted photoelectric effect and femtosecond high order harmonic radiation. *Physical Review Letters*, 76(14):2468, 1996.

[244] M Meyer, D Cubaynes, P O'keeffe, H Luna, Patrick Yeates, Eugene T Kennedy, John T Costello, P Orr, R Taïeb, A Maquet, et al. Two-color photoionization in xuv free-electron and visible laser fields. *Physical Review A*, 74(1):011401, 2006.

[245] Adrian L Cavalieri, Norbert Müller, Th Uphues, Vladislav S Yakovlev, Andrius Baltuška, Balint Horvath, B Schmidt, L Blümel, R Holzwarth, Stefan Hendel, et al. Attosecond spectroscopy in condensed matter. *Nature*, 449(7165):1029, 2007.

[246] Luis Miaja-Avila, C Lei, M Aeschlimann, JL Gland, MM Murnane, HC Kapteyn, and G Saathoff. Laser-assisted photoelectric effect from surfaces. *Physical Review Letters*, 97(11):113604, 2006.

[247] CA Arrell, J Ojeda, L Mewes, J Grilj, F Frassetto, L Poletto, F Van Mourik, and M Chergui. Laser-assisted photoelectric effect from liquids. *Physical Review Letters*, 117(14):143001, 2016.

[248] JM Schins, P Breger, P Agostini, RC Constantinescu, HG Muller, A Bouhal, G Grillon, A Antonetti, and A Mysyrowicz. Cross-correlation measurements of femtosecond extreme-ultraviolet high-order harmonics. *Journal of the Optical Society of America B*, 13(1):197–200, 1996.

[249] Jan Metje, Mario Borgwardt, Alexandre Moguilevski, Alexander Kothe, Nicholas Engel, Martin Wilke, Ruba Al-Obaidi, Daniel Tolksdorf, Alexander Firsov, Maria Brzhezinskaya, Alexei Erko, Igor Y.u. Kiyan, and E. F. Aziz. Monochromatization of femtosecond XUV light pulses with the use of reflection zone plates. *Optics Express*, 22(9):10747–10760, 2014.

[250] J Michael Hollas. *Modern spectroscopy*. John Wiley & Sons, 2004.

[251] Graham Fleming. *Chemical applications of ultrafast spectroscopy*. Oxford University Press, New York, NY, 1986.

[252] Alfons Kawski. Fluorescence anisotropy: theory and applications of rotational depolarization. *Critical Reviews in Analytical Chemistry*, 23(6):459–529, 1993.

[253] Oliver Schalk and Andrey E Boguslavskiy. Anisotropy in time-resolved photoelectron spectroscopy in the gas phase. *The Journal of Physical Chemistry A*, 121(50):9612–9618, 2017.

[254] Oliver Schalk and Andreas N Unterreiner. The influence of rotational diffusion on transient anisotropy in ultrafast experiments. *Physical Chemistry Chemical Physics*, 12(3):655–666, 2010.

[255] Oliver Schalk, Andrey E Boguslavskiy, Michael S Schuurman, Rasmus Y Brogaard, Andreas N Unterreiner, Anna Wrona-Piotrowicz, Nick H Werstiuk, and Albert Stolow. Substituent effects on dynamics at conical intersections: cycloheptatrienes. *The Journal of Physical Chemistry A*, 117(40):10239–10247, 2013.

[256] Katharine L Reid. Photoelectron angular distributions. *Annual Review of Physical Chemistry*, 54(1):397–424, 2003.

[257] Katharine L Reid. Photoelectron angular distributions: developments in applications to isolated molecular systems. *Molecular Physics*, 110(3):131–147, 2012.

[258] Guorong Wu, Paul Hockett, and Albert Stolow. Time-resolved photoelectron spectroscopy: from wavepackets to observables. *Physical Chemistry Chemical Physics*, 13(41):18447–18467, 2011.

[259] Andrea Volpato, Luca Bolzonello, Elena Meneghin, and Elisabetta Collini. Global analysis of coherence and population dynamics in 2d electronic spectroscopy. *Optics Express*, 24(21):24773–24785, 2016.

[260] Ivo HM van Stokkum, Delmar S Larsen, and Rienk van Grondelle. Global and target analysis of time-resolved spectra. *Biochimica et Biophysica Acta (BBA)-Bioenergetics*, 1657(2-3):82–104, 2004.

[261] P Fita, E Luzina, T Dziembowska, Cz Radzewicz, and A Grabowska. Chemistry, photophysics, and ultrafast kinetics of two structurally related schiff bases containing the naphthalene or quinoline ring. *The Journal of Chemical Physics*, 125(18):184508, 2006.

[262] Giulio Cerullo and Sandro De Silvestri. Ultrafast optical parametric amplifiers. *Review of Scientific Instruments*, 74(1):1, 2003.

[263] Motohiko Ito, Yoshimasa Kataoka, Tatsuya Okamoto, Mikio Yamashita, and Taro Sekikawa. Spatiotemporal characterization of single-order high harmonic pulses from time-compensated toroidal-grating monochromator. *Optics Express*, 18(6):6071–6078, 2010.

[264] Luca Poletto, Paolo Villoresi, Fabio Frassetto, Francesca Calegari, Federico Ferrari, Matteo Lucchini, Giuseppe Sansone, and Mauro Nisoli. Time-delay compensated monochromator for the spectral selection of extreme-ultraviolet high-order laser harmonics. *Review of Scientific Instruments*, 80(12):123109, 2009.

[265] Niklas Ottosson, Manfred Faubel, Stephen E Bradforth, Pavel Jungwirth, and Bernd Winter. Photoelectron spectroscopy of liquid water and aqueous solution: Electron effective attenuation lengths and emission-angle anisotropy. *Journal of Electron Spectroscopy and Related Phenomena*, 177(2-3):60–70, 2010.

[266] M Michaud, A Wen, and L Sanche. Cross sections for low-energy (1–100 ev) electron elastic and inelastic scattering in amorphous ice. *Radiation Research*, 159(1):3–22, 2003.

[267] Bernd Winter. Liquid microjet for photoelectron spectroscopy. *Nuclear Instruments and Methods in Physics Research Section A: Accelerators, Spectrometers, Detectors and Associated Equipment*, 601(1-2):139–150, 2009.

[268] Robert Seidel, Stephan Thürmer, and Bernd Winter. Photoelectron spectroscopy meets aqueous solution: studies from a vacuum liquid microjet. *The Journal of Physical Chemistry Letters*, 2(6):633–641, 2011.

[269] GLJ Bailey, S Fordham, and JT Tyson. The surface structure of liquid mercury. *Proceedings of the Physical Society*, 50(1):63, 1938.

[270] Hans Siegbahn and Kai Siegbahn. Esca applied to liquids. *Journal of Electron Spectroscopy and Related Phenomena*, 2(3):319–325, 1973.

[271] M Faubel, S Schlemmer, and JP Toennies. A molecular beam study of the evaporation of water from a liquid jet. *Zeitschrift für Physik D Atoms, Molecules and Clusters*, 10(2-3):269–277, 1988.

[272] M Faubel and Th Kisters. Non-equilibrium molecular evaporation of carboxylic acid dimers. *Nature*, 339(6225):527, 1989.

[273] Bernd Winter, Ramona Weber, Ingolf V Hertel, Manfred Faubel, Pavel Jungwirth, Eric C Brown, and Stephen E Bradforth. Electron binding energies of aqueous alkali and halide ions: EUV photoelectron spectroscopy of liquid solutions and combined ab initio and molecular dynamics calculations. *Journal of the American Chemical Society*, 127(19):7203–7214, 2005.

[274] Naoya Kurahashi, Shutaro Karashima, Ying Tang, Takuya Horio, Bumaliya Abulimiti, Yoshi-Ichi Suzuki, Yoshihiro Ogi, Masaki Oura, and Toshinori Suzuki. Photoelectron spectroscopy of aqueous solutions: Streaming potentials of NaX (X= Cl, Br, and I) solutions and electron binding energies of liquid water and X^-. *The Journal of Chemical Physics*, 140(17):174506, 2014.

[275] Andreas Oelsner, Martin Rohmer, Christian Schneider, Daniela Bayer, Gerd Schönhense, and Martin Aeschlimann. Time-and energy resolved photoemission electron microscopy-imaging of photoelectron time-of-flight analysis by means of pulsed excitations. *Journal of Electron Spectroscopy and Related Phenomena*, 178:317–330, 2010.

[276] Manfred Faubel, Björn Steiner, and J Peter Toennies. Photoelectron spectroscopy of liquid water, some alcohols, and pure nonane in free micro jets. *The Journal of Chemical Physics*, 106(22):9013–9031, 1997.

[277] B Winter, R Weber, W Widdra, M Dittmar, M Faubel, and IV Hertel. Full valence band photoemission from liquid water using euv synchrotron radiation. *The Journal of Physical Chemistry A*, 108(14):2625–2632, 2004.

[278] W Gädeke, EE Koch, G Dräger, R Frahm, and V Saile. Electronic structure and local geometry of $Na_2[Fe(CN)_5NO].2H_2O$ single crystals investigated by polarization-dependent x-ray absorption spectroscopy. *Chemical Physics*, 124(1):113–119, 1988.

[279] T Hertel, E Knoesel, M Wolf, and G Ertl. Ultrafast electron dynamics at Cu (111): response of an electron gas to optical excitation. *Physical Review Letters*, 76(3):535, 1996.

[280] Ottó Horváth and Kenneth L Stevenson. *Charge transfer photochemistry of coordination compounds*. Wiley-VCH, 1993.

[281] Mihail Atanasov and Thomas Schönherr. The unique spectroscopic behavior of the Fe (III)-nitroprusside: a DFT study of the vibronic coupling in the ground and in the lowest excited state. *Journal of Molecular Structure: THEOCHEM*, 592(1-3):79–93, 2002.

[282] Takeshi Ishikawa and Kiyoshi Tanaka. Theoretical study of the photoinduced transfer among the ground state and two metastable states in $[Fe(CN)_5NO]^{2-}$. *The Journal of Chemical Physics*, 122(7):074314, 2005.

[283] Balkrishna V Sukhatme. A two sample distribution free test for comparing variances. *Biometrika*, 45(3/4):544–548, 1958.

[284] Theodore S Donaldson. Robustness of the f-test to errors of both kinds and the correlation between the numerator and denominator of the f-ratio. *Journal of the American Statistical Association*, 63(322):660–676, 1968.

[285] Milton Abramowitz and Irene A Stegun. *Handbook of mathematical functions with formulas, graphs, and mathematical tables*, volume 55. US Government Printing Office, 1964.

[286] PCB Phillips. The true characteristic function of the f distribution. *Biometrika*, 69(1):261–264, 1982.

[287] Björn O Roos, Roland Lindh, Per-Åke Malmqvist, Valera Veryazov, and Per-Olof Widmark. New relativistic ANO basis sets for transition metal atoms. *The Journal of Physical Chemistry A*, 109(29):6575–6579, 2005.

[288] Marvin Douglas and Norman M Kroll. Quantum electrodynamical corrections to the fine structure of helium. *Annals of Physics*, 82(1):89–155, 1974.

[289] Jun Chang, AJ Fedro, and Michel van Veenendaal. Ultrafast electron dynamics theory of photo-excited ruthenium complexes. *arXiv preprint arXiv:1003.4752*, 2010.

[290] E Coronado, S Klokishner, O Reu, and B Tsukerblat. A pseudo-Jahn–Teller model of the photochromic effect in sodium nitroprusside. *Polyhedron*, 22(14-17):2527–2535, 2003.

[291] M Buchs, Claude A Daul, PT Manoharan, and Carl-Wilhelm Schläpfer. Density functional study of nitroprusside: Mechanism of the photochemical formation and deactivation of the metastable states. *International Journal of Quantum Chemistry*, 91(3):418–431, 2003.

[292] Bernd Winter and Manfred Faubel. Photoemission from liquid aqueous solutions. *Chemical Reviews*, 106(4):1176–1211, 2006.

[293] Nicholas Engel, Sergey I Bokarev, Alexandre Moguilevski, Azhr A Raheem, Ruba Al-Obaidi, Tobias Möhle, Gilbert Grell, Katrin R Siefermann, Bernd Abel, Oliver Kühn, Mario Borgwardt, Igor Yu. Kiyan, Saadullah G Aziz, and Emad F. Aziz. Light-induced relaxation dynamics of the ferricyanide ion revisited by ultrafast XUV photoelectron spectroscopy. *Physical Chemistry Chemical Physics*, 19(22):14248–14255, 2017.

[294] Jens Aßmann, Matthias Kling, and Bernd Abel. Watching photoinduced chemistry and molecular energy flow in solution in real time. *Angewandte Chemie International Edition*, 42(20):2226–2246, 2003.

[295] Rebekka S von Benten and Bernd Abel. On the nature of intramolecular vibrational energy transfer in dense molecular environments. *Chemical Physics*, 378(1-3):19–26, 2010.

[296] Pengyun Yu, Fan Yang, Juan Zhao, and Jianping Wang. Hydration dynamics of cyanoferrate anions examined by ultrafast infrared spectroscopy. *The Journal of Physical Chemistry B*, 118(11):3104–3114, 2014.

List of Publications

1. **A. A. Raheem**, M. Wilke, M. Borgwardt, N. Engel, S. I. Bokarev, G. Grell, S. G.Aziz, O. Kühn, I. Y. Kiyan, C. Merschjann *et al*, "Ultrafast kinetics of linkage isomerism in $Na_2[Fe(CN)_5NO]$ aqueous solution revealed by time-resolved photoelectron spectroscopy," Structural Dynamics, vol. 4, no. 4, p. 044031, 2017.

2. N. Engel, S. I. Bokarev, A. Moguilevski, **A. A. Raheem**, R. Al-Obaidi, T. Möhle, G. Grell, K. R. Siefermann, B. Abel, S. G. Azi*et al*, "Light-induced relaxation dynamics of the ferricyanide ion revisited by ultrafast xuv photoelectron spectroscopy," Physical Chemistry Chemical Physics, vol. 19, no. 22, pp. 14 248–14 255, 2017.

3. R. Al-Obaidi, M. Wilke, M. Borgwardt, J. Metje, A. Moguilevski, N. Engel, D. Tolksdorf, **A. Raheem**, T. Kampen, S. Mähl *et al*, "Ultrafast photoelectron spectroscopy of solutions: space-charge effect," New Journal of Physics, vol. 17, no. 9, p. 093016, 2015.

4. A. Moguilevski, M. Wilke, G. Grell, S. I. Bokarev, S. G. Aziz, N. Engel, **A. A. Raheem**, O. Kühn, I. Y. Kiyan, and E. F. Aziz, "Ultrafast spin crossover in $[Fe^{II}(bpy)_3]^{2+}$: Revealing two competing mechanisms by extreme ultraviolet photoemission spectroscopy," ChemPhysChem, vol. 18, no. 5, pp. 465–469, 2017.

Articles in preparation

1. Nataliia Kuzkova, Azhr A. Raheem, Christoph Merschjann, Iain Wilkinson and Igor Yu. Kiyan, "Effect of liquid environment on photoinduced relaxation dynamics of $[Fe(CN)_6]^{3-}$".

2. Azhr A. Raheem, Christoph Merschjann, Igor Yu. Kiyan and Iain Wilkinson, "Investigation of the MS1 state formation in nitroprusside aqueous solution measured by XUV photoemission spectroscopy".

Acknowledgements

First of all, I want to thank and state my gratitude to God the most merciful for giving me many good things in my life.

I would like to express my sincere gratitude to my first supervisor Dr. Iain Wilkinson for helping me in finalizing my study and my thesis, for frequent motivation, for sharing his experience, substantial scientific discussion and lots of scientific inspiration.

Also, I would thank Prof. Martin Weinelt from Freie Universitat Berlin for being the second reviewer of my thesis.

I want to thank Dr. Christoph Merschjann for supervising my Ph.D. thesis. I am extremely thankful and indebted to him for sharing his expertise, his sincere and valuable guidance and the encouragement extended to me.

I would also like to thank my co-supervisor Dr. Igor Kiyan for taking care of the laser system, for the technical assistance and for co-supervising my thesis. His experience and suggestions were always helpful to me.

Very special thanks to Dr.Martin Wilke, who supported me in the experiments investigating the ultrafast dynamics in the nitroprusside aqueous solution. I am additionally grateful for his continued support in learning about Mathematica during the data analysis.

I am thankful to my group members for their friendly advice during the project work. I am sincerely grateful to them for sharing their truthful and illuminating views on a number of issues related to the research. Therefore, I would thank Dr.Ruba Al-Obaidi, Mr.Nicholas Engel, Dr.Mario Borgwardt, Dr.Jan Metje, and Ms.Nataliia Kuskova.

I would like to express my deepest appreciation to my family who supported me during my Ph.D. study.

Furthermore, I am using this opportunity to express my gratitude to everyone who supported me throughout my Ph.D. study.

Selbständigkeitserklärung

Hiermit versichere ich, die vorliegende Arbeit selbstständig und ausschließlich unter Benutzung der angegebenen Quellen und Hilfsmittel verfasst zu haben.

Ich erkläre weiterhin, dass die vorliegende Arbeit nicht im Rahmen eines früheren Promotionsverfahrens an einer anderen Stelle eingereicht worden ist.

Azhr Abdulzahraa Raheem
Berlin, den 2019